Thèse de doctorat

Université de Limoges

Université de Limoges

ED 609 - Sciences et Ingénierie des Matériaux, Mécanique, Énergétique (SIMME)

Institut de Recherche sur les Céramiques (IRCER) – UMR CNRS 7315

Thèse pour obtenir le grade de
Docteur de l'Université de Limoges
Matériaux Céramiques et Traitements de Surface

Présentée et soutenue par
Dmitrii IVCHENKO

Le 20 Décembre 2018

Modélisation et dimensionnement d'un procédé de dépôt physique en phase vapeur assisté par plasma thermique

Thèse dirigée par **Gilles MARIAUX**, **Simon GOUTIER**, **Tatiana E. ITINA**

JURY :

Rapporteurs
Pascal BRAULT, Directeur de Recherche, GREMI, Université d'Orléans
Ludovic HALLO, Ingénieur-chercheur-HDR, CEA Cesta, Le Barp

Examinateurs
Georg MAUER, Docteur, Institut für Energie- und Klimaforschung, Jülich (Allemagne)
Pascal ANDRÉ, Professeur, LPC, Université de Clermont-Ferrand
Tatiana E. ITINA, Directrice de Recherche CNRS, LHC, Université Jean Monnet
Simon GOUTIER, Maitre de Conférences, IRCER, Université de Limoges
Gilles MARIAUX, Professeur, IRCER, Université de Limoges

Invités
Marjorie CAVARROC, Docteur, SafranTech, Magny-les-Hameaux
Alexander BARTH, Ingénieur, Oerlikon Metco AG, Wohlen (Suisse)
Armelle VARDELLE, Professeur, IRCER, Université de Limoges

PhD thesis

Université de Limoges

Université de Limoges

ED 609 - Sciences et Ingénierie des Matériaux, Mécanique, Énergétique (SIMME)

Institute of Research on Ceramics (IRCER) – UMR CNRS 7315

A thesis presented for the degree of

Doctor of philosophy of the University of Limoges

Ceramic Materials and Surface Treatments

Presented by

Dmitrii IVCHENKO

December 20, 2018

Modeling and design of a physical vapor deposition process assisted by thermal plasma (PS-PVD)

Supervisors: **Gilles MARIAUX**, **Simon GOUTIER**, **Tatiana E. ITINA**

JURY :

Referees

Pascal BRAULT, Research Director, GREMI, University of Orléans
Ludovic HALLO, Research Engineer, CEA Cesta, Le Barp

Inspectors

Georg MAUER, Doctor, Institut für Energie- und Klimaforschung, Jülich (Germany)
Pascal ANDRÉ, Professor, LPC, University of Clermont-Ferrand
Tatiana E. ITINA, CNRS Research Director, LHC, Jean Monnet University
Simon GOUTIER, Associate Professor, IRCER, University of Limoges
Gilles MARIAUX, Professor, IRCER, University of Limoges

Invited members

Marjorie CAVARROC, Doctor, SafranTech, Magny-les-Hameaux
Alexander BARTH, Engineer, Oerlikon Metco AG, Wohlen (Switzerland)
Armelle VARDELLE, Professor, IRCER, University of Limoges

Dedicated to Sci-Hub project and all the people supporting it.

“Most of the time spent wrestling with technologies that don't quite work yet is just not worth it for end users, however much fun it is for nerds.”

-Douglas Adams, The Salmon of Doubt

Acknowledgments

I would like to express my sincerest gratitude to the Région Limousin (later merged into the Région Nouvelle-Aquitaine) for providing the financial support for this thesis. I would also like to offer my special thanks to my supervisors Gilles Mariaux, Simon Goutier and Tatiana E. Itina for their flawless guidance, continuous support and encouragement. I am particularly grateful to Prof. Gilles Mariaux for investing so much time and effort into this work, for introducing me into the bizarre yet intriguing French culture and for being a reliable ally.

Apart from my supervisors, I would like to thank Prof. Armelle Vardelle for her constructive suggestions, incredibly useful criticism and willingness to invest her time and effort into pushing the boundaries of what can be achieved.

Assistance provided by Prof. Michel Vardelle and Marina Soustre during the experimental studies was greatly appreciated.

I also express my gratitude to Prof. Pascal André of Laboratoire de Physique de Clermont, France, and Dr. Anthony B. Murphy of The Commonwealth Scientific and Industrial Research Organisation (CSIRO), Australia, for the calculations of gas properties at low pressures, to Dr. Georg Mauer and Wenting He of Institut für Energie- und Klimaforschung, Jülich, Germany, for providing valuable experimental data needed for my model validation, and to Dr. Svetlana E. Selezneva of General Electric Global Research Center, Albany, New York, for sharing her knowledge concerning rarefied gas dynamics and Monte Carlo simulations.

And, finally, I would like to thank my dearest friends Igor, Rodion, Midoo and Chris for their fruitful discussion, emotional support and making me truly understand that friendship has no borders.

Authors' rights

Table of Contents

Acknowledgments 7

Authors' rights 8

Table of Contents 9

Abbreviations, Symbols and Nomenclature 11

Introduction 17

Chapter I. Process Review 21

I.1. Introduction 21

I.2. Thermal Barrier Coatings 21

I.3. TBC Deposition Processes 22

I.4. Conclusion 41

Chapter II. Review of Existing Models 43

II.1. Introduction 43

II.2. Plasma Flow Modeling 43

II.3. Powder Transport and Evaporation 72

II.4. Nucleation and Coating Deposition 80

II.5. Conclusion 89

Chapter III. Model of the Proposed System 91

III.1. Introduction 91

III.2. CFD-based Models 92

III.3. Linked DSMC and Nucleation and Growth Model of the Low Pressure Chamber 108

III.4. Conclusion 118

Chapter IV. System Design 121

IV.1. Introduction 121

IV.2. Determination of Torch Operating Parameters 123

IV.3. Estimation of Initial Dimensions 124

IV.4. Nozzle Design Refinement 129

IV.5. Nozzle Design Optimization 135

IV.6. Conclusion 158

General Conclusion and Perspectives 161

1. High Pressure Chamber 161

2. Expansion Nozzle 162

3. Low Pressure Chamber 164

References 166

Annexes 177

Annex A. Reference Data 178
Annex B. Variable Step Numerical Scheme 180
Annex C. Boundary Profiles on the Expansion Nozzle Outlet 181
List of Illustrations 184
List of Tables 189

Abbreviations, Symbols and Nomenclature

List of Abbreviations

2T	Two-temperature
APS	Atmospheric plasma spraying
CAPS	Controlled atmosphere plasma spraying
CCD	Charge-coupled device
CFD	Continuum fluid dynamics
CMAS	Calcium–magnesium–aluminosilicate
CNT	Classical nucleation theory
DC	Direct current
DPM	Discrete phase model
DSMC	Direct simulation Monte Carlo
EB-PVD	Electron beam physical vapor deposition
ETP	Expanding Thermal Plasma
FCT	Furnace cycling test
FVM	Finite volume method
GLL	Gradient-length local
HPC	High pressure chamber
IATA	The International Air Transport Association
IEA	The International Energy Agency
KNT	Kinetic nucleation theory
LME	Local Maxwell equilibrium
LPC	Low pressure chamber
LSE	Local Saha equilibrium
LTE	Local thermal equilibrium
NTC	No time counter
PE	Planck equilibrium
PLTE	Partial local thermodynamic equilibrium
PS	Proposed system
PS-CVD	Plasma spray chemical vapor deposition
PSDF	Particle size distribution function
PS-PVD	Plasma spray-physical vapor deposition
PVD	Physical vapor deposition

RANS	Reynold-averaged Navier-Stokes
SEM	Scanning electron microscope
SPPS	Solution precursor plasma spray
SPS	Suspension plasma spray
SSDM	Structure spatial distribution model
SZM	Structure zone model
TBC	Thermal barrier coating
TCE	Total collision energy
TE	Thermodynamic equilibrium
TGO	Thermally grown oxide
VHS	Variable hard sphere
VLPPS	Very low pressure plasma spray
VSS	Variable soft sphere
YZS	Yttria-stabilized zirconia

Latin Symbols

a_c	accommodation coefficient	
b	miss distance	m
c	molecular velocity	m/s
c_p	specific heat of the gas	J/kg/K
C_p	specific heat of a particle	J/kg/K
d	diameter	m
D	diffusion coefficients	m^2/s
E	specific energy	J/kg
F	force	N
f	probability density function	
F_N	scale factor	
G	free energy	J
g	gravitational acceleration or number of monomers in a g-mer	m/s^2 or unitless
h	specific enthalpy or heat transfer coefficient	J/kg or $W/m^2/K$
J	diffusion flux or nucleation rate	$kg/m^2/s$ or $m^{-3}s^{-1}$
K	forward reaction rate	
k	thermal conductivity or turbulent kinetic energy	W/m/K or J/kg
k_B	Boltzmann constant	J/K
L	latent heat of vaporization	J/kg
m	mass	kg
M	molar mass	kg/mol
n	number density	m^{-3}
N	number of molecules	
Na	Avogadro constant	mol^{-1}
P	probability	
p	static pressure	Pa
q_f	heat flux	W
R	ideal gas constant	J/K/mol
R_f	random fraction	
S	source term or supersaturation ratio	
T	temperature	K
t	time	s

v	velocity	m/s
V	volume	m^3
v_1	monomer volume	m^3
X	mass fraction of liquefied material in the particle	
x	molar fraction	
Y	mass fraction of the gas mixture component	
Z	relaxation factor	

Greek Symbols

α	empirical factor of VSS model or angle	
β	inverse most probable speed	s/m
Γ	general diffusion coefficient or gamma function	
Δ	change of a quantity	
ΔH	latent heat of meting	J/kg
ε	turbulence dissipation rate or emissivity	J/kg/s or unitless
ζ	number of internal degrees of freedom	
η	Arrhenius exponent	
θ	angle between velocity vector components or dimensionless surface energy	° or unitless
Θ	characteristic temperature	
κ_g	thermal conductivity of the gas	W/m/K
Λ	pre-exponential factor in the Arrhenius law	
μ	molecular viscosity	kg/m/s
π	pi	
ρ	flow density	kg/m^3
σ	collision cross-section or Stefan-Boltzmann constant	m^2 or $W/m^2/K^4$
τ	stress tensor or characteristic time	N/m^2 or s
ϕ	general variable	
χ	deflection angle	
ω	specific dissipation rate	1/s
Ω	solid angle	
ω	temperature exponent of the coefficient of viscosity	

Dimensionless Numbers

Bi	Biot number
B_m	Spalding mass transfer number
B_t	Spalding heat transfer number
Kn	Knudsen number
M	Mach number
Nu	Nusselt number
Pe	Péclet number
Pr	Prandtl number
Re	Reynolds number
Sc	Schmidt number
Sh	Sherwood number
Stk	Stokes number

Indices

act	actual
$coal$	coalescence
$coll$	collision
eff	effective
exc	excitation
f	fusion
hom	homogeneous
i	species in a gas
j	gas mixture component
m	melting
p	powder particle or gas species type
rad	radiation
ref	reference
rot	rotational
$Saha$	Saha
sim	simulated
t	turbulent
vap	vapor
vib	vibrational

Introduction

The air transportation and energy generation industries are facing a tremendous augmentation of demand in the developing countries of East and South Asia as well as the Middle East. The International Air Transport Association (IATA) expects 7.2 billion passengers to travel in 2035, a doubling of the 3.8 billion air travelers in 2016. In addition, the International Energy Agency (IEA) projects a 2% yearly increase in electricity production till 2040 [1] (Figure 1).

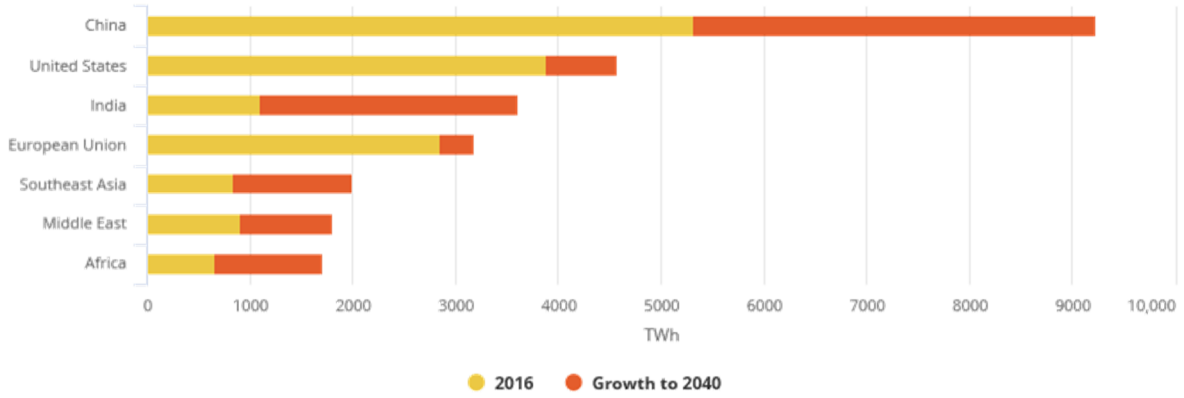

Figure 1: Electricity demand by selected region [1]

Both increases will come with a growth in gas turbine production and use for aircraft propulsion and power generation. In 2016, market forecasters estimated a production of nearly 228,000 aviation gas turbine engines valued at $1.232 trillion through 2030 and 5,480 power generation gas turbine engines worth $105.3 billion over the next decade [2].

To ameliorate the performance of gas turbines, the approach that has been developed since the 1980s for aviation turbines and more recently for land-based turbines is the application of a thermal barrier on the blades and guide vanes. Thermal barriers are also applied on other less mechanically stressed parts such as the walls of combustion chambers and the turbine rings.

The thermal barriers currently used in the hot sections of turbines (Figure 2), whether they are aeronautic or land-based consist of a multilayer system: a ceramic top coat, a metallic bond coat, and a thermally-grown oxide “TGO” layer that is formed due to the oxidation of the bond coat before deposition of the top coat or as a result of oxygen inward diffusion through the top coat at the thermal barrier coatings (TBC) operation temperatures. The main function of the ceramic top coat layer is to provide thermal insulation. It is generally deposited by electron beam physical vapor deposition (EB-PVD) or atmospheric plasma spraying (APS) on the less mechanically sophisticated parts (Figure 3). APS uses direct plasma guns to melt the top coat material and propel it towards the substrate, while EB-PVD relies on the electron beam that displaces the ingot atoms that eventually spread towards the surface to be coated.

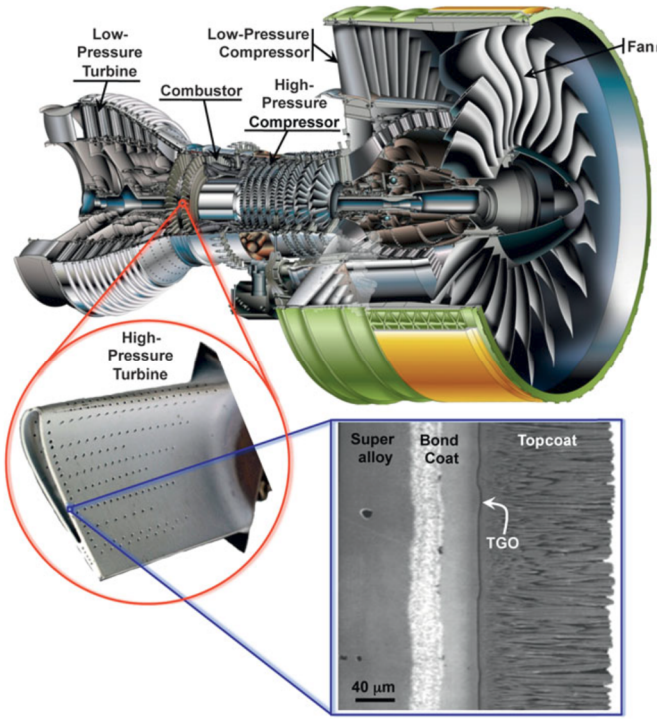

Figure 2: Cutaway view of Engine Alliance GP7200 aircraft engine, photograph of a turbine blade (~10 cm long) with thermal-barrier coating (TBC) from the high-pressure hot section of the engine, and a scanning electron microscope (SEM) image of a cross-section of an electron beam physical vapor deposited 7 wt% yttria-stabilized zirconia TBC [3]

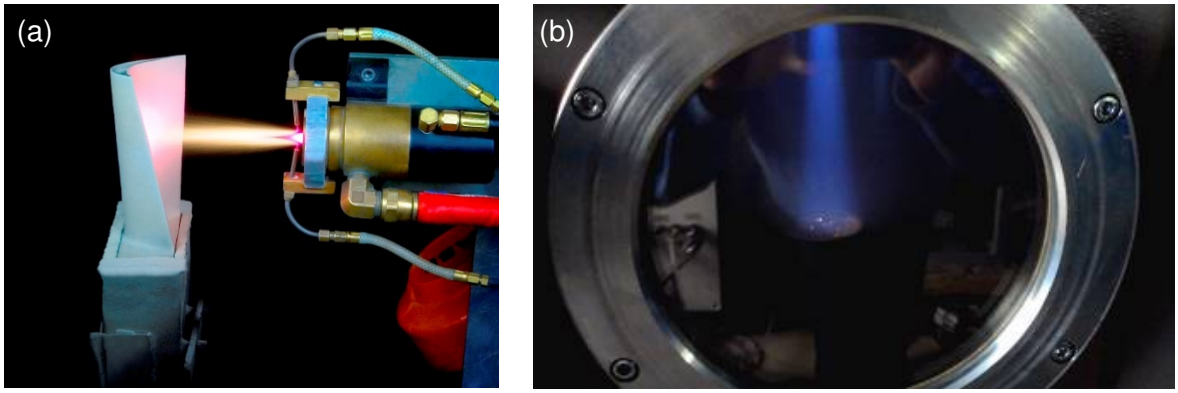

Figure 3: (a) TBC coating deposition on a turbine blade by APS, (b) Physical vapor jet generated during EB-PVD [4, 5]

Both the deposition techniques have some advantages and drawbacks. APS coatings that are shown in Figure 4 (a) are rather cheap, fast to deposit (up to 250 µm/min), and have a low thermal conductivity (~1 W/m/K), but their lamellar microstructure is not resilient to thermomechanical stresses. On the contrary, columnar EB-PVD coatings like the one shown in Figure 4 (b) provide a better thermal stress resistance, but they are slower to deposit (about 12 µm/min), have a higher thermal conductivity (~2 W/m/K), require medium-vacuum conditions (~1 Pa) and are characterized by high capital and operating expenditures.

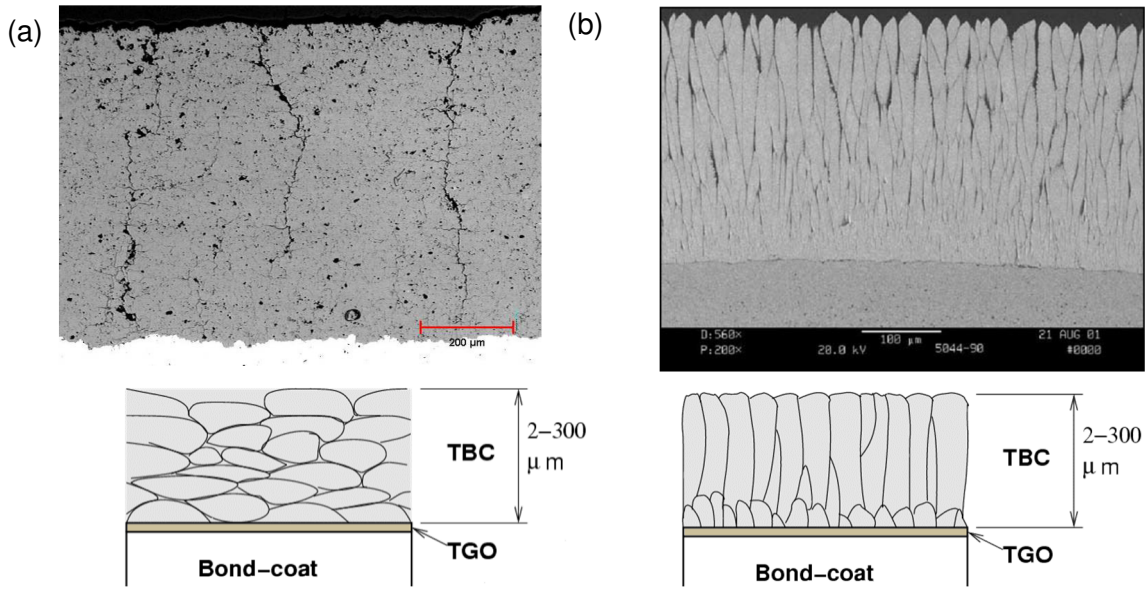

Figure 4: (a) APS and (b) EB-PVD thermal barrier coatings and their schematic microstructures [6, 7]

To bridge the gap between APS and EB-PVD, new technologies are emerging: suspension and solution plasma spraying and plasma spray - physical vapor deposition (PS-PVD). Their objective is to create a finely-structured coating built by very small particles/clusters and/or vapor deposition.

Plasma spray physical vapor deposition is a rapidly developing technology making it possible to produce finely structured coatings by vapor and fine melted particle deposition at pressures ranging from 10 to 200 Pa [8] (Figure 5). The process uses a thermal plasma spray torch adapted to the very low-pressure conditions to produce vapor. It aims to combine the high deposition rate of atmosphere plasma spray and the columnar structure of the coatings deposited by electron beam physical vapor deposition [9, 10].

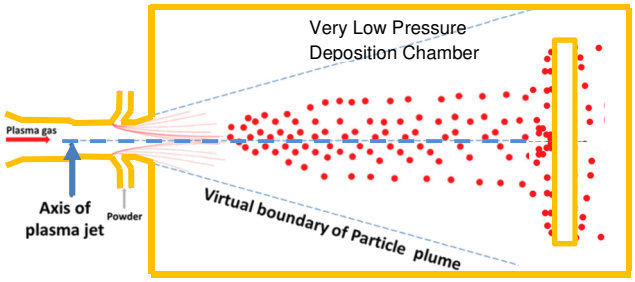

Figure 5: PS-PVD process schematic [11]

Current PS-PVD systems are capable of deposition at rates up to 100 µm/min. However, the major disadvantage of the process is a low heat transfer between the plasma jet and powder particles in low vacuum. This can be solved by increasing the residence time of powder particles in the hot and dense part of the jet. This is the main idea of the present study that consisted in designing a two-chamber system (referred to as the proposed system or PS). The latter is comprised of a high pressure chamber (HPC), designed to achieve maximal powder evaporation, connected to a low pressure deposition chamber (LPC) by an expansion nozzle, the design of which is adjusted to control the gas flux from the high pressure chamber and maintain low vacuum in the low pressure chamber (Figure 6). More favorable plasma-particle heat exchange conditions in the HPC could also allow using plasma torches with lower electric

power in comparison with the typical PS-PVD ones (e.g. 40 kW instead of 150 kW) and coarser powder particles (10- µm in diameter instead of 1 µm).

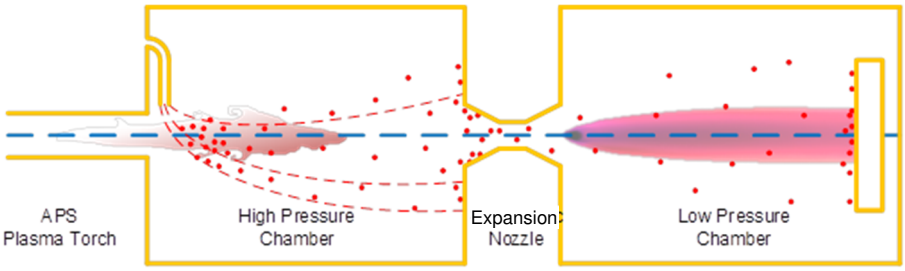

Figure 6: Proposed process schematic

However, such a system can raise several problems, such as:

1) The expansion nozzle erosion due to the high heat flux brought by the hot gas;
2) And nozzle clogging due to the condensation of vapor.

These problems can be solved by a careful adjustment of the nozzle design and spray parameters. Thus, the objective of the present work is to perform a modeling-based design of the proposed system and to prove its feasibility. In this work, a numerical model was developed and used to determine the geometry and spray parameters of the proposed system, which favor the powder evaporation, ensure a sufficient vapor content near the substrate to get EB-PVD-like coating microstructures, and solve the two problems, mentioned above. This manuscript describes the approach we have followed and the main results we have obtained.

The work is structured in four chapters.

The first chapter is dedicated to a literature review of the deposition processes related to PS-PVD. It summarizes the operation principles and the effect of the operating parameters on the resulting coating. Based on the literature review, a new deposition process is proposed.

The second chapter reviews the modeling techniques used for plasma spray processes, non-continuum flow and gas phase nucleation and growth and finally, introduces the approach and methodology of this study.

The third chapter describes the model of the proposed system based on the main findings exposed in the second chapter, presents the methods used to validate the model and the results of the validation step.

Finally, the fourth chapter presents the numerical study and main results, and demonstrates the proof of feasibility of the proposed PS-PVD process. For appropriate classical spray conditions, the proof of feasibility will be mainly based on the estimation of:

- material deposition rate on the expansion nozzle wall;
- nozzle wall heat resistance;
- and estimation of the flow composition and its evolution (vapor, cluster density and size) in the expanded jet.

The expansion nozzle geometry will be optimized by varying the divergence angle.

Chapter I. Process Review

I.1. Introduction

Deposition of finely-structured and stress-resilient **thermal barrier coatings** (TBC) (section I.2) is a subject of numerous studies performed by the thermal spray community. **Current technologies** (section I.3), such as atmosphere plasma spray (APS) and electron beam physical vapor deposition (EB-PVD), do not allow the efficient and fast deposition of such coatings. Novel deposition techniques like suspension and solution precursor plasma spray (SPS and SPPS, respectively) and plasma spray physical vapor deposition (**PS-PVD**) (section I.3.4) allow a faster deposition of finely structured TBCs.

This chapter highlights the state of the art in the ongoing development of PS-PVD processes and other related plasma spray process from the applied, engineering point of view. Without an in-depth explanation of physical processes involved in the deposition, it describes in basic terms atmospheric (APS) and controlled atmosphere plasma spray (CAPS), SPS and SPPS, EB-PVD and PS-PVD. Resulting coatings that can be deposited using these processes are shown and discussed. Particular attention is paid to the influence of spray parameters variation on the morphology of the resulting coating. Pros and cons of each technology are highlighted. In conclusion of this chapter, optimal parameters for deposition of finely structured TBCs are summarized and a new way to improve the PS-PVD process is introduced (section I.4).

I.2. Thermal Barrier Coatings

Thermal barrier coatings (TBC) are protective coatings applied to the surface of hot metallic sections in gas turbine engines [12]. The principal applications of gas turbines are power generation and aircraft propulsion. The application of TBCs increases heat and corrosion resistance of turbine parts, especially that of combustion chambers and turbine blades that are made of superalloys. This leads to an increase in turbine efficiencies, extends their lifetime and reduces maintenance frequency.

The conventional TBC system shown in Figure 7 consists of a ceramic top coat, a metallic bond coat, and a thermally grown oxide (TGO) layer that forms due to thermal oxidation before deposition the top coat and by oxidation of the bond coat by inward diffusion of oxygen through the top coat during the use of the coated part.

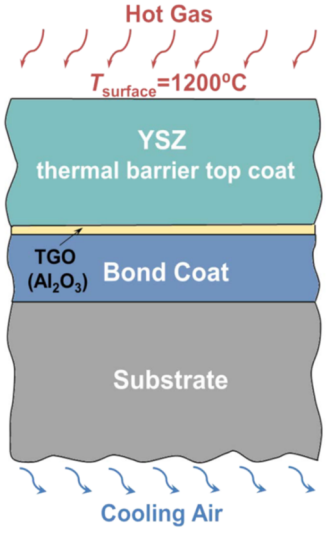

Figure 7: A standard TBCs [12]

The main role of the bond coat, usually composed of aluminum-rich materials ((Ni,Co)CrAlY), is to protect the substrate from oxidation by providing TGO layer with alumina. It also compensates the difference of thermal expansion coefficients between the substrate and the top coat. Ceramic top coat, traditionally composed of 6-8 wt. % yttria-stabilized zirconia (6YSZ - 8YSZ) [13], provides the thermal insulation. The choice of 7YSZ as a top coat material is justified by its good thermal stability, low thermal conductivity (0.7-2.6 W m^{-1} K^{-1}) [14, 15], high coefficient of thermal expansion (11 × 10^{-6} K^{-1}) [16], high fracture toughness, and high melting point (2,700 °C).

The properties of the resulting coatings are strongly dependent on their microstructure and therefore on the coating deposition process.

I.3. TBC Deposition Processes

Deposition of ceramic layers of TBCs requires substantial power input to the ceramics used as a coating material. High power/enthalpy levels are needed to ensure material liquefaction or evaporation, since deposition from a liquid or vapor phase provides the necessary adhesion to the substrate and leads to preferred coating microstructure and properties. These points will be discussed below. Such levels of enthalpy can be reached in various techniques. The most widely used techniques for deposition of TBCs are atmospheric plasma spray (APS) and electron-beam physical vapor deposition (EB-PVD). However, in recent years, several new promising technologies have emerged. They include suspension plasma spray (SPS), solution precursor plasma spray (SPPS) and plasma spray – physical vapor deposition (PS-PVD). In this section, we discuss and compare some of the aforementioned deposition techniques.

I.3.1. APS

I.3.1.1. Process Overview

Atmospheric plasma spray along with SPS and SPPS belongs to the family of thermal spray techniques. Thermal spray is a common name of a group of processes where the coating materials are fed to a high-enthalpy jet in which they are accelerated and heated to their melting or evaporation temperatures [17]. The resulting droplets or vapor are accelerated in a gas stream and deposited onto the surface of the substrate. On impact, the droplets spread and solidify on the solid surface, forming overlapping and interlocking lamellae that build the coating, while vapor contributes to the growth of coating by nucleation, condensation, and adsorption, resulting in a very fine microstructure.

A schematic of atmospheric plasma spray is shown in Figure 8. In APS, thermal plasma is produced by a rapid ohmic heating of the plasma-forming gas in a DC-torch at pressures close to one atmosphere, with arc current up to 3 kA and power level up to 150 kW. The plasma jet develops in atmospheric air (if surrounding gas composition and pressure are controlled, the process is called controlled atmosphere plasma spraying or CAPS). A plasma-forming gas (usually argon with the addition of nitrogen, hydrogen, or helium) is introduced between a concentric tungsten cathode and a water-cooled copper anode. Argon is generally chosen as primary plasma-forming gas because it is chemically inert and dense, and so is capable of pushing the anodic arc root downstream, increasing the arc voltage and enthalpy transferred to it. Nitrogen, hydrogen, and helium are added to the primary gas to increase the mixture thermal conductivity and enhance the heat transfer to the processed powder particles. The diatomic gases also increase the mixture's specific enthalpy. An electric arc is initiated between electrodes by a starting circuit, consisting of a high voltage transformer and capacitor, which

allows the breakdown of a spark gap. The breakdown leads to high induced voltage spike in the power supply circuit, resulting in a breakdown of the arcing gap and initiation of the current flow. The arc heats the gas through Joule effect to high temperatures (up to 30,000 K inside the nozzle and up to 15,000 K at the nozzle exit). The resulting heating causes the increase in gas volume, leading to a rapid expansion of the ionized gas through the nozzle. At the nozzle exit, the gas velocity ranges from 500 to 2,500 m/s, which is subsonic for corresponding temperatures. The ceramic micrometric (1 – 100 µm) powder particles are injected into the flow internally in the nozzle or shortly after the flow leaves the nozzle by a carrier gas flow (generally argon) issuing from an injector. They are heated up to their melting temperatures and accelerated towards the substrate by the flow, reaching velocities up to 700 m/s upon the impact. Fully or partially molten particles reach the substrate where they pile up, form lamellae and re-solidify, forming the coating [18].

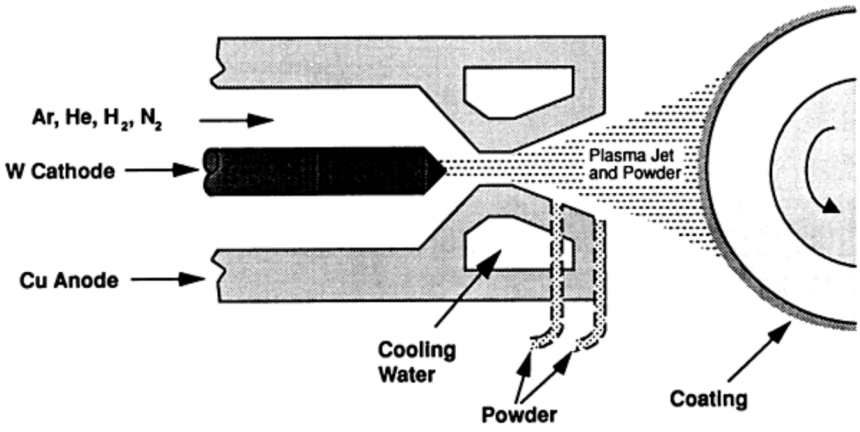

Figure 8: APS process schematic. Courtesy of Praxair Surface Technologies, Inc

The advantages of APS are in its low capital cost and high deposition rates (125-250 µm/min). The high speed of particles at impact on the substrate leads to their deformation and formation of splats – pancake-alike structures. The rapid solidification of splats causes tensile quenching stresses, resulting in the formation of microcracks [19] (Figure 9), and low adhesive bond strength (19.9 MPa) [20], while imperfect splat contacts are leading to high porosities (10-20 vol.%). Coatings with such microstructures have low thermal conductivities (0.9-1.1 W/m/K [7]) and elastic moduli (13-24 GPa [21]), which result in a satisfactory thermal insulation and reasonable thermo-mechanical performance.

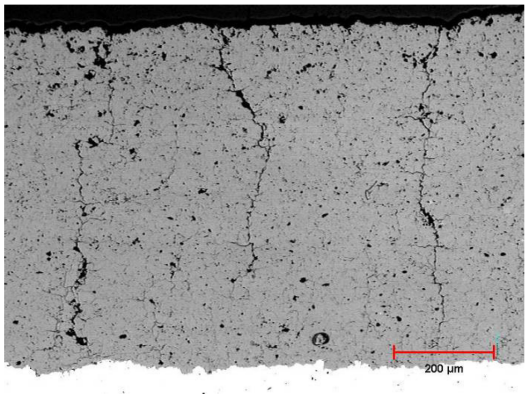

Figure 9: TBC deposited by APS [7]

The disadvantages of APS are low adhesive strength and sensitivity towards the change of spraying parameters, such as standoff distance (or spray distance) and presence of shroud

gas. Moreover, the difference between thermal expansion coefficients of TBC layers associated to their lamellar structure substantially reduces the thermal shock resistance of the coating at the operation temperatures of coated parts. Because of the lower strain tolerance, TBCs produced by APS are typically used for protection of stationary components of aircraft engines like combustion chambers [22, 23]. APS TBCs are also more vulnerable to calcium–magnesium–aluminosilicate (CMAS) attack compared to coatings produced by other techniques. CMAS is an oxide mixture designed to simulate typical airborne contaminants that can be encountered by zirconia-coated parts of airplane jet engines. CMAS penetrates coating through cracks and progressively reduces its thickness, causing it to spall-off prematurely. This issue could be resolved by depositing gadolinium zirconate instead of zirconia. Addition of gadolinium prevents CMAS penetration due to the formation of crystalline layer at CMAS/gadolinium zirconate interface [24].

APS conditions are chosen to favor the particle heating. As mentioned earlier, this can be done by the addition of gases with high specific enthalpy and thermal conductivity. The particle heating can be improved at the expense of their velocity (which leads to increase of powder residence time in the jet) or by the treatment of powder prior, during its manufacturing process (agglomeration, sintering). The flight time, which typical value is around one ms, can be increased by decreasing the jet velocity or by acting on the particle trajectory. The former can be achieved by using nozzles with a larger diameter (the maximal diameter is limited due to possible ignition difficulties, loss of plasma symmetry and the increase of azimuthal non-uniformity of flow parameters), and the latter - by changing the injection direction and velocity.

According to a numerical study conducted by de Sousa [25], the addition of 25 mol% of hydrogen to argon plasma results in three times higher jet enthalpies and velocities, two times higher particle velocities, full powder melting (in case of pure argon under typical APS conditions only 75% of 50-µm particles were melted) and three times higher fraction of vaporized powder at 100 mm downstream of the torch exit along the torch axis. The variation of current from 300 A to 600 A leads to a doubling of gas enthalpy and velocity, an increase by 50 % of particle velocity and by 75% of particle melted fraction. An increase in the torch nozzle diameter from 6 mm to 10 mm brings about a doubling of the flow temperature from 2,000 K to 4,000 K at the substrate location, and decrease by two of the flow velocity, a 2.5-times decrease in particle velocity, and an increase of the melted particles fraction from 25% to 90%. An experimental study by Fuzet [26] confirms the numerical trends, showing that 19.8-µm particles lose only 2.8 µm in diameter in the case of a 6-mm nozzle, while 6.8-µm reduction is observed with a 10-mm nozzle, which is attributed to an increased flight time of the particles and higher plasma jet temperatures.

I.3.1.2. Plasma Torch Operation

In APS, SPS, SPPS and PS-PVD process plasma jet is generated in direct current (DC) plasma torches from a continuously flowing gas heated by an electric arc inside a nozzle [18]. A conventional plasma torch used in APS processes (e.g. 50 kW Oerlikon Metco F4 plasma torch) is shown in Figure 10.

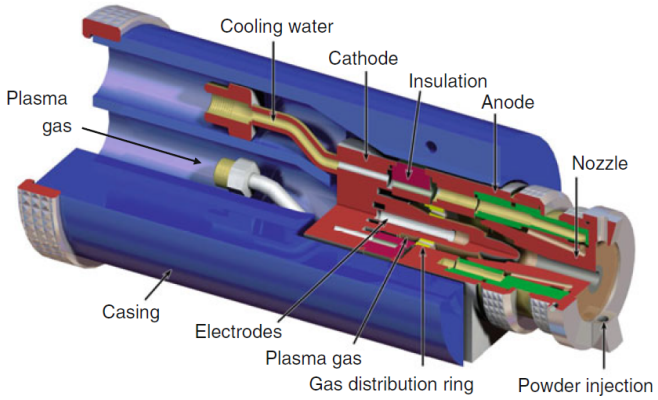

Figure 10: Schematic CAD drawing of F4 plasma gun interior [18]

Electric arc generates the high-temperature plasma through resistive energy dissipation by the current flowing through the gas. To allow the current to flow through the gas, the gas temperatures must be sufficiently high to have considerable degrees of ionization resulting in sufficiently high electrical conductivities. For most plasma-forming gases, the required temperatures are ~8,000 K and above at atmospheric pressure. The electric arc inside a plasma torch can be divided into the cathode region, the arc column region, and the anode region, as illustrated in Figure 11 [18].

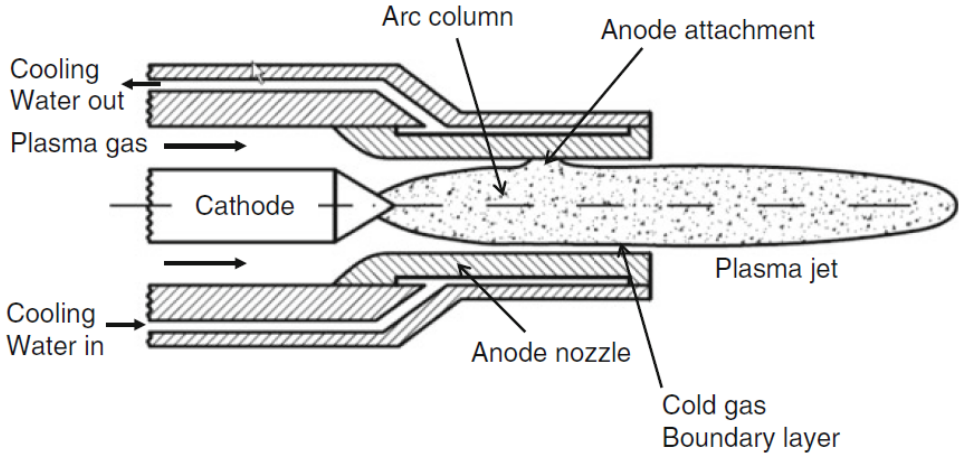

Figure 11: Schematic drawing of a typical plasma spray gun [18]

Cathode supplies electrons to the arc through thermal electron emission. Materials for cathodes should have high melting temperatures and low work functions to ensure structural stability by reducing cathode's operating temperature. Typically, cathodes are produced from tungsten with the addition of 1-2 wt.% of a material with a low work function (ThO_2, La_2O_3, LaB_6). Heat loss from the plasma to cathode material causes arc constriction near the cathode, increasing the pressure in the boundary region. The induced pressure difference contributes to the increase of gas flow velocity. Arc temperatures in the cathode region can reach 20,000-30,000 K, resulting in high degrees of ionization.

The arc column characteristics are controlled by the torch inner geometry, arc current, plasma gas flow rate and composition. The Joule dissipation, equal to the product of current density and electric field strength, is balanced by the heat losses to the surroundings. The decrease of the nozzle diameter or increase of plasma gas flow rates results in greater heat losses and requires a higher voltage to compensate them [18].

The anode collects electrons, closing the electrical circuit of the plasma torch. It is usually made of copper and cooled by water. For arc currents between 300 and 1,000 A, the nozzle diameter varies between 6 and 10 mm. The overall losses to the cooling water usually add up to ~50% of the input power, forming a cold boundary layer near anode walls, while the remaining power is transferred to plasma gas enthalpy.

According to Steenbeck's minimum principle, the attachment between the arc column and the anode is formed at the position where the overall voltage drop is minimal. This means that in the ideal stationary case, the preferred attachment point is located on the anode part closest to the cathode. However, because of the high velocities of the cold gas in this region, the arc undergoes a strong cooling, which increases its voltage. Moreover, the arc attachment experiences a significant drag from the cold gas of the boundary layer. Consequently, the attachment keeps moving downstream from the initial position until the arc voltage becomes sufficiently high for a breakdown to occur. This event is called a restrike. Conventional plasma torches usually work in a restrike mode when hydrogen is present in the gas mixture [18, 27]. This happens due to the increase of the thickness of the cold boundary layer that separates the arc from the anode wall (due to the increase of thermal conductivity by H_2). With pure Ar, the take-over mode without arc breaking prevails (the arc root moves downstream and upstream continuously). In restrike mode, the total amplitude fluctuations of the voltage reach values of 30-70% of the average voltage value, with a frequency between 4 and 6 kHz, as can be seen in Figure 12. Regardless of the mode, arc current stays at the fixed level.

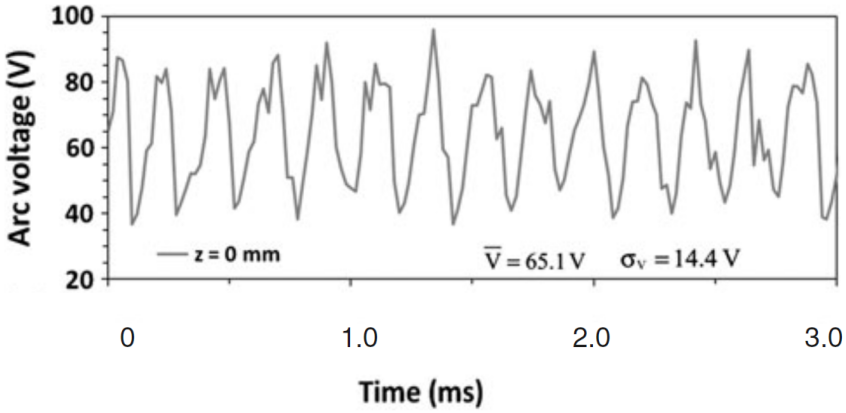

Figure 12: Arc voltage evolution (F4 plasma gun, Ar-H_2 (45-10 slm), 500 A) [27]

In DC plasma torches, the anode attachment instability has a considerable effect on the plasma jet stability and characteristics, its turbulent mixing with the ambient gas and in-jet powder behavior [28]. The arc voltage fluctuation causes plasma jet temperature and velocity fluctuations at the nozzle exit. This results in the inhomogeneous treatment of powder particles, introduced in the jet further downstream. Experimental observations and numerical predictions show that the flow in the torch nozzle is usually laminar, and turbulence starts developing only after the flow leaves the torch and is enhanced by jet fluctuations [29].

High temperature/enthalpy levels result in a variety of additional phenomena. Diatomic gases like H_2 and N_2 undergo dissociation; neutral atoms are being excited and ionized (except helium due to a high ionization temperature); hot gas emits radiation. The imbalance between these processes results in numerous types of disequilibrium, observed in thermal plasma in the near-cathode area [30–32]. The rest of the flow apart from the near-cathode and jet fringes is considered to be in local thermal equilibrium.

The nozzles of DC plasma torches working under near-atmospheric pressure do not provide enough acceleration for the jet to reach a supersonic velocity. In the nozzle, plasma ionization degree may exceed 30%. The rapid expansion through the nozzle and mixing with the surrounding cold gas decrease plasma jet temperature and reduce the ionization degree to less than 3% [33]. When the ionization degree is low (<10%), the effect of the charged components on the jet structure can be ignored [34]. The prediction of electromagnetic phenomena is crucial to understanding the operation of plasma torches and non-stationary effects. However, this is left beyond the scope of the present study. Nevertheless, the presence of flow parameters fluctuations will be acknowledged during the interpretation of the numerical simulation results, even if they will not be taken into account in the model.

I.3.1.3. Powder Injection

The powder injection parameters have a significant impact on particle trajectory and residence time in the plasma jet. The particle trajectory determines its heating and acceleration and greatly influences the quality of the coating. Conventional APS plasma torches, like F4, as schematically shown in Figure 13, use the *radial* injection. On one hand, if a particle is too small (<5 µm in diameter) or has a low injection velocity, it cannot be efficiently injected into the plasma jet core due to its lack of momentum. On the other hand, the heavy particles can be energetic enough, so they can cross the plasma jet. Furthermore, small particles that failed to enter the jet core will stay on its periphery. Such particles can undergo melting due to relatively small velocities and high residence times. Heavy particles that crossed the plasma jet core will travel in the low-velocity peripheral region of the jet as well, but unlike the light particles, their small specific surface will not allow the full melting upon reaching the substrate. The particle momentum is adjusted by the carrier gas flow rate. Roughly, to achieve a good penetration, the particle force should be close to the force imparted to it by the plasma along its trajectory ($S_p \rho v^2$, where S_p is the particle cross section and ρ and v, the gas density and velocity).

With the radial injection, the powder can be injected in perpendicularly to the jet axis or at a positive or negative (backward injection) angles with respect to perpendicular direction. Depending on the position of powder feeder, the injection can be internal (inside of the plasma torch) or external (shortly after the torch outlet). Backward injection results in higher particle temperatures, but lower particle velocities [35].

Plasma torches with internal injection (also known as axial injection) provide a more uniform heating and acceleration of particles. The design of conventional plasma torches does not allow axial injection. This type of injection is only possible for multi-electrode torches, like Northwest Mettech Axial III, but their prices and maintenance expenditures are substantially higher or through hollow cathodes [36, 37]. However, if the latter have been successfully tested in the laboratory, they are not commercially available, in particular, because of the problem of cathode tip erosion.

For multi-electrode plasma torch, the internal injection may lead to nozzle clogging by partially or fully melted particles, driven by various factors, like the high inertia of heavy particles, flow instabilities, and thermophoretic force. This reduces the nozzle cross section and results in a change in plasma jet characteristics: jet velocity increases, reducing the residence time and heat transferred to particles and ultimately affecting the resulting coating properties.

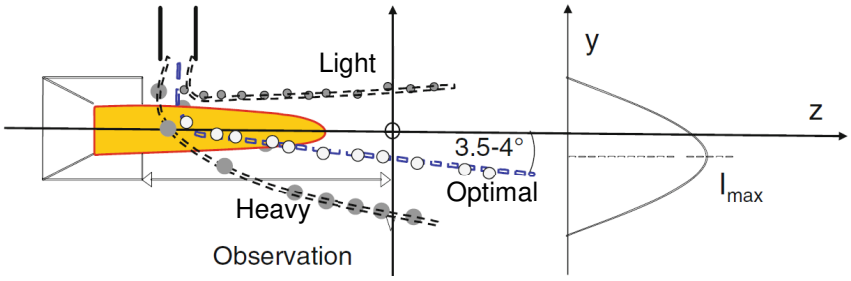

Figure 13: Schematic representation of trajectories of particles with different masses. The heavy particles cross the plasma jet, while the light particles do not enter the plasma jet core. The size distribution of the particles results in a particle flux distribution indicated in the inset figure [18]

I.3.1.4. Materials for Atmospheric Plasma Spray

The initial raw powders for thermal spray are commonly produced via crushing, grinding or milling. In such processes, the powder size distribution is broad which may lead to the injection problems discussed above and coarse microstructures formed by lamellae piling up onto the substrate. To get a refined microstructure, smaller particles around one micron in diameter should be sprayed but there is an injection problem due the aggregation of the fine particles in the feeding system, and due to their low inertia, that requires a very high carrier gas flow rate to give them enough momentum to reach the jet core and melt. However, such carrier gas flow rate cools down the plasma excessively. There are two methods to avoid this issue:

- Use of a dense liquid carrier instead of a gas carrier;
- Use of agglomerated heavy particles that can be separated back to original micrometric particles when exposed to the hot jet core.

The first approach uses suspension and solution precursor plasma spraying (SPS and SPPS, respectively). In SPS micrometric particles are mixed with a solvent and in SPPS solution precursors (e.g. on zirconyl nitrate and yttrium nitrate salts for YSZ powder) are dissolved in water or ethanol [38]. The second approach uses coarse agglomerated powders (d_{50}=20-90 µm). Typical size distributions of commercially available agglomerated YZS powders are shown in Figure 14.

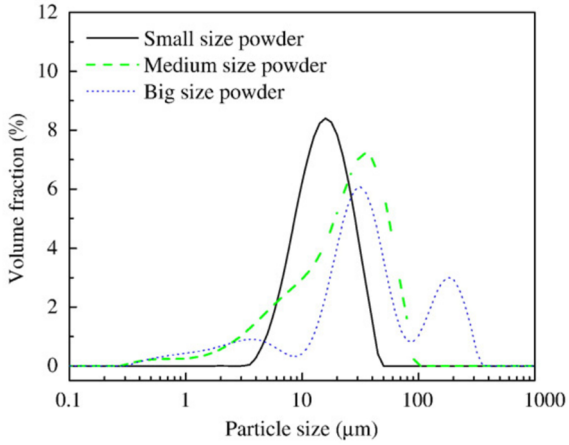

Figure 14: Size distributions of commercially available YSZ powders of size ranges [39]

Agglomerated particles are produced by spray drying technique. In this technique, small particles about one micron in diameter are mixed with a water-based liquid with the addition of

a stabilizing surface active binder. Drops of suspension are produced with an atomizer and sprayed into a drying chamber where they are heated either by a stream of hot air or by the radiation of the hot chamber wall or both in some cases. The resulting powder may contain traces of the organic binder and a sintering process can be used to evaporate it [18]. During the plasma spray deposition process, agglomerated particles can be fragmented into micrometric particles, facilitating the melting process. Typical agglomerated powders are shown in Figure 15. The agglomerated and sintered particles of the Metco 231A powder have a rough surface that favors their heating due to the increase of the specific surface.

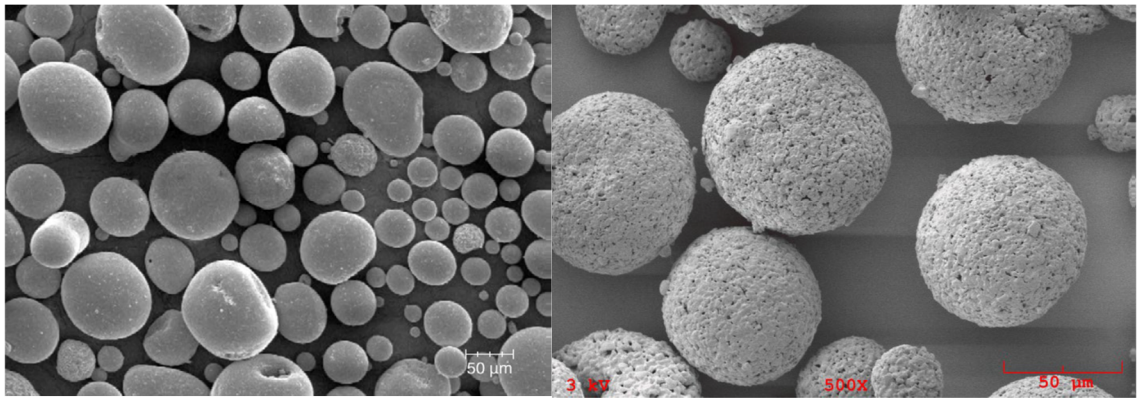

Figure 15: Scanning electron microscope (SEM) photomicrographs of typical Oerlikon-Metco agglomerated and sintered yttria-stabilized zirconium oxide materials (left - Metco 204D, right: Metco 231A) [40]

I.3.2. SPS and SPPS

Suspension and solution precursor plasma spray are emerging technologies based on APS. They use the same equipment (e.g. F4 or Triplex plasma torches) and operate under rather similar conditions (electric power level, plasma forming gas flow rate, etc.).

SPS uses sub-micron sized particles. In comparison with APS, the injection method differs: as mentioned in the previous section, powder particles are suspended in a liquid that replaces the carrier gas of APS, allowing a proper injection of the small particles into the hot jet core. Injection of such powders by a carrier gas won't be efficient – it requires increased carrier gas flow rates, which results in plasma jet cooling and reduced heat transfer to powder. Nonetheless, the evaporation of the solvent also results in plasma jet cooling, but to a lower extent. Liquid jet injected into the plasma flow undergoes fragmentation, which results in a particular droplet size distribution dictating the resulting coating morphology [41]. The main advantages of thermal barrier coatings, produced by SPS are a good calcium–magnesium–aluminosilicate (CMAS) attack resistance [42], high porosity (30-40%), low thermal conductivity (0.56-1.80 W/m/K) and slow Young's modulus [43]. Typical microstructures achievable using SPS are shown in Figure 16. SPS provides the easiest and cheapest way of producing thermal barrier coatings with columnar microstructures that are highly valued for the parts working at high thermal loads. Unlike the columnar-structured coatings produced by EB-PVD, SPS coatings have higher porosities in the direction normal to the substrate surface, which results in lower thermal conductivities in comparison with EB-PVD coatings. Indeed, in SPS the material that is being deposited is present in the form of vapor and liquid phases, whereas the EB-PVD coatings are formed mostly from the vapor phase. The resulting columns, however,

are about ten times larger than the ones of EB-PVD. More information on the advantages of columnar microstructures can be found in the section devoted to EB-PVD.

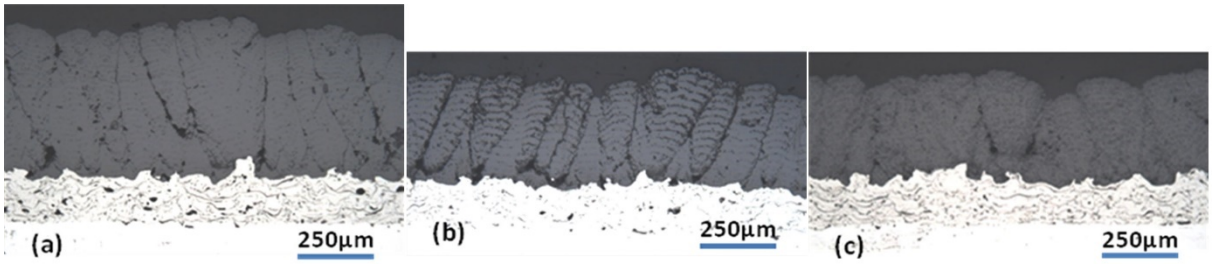

Figure 16: Columnar microstructures of 8YSZ-TBCs applied by SPS process. (a) Dense columnar microstructure obtained at an electric power of 40 kW; (b) dense and porosity-laminated columnar microstructure; and (c) porous columnar microstructure at an electric power of 37 kW and/or a spray distance of 85 mm [44]

The major issue of coatings produced by SPS is lack of vertical cracks in comparison with columnar coatings, produced by EB-PVD. This lowers the amount of heating and cooling cycles a coating can withstand before losing its adhesion to the substrate surface (known as thermal cycling resistance). However, there are ways of dealing with this issue like the use of substrates with rough surfaces (high roughness triggers the growth of spatially distinguished columns) or a careful selection of torch power and spray distance, as illustrated by Figure 16. Another issue is high thermal stresses that form in the coating due to a reduced spray distance in comparison with APS that leads to higher substrate temperatures during the deposition process.

SPPS is another development of APS technology. It uses solution precursors dissolved in water or organic solvent (e.g., ethanol). When introduced into the plasma jet, precursors form particles, while the solvent is being evaporated. Such approach allows generation of a broad variety of microstructures (depending on the solution composition and plasma torch operating conditions [45]) that favor CMAS resistance, thermal cycle durability, low thermal conductivity (1-1.3 W/m/K [46]) and erosion resistance. Nevertheless, the process has some disadvantages – precursors need enough time to react and form zirconium dioxide, thus restricting the minimal droplet travel distance and/or maximal droplet velocity. Another problem is the fragmentation of the liquid that leads to high variations in the resulting coating composition. A typical SPPS TBC is shown in Figure 17.

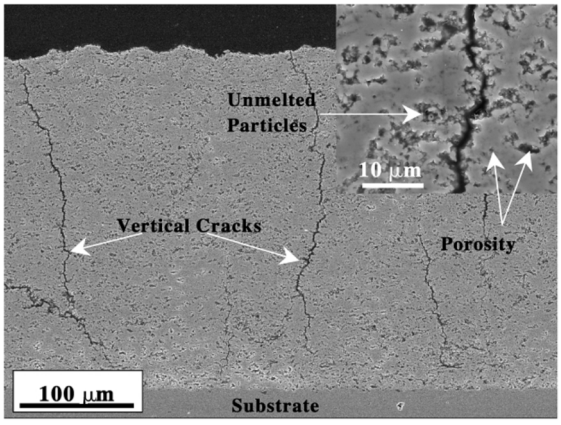

Figure 17: SEM micrograph of a polished cross-section view of an SPPS TBC [20]

I.3.3. EB–PVD

I.3.3.1. Process Overview

Electron-beam physical vapor deposition is a physical vapor deposition (PVD) processes [47]. Methods of this class are based on coating material evaporation from a condensed phase with a subsequent condensation of the physical vapor on the substrate.

The schematics of the EB–PVD equipment is shown in Figure 18 (a). An electron beam formed at 2000 °C in an electron gun is accelerated by an electric field (with the voltage around 20-25 kV) in a high vacuum environment (10^{-2}-10^{-3} Pa) and hits materials in the ingot located in a medium vacuum (~1 Pa) deposition chamber, shown in Figure 18 (b). The high kinetic energy of electrons causes melting and evaporation of the ingot material. Physical vapor, formed during this process, spreads throughout the chamber and is being adsorbed on the substrate located within the line of sight. High vacuum conditions allow the free passage of electrons emitted from the electron gun to the ingot; they also help to avoid the oxidation of the ingot material if it is made of metal.

Atoms are absorbed by the nucleation centers that growth in feather-like columnar crystal structures shown in Figure 19. The columnar structure of the coating is caused by the dependence of the crystal growth rate on crystal orientation – some crystal orientations grow faster than others. The faster-growing columns block the growth of the slower growing ones, resulting in coarsening of columnar grains farther from the substrate [48]. Such structures serve the same purpose as vertical cracks of APS coatings, providing a high degree of mechanical compliance [7] and more stress relief on thermomechanical loading at the interface, characterized by low in-plane Young's moduli [21, 49].

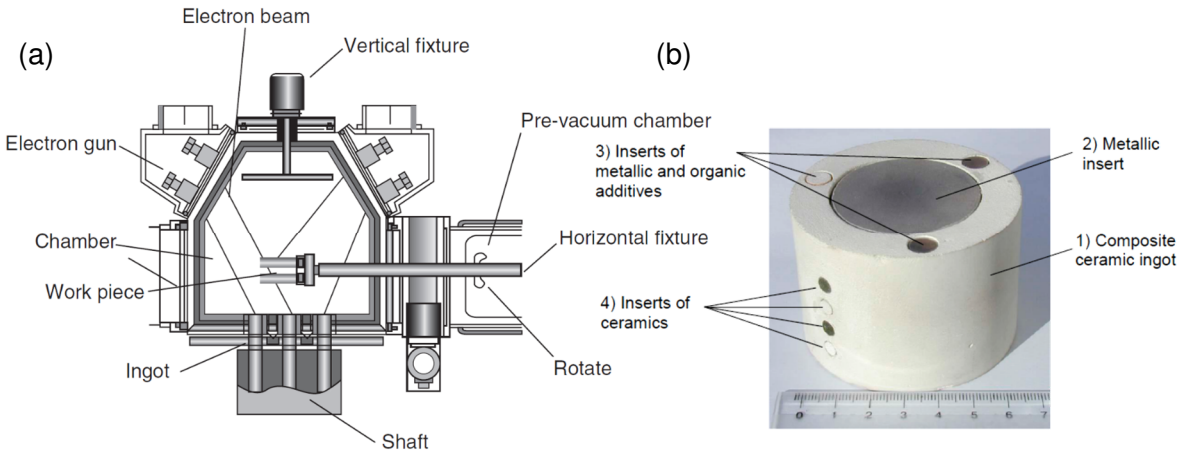

Figure 18: (a) EB–PVD equipment schematic [47], (b) EB–PVD ingot [50]

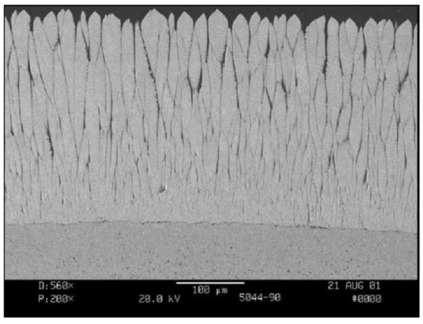

Figure 19: TBC deposited by EB–PVD process [7]

However, the lack of pores in the direction normal to the surface results in thermal conductivity values higher than the ones of APS TBCs (1.5-2.0 W/m/K) [51, 52]. Furthermore, the necessity to sustain the high vacuum, low deposition rates (5 µm/min) and line of sight deposition mode make EB–PVD coatings expansive in comparison with APS TBCs. Nevertheless, high adhesion and good thermal cycling resistance make EB–PVD TBCs the best fit for moving turbine parts [9, 23, 47].

I.3.3.2. EB-PVD Structure Zone Model

For the coatings produced by EB-PVD, it was found that depending on the substrate homologous temperature (a ratio between substrate surface temperature T_s and its melting temperature T_m) and deposition pressure three characteristic structural zones can be distinguished [50, 53], as shown in Figure 20.

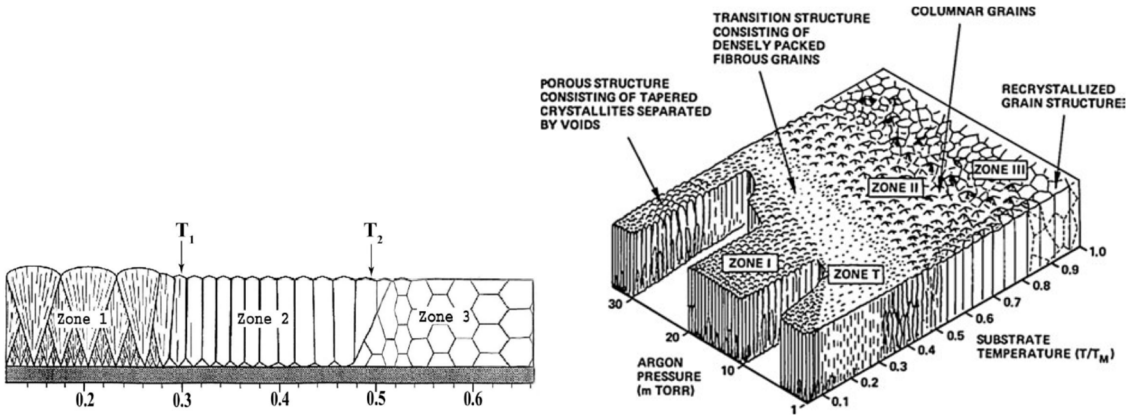

Figure 20: Schematic of condensate structure depending on substrate temperature T_s/T_m (T_m is the melting temperature) [50]

According to the structure zone model (SZM) proposed by Thornton for sputter deposition [53] in the substrate low-temperature zone (T_s < T_1, zone 1) the condensates have a porous structure with tapered crystallites with rough surfaces that are formed owing to low adatom mobility (slow surface diffusion). In the second zone (T_1 – T_2, zone 2) the condensates are characterized by a columnar structure with a predominantly crystallographic orientation. The transitional zone T combines the structures observed in zones 1 and 2. The width of the columnar crystallites increases with temperature in the T_1 – T_2 range from fractions of one micrometer up to several micrometers. In the high-temperature zone (T_s>T_2, zone 3) a practically pore-free structure of the ceramic layer forms [50]. Thornton's SZM can be applied to EB-PVD or PS-PVD, however, instead of argon pressure, vapor impingement rate should be used as the second parameter.

I.3.4. PS–PVD

I.3.4.1. Process Overview

Plasma Spray – Physical Vapor Deposition (PS–PVD) is a new addition to the family of thermal spray processes to produce thermal barrier coatings. It bridges the gap between thermal spray and PVD techniques by using high power plasma torches adapted to the very low-pressure conditions to produce physical vapor deposited coatings [8].

In PS–PVD, thermal plasma is produced by APS-like plasma torches, adapted to very low pressure (50-200 Pa) conditions by the use of internal injections in the nozzle throat and

convergent-divergent shapes of torch nozzles. Torches typically used in PS-PVD (e.g., F4-VB with a maximal power output of 50 kW and 03CP with 180 kW power output) have an internal powder injection due to low plasma-particle heat exchange under very low pressure. The plasma jet expands through the nozzle into the low-pressure chamber, where the pressure ranges from 50 to 200 Pa. Because of a substantial pressure difference between the torch and coating chamber, the plasma jet rapidly expands and accelerates to supersonic velocities (M>2) and generates shock waves. The electrical power range achieved in PS-PVD allows the jet to be heated up to 10,000 K, enabling nearly full evaporation of the injected ceramic powder.

Very low pressure controlled atmosphere limits substrate oxidation during coating formation [54] and enlarges the plasma plume, resulting in larger areas, covered with homogeneous coatings. In comparison with APS, where plasma jets are about 50 mm in length and 10 mm in diameter, PS-PVD plasma jets reach up to 2 m in length and 50 mm in diameter, as illustrated by Figure 21.

Depending on the feedstock material, operating conditions and spray parameters, PS-PVD coatings can have various microstructures, varying from dense APS-like lamellar microstructures to EB-PVD-like columnar microstructures. Examples of such coatings are shown in Figure 23. Very fine agglomerated powders (typically <25 µm, composed of particles around 1 micron) and high electric power levels (>100 kW) are required to ensure the efficient evaporation of the processed powder. A typical PS-PVD powder is shown in Figure 22. Current PS–PVD systems are capable of deposition at rates up to 240 µm/min (03CP plasma gun with 150 kW of electric power, deposition on tungsten or graphite substrates) [48].

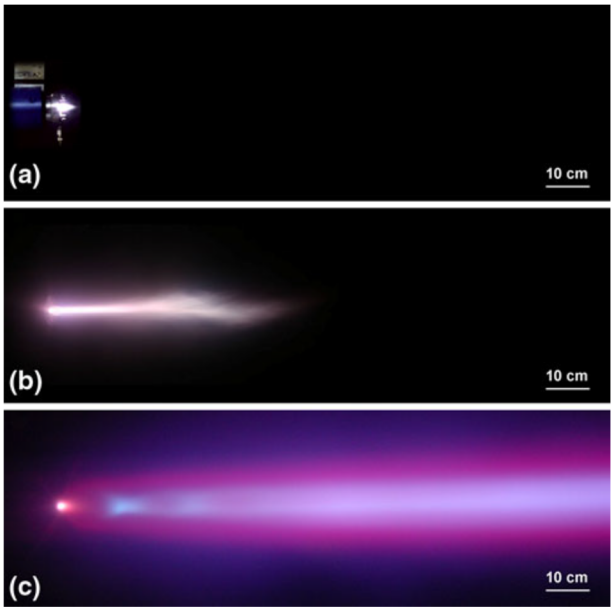

Figure 21: Images of the plasma jet expanding at different pressures (a) 95 kPa (950 mbar/APS), (b) 5 kPa (50 mbar/VPS/ LPPS), and (c) 0.1 kPa (1 mbar/PS-PVD) [8]

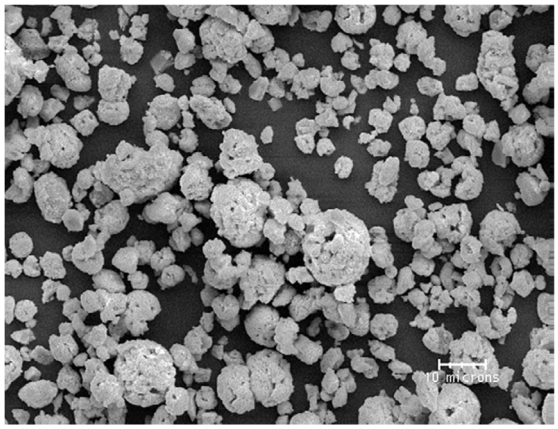

Figure 22: SEM photomicrograph of Metco 6700 spray-dried powder with d_{50}=10 µm [40]

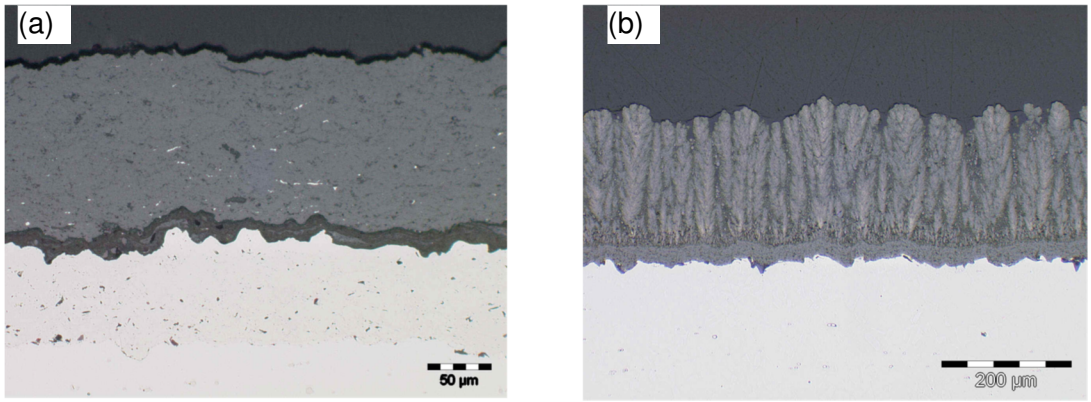

Figure 23: (a) Dense TBC multilayer system consecutively build-up with PS-PVD technology [54], and (b) TBC multilayer with a columnar structured EB-PVD-like coating on top of the dense ceramic interlayer and metallic bond coat as deposited subsequently with PS-PVD technology [54]

The question of the coating morphology variation with spray conditions is an intensively researched topic. PS-PVD coating microstructure is highly dependent on the powder heating and, consequently, on a number of factors, such as the *plasma gas nature, net electric power of the torch, spray distance, powder feed rate, size and morphology of the powder particles, substrate temperature, and torch nozzle shape*. The complete set of factors is shown in Figure 24.

	Torch	Plasma jet	Particles	Substrate
Input parameters	•Current •Plasma gas composition •Flow rate •Nozzle design, erosion •Cooling water flow		•Size distribution •Morphology •Feed rate •Carrier gas flow rate	•Substrate material •Pretreatment •Motion
Operating Characteristics	•Voltage •Voltage fluctuations •Thermal efficiency	•Stability •Geometry •Plasma gas properties •T & V distributions	•Particle trajectory •T_p & V_p distributions •n_p flux distribution	•Coating properties •Porosity •Mechanical properties •Deposition efficiency
	•Torch set up	•Atmosphere •Pressure •Humidity		

Figure 24: Factors influencing the coating properties in plasma spray process [18]

I.3.4.2. PS-PVD Structure Zone Model

PS-PVD structure zone model (SZM) developed by Mauer [55] describes the variation of coating morphology with substrate temperature and powder feed rate. It shows consistency with a similar model by Thornton [53] and Movchan [50] for EB-PVD coatings. The diagram is shown in Figure 25.

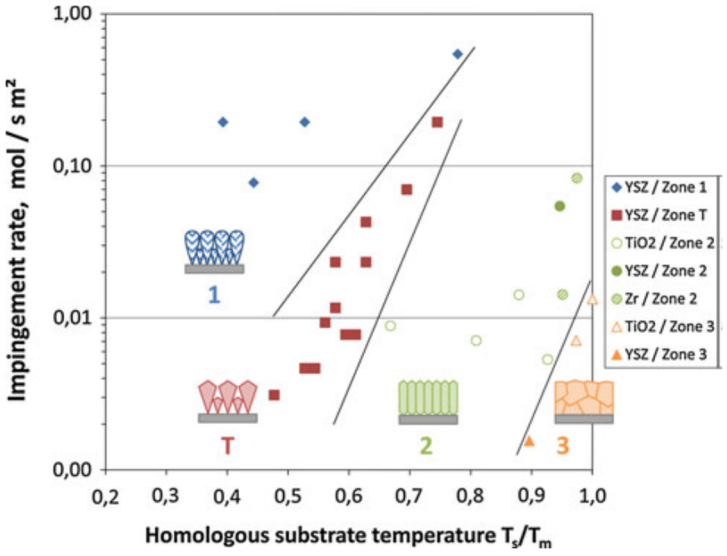

Figure 25: PS-PVD structure zone model [55]

SZM has two parameters: the substrate surface temperature and the impingement rate of the coating molecules. Both of them directly affect adatom surface mobility. As in Thornton's model, coating growth in zone 1 is dominated by the slow surface diffusion. The lack of adatom mobility results in a shadowing effect, which creates tapered porous (25-30%) columnar-structured coatings (Figure 23b). The increase of the surface temperature facilitates surface diffusion and results in the formation of oblique and more narrow columns (transitional zone T) and eventually leads to the growth of compact columnar structures with faceted surfaces (zone 2). If the surface temperature is sufficiently high (zone 3), bulk diffusion takes place, resulting in the formation of a dense coating with smooth polyhedral structures (Figure 23).

As shown by Mauer's SZM, the formation of porous columnar coatings – the coatings with preferential EB-PVD-like structure – requires either low substrate temperatures (<0.5T_m) or high deposition rates (corresponding powder feed rate is ~ 20 g/min) and is highly sensitive to plasma flow conditions acting on the morphology through shadowing effect. Deposition of closely-packed columnar structures is only possible at high substrate temperatures (>0.5T_m) and low deposition rates (corresponding powder feed rate is ~ 2 g/min).

I.3.4.3. Coating Structure Spatial Distribution Model

When the substrate temperature and powder feed rate are held constant, as shown by Li [56], a spatial variation of coating structures is observed. Li's structure distribution model is shown in Figure 26.

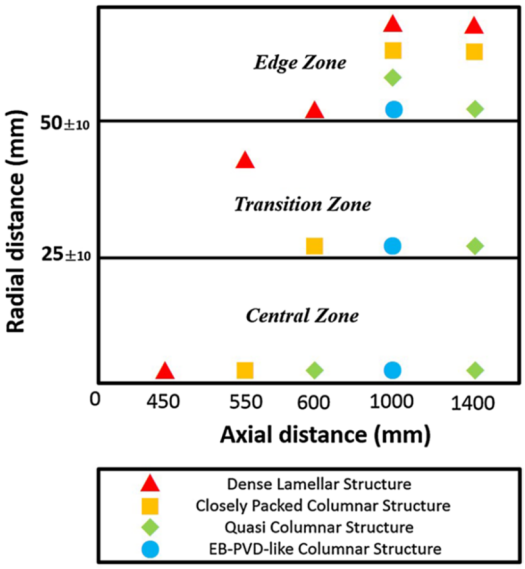

Figure 26: Structure spatial distribution model (SSDM) of PS-PVD YSZ coatings [56]

For given torch operating conditions but various spray distances, the coating microstructure was studied as a function of its position in the radial direction of the substrate. Corresponding to the different thermal treatment of the powder particles with the variation of plasma gas temperature, coating morphologies in the center of the substrate may vary from EB-PVD-like columnar to dense lamellar. This change can be attributed to the variation of vapor and liquid droplets content in the jet: at short distances (~450 mm in the axial direction) from the plasma torch, the powder particles are assumed to be melted, but not fully evaporated. As the residence time of droplets in the plasma jet core increases, so does the powder vaporization degree. Similar variation is observed along the substrate surface in the radial direction – here coating growth can also be driven by molten or even partially molten particles which were unable to enter the core of the plasma jet and start vaporizing.

I.3.4.4. Plasma Gas Selection

Various studies show the effect of the plasma gas on the coating process. As explained in I.3.1.1, plasma forming gas should favor the heat transfer to powder particles. This is achieved by using dense argon, capable of pushing the arc root downstream, increasing arc's voltage and thus maximizing the power transferred to the gas, with the addition of gases with high thermal conductivities and/or specific enthalpies like N_2, H_2 or He that increase the heat flux to the particle.

Thermal conductivity affects the degree of ionization. Mauer [33, 57] has shown that heat transfer from the jet to a powder particle under PS-PVD conditions is mostly driven by ions, thus higher degrees of powder evaporation are possible in plasma gases with larger degrees of ionization. For 35 slm Ar / 60 slm He mixture it was estimated that ions are responsible for 63% of the heat flux to the powder particle placed into the plasma torch throat while the gas ionization degree is about 27% in the same region. In 100 slm Ar / 10 slm H_2 plasma ionization degree was 18%, but ions were accountable for 42% of the heat flow. In other words, gases with low energies of ionization (such as hydrogen in Ar/H_2 mixture or argon in Ar/He mixture) contribute to the increase of thermal conductivity of plasma gas mixture. Figure 28 shows that enthalpy transferred to powder particles from Ar/He mixture is sufficient to evaporate spherical particles up to 1 µm in diameter, whereas Ar/H_2 mixture is only capable of evaporating particles up to 0.55 µm. Corresponding photographs of plasma jets are shown in Figure 27.

Even though PS-PVD consumes a substantial amount of energy, only small particles with diameters below one micron can be fully evaporated. For this particular reason, only fine agglomerated powders can be used. E.g., Metco 6700 agglomerated powder with particles 10 µm in diameter. When exposed to hot plasma, organic binder evaporates and power grains disintegrate into finer (~1 µm) particles.

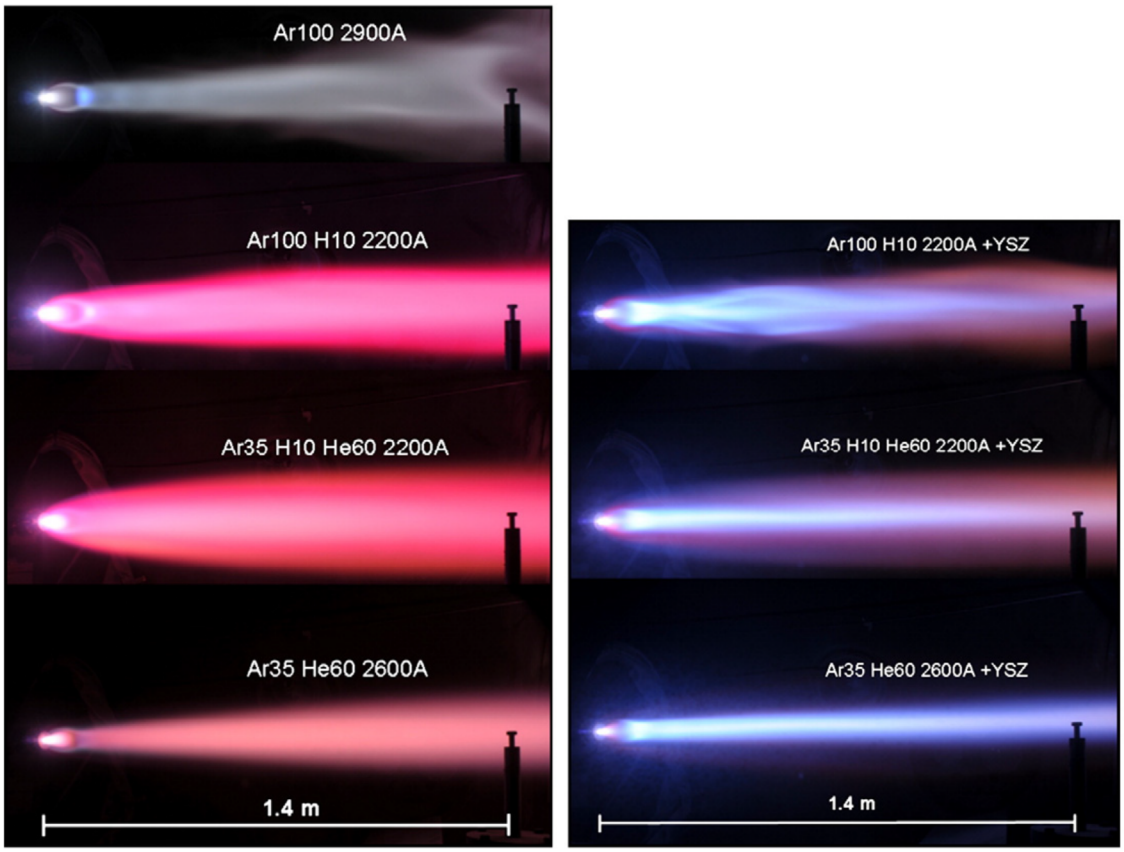

Figure 27: Photographs of PS-PVD plasma jets using different gas compositions; on the left without any powder, on the right with YSZ powder injection. Chamber pressure and net power input were kept constant at 200 Pa and 60 kW, respectively, in all cases; the numbers denote the argon, helium and hydrogen flows (slpm) as well as the arc currents (A) [58]

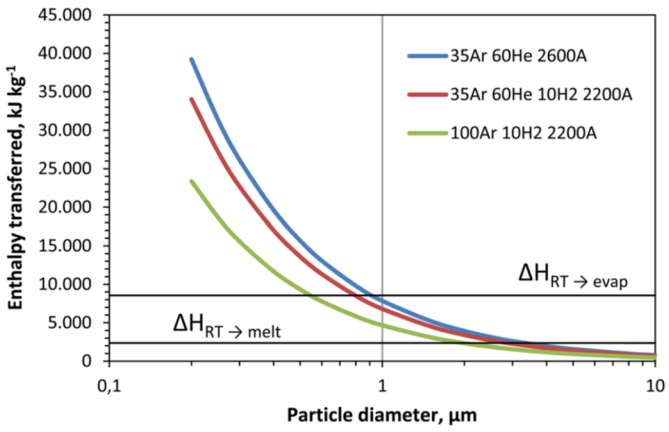

Figure 28: Calculated enthalpy transferred to spherical particles for three investigated plasma parameters as a function of the particle diameter; the horizontal lines indicate the mass-specific enthalpies which are required to melt and evaporate the particles, respectively [57]

I.3.4.5. Influence of PS-PVD Plasma Torch Nozzle Design

In Mauer's experiments, 150 kW (60 kW net) Oerlikon Metco O3CP plasma guns were used. This allowed complete evaporation of particles up to one µm in diameter, leading to the production of EB-PVD-like coatings (Figure 23b). The use of plasma guns designed for lower power inputs, like Oerlikon Metco F4, as illustrated by Gao [59], resulted in dense homogeneous coatings formed from liquid particles (Figure 23).

A number of studies were focused on the possibilities of enhancing the plasma torch geometry to favor the particles evaporation. Bolot and Sokolov have introduced a bell-shaped De Laval nozzle as an extension of the F4-type cylindrical nozzle, which improved jet and thus coating uniformity in the radial direction but lowered the gas temperature due to increased heat losses caused by the necessity of nozzle cooling [60]. Sun et al. [61] have shown the effect of the torch nozzle design on the very low pressure plasma spray (VLPPS) coating characteristics. Two nozzles with internal injection were considered – a short anode cylindrical nozzle and a long anode divergent nozzle. Schematics of the nozzles are shown in Figure 29. In this study, the use of a longer and divergent nozzle resulted in the formation of a more uniform jet, an increase in particle velocity and jet temperature and a decrease of the particle jet dispersion. These effects were attributed to a lower degree of under-expansion that led to the reduction of radial jet velocity component after the nozzle outlet. More detailed description under-expanded flow physics is given in the subsequent chapters. The opening angle of the divergent part was about 26°, though no reasoning behind this choice was specified.

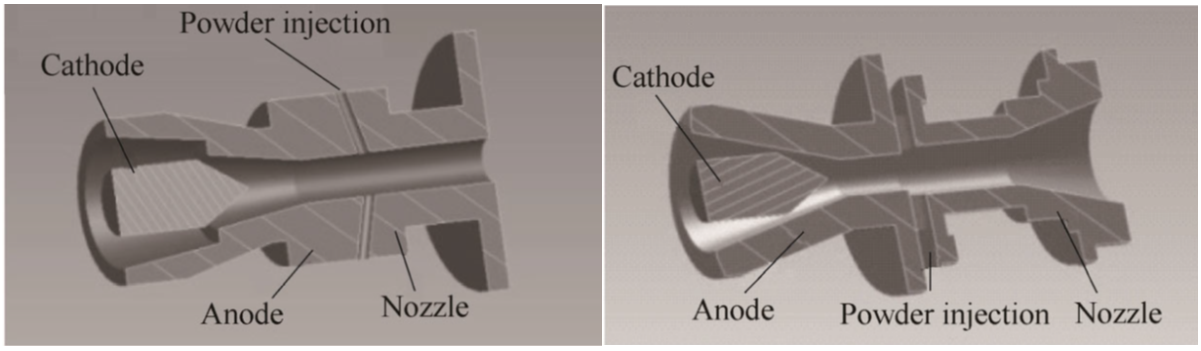

Figure 29: Schematic CAD design of two nozzles (left – short anode nozzle, right – long anode nozzle) [61]

Recent studies have shown that the powder evaporation happens mainly between the injection point within the plasma torch and the torch outlet where temperature and pressure are maximum. Only particles that are smaller than 1 µm can be fully evaporated during their flight inside the nozzle [57]. Some additional evaporation may happen in the expanded plasma jet outside the nozzle but as shown by Liu et al [62], even if the heat flux to the particle in the expanded jet is 100 times lower than the one inside the plasma torch nozzle, its residence time is much higher than in the nozzle, and thus, molten particles with diameter around 0.28 µm at the nozzle outlet can be fully evaporated in the open jet [62] for spray distance of about 450 mm.

I.3.5. Comparison of the Processes

Table 1 compares operating parameters and deposition results of the aforementioned processes.

Table 1: Operating parameters of APS, EB-PVD and PS-PVD processes [12, 17, 47, 63]

Parameter	APS	EB-PVD	PS-PVD
Electric power, kW	50-120	40	50-200
Chamber pressure, Pa	10^5	1	50-1,000
Plasma gas	Ar, H_2, He, N_2	Ar	Ar, H_2, He, N_2
Flowrate, slm	<100	-	<200
Deposition distance, m	0.05-0.10	0.25	0.50-2.00
Powder feed rate, g/min	10-50	-	1-30
Particle diameter, μm	10-100	-	1-20
Flow velocity	Subsonic	Subsonic	Supersonic
Gas flow temperature at injection point, K	~10,000	1,000-2,000	~10,000
Substrate temperature, K	600-700	900	~900

Table 2 compares deposition results of APS, EB-PVD, and PS-PVD. All the data were taken from contemporary literature. A relative number of thermal cycles to failure was determined in furnace cycling tests (FCT), where the samples were heated up to 1,400 K during 6 minutes, kept hot for a period of 50 minutes and cooled down to room temperature for 4 minutes [64, 65]. The number of thermal cycles to failure under calcium-magnesium-aluminum-silicate (CMAS) attack was determined in a burner test facility. Each thermal cycle consisted of a 5-min heating phase, in which the burner flame was positioned on the specimen surface, and a 2-min cooling phase, during which the burner was moved away and compressed air instead was directed onto the surface for rapid cooling [66].

Table 2: Deposition characteristics of APS, EB-PVD and PS-PVD processes [8, 12, 17, 47, 49, 63–70]

Parameter	APS	EB-PVD	PS-PVD
Deposition rate, µm/min [69]	125-250	5	<200
Deposition area	line-of-sight	line-of-sight	non-line-of-sight
Deposited material state	Liquid droplets	Physical vapor	Physical vapor and liquid droplets
Bonding type	Mechanical	Diffusion	Mechanical and diffusion
Thermal conductivity, W/m/K	0.9-1.1	1.5-2.0	0.5-1.9
Porosity, vol.% [69]	10-20	10-15	10-60
Microstructure	Dense lamellar	Columnar	Dense lamellar - Columnar
Relative number of thermal cycles to failure [64, 65, 68]	0.50 (100-400)	1.00 (450 cycles)	1.50 (500-700 cycles)
Bond strength, MPa [67, 70]	20-45	>65	36
Relative erosion resistance [64]	0.30	1.00	0.50
Typical thickness, µm	200-3,000	100-300	100-1,000
Thermal stress at working temperature, MPa [12]	100	30	30
Number of thermal cycles to failure under CMAS attack [66]	150	120	70-175
Cost per µm	Low	High	Medium

I.3.6. Preferential PS-PVD parameters

The tables of section I.3.5 give a range of possible operating parameters and deposition results that can be achieved with PS-PVD, while section I.3.4 highlights how the choice of these parameters affects the coating process. The information given in these sections can be used to determine the most preferable conditions needed for the production of coatings with specified microstructures.

To get a finely-structured EB-PVD-like coating with PS-PVD a high-power plasma gun (e.g., 03CP) with internal powder injection and divergent nozzle should be used. Plasma forming gas should contain helium or argon as the main component and a diatomic gas (hydrogen or nitrogen) as a secondary component. Fine agglomerated powder (d_{50}=10 µm) should be used as a feedstock material and injected at a low feed rate (20 g/min). The substrate temperature should be maintained at the maximum achievable level (typically less than $0.4T_m$), to ensure high adatom mobility which favors the growth of columnar coatings. The substrate should be placed far enough from the torch where the amount of physical vapor or concentration of nanoclusters is maximal.

In fact, the production of a dense lamellar coating does not require the complete evaporation of the powder. Thus, a lower power plasma gun (e.g., F4-VB) or a less fine powder can be used, or a lower spray distance could be set. If the substrate can be preheated to a temperature

higher than $0.8T_m$ and powder feed rate kept lower than 2 g/min, a dense coating with smooth polyhedral structures can be deposited.

I.4. Conclusion

Technologies of TBC production have considerably evolved during the last decades, each having its own advantages and shortcomings. APS coatings are cheap and fast to produce but do not fit for moving parts, subjected to periodic mechanical and thermal stresses. EB-PVD coatings are expensive and slow to deposit, but they provide higher resilience and thermal stress resistance. SPS, SPPS and PS-PVD seem to be a viable alternative to conventional technologies. In the present study, we will concentrate on the PS-PVD process. The latter makes the deposition of EB-PVD-like coating possible with higher deposition rates and at lower prices, but it requires powerful plasma torches, helium as the plasma forming gas and fine powders to operate.

In response to these drawbacks, we offer a new deposition system, which combines elements of APS and PS-PVD. The idea is to increase the amount of heat received by a powder particle by acting on its residence time in the hot and dense region of the plasma jet. This is achieved by the following means:

- Introduction of a controlled atmosphere chamber with near-atmospheric pressure between the torch nozzle and the deposition chamber;
- Use of an APS/CAPS plasma torch with a nozzle diameter larger than that of the PS-PVD torch nozzles – higher nozzle diameter should lead to lower plasma flow velocity and turbulent mixing;
- Use of argon/hydrogen mixture as plasma-forming gas – the use of hydrogen should provide sufficient specific enthalpy and heat conductivity for zirconia particle melting and evaporation.

The controlled atmosphere high pressure chamber (HPC) should allow the full evaporation of the fine agglomerated powders used in PS-PVD and substantial evaporation of coarser powders usually utilized in APS/CAPS. The hybrid CAPS-PS-PVD process will be referred to as the proposed system (PS) in the following sections.

The schematics of the process is shown in Figure 30. A sonic nozzle designated as “expansion nozzle” will ensure the gas expansion between the two chambers.

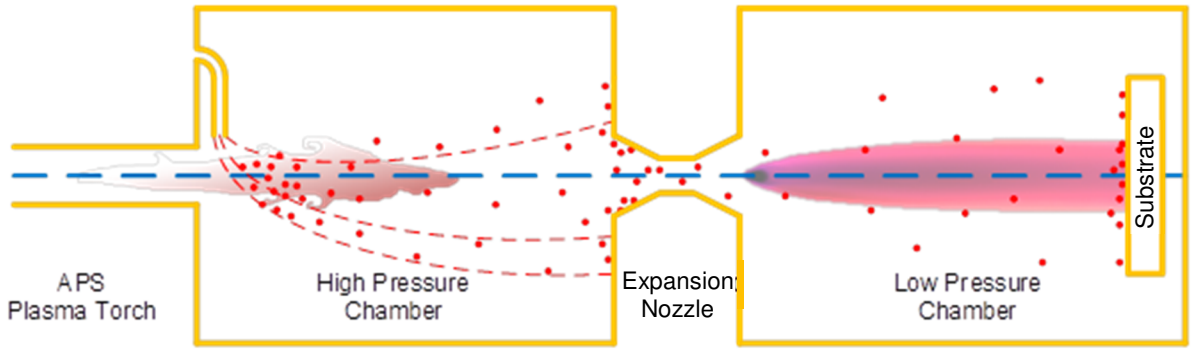

Figure 30: Schematic of the proposed system

The two-chamber design is a unique feature of the PS. Each chamber is characterized by specific operating conditions, which make the design of the system a non-trivial task:

- The high enthalpy of gas in the HPC requires efficient cooling of the chamber and expansion nozzle walls, creating a cold boundary layer where supersaturated physical vapor can start uncontrollable deposition, resulting in material losses and clogging of the nozzle;
- The low pressure of the second chamber causes the rapid expansion of the hot gas jet, compounded by rarefaction effects and intense shocks.

It must be noted, that if powder evaporation is not complete, liquid droplets could also contribute to nozzle clogging. This effect is not considered in the present study since technical solution allowing separation of non-fully vaporized particles from the vapor jet exists. This solution is based on the powder-vapor inertia difference and it's thoroughly described in the thesis of Pierre Fuzet [26].

In the present study, the system is designed to ensure process' feasibility by means of numerical modeling. However, the choice of numerical models to describe the process requires a deep understanding of physical phenomena taking place in the system.

Chapter II. Review of Existing Models

II.1. Introduction

The goal of the present chapter is to choose a set of appropriate models that will be used to prove the feasibility of two-chamber PS-PVD and perform its design.

In fact, design of the hybrid CAPS-PS-PVD deposition technique requires a deep understanding of the physical phenomena taking place at the different steps of this sequential process and their effect on each other. The previous chapter has clearly illustrated the variety of coating microstructures and properties that can be obtained with this class of processes. As it is hard to control coating morphology due to numerous physical phenomena and related factors (Figure 24) contributing to the result, a better understanding of these processes, listed in Figure 31, can eventually provide means of control over the deposition procedure.

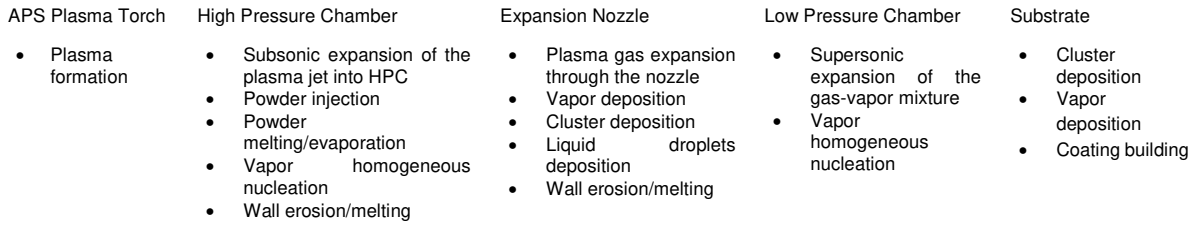

Figure 31: Physical phenomena associated with the proposed system

This chapter provides an in-depth description of the key phenomena typically associated with APS and PS-PVD processes relevant to proposed system's (PS) design and contains a review of the conventional modeling techniques used to simulate these processes. All the processes are assembled into three major sections. The first section is devoted to the gas flow physics and modeling, the second one describes powder-related phenomena like transport in the plasma flow and particle evaporation, and the last section highlights deposition-related phenomena, like condensation through nucleation. The chapter concludes with the list of the modifications required to make it suitable to the PS conditions.

II.2. Plasma Flow Modeling

There are four distinct regions in the PS: the nozzle of the plasma torch, the high pressure chamber (HPC), expansion nozzle and the low pressure chamber (LPC). The flow conditions vary drastically between the regions, as illustrated in Table 3. Each set of conditions is unique and requires a proper modeling approach. In this section, we review how similar flows are treated in the literature, with the exception given for the torch nozzle flow. This part of the flow is highly ionized, axially asymmetric and requires non-stationary 3D simultaneous simulation of fluid mechanics and electromagnetic phenomena. The complexity of the phenomena observed in this region makes it a challenging topic, explored in numerous studies. In the present work, the effects of the phenomena taking place in the torch nozzle on the downstream flow are not addressed. To decrease the complexity of the model this region is treated as a part of the HPC.

Table 3: Qualitative comparison of the flow conditions in the different parts of the proposed system with reference to the standard conditions (low temperature, high pressure, zero gradients, very small mean free path, local thermal equilibrium, no turbulence)

Parameter	Torch nozzle	HPC	Expansion nozzle	LPC
Average temperature	Very high	High	Medium	Medium
Temperature gradient	Very high	Medium	High	Very high
Average pressure	High	High	Medium	Very low
Pressure gradient	Very low	Very low	Very high	Very high
Flow velocity	Medium	Medium	High	Very high
Mean free path	Very small	Very small	Medium	Very small
Degree of non-equilibrium	High	Low	Low	High
Turbulence intensity	Low	High	Low	Low

The unique combinations of the flow parameters in each part of the system give rise to various effects and cause different flow regimes, which have a direct impact on the choice of the modeling procedure. Before addressing the models used to describe the flows, the concept of local thermal equilibrium will be introduced, and flow regimes will be defined.

II.2.1. The Concept of Local Thermal Equilibrium

On a microscopic level, particles and photons composing thermal plasma are involved in a large variety of processes. If a certain balance is achieved, distribution functions and corresponding temperatures can describe statistically large numbers of plasma particles. The four main types of balance mechanisms are [30, 71]:

- Kinetic energy exchange and conservation, described by Maxwell distribution – a function of the kinetic or translational temperature T,
- Excitation and de-excitation, described by Boltzmann distribution – a function of excitation temperature T_{exc},
- Ionization and recombination, characterized by Saha distribution and Saha temperature T_{Saha},
- Emission and absorption, characterized by Planck distribution and radiation temperature T_{rad}.

The state when $T=T_{exc}=T_{Saha}=T_{rad}$ is called thermodynamic equilibrium (TE). In practice, this state is never achieved and can only be approached. In thermal plasmas, different degrees of departure from TE are observed as shown in Figure 32. When a part of the emitted radiation is not reabsorbed, Planck equilibrium (PE) vanishes, and the weakest form of departure from TE called *local thermal equilibrium* (LTE) is observed. If there is no kinetic energy balance between heavy particles and electrons, a deviation from local Maxwell equilibrium (LME) occurs. Now velocities of light and heavy species (molecules, atoms, ions) are still distributed according to the Maxwell distribution, but an additional electron temperature T_e should be introduced to describe the electron velocity distribution separately. This leads to the two-temperature (2T) thermal plasma model.

In expanding plasma jets, another type of disequilibrium may occur, when atoms close to the ground stated de-excite radiatively, instead of following a more common electron-induced mechanism. This situation is called partial local thermodynamic equilibrium (PLTE) [30].

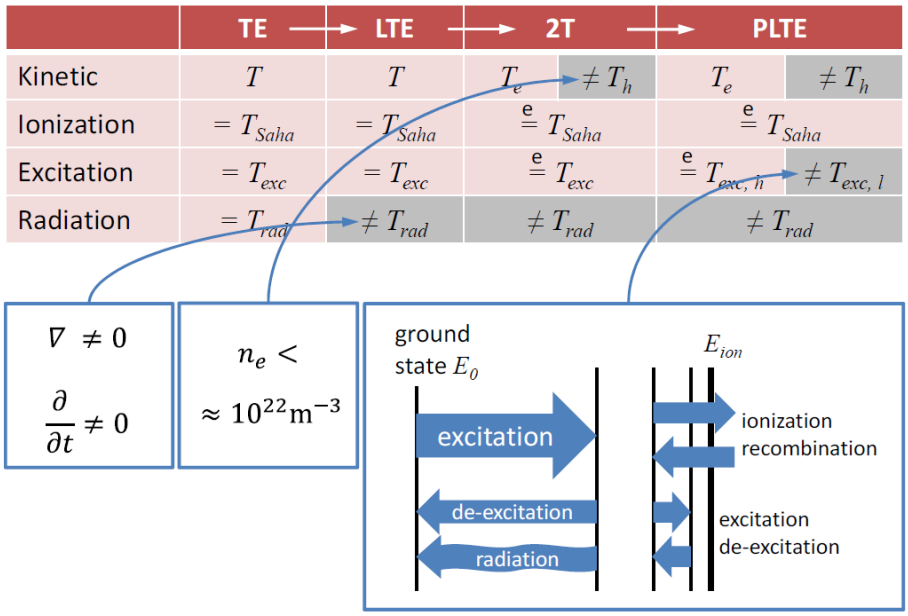

Figure 32: Different stages of departure from thermodynamic equilibrium in thermal plasmas [30]

When characterizing plasma flow by its temperature, it is important to realize that commonly used thermodynamic temperature may not be an appropriate parameter to describe nonequilibrium plasma flows. It is only possible when a flow is in LTE, which requires that heavy particles interact with each other at a sufficient rate. In practice, this means that local gradients of plasma properties (temperature, density, thermal conductivity, viscosity, etc.) should be small enough for plasma gas species to have sufficient time to equilibrate with the surroundings during its diffusion or convection [34]. Under APS conditions deviations from LTE are observed near the electrodes, but also in the plasma–cold-flow interaction regions. Under PS-PVD conditions, additional deviations can appear due to the low pressure in general and in the shockwaves in particular.

II.2.2. Continuum Flow and Rarefied Flow

The plasma flow in APS (or in HPC in the considered case) and in the supersonic nozzle is typically considered to be a continuum medium. Therefore, its behavior can be described numerically or experimentally in terms of “macroscopic” fields like temperature, pressure, velocity and enthalpy without acknowledging the fact that any gas is composed of a huge number of discrete molecules. Under continuum assumption plasma gas is considered as a continuous homogeneous matter with no voids or free space [72]; the mean free path of plasma gas species is then significantly smaller than any characteristic dimension of the flow.

Nevertheless, such a treatment of the flow under VLPPS conditions (or in the LPC in this study) may no longer be valid – with a substantial pressure decrease, compounded by intense shocks, *rarefaction effect* may occur. The number of molecules in certain plasma jet regions may become insufficient for an adequate “macroscopic” description. It can also contribute to the appearance of various types of disequilibria, following the mechanisms described in the previous section.

The rarefaction degree is usually described by the Knudsen number (Kn), which is the ratio between the molecular mean free path λ (average distance between intermolecular collisions) and a characteristic physical length scale of the flow L:

$$\mathrm{Kn} = \frac{\lambda}{L} \tag{1}$$

Flow regimes can be approximately defined through corresponding Knudsen numbers as follows:

$\mathrm{Kn}<0.001$	continuum regime
$0.001<\mathrm{Kn}<0.1$	temperature jump (slip flow) regime
$0.1<\mathrm{Kn}<10$	transition regime
$10<\mathrm{Kn}$	free molecular flow regime

When the mean free path is small enough in comparison with the macroscopic length scale of interest ($\mathrm{Kn}<0.01$), a continuum flow prevails. In this flow regime, the frequent intermolecular collisions drive the distribution of molecular velocities toward the equilibrium Maxwellian velocity distribution. The same can be applied to reacting fluxes: a sufficiently high frequency of collisions between molecules leads to chemical equilibrium. When a small control volume (or a probe volume) is in an LTE state, the velocity distribution in this volume is isotropic. Thus, it is possible to average the microscopic properties of gas particles (kinetic and internal energy, velocities) into macroscopic properties (pressure, temperature…) that vary continuously in space and are compatible with the scale of the system.

Rarefaction has also a significant impact on heat exchange and momentum transfer. The linear relations between the stress tensor and velocity gradient (Newton's law of viscosity), and between the thermal heat flux and temperature gradient (Fourier's law), become nonlinear in rarefied flows. These phenomena are usually referred to as *the breakdown of the continuum fluid dynamics*. A proper treatment of the flows, where the breakdown is possible, is required for both experimental and numerical studies [57, 73].

Rarefaction phenomenon can be observed for different scales. Even if the jet is not rarefied, this may not be the case for powder particles with characteristic size (diameter) much lower, than the mean free path of surrounding gas molecules [74]. The effects of rarefaction phenomenon on the feedstock powder are highlighted in the sections below.

II.2.3. Plasma Flow under APS Conditions

II.2.3.1. Non-stationary Aspects of the Flow

The plasma flow in the high pressure chamber is characterized by a high temperature and velocity instability associated with the arc voltage and, thus, torch power fluctuations. A considerable level of turbulence caused by the mixing of the plasma flow with the colder and denser gas at rest in the HPC further contributes to jet instability. Figure 33 illustrates the onset of turbulent flow in APS. The fluctuations of the laminar plasma jet leaving the torch leads to the formation of eddies and entrainment of cold surrounding gas into the jet, leading to a rapid reduction of the jet temperature. Cold gas bubbles can reach the jet axis without breaking up

until several nozzle diameters downstream from the torch nozzle outlet, increasing the inhomogeneity of the flow in the transitional region [29].

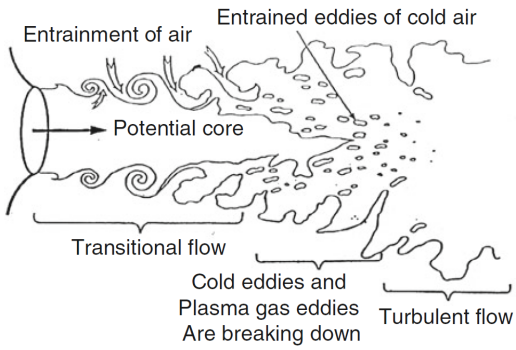

Figure 33: Schematic of the large-scale turbulence and cold gas entrainment in a plasma jet issuing into a cold gas environment [18]

Experimental studies have shown that the temperature and velocity variations of Ar plasma over 200 ms at 11 mm downstream of the torch exit can reach 2,000 K (mean temperature is 12,000 K) and 200 m/s respectively for a torch operating at 600 A [18]. Figure 34 shows how the maximal jet temperature at a given axial location changes from measurement to measurement.

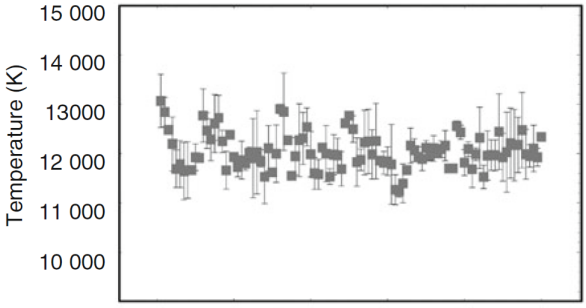

Figure 34: Hundred consecutive measurements of the peak temperature [18]

Despite the jet instability, prediction of the time-averaged behavior of thermal plasma outside of the torch in APS and thus in HPC is usually successfully made by means of the one-temperature Continuum Fluid Dynamics (CFD) approach with an appropriate turbulence model to account for turbulence-related fluctuations [75–79]. This technique consists in the representation of the simulated domain as a finite set of control volumes used to approximate the conservation equations of mass, momentum, species or mixture components and energy (usually enthalpy) by a finite volume approach. The diffusion phenomena are considered by introducing phenomenological relations between stress tensor and velocity gradient and between heat flux and temperature gradients.

II.2.3.2. Modeling Assumptions

CFD approach, typically used for APS modeling, is based on the following assumptions:

- The plasma gas is a continuum medium, which implies that it can be described in terms of temperature, pressure, enthalpy and bulk velocity ($\mathrm{Kn}<0.01$);
- The gas is in local thermal equilibrium (LTE), which means that some moderate gradients of temperature, density and other gas properties can be present, but they

should be low enough so that a gas molecule can have enough time to adopt the temperature of the surrounding medium during its diffusion or convection.

Additional assumptions, specific for APS modeling, include the following:

- The ionization degree is low enough for electromagnetic phenomena to be ignored (under the spray conditions of the study, the temperature in the spraying chamber was low enough to ignore atom ionization: near the torch outlet, the maximal ionization degree was about 2.5% at 10^5 Pa and 10^4 K);
- Demixing and chemical reactions between the different gases composing plasma gas, carrier gas, and ambient gas are not considered;
- The gas is a Newtonian fluid, with a linear relation between the stress tensor and velocity gradient;
- Thermal radiation effect on gas's enthalpy is negligible;
- The flow is stationary and time-averaged quantities can adequately represent it.

The validity of these assumptions was experimentally tested [25, 26] under classical APS conditions.

II.2.3.3. General Conservation Equation

The idea behind a broad range of conservation equations presented in this chapter can be demonstrated by the general transport or conservation equation, written in the differential form:

$$\frac{\partial(\rho\phi)}{\partial t} + div(\rho\phi\vec{v}) = div\left(\Gamma_\phi grad\phi\right) + S_\phi \tag{2}$$

where ϕ is a general variable (unity, flow velocity vector $\vec{v}$, specific energy or mixture component mass fraction), ρ is the flow density and Γ_ϕ is the diffusion coefficient for ϕ.

In equation (2), the terms on the left-hand side represent the rate of variation of ϕ in the considered volume and the rate of flow of ϕ in/out of fluid element (advection); the terms on the right-hand side show the rate of variation of ϕ due to diffusion and the rate of variation of ϕ due to the source S_ϕ

II.2.3.4. Basic Fluid Flow and Heat Transfer

The plasma jet dynamics and its mixing with the surrounding gas are tied to the mass conservation equations of fluid and energy conservation equation for multi-component flow. These equations are expressed in instantaneous quantities.

The mass conservation equation, or continuity equation, is written as follows:

$$\frac{\partial\rho}{\partial t} + \nabla\cdot(\rho\vec{v}) = S_m \tag{3}$$

where ρ is the flow density, $\vec{v}$ is the flow velocity vector and S_m is the mass source, that can represent the vapor generation due to the vaporization of melted particles.

The momentum conservation equations are:

$$\frac{\partial}{\partial t}(\rho\vec{v}) + \nabla\cdot(\rho\vec{v}\vec{v}) = -\nabla p + \nabla\cdot(\bar{\bar{\tau}}) + \rho\vec{g} \tag{4}$$

where p is the static pressure, $\bar{\bar{\tau}}$ is the stress tensor and $\vec{g}$ is the gravitational acceleration.

The stress tensor for a Newtonian fluid can be written as follows:

$$\bar{\bar{\tau}} = \mu\left[\left(\nabla\vec{v} + \nabla\vec{v}^{T}\right) - \frac{2}{3}\nabla\cdot\vec{v}I\right] \tag{5}$$

where μ is the molecular viscosity and I is the unit tensor.

The energy equation is given by:

$$\frac{\partial}{\partial t}(\rho E) + \nabla\cdot\left(\vec{v}(\rho E + p)\right) = \nabla\cdot\left(k_{eff}\nabla T - \sum_{j} h_j\vec{J}_j + \left(\bar{\bar{\tau}}_{eff}\cdot\vec{v}\right)\right) + S_h \tag{6}$$

where E is the specific energy of the flow (J/kg), k_{eff} is the effective conductivity ($k_{eff} = k + k_t$, where k is the gas thermal conductivity, k_t is the turbulent thermal conductivity, defined by the choice of the turbulence model, in instantaneous form of the equation the turbulent component is absent), $\bar{\bar{\tau}}_{eff}$ is the effective stress tensor, $\vec{J}_j$ is the diffusion flux of gas mixture component j, and S_h is the enthalpy source, that can represent the energy consumption during vaporization of melted particles.

Together, equations (3), (4) and (6) are called the *Navier-Stokes equations*.

The energy variable in (6) can be written in terms of enthalpy of mixture component j h_j with the mass fraction Y_j:

$$E = \sum_{j} Y_j h_j - \frac{p}{\rho} + \frac{v^2}{2}. \tag{7}$$

In equation (7) the enthalpy of mixture component j is calculated by integrating the specific heat of the corresponding component:

$$h_j = \int_{T_{ref}}^{T} c_{p,j}\,dT \tag{8}$$

where T_{ref} is a reference temperature, and $c_{p,j}$ – the specific heat of mixture component j.

The mass fraction of component Y_j is predicted through the solution of a convection-diffusion conservation equation:

$$\frac{\partial}{\partial t}\left(\rho Y_j\right) + \nabla\left(\rho\vec{v}Y_j\right) = -\nabla\cdot\vec{J}_j + S_j \tag{9}$$

where S_j is the variation rate of mixture component j due to the dispersed phase (vaporization of melted droplets).

The mass diffusion phenomenon for turbulent flows can be described by the following equation:

$$\vec{J}_j = -\left(\rho D_{j,m} + \frac{\mu_t}{Sc_t}\right)\nabla Y_j - D_{T,j}\frac{\nabla T}{T} \tag{10}$$

where $D_{j,m}$ and $D_{T,j}$ are the mass and thermal diffusion coefficients for component j, respectively, and Sc_t is the turbulent Schmidt number ($\mathrm{Sc}_t = \mu_t / \rho D_t$ where μ_t is the turbulent viscosity and D_t is the turbulent diffusivity).

II.2.3.5. Turbulence Modeling

As mentioned by Mariaux and Shigeta [80, 81], even if the Reynolds number is low inside the plasma torch (Re ~ 1,000) and in the jet core, the turbulence rapidly develops at the jet fringes (Re ~ 9,000) due to the velocity and density gradients favoring the formation of eddies of various scales. For simulations of APS, a k-ε turbulence model is very often used [75–77]. This model assumes that the turbulence is isotropic and fully developed.

Recent studies show, that the Shear-Stress Transport (SST) k-ω turbulence model may be a better choice for thermal plasmas [26, 81]. In this model, non-fully developed turbulence is considered, which makes it a good fit for the cases where the laminar-turbulent transition occurs [82, 83].

Both models return time-averaged predictions for the turbulent velocity components (the same applies to different scalar quantities, e.g. pressure or energy):

$$\vec{v} = \bar{\vec{v}} + \vec{v}' \tag{11}$$

where $\bar{\vec{v}}$ and $\vec{v}'$ are mean and fluctuating velocity vector components.

Replacing the overall velocity in equation (4) by the expression (11) and taking time average yields the following equation:

$$\frac{\partial}{\partial t}(\rho v_i) + \frac{\partial}{\partial x_j}(\rho v_i v_j) = -\frac{\partial p}{\partial x_i} + \frac{\partial}{\partial x_j}\left[\mu\left(\frac{\partial v_i}{\partial x_j} + \frac{\partial v_j}{\partial x_i} - \frac{2}{3}\delta_{ij}\frac{\partial v_k}{\partial x_k}\right)\right] + \frac{\partial}{\partial x_j}\left(-\rho\overline{v_i' v_j'}\right) \tag{12}$$

Together, equation (3) and (12) form the so-called Reynold-averaged Navier-Stokes (RANS) equations. In this case, velocities and other variables present in these equations represent time-averaged values.

To form a closed set of equations the term $-\rho\overline{v_i' v_j'}$, which is called the Reynolds stress and represents the turbulence effect, should be modeled. In both k-ε and k-ω models, this term is related to the mean velocity gradients by the Boussinesq hypothesis:

$$-\rho\overline{v_i' v_j'} = \mu_t\left(\frac{\partial v_i}{\partial x_j} + \frac{\partial v_j}{\partial x_i}\right) - \frac{2}{3}\left(\rho k + \mu_t\frac{\partial v_i}{\partial x_j}\right)\delta_{ij} \tag{13}$$

where k is the turbulent kinetic energy, which is a new variable to be defined. This model is based upon the assumption of isotropy of the turbulent viscosity μ_t. To determine the values of μ_t, the solution of two additional transport equations is required.

Even if the RANS approach with a first closure model (k-ε or k-ω) is not the best choice for non-isotropic non-fully developed turbulence, it is usually adopted due to its light CPU resource requirements. Both models are phenomenological, with coefficients based on a broad set of experimental data.

The realizable k-ε model is commonly used under APS conditions due to its robustness, economy and acceptable accuracy. Its major shortcomings are low sensitivity to adverse pressure gradients making it unsuitable for converging nozzles, and sensitivity of the solution towards the discretization in the viscous sublayer of the near-wall region. The latter further complicates modeling process of the flow inside nozzles, forcing the creation of extremely fine meshes capable of resolving steep gradients of the viscous sublayer. To avoid this problem implementation of near-wall laws (empirically-based velocity profiles) is required. The biggest

shortcoming of the model is so-called “round-jet anomaly”, which leads to extremely poor predictions of axisymmetric jet spread rates.

SST k-ω model seems to be a better choice for APS. It is more adapted to compressibility effects, high velocity gradients near walls and laminar/turbulent transition of compressible flow (which happens when the flow leaves the torch nozzle and when it enters the expansion nozzle). In the thesis report of de Sousa [25], it was shown that under classic APS conditions the SST k-ω model gives the best predictions of plasma temperature and velocity as compared with experimental data.

a. Realizable k-ε Model

The realizable k-ε model is based on the standard k-ε model, a semi-empirical two-equation model, which consists of the model transport equations for the turbulence kinetic energy k and its dissipation rate ε that must be defined:

$$\begin{cases} \dfrac{\partial}{\partial t}(\rho k)+\dfrac{\partial}{\partial x_j}(\rho k v_j)=\dfrac{\partial}{\partial x_j}\left[\left(\mu+\dfrac{\mu_t}{\sigma_k}\right)\dfrac{\partial k}{\partial x_j}\right]+G_k+G_b-\rho\varepsilon-Y_M \\ \dfrac{\partial}{\partial t}(\rho \varepsilon)+\dfrac{\partial}{\partial x_j}(\rho \varepsilon v_j)=\dfrac{\partial}{\partial x_j}\left[\left(\mu+\dfrac{\mu_t}{\sigma_\varepsilon}\right)\dfrac{\partial \varepsilon}{\partial x_j}\right]+\rho C_1 S\varepsilon-\rho C_2\dfrac{\varepsilon^2}{k+\sqrt{\nu\varepsilon}}+C_{1\varepsilon}\dfrac{\varepsilon}{k}C_{3\varepsilon}G_b \end{cases} \quad (14)$$

where $C_1=\max\left[0.43,\dfrac{\eta}{\eta+5}\right]$, $\eta=S\dfrac{k}{\varepsilon}$, $S=\sqrt{2S_{ij}^2}$, $S_{ij}=\dfrac{1}{2}\left(\dfrac{\partial v_j}{\partial x_i}+\dfrac{\partial v_i}{\partial x_j}\right)$, G_k is the source term for turbulent kinetic energy due to mean velocity gradients, G_b is the energy source due to buoyancy, Y_M is the effect of compressibility, C_2 and $C_{2\varepsilon}$ are constants and σ_k and σ_ε are the turbulent Prandtl numbers for k and ε.

The turbulent viscosity in the k-ε model is given by:

$$\mu_t=\rho C_\mu\frac{k^2}{\varepsilon} \quad (15)$$

where C_μ is a variable factor, dependent on the mean strain and rotation rates, the angular velocity of the system rotation, and values of k and ε.

b. SST k-ω model

The transport equations for SST k-ω model are the following:

$$\begin{cases} \dfrac{\partial}{\partial t}(\rho k)+\dfrac{\partial}{\partial x_j}(\rho k v_j)=\dfrac{\partial}{\partial x_j}\left[\Gamma_k\dfrac{\partial k}{\partial x_j}\right]+G_k-Y_k \\ \dfrac{\partial}{\partial t}(\rho \omega)+\dfrac{\partial}{\partial x_j}(\rho \omega v_j)=\dfrac{\partial}{\partial x_j}\left[\Gamma_\omega\dfrac{\partial \omega}{\partial x_j}\right]+G_\omega-Y_\omega+D_\omega \end{cases} \quad (16)$$

where ω is the specific dissipation rate, G_ω is the source of ω, Γ_k and Γ_ω ($\Gamma_i=\mu+\dfrac{\mu_t}{\sigma_i}$, i = k, ω) are the effective diffusivity of k and ω, σ_ω is the turbulent Prandtl number for ω, Y_k and Y_ω represent the dissipation of k and ω and D_ω is the cross-diffusion term.

The turbulent viscosity for in the k-ω model is defined by:

$$\mu_t = \frac{\rho k}{\omega} \frac{1}{\max\left[\frac{1}{\alpha^*}, \frac{SF_2}{a_1 \omega}\right]} \tag{17}$$

where the purpose of the coefficient α^* is to correct the turbulent viscosity in case of low Reynolds numbers ($\alpha^* = \alpha_\infty^* \left(\frac{\alpha_0^* + \mathrm{Re}_t / R_k}{1 + \mathrm{Re}_t / R_k} \right)$, $\mathrm{Re}_t = \frac{\rho k}{\mu \omega}$, $R_k = 6$, $\alpha_0^* = \frac{\beta_i}{3}$, $\beta_i = 0.072$, $\alpha_\infty^* = 1$), S is the strain rate magnitude, $F_2 = \tanh\left(\max^2\left[2\frac{\sqrt{k}}{0.09\omega y}, \frac{500\mu}{\rho y^2 \omega} \right] \right)$, where y is the distance to the wall.

Through the coefficient α^* this model is able to control the production and dissipation of turbulent energy at low Reynolds numbers and, especially, in the viscous sublayer of near-wall regions without using near-wall laws [82].

II.2.3.6. Plasma Gas Thermodynamic and Transport Properties

The solution of RANS equations (3), (6), (9) and (12) requires the knowledge of thermodynamic (enthalpy, specific heat, density) and transport (viscosity, speed of sound, thermal conductivity, diffusivity) properties of the gas mixture. The relation between various thermodynamic quantities for a gas is usually described by the equation of state. The ideal gas law is often used to describe the relationship between the fluid density, temperature and pressure, whereas gas thermodynamic and transport properties are usually considered to depend solely on temperature [60, 84]. Under APS conditions, application of the ideal gas law is compounded by a complex flow chemistry and the presence of ions. Therefore, the change of gas composition should be taken into account. The plasma gas properties are usually calculated using the Chapman–Enskog method [85–87], while the equilibrium composition is estimated using the method of minimization of Gibbs free energy [88].

Under APS/CAPS conditions, as well as in any other deposition process, gas mixtures are not uniform – the initial uniform plasma gas is being mixed with the background gas, with carrier gas and with vapor, generated by vaporization of the material to be deposited. Chemical reactions between the mixture components are rather likely and they have a significant influence over the resulting mixture properties. Ideally, a set of properties should be generated for a broad range of possible proportions of the components. Under APS conditions, such an approach is complicated by the number of possible combinations: at least three gases (Ar, H_2 and ZrO_2) are present in the domain simultaneously, with the composition of each one evolving with pressure and temperature. To reduce the complexity of the task, simplified mixing rules were proposed by Gleizes et al [89].

According to Gleizes, thermodynamic and transport properties of such mixtures can be calculated by a simple weighting of each *component* (plasma forming gas, carrier gas, and ambient gas, or Ar, H_2, etc. depending on the available gas properties) properties by its content in the mixture. This approach does not take into account the chemical reactions between the mixture components. However, this reduces the complexity of properties calculation, providing results with a sufficient accuracy.

a. Plasma Gas Composition and Properties

The calculation of thermodynamic and transport properties for each "pure" component (Ar/H_2 mixture, carrier gas, etc.) requires knowledge of the plasma gas composition at different temperatures and pressures. The method of minimization of Gibbs free energy [88] is generally used to calculate the composition under the assumption of LTE, which implies:

- The velocity distribution of each species is Maxwellian;
- The population density of excited states for each species follows a Boltzmann distribution;
- Chemical equilibrium;
- The translational temperatures (for a Maxwellian distribution), the excitational temperatures (for a Boltzmann distribution) and the reaction temperatures (for concentrations calculation at chemical equilibrium) are equal;
- The composition of each "pure" gas varies with pressure and temperature due to dissociation, recombination, ionization and various chemical reactions between its components. E.g. for pure argon plasma under certain conditions the following species will be present in substantial concentrations: Ar, Ar^+, Ar^{2+}, Ar^{3+},e^-. The gas, composed of the same species, is considered to be ideal.

Even though the composition of the gas varies, each gas from now on will be referred to according to its composition under the standard conditions.

Plasma has to be optically-thin, so that collisional properties would govern transitions and reactions rather than radiative ones. Gradients of temperature and other properties have to be appropriately small, so that diffusion rates are smaller than equilibration rates for each species, and convective flow rates also have to be smaller than equilibration rates for each species. These conditions are usually satisfied in thermal plasmas around atmospheric pressures except from the regions close to electrodes [87]. The typical equilibrium compositions of Ar/H_2 and ZrO_2 (denoted as "pure" gases) plasmas are shown in Figure 35.

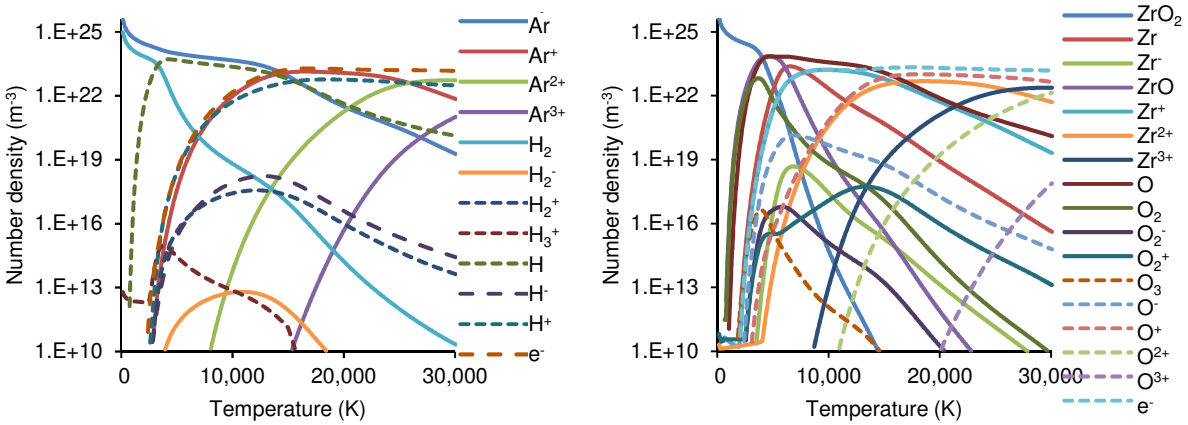

Figure 35: Equilibrium compositions of Ar/H_2 mixture (left) and ZrO_2 vapor (right) at 1 atm [86]

When the composition of a "pure" gas *j* is known, the plasma density and the specific enthalpy per unit mass are given by:

$$\rho_j = \sum_i n_i m_i \,, \tag{18}$$

$$h_j = \frac{1}{\rho}\sum_i n_i m_i \left(\frac{h_i + 4k_B T D_i}{3} \right) \tag{19}$$

where n_i is the number density of species i composing the gas j, m_i is their mass, h_i is their enthalpy per unit mass and D_i is the Debye–Hückel correction of i^{th} species, $D_i = -(eZ_i)^2 / (8\pi\varepsilon_0 k_B T \rho_D)$, where e = 1.6 × 10^{-19} C, ε_0 = 8.85 × 10^{-12} F/m, ρ_D is the Debye radius and Z_i is the charge number of species i.

The specific heat is obtained directly from the enthalpy by taking a partial temperature derivative under fixed pressure:

$$c_{pj} = \left(\frac{\partial h_j}{\partial T} \right)_p . \tag{20}$$

The transport properties are calculated using the Chapman-Enskog method [90], based upon the first-order solution of the Boltzmann equation. Calculation of transport coefficients requires the knowledge of the collision integrals. A collision integral is a binary collision cross section averaged over the Maxwellian spectrum; it is a term of the Boltzmann equation that describes the influence of particle collisions on the evolution of the particle distribution function. In the Chapman-Enskog method, collision integral is derived from the intermolecular potentials.

The viscosity of a gas is proportional to $(m_i T)^{1/2} / \Omega_i$, where Ω_i is the collision cross section of i^{th} species. The thermal conductivity has three components: translational, internal and reaction conductivities. The translational component is connected with the transport of translational energy. It is proportional to $c_{p,i} (T/m_i)^{1/2} / \Omega_i$. The presence of the second component – the internal conductivity – is caused by transport of internal energy, and the reaction thermal conductivity is that due to the thermal transport caused by the release of the reverse reaction enthalpy by the products of the reactions diffusing into a lower temperature region in thermal plasma.

Figure 36 shows the temperature variation of the specific heat at constant pressure and viscosity of Ar/H_2 gas mixture at 100 Pa and 10^5 Pa.

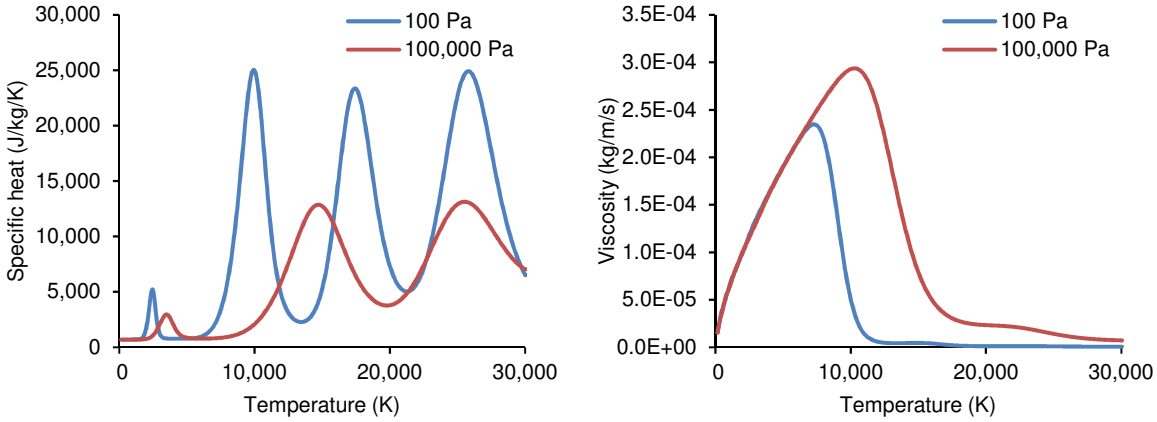

Figure 36: Specific heat and viscosity of 80 vol%Ar/20 vol%H_2 gas mixture at 100 Pa and 10^5 Pa [86]

b. Mixing Rules

Under APS/CAPS conditions at least three “pure” gases (e.g. Ar/H_2, Ar and ZrO_2) are present in the calculation domain simultaneously. Thermodynamic and transport properties for each “pure” component can be calculated according to the aforementioned description. According to Gleizes et al [89], the following simplified expressions can be introduced for the gas mixture.

The mass density of the mixture is defined as follows:

$$\rho = \frac{pM}{RT}, \tag{21}$$

where R is the universal gas constant, M is the average molar mass of the mixture, $M = \left(\sum_j \frac{c_j Y_j}{M_{j,ref}} \right)^{-1}$, Y_j is the mass fraction of j^{th} component of the mixture (e.g. Ar with all its ions), $M_{j,ref}$ is the molar mass of j^{th} component at reference pressure and temperature, c_j is the correction factor which shows the change of gas composition with pressure and temperature, $c_j(p,T) = M_{j,ref} / M_j(p,T)$, where M_j is the molar mass, calculated with the actual gas composition taken into account. The pressure and temperature reference values are p_{ref} = 10^5 Pa and T_{ref} = 300 K, respectively.

The molar fraction x_j is calculated as follows:

$$x_j = \frac{Y_j M}{M_j}. \tag{22}$$

The specific enthalpy and the specific heat are given by:

$$\phi = \sum_j Y_j \phi_j, \tag{23}$$

where ϕ_j is a property of j^{th} component.

The speed of sound, the plasma gas viscosity and the thermal conductivity are defined as:

$$\phi = \sum_j x_j \phi_j. \tag{24}$$

II.2.3.7. Numerical Scheme

For a numerical solution, partial differential RANS equations are represented in an algebraic form generally using the finite volume method (FVM). In this method, the simulation domain is discretized into a finite set of control volumes with sizes V, compatible with the continuum assumption. The conservation equations (2) can be written in the integral form as follows:

$$\frac{\partial}{\partial t} \int_V \rho \phi dV + \oint_A \rho \phi \vec{v} d\vec{A} = \oint_A \Gamma_\phi \nabla \phi d\vec{A} + \int_V S_\phi dV, \tag{25}$$

where V is an arbitrary control volume and A is the surface area of this volume. Here, the second term on the left-hand side represents the convective flux and the first term on the right-hand side represents the diffusion flux. The exact transition from volume to surface integrals for these terms makes the method inherently conservative, which means that the conservation law will be still valid in the algebraic form.

For a given rectangular mesh cell equation (25) is:

$$\frac{\partial \rho \phi}{\partial t} V + \sum_{f=1}^{N_f} \rho_f \vec{v}_f \phi_f \vec{A}_f = \sum_{f=1}^{N_f} \Gamma_f \nabla \phi_f \vec{A}_f + S_\phi V \ , \tag{26}$$

where ϕ_f is the fraction of ϕ convected through the face f, N_f is the number of faces closing the cell and A_f is the area of the face. This equation can be linearized and solved for the unknown variables ϕ and ϕ_f for each cell.

Depending on the set of independent variables ϕ selected to resolve equations (26) two types of solution algorithms can be utilized: pressure-based solver or density based solver. In both methods, the velocity field is obtained from the momentum equations (12) is used to obtain the density (3) whereas the pressure distribution is determined from the equation of state. Alternatively, in the pressure-based approach, the pressure distribution is extracted by solving a pressure or pressure correction equation which is obtained by manipulating the continuity and momentum equations (3), (4) [82].

The pressure-based approach was initially developed by A.J. Chorin [91] for low-speed incompressible flows, while the density-based approach was mainly used for high-speed compressible flows. However, both methods have been extended and reformulated to solve and operate for a wide range of flow conditions beyond their traditional or original intent [82]. The flow under APS conditions can be considered as weakly-compressible, and thus pressure-based solvers can be used. Taking into account the plasma jet in the torch nozzle, where it can reach high velocities and compressibility effects become apparent requires the use of density-based solvers.

There is plenty of free and commercial FVM solvers available. The most popular free solvers, available under GPL, BSD or similar licenses are Code_Saturne [92], OpenFOAM [93], OpenFVM [94]. These codes are usually open-source, which provides an opportunity to modify them and couple or link with other modeling tools, creating complex multi-physics models. However, the use of free software can be complicated due to the lack of communication with the developer, low frequency of updates or a steep learning curve due to the absence of the graphical user interface (GUI).

Commercial solvers have no drawbacks of the free solvers, but their internal structure is usually not open to users. The most common commercial solvers include ANSYS CFX, ANSYS Fluent [95], COMSOL Multiphysics [96], PHOENICS [97].

CFD codes can produce a solution on structured hexahedral or unstructured tetrahedral meshes. Tetrahedral meshes can be generated automatically, however, this leads to a slower convergence, due to possible numerical noise in the calculation of gradients caused by random orientations of mesh cell faces. This problem can be solved by the use of manually built structured hexahedral mesh with cells approximately tangent to the flowlines.

II.2.4. Gas Expansion through the Nozzle

II.2.4.1. Flow Physics

HPC and LPC are connected with a convergent-divergent supersonic nozzle, schematically depicted in Figure 37.

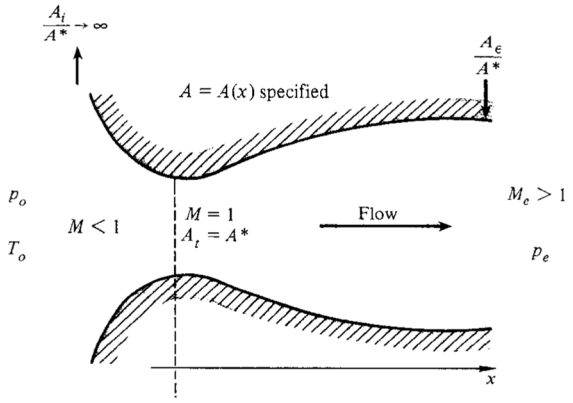

Figure 37: Supersonic nozzle [98]

As the plasma gas flows through the converging conical frustum, because of a decrease of the nozzle cross-section area, the velocity of the flow and its pressure gradually increase. The substantial pressure difference between the HPC (about one atmosphere) and the LPC further accelerates the flow, allowing it to reach sonic velocity in the critical cross-section of the nozzle ("throat", A_t). Once sonic velocity is reached (at the critical cross-section A_t=A*), upstream flow becomes independent on the conditions downstream from the throat, since any perturbation in the gas can spread only with the sonic velocity, thus mass flow rate through the nozzle becomes dependent only on the throat cross section and on the conditions upstream, such as pressure and temperature. Furthermore, when sonic velocity is reached, the flow compressibility effects become apparent. Further advancement of the flow along the divergent part of the nozzle, if its shape allows this, is accompanied by a gradual expansion and continuing acceleration up to supersonic velocities. Due to a gradual expansion inside of the nozzle, this part of the flow is usually considered adiabatic and isentropic [33, 59, 99].

Nozzles are typically designed for a specific jet velocity, expressed by the dimensionless Mach number (M) – a ratio between the flow velocity and the local speed of sound. Gradual expansion downstream from the throat is accompanied by the increase of the Mach number. As mentioned in I.3.4.5, the design of the divergent part, as well as the downstream pressure, determine the shape of the flow downstream. For a given Mach number on the nozzle outlet, if the pressure inside of the jet is higher than the surrounding pressure, the jet is called under-expanded. For the cases when the pressure is lower, the jet is called over-expanded and if the pressures are equal the jet is perfectly expanded.

A density-based solution of RANS equations with the k-ω turbulence model to estimate the flow parameters on the nozzle outlet seems to be a viable option when the nozzle geometry is known [100, 101]. However, when a study requires nozzle size adjustment or if target parameters (Mach number or mass flow rate) on the nozzle outlet are fixed, alternative, simplified methods to solve Navier-Stokes equations could be used. Within the framework of the present study, this approach will be used to make an initial estimation of the expansion nozzle diameter.

II.2.4.2. Model Assumptions

The initial estimation of the nozzle diameter can be made under the following assumptions:

- The gas flow is isentropic, the heat losses through the nozzle walls are negligible;
- The flow is steady and inviscid, due to the first assumption;
- The gas is assumed to be ideal and compressible.

II.2.4.3. One-Dimensional Isentropic Flow

Under the aforementioned assumptions, the equations of mass, momentum and energy conservation along the nozzle axis, as well as the adiabatic process equation are given by:

$$\dot{m} = Av\rho = const\,, \tag{27}$$

$$pA + \rho v^2 A = const\,, \tag{28}$$

$$\frac{v^2}{2} + h = h_0 = const\,, \tag{29}$$

where $\dot{m}$ is the mass flow rate through the cross section with the area A, v is the radially averaged gas velocity, p and ρ are the gas static pressure and density respectively and h is the specific enthalpy of the gas.

For isentropic flow through the nozzle shown in Figure 37, that is if there are no shockwaves inside the nozzle, the adiabatic process equation for the ideal gas can be written as:

$$\frac{p_2}{p_1} = \left(\frac{\rho_2}{\rho_1}\right)^{\gamma} = \left(\frac{T_2}{T_1}\right)^{\gamma/(\gamma-1)}, \tag{30}$$

where subscript 1 marks nozzle inlet conditions and subscript 2 denotes the conditions at any given point downstream from the inlet.

Using the equations (27)-(30) the equation for critical cross section A^* where the flow is sonic (M=1) can be derived as [98]:

$$A^* = \dot{m}\left(\gamma p_0 \rho_0\right)^{-\frac{1}{2}} \left(\frac{2}{1+\gamma}\right)^{-\frac{1+\gamma}{2(\gamma-1)}}, \tag{31}$$

where $\dot{m}$ is the mass flow rate through the nozzle.

Assuming that the flow is isentropic, that is if there are no shocks, nozzle outlet cross section can be estimated for a targeted Mach number using the following expression:

$$\frac{A}{A^*} = \frac{1}{\mathrm{M}} \left(\frac{2 + (\gamma-1)\mathrm{M}^2}{\gamma+1}\right)^{\frac{\gamma+1}{2(\gamma-1)}} \tag{32}$$

II.2.4.4. Method of Characteristics

The method of characteristics allows getting a two-dimensional solution of mass and momentum conservation equations [98]. The essence of the method is in the reduction of these partial differential equations to simpler ordinary differential equations, which can be easily integrated if some initial conditions are given. The method is widely used for the nozzle design [102–104]. This method, however, is not used in the present work due to the engineering restrictions, discussed in the following chapters.

II.2.5. Plasma Flow under VLPPS conditions

II.2.5.1. Flow Physics

The length of the divergent part of the expansion nozzle cannot be too large as heat losses through the walls can noticeably reduce system thermal efficiency. This limits the minimal pressure the gas can reach while approaching the nozzle outlet without energy dissipation. When the nozzle is "shorter" than it should be to decrease the pressure without energy dissipation to these of the downstream chamber, the nozzle outlet pressure is higher than the chamber pressure, it creates the so-called underexpanded jet. This leads to an additional expansion of the plasma gas flow. The structure of an underexpanded plasma jet is shown in Figure 38.

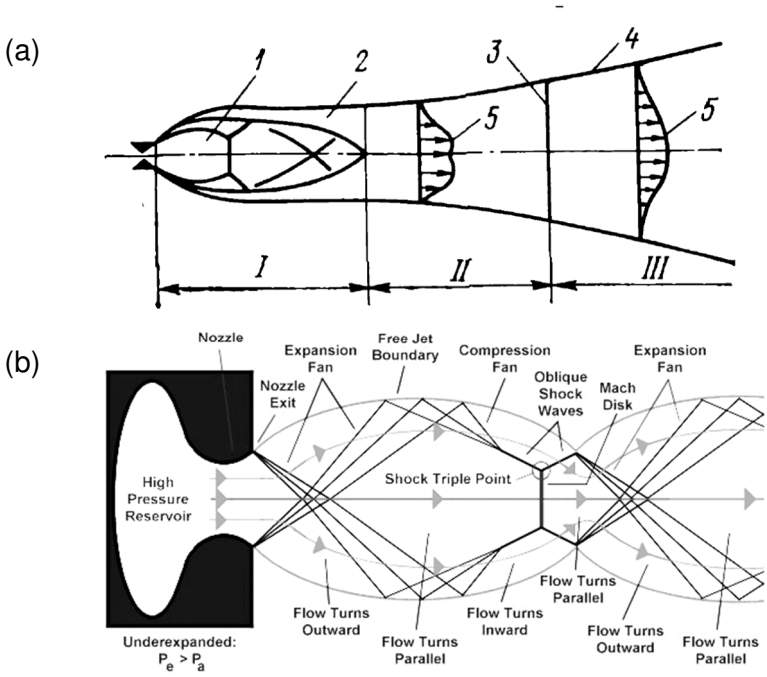

Figure 38: (a) - Supersonic under-expanded plasma jet structure: I – initial zone, II – transitional zone, III – main zone, 1 – free expansion region, 2 – jet boundary layer, 3 – plane where pressure inside of the jet equalizes with chamber pressure, 4 – jet boundary, 5 – radial profiles of velocity [105]; (b) - Wave structures in the initial region of the underexpanded flow [106]

The initial zone (I) is characterized by the presence of various waves, typical for supersonic ($M>1$) flows. Among them, there are *shock waves* – localized regions of the supersonic jet, where an abrupt change of the gas properties by a large amount occurs, due to a sudden decrease in the flow area. Across a shock wave the Mach number decreases, the static pressure increases, and the total pressure decreases, signifying the process' irreversibility. *Prandtl-Meyer expansion waves* are processes, which occur if a sudden increase of the flow area happens. Along the expansion waves the increase of the Mach number occurs, while the static pressure decreases, and the total pressure and entropy stay constant.

While exiting the nozzle, the supersonic flow, driven by the lower ambient pressure, turns outward from the centerline. This process is described by a series of expansion waves (collectively referred to as an expansion fan), trying to equalize the jet pressure with the ambient chamber pressure. The maximal turn angle of the supersonic flow leaving the nozzle is fixed for a known Mach number on the nozzle outlet. The waves emitted from radially opposite sides of the nozzle outlet are eventually meeting and deflecting from each other. At a

certain distance from the nozzle exit, the flow becomes overexpanded – its pressure falls below the ambient one. As a result, the flow starts turning inward. The expansion waves are reaching the contact discontinuity (at the free jet boundary) and reflect inward. These reflected waves are referred to as a compression fan. The compression fan forces the flow to turn inward and increases the pressure. Eventually, compression waves merge into an oblique shock – a shock wave, which is inclined with respect to the flow direction. The compression continues downstream, where a normal shock wave (Mach disk) is formed. Compression is accompanied by an abrupt temperature increase, making the Mach disc become visible, as it can be noticed in Figure 39. In the Mach disk, the flow becomes too compressed, with the jet pressure exceeding the ambient pressure value. This leads to the formation of a new oblique shock and a new expansion fan and the process repeats. The area between two Mach disks is usually referred to as a "barrel". The cycle continues through the transition zone (II) until the jet pressure becomes equal to the ambient pressure (location 3) [106, 107].

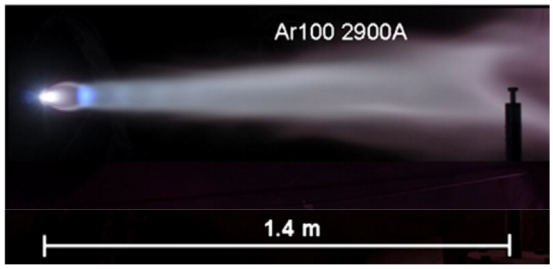

Figure 39: Photograph of PS-PVD plasma jets emitted from 03CP plasma torch. Chamber pressure and net power input were kept constant at 200 Pa and 60 kW [58]

II.2.5.2. Nonequilibrium Phenomena in Supersonic Plasma Flow

When a hot plasma jet expands through the divergent part of the nozzle, it accelerates from 1,000 m/s to 3,000-6,000 m/s. Considering the length of this part (~1-3 cm), the time needed for the flow to pass through it has the same order of magnitude as the chemical relaxation time (~10 μs). Thus, chemical reactions do not happen over such distance and the flow is considered chemically frozen.

When the flow exits the nozzle and enters the free expansion region (Figure 38a, 1), deviations from LTE are observed. Since the flow was chemically frozen prior to the entry, local Saha equilibrium (LSE) is violated. Fast expansion does not allow reestablishment of LSE. As shown by Chou and Jenkins [108, 109], the expansion of heavy particles could be considered adiabatic, however, the effect of the recombination on the electron temperature is substantial. As reported by Selezneva and Usami [84, 110], a violation of LME is also observed – the kinetic energy of macroscopic movement of molecules leaving the torch is mostly transformed into the energy of random movement in the axial direction, while the radial component is less affected. Molecular velocity can no longer be characterized by a single translational temperature and one isotropic molecular velocity distribution – separate axial and radial temperatures should be introduced to indicate the difference in molecular velocity distributions in the free expansion region. The unbalance between these temperatures is compounded by the *rarefaction*, caused by the abrupt pressure decrease. The rarefaction phenomenon decreases the frequency of gas molecules collisions and results in a transition from continuum flow to slip flow and, eventually, to free molecular flow ($\mathrm{Kn}>0.01$). These phenomena are resulting in the *continuum breakdown*. This issue will be addressed in the flow modeling section.

In the downstream part of the initial region (Figure 38a, 1, Figure 38b) deviation from LTE is also observed, especially in the first Mach diamond, where disequilibrium induced by the free expansion region is still apparent [73]. Additional disequilibrium here is caused by a rapid compression, accompanied by temperature growth. Ionization process does not contribute to deviation from LTE significantly, since in the preceding expansion the flow was chemically frozen and thus overpopulated with electrons. After the flow passes the Mach diamond, a slow relaxation towards equilibrium occurs.

II.2.5.3. Direct Simulation Monte Carlo Approach

CFD approach is widely used for the flow modeling under PS-PVD conditions [11, 60, 111–116]. However, such an approach might be incorrect under these conditions for the following reasons:

- The conservation equations assume the fluid to be a continuum medium;
- The linear relations between the stress tensor and velocity gradient (Newton's law of viscosity), and between the thermal heat flux and temperature gradient (Fourier's law), classically used in the conservation equations, become nonlinear in rarefied flows [90];
- The turbulence models can yield significant errors when applied to supersonic flows [117].

These facts result in the underestimated gradient values and lead to the broadening of the shock waves. Several approaches can be used to predict the behavior of the rarefied non-equilibrium flow more accurately. If rarefaction effects are not too apparent, but disequilibrium effects are possible, 2T CFD models can be used [118]. For more complex cases with rarefaction, there are methods, which involve the use of the conservation equations that are still valid for larger deviations from the equilibrium conditions, with a correction of the stress tensor and heat flux vector to account for rarefaction effects [90, 119, 120]. But these methods still require the continuum assumption. Another way is to use a more general kinetic approach, where the gas is composed of a huge number of individual particles involved in binary collisions with each other. This approach is based on a statistical description of positions and velocities of the particles and involves the solution of the Boltzmann equation in terms of the phase space distribution function [121]. However, both approaches are too complicated for practical applications and have significant computational cost.

An alternative is to use numerical method for solving the Boltzmann equation based on the so-called direct simulation Monte Carlo (DSMC), which has received a wide recognition in recent years [84, 122]. It involves the direct simulation performed by following the evolution of the statistically representative number of gas molecules. The result of simulations is interpreted as a solution of the Boltzmann equation because it is built upon the same assumptions.

II.2.5.4. General Description and Assumptions

In the classical kinetic theory, derived by Ludwig Boltzmann, the gas state is characterized by a probability density function for the position and momentum of a molecule. This function can be obtained as a solution of the Boltzmann equation [123], derived according to the following assumptions:

- The dilute gas assumption, which implies that the volume per molecule is much larger than the volume of a single molecule or species, and thus the probability of triple collisions is insignificant and interaction between molecules can be considered as instantaneous;
- Molecular chaos, which assumes that velocities/internal energies of colliding particles are uncorrelated, so that the probability of finding a pair of molecules in a particular two particle configuration is a product of the probabilities of finding the individual molecules in the two corresponding one particle configurations.

The Boltzmann equation for species p of the mixture for the infinitesimal phase space element $d\vec{c}d\vec{r}$ can be written as:

$$\frac{\partial}{\partial t}\left(n_p f_p\right) + \vec{c}_p \cdot \frac{\partial}{\partial \vec{r}}\left(n_p f_p\right) + \vec{F} \cdot \frac{\partial}{\partial \vec{c}}\left(n_p f_p\right) = \sum_{q=1}^{s} \int_{-\infty}^{\infty} \int_{0}^{4\pi} n_p n_q \left(f_p^{\,*} f_{1q}^{*} - f_p f_{1q}\right) c_{rpq} \sigma_{pq} d\Omega d\vec{c}_{1q} \,, \quad (33)$$

where $f_p = f_p(\boldsymbol{c}_p)$ is a single species probability density function in velocity space, the asterisk denotes the post-collision values, $\vec{\boldsymbol{c}}_p$, n_p are the velocity and number density of molecules p, $\vec{F}$ is the external force field, s is the total number of gases in the mixture, c_{rpq} and σ_{pq} are the relative speed and collision cross-section of molecules p and q respectively, and $d\Omega$ is the unit solid angle. Collision cross-section is a parameter which represents the probability of collision between molecules. Imagine a flux of molecules flying in the normal direction to a wall composed of one layer of the molecules of the same species. Some of the molecules from the flux collide with the wall and scatter, others pass the wall without any interaction. The collision cross section can be defined as a ratio between the number of scattered molecules to the total number of the molecules that reached the wall per unit surface of the wall. In simpler terms, collision cross-section may be described as the area of a circle with a radius which is equal to the distance between the centers of two colliding molecules in the moment of collision.

In the equation (33), the summands on the left-hand side represent the rate of change of the number of molecules in the infinitesimal phase space element $d\vec{c}d\vec{r}$, the convection of molecules from the volume $d\vec{r}$ by the molecular velocity $\vec{\boldsymbol{c}}_p$ and the "convection" of molecules from the volume $d\vec{c}$ due to the external force $\vec{F}$. The right-hand side represents the scattering of molecules into and out of $d\vec{c}d\vec{r}$ as a result of intermolecular binary collisions and is called the collision term.

For s species s Boltzmann integro-differential equations have to be solved. The complexity of the collision term makes analytical and numerical solutions of the equations a considerable challenge.

The Direct Simulation Monte Carlo (DSMC) approach may be a good alternative to the numerical solution of Boltzmann equations. The DSMC is a method for simulation of gas flows at a molecular level based on random sampling. Since the DSMC method is based on the same assumptions as the kinetic theory, it is believed that the method is capable of producing the exact solution of the Boltzmann equation when time step and cell size tend to zero [123].

Additional computational approximations of the DSMC method are the following [123]:

- The gas can be represented by a reduced number of molecules with a scale factor F_N – the ratio of the number of simulated molecules to the number of actual molecules. The real/correct collision frequencies are however used since they are artificially increased by the same ratio;

• The molecular motion and collisions are uncoupled and occurring once per designated time step;
• A binary collision is a stochastic event and can happen only between two molecules positioned in the same cell.

II.2.5.5. Simulated Processes and DSMC Code Structure

In real gases, molecules undergo translational movement and movement caused by the external force fields. The gas molecules participate in binary collisions with each other and with the walls, resulting in scattering or in chemical reactions. DSMC codes are designed to simulate the entire set of events, which may happen to a molecule. The implementation of the DSMC approach is highlighted on a flowchart of a classical DSMC code DS2V [124] shown in Figure 40.

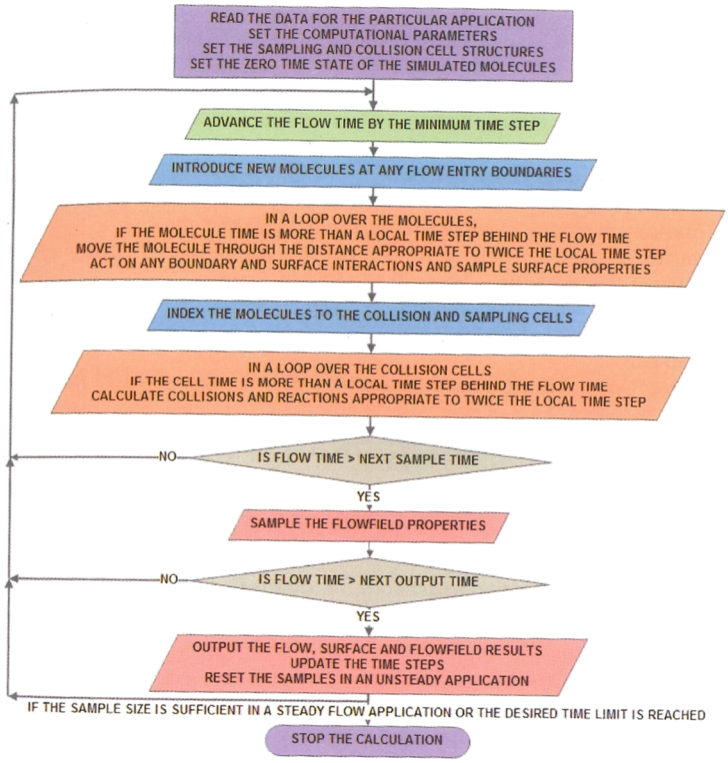

Figure 40: The flowchart for the DS2V program [124]

The code uses two grids built upon the simulated domain: a collision and a sampling grid. During simulation, a statistically representative number of molecules is introduced into the system. Each molecule is characterized by its coordinates in the physical space, velocity vector and internal energy and represents F_N real molecules. These molecules are involved in a translational movement with velocities corresponding to the initial velocity distribution. The collision grid is chosen to ensure a sufficient number of colliding molecules per cell. At each time step, according to the ‘‘no time counter’’ scheme (NTC), a number of possible collision pairs are selected in every cell according to their relative velocity and collision cross section. Collisions occur between some of the selected molecules with a probability proportional to the collision frequency. Post-collision velocity magnitude is determined through the conservation of mass, momentum and energy. The scattering direction is chosen randomly, according to

the variable hard sphere (VHS) or variable soft sphere (VSS) molecular models that describe the variation of molecular collision cross section with temperature and level of scattering anisotropy [124].

According to the desired frequency, once in several time steps the sampling of the flow field properties is performed: the microscopic flow properties (molecular velocities, number densities) are averaged into macroscopic properties (temperatures, pressures, bulk velocities of the flow) in each cell of the sampling grid. The flow chemistry is described by the Bird's total collision energy (TCE) model.

a. Generation of Reference States

DSMC simulation starts with the generation of a uniform equilibrium gas, which enters the simulation domain. The amount of the simulated molecules entering the domain is determined by the number density of real molecules and the ratio $F_N=n_{ac}/n_{sim}$. The molecules are evenly spaced along the boundary.

Molecular velocity $\vec{c}_p$ in kinetic approach is represented as a sum of the mass average velocity of the flow $\vec{c}_0 = \vec{v}$ and the thermal velocity of the molecule $\vec{c}'_p$:

$$\vec{c}_p = \vec{c}_0 + \vec{c}'_p , \tag{34}$$

where $\vec{c}_0 = \frac{1}{\rho}\sum_{p=1}^{s}\left(m_p n_p \vec{\bar{c}}_p\right) = \frac{\overline{m\vec{c}}}{\bar{m}}$ and m_p is the molecule mass.

The initial Maxwellian equilibrium thermal velocity distribution function of species p in a gas mixture with temperature T has the following form:

$$f_{0,p}\left(c'_p\right) = \left(\frac{m_p}{2\pi k_B T}\right)^{\frac{3}{2}} \exp\left(-\frac{m_p c'^2_p}{2k_B T}\right) = \frac{\beta^3}{\pi^{3/2}} \exp\left(-\beta^2 c'^2_p\right), \tag{35}$$

where $\beta = \sqrt{m_p/(2k_B T)}$, velocity changes from 0 to $+\infty$.

The distribution function for a thermal velocity component is:

$$f_{0,p,u'}\left(u'_p\right) = \left(\frac{\beta}{\pi^{1/2}}\right) \exp\left(-\beta^2 u'^2_p\right). \tag{36}$$

Equation (36) is defined for velocities varying from $-\infty$ to $+\infty$. The functions (35) and (36) are plotted in Figure 41.

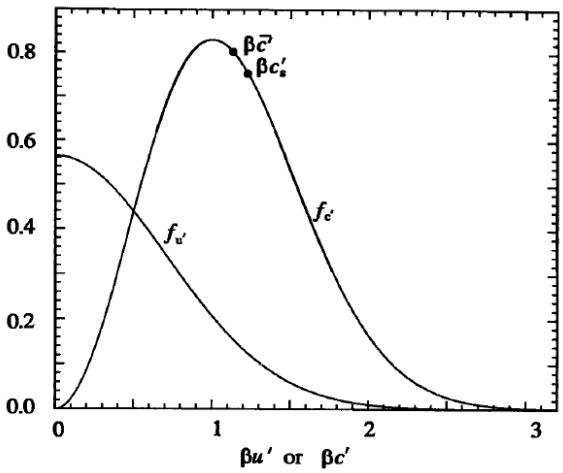

Figure 41: Maxwellian distribution functions for the molecular velocity and for a molecular velocity component

There are two major methods of random state generation: acceptance-rejection method and inverse-cumulative method. The use of these methods is described below on the example of thermal velocity component and total thermal velocity.

a.i. Acceptance-Rejection Method

Velocity sampling from the distribution (36) is managed by the acceptance-rejection method [124]. In this method, velocity is being limited by the arbitrary cut-off values in place of infinities. These values for lower and upper limits are $-3/\beta$ and $+3/\beta$. On the first step of the method, a value of u_p' is chosen randomly on the basis of u_p' being uniformly distributed between the specified limits:

$$u_p' = \left(-3 + 6R_f\right)\Big/\beta\,, \tag{37}$$

where R_f is a random fraction that is uniformly distributed between 0 and 1.

Then the distribution function (36) is normalized to 0-1 range by dividing it by its maximum value:

$$f'_{0,p,u'} = f_{0,p,u'}\Big/ f_{\max} = \exp\left(-\beta^2 u_p'^2\right). \tag{38}$$

The normalized function $f'_{0,p,u}$ is then calculated for the value u_p' and the new value for R_f is generated. If $f'_{0,p,u'} > R_f$, u_p' is accepted. Otherwise, the value of u_p' is rejected and the process repeats until a value is accepted.

a.ii. Inverse-Cumulative method

If the cumulative distribution $F_x = \int_a^x f_x dx = R_f$ for random value x defined from a to b can be inverted so that the function $x = x\left(a, b, R_f\right)$ is obtained, the inverse-cumulative method of sampling can be used.

When applied to the distribution of total thermal velocity in two-dimensional case $f_{0,p,r,\theta} = f_{0,p,u'} f_{0,p,w'}$ the method provides the following expressions for thermal velocity components in x and y directions:

$$u'_p = r\cos\theta \quad \text{and} \quad w'_p = r\sin\theta, \tag{39}$$

where $r = \left[-\ln\left(R_f\right)\right]^{1/2} \Big/ \beta$, $\theta = 2\pi R_f$ and $\vec{c}'_p = \left(u'_p, w'_p\right)$.

After the thermal component $\vec{c}'_p$ of molecular velocity $\vec{c}_p$ is known, it is added to the mass average velocity of the flow $\vec{c}_0$ to form the final value to be used for the molecule.

b. Translational Movement

Since collisions and molecule movement in DSMC are uncoupled, between collisions molecules are involved in translational movement governed by Newton's laws of motion, expressed in the following equation of motion:

$$\Delta\vec{r} = \vec{c}_p \Delta t_{coll} + \frac{\vec{F}\Delta t_{coll}^2}{2m_p}, \tag{40}$$

where $\Delta\vec{r}$ is the increase of the molecule's radius vector, Δt_{coll} is the time step between collisions, $\vec{F}$ is the external force field (e.g. Lorentz force created by the external electromagnetic field).

c. Binary Collisions

In DSMC, molecules are represented as spherical objects and the flow field is divided into collision cells. In any collision cell with the volume V_c containing $F_N N$ real molecules the probability P of collision between two molecules simulated over time interval Δt_{coll} equals to the ratio of volume covered by their total collision cross-section moving at the relative speed between them to the cell volume:

$$P = F_N \sigma_{pq} c_{rpq} \Delta t / V_c \tag{41}$$

This means that if during the time step two molecules are able to approach each other on the distance less than their average diameter, a collision takes place.

Any combination of two molecules in a cell is considered as a potential collision pair, but for some of them the probability of collision is negligible, which may lead to a significant noise if the number of simulated molecules in the cell is small. Thus, to reduce this possible noise, modern DSMC codes use the no time counter (NTC) method where only a fraction of molecules are chosen to participate in collisions, but the probability of their collision is increased proportionally. In the NTC method, the following number of pairs is selected:

$$N_{pairs} = \tfrac{1}{2} N\left(N-1\right) F_N \max_{p,q}\left(\sigma_{pq} c_{rpq}\right) \Delta t_{coll} / V_c, \tag{42}$$

where N is the number of simulated molecules in the collision cell.

The probability of a collision between molecules in the selected pairs is:

$$\frac{P}{P_{\max}} = P_{pq} = \frac{\sigma_{pq} c_{rpq}}{\max_{p,q}\left(\sigma_{pq} c_{rpq}\right)} \tag{43}$$

Acceptance-rejection method, described earlier, is used with the probability P_{pq} to determine the final set of collision pairs.

The knowledge of the total collision cross-section is essential for collision procedures. This parameter is measured in area units and its meaning can be illustrated by Figure 42.

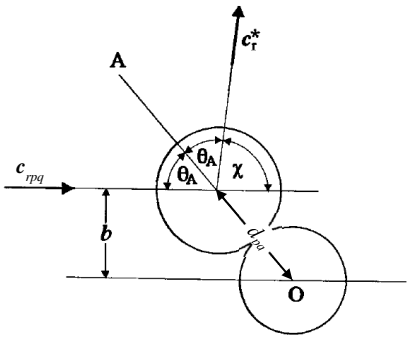

Figure 42: Collision scheme of two hard sphere molecules

Any planar collision can be described by two impact parameters – the angle φ between the collision plane and the plane of reference and the miss distance b between lines through the centers of the molecules that are parallel to the initial relative velocity in the center of mass frame of reference. For a collision to happen the distance b has to be smaller than the mean diameter of the molecules:

$$d_{pq} = \left(d_p + d_q\right)/2\,, \tag{44}$$

or, in other words, the incident molecule needs to be hitting the target with the area equal to

$$\sigma_{pq} = \pi d_{pq}^2 \tag{45}$$

The molecular diameter is a characteristic of a molecule, which indicates the area around the molecule where the intermolecular force field is significant. A typical intermolecular force field is shown in Figure 43.

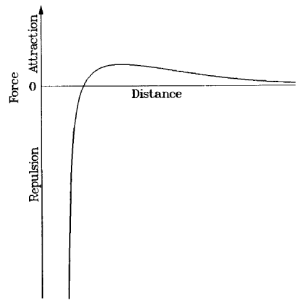

Figure 43: Intermolecular force field

The concept of molecular diameter is based on the assumption of spherical symmetry of intermolecular force fields. Even though it may not be the case for polyatomic molecules, symmetry, this concept is a good approximation considering the isotropy of molecular orientation distribution.

Modern DSMC codes use several phenomenological molecular models, adjusted to give realistic transport properties at the macroscopic level. All of them are based on the first order solution of the Boltzmann equation [90] and adjusted to match the real transport properties at reference temperatures and their variation with temperature. In the Variable Hard Sphere (VHS) model, the molecular diameter is connected to molecular viscosity by the following relation:

$$d_{p,ref}^{VHS} = \left\{ \frac{15(m_p k_B T/\pi)^{1/2}}{2(5-2\omega_p)(7-2\omega_p)\mu_p} \right\}^{1/2}, \tag{46}$$

where ω_p is the temperature exponent of the coefficient of viscosity for gas p with $\mu_p \propto T^{\omega_p}$. The VHS diameter varies with the relative translational energy, following the inverse power law v:

$$d_p^{VHS} = d_{p,ref}^{VHS} \left(c_{rpq,ref} / c_{rpq} \right)^v, \tag{47}$$

where the subscript *ref* signifies reference values.

The post-collision quantities can be easily obtained using momentum and energy conservation equations. Thus, the deflection angle χ in the VHS model is given by the solution these equations:

$$\chi = 2\arccos\left(b / d_p^{VHS} \right) \tag{48}$$

VHS model scattering is isotropic in the center of mass (COM) frame of reference.

The Variable Soft Sphere model is an extension of the VHS model, adjusted to match the real values of Schmidt number $Sc = \mu_p / \left(\rho_p D_{p,m} \right)$ and thus, fitting the experimentally obtained diffusion coefficients $D_{p,m}$. In this model equations (46) and (48) are modified with the empirical factor α:

$$d_{p,ref}^{VSS} = \left\{ \frac{5(\alpha+1)(\alpha+2)(m_p k_B T/\pi)^{1/2}}{4\alpha(5-2\omega_p)(7-2\omega_p)\mu_p} \right\}^{1/2}, \tag{49}$$

$$\chi^{VSS} = 2\arccos\left[\left(b / d_p^{VSS} \right)^{1/\alpha} \right], \tag{50}$$

where $\alpha = 10 / \left[Sc\left(21 - 6\omega_p\right) - 5 \right]$.

Therefore, the VSS model should be applied for gas mixtures, where the accurate prediction of the mass diffusion coefficient is required. Introduction of α distorts the isotropy of scattering in the COM frame of reference. Setting alpha to unity converts the VSS model into a VHS model.

Because the miss distance b in DSMC is a random variable, which varies from 0 to d_p, the direction of the post-collision relative velocity can be set using the inverse-cumulative method as demonstrated in the equations (39):

$$\cos\chi = 2R_f^{1/\alpha} - 1 \tag{51}$$

The magnitude of post-collision relative velocity is calculated from momentum and total collision energy conservation. The latter takes into account the relative kinetic energy, the internal energies of molecules and the heats of formation of each molecule, if chemical reactions occur.

d. Post-Collision Energy

For polyatomic molecules, internal energy modes should be taken into account. DSMC approach considers internal kinetic energies associated with various degrees of freedom of the molecule. E.g., as it is shown in Figure 44, a diatomic molecule has two rotational and one vibrational degrees of freedom, thus rotational and vibrational energies should be considered when the calculation of the post-collisional velocity takes place.

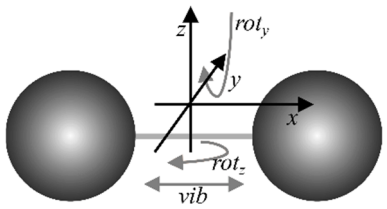

Figure 44: Degrees of freedom of a diatomic molecule

Following the Larsen-Borgnakke approach [125], a random fraction of the total collision energy E_c is assigned to rotational energy of the molecule through the acceptance-rejection procedure with the probability ratio:

$$\frac{P}{P_{\max}} = \left\{ \frac{\zeta/2+1/2-\omega_p}{\zeta/2-1} \left(\frac{E_{rot,p}}{E_c} \right) \right\}^{\zeta/2-1} \left\{ \frac{\zeta/2+1/2-\omega_p}{3/2-\omega_p} \left(1-\frac{E_{rot,p}}{E_c} \right) \right\}^{3/2-\omega_p}, \tag{52}$$

where ζ is the number of internal degrees of freedom and $E_{rot,p}$ is the random value of rotational energy of molecule p, $E_{rot,p} \le E_c$.

Despite the quantum nature on internal modes, Larsen-Borgnakke approach treats rotational energy changes continuously. The assumption can be applied because the number of available states is usually high enough.

The number of available vibrational modes is low. The majority of DSMC codes adopt the simple harmonic model with uniformly spaced vibrational energy levels. A random fraction of the total collision energy is transferred into vibrational energy by the acceptance-rejection procedure with the following probability ratio:

$$\frac{P}{P_{\max}} = \left(1-\frac{i^* k_B \Theta_{vib}}{E_c} \right)^{3/2-\omega_p}, \tag{53}$$

where i^* is the number of post-collision state, Θ_{vib} is the characteristic vibrational temperature.

If the gas is initially not in an equilibrium state, in the absence of external perturbations, intermolecular collisions will drive all the energy distributions, including the internal energy distributions, towards the equilibrium. The time needed for a disturbance to the equilibrium state to decrease e times of its original value is called the relaxation time. This time equals to Z/ν, where ν is the mean collision rate, $\nu = \sigma_{pq} n \bar{c}_{rpq}$. Z is a temperature dependent function,

based on the experimental data. To recreate the experimentally observed relaxation times, the energy adjustment procedure is applied to one collision in every Z collisions.

e. Chemical Reactions

The flow chemistry is described by the Bird's Total Collision Energy (TCE) model. To determine the probability of a chemical reaction, the coefficients of the modified Arrhenius equation are used:

$$K(T) = \Lambda T^{\eta} e^{-E_a/k_B T}, \tag{54}$$

where K is the forward reaction rate, Λ is the pre-exponential factor, η is the Arrhenius exponent and E_a is the Arrhenius activation energy.

If $E_c > E_a$, reacting pairs are chosen through the acceptance-rejection procedure with the following probability of reaction:

$$P_{reac} = \frac{\pi^{1/2}\varepsilon\Lambda T_{ref}^{\eta}}{2\sigma_{ref}\left(k_B T_{ref}\right)^{\eta-1+\omega_{pq}}} \frac{\Gamma\left(\overline{\zeta}+5/2-\omega_{pq}\right)}{\Gamma\left(\overline{\zeta}+\eta+3/2\right)} \left(\frac{m_r}{2k_B T_{ref}}\right)^{1/2} \frac{\left(E_c-E_a\right)^{\eta+\overline{\zeta}+1/2}}{E_c^{\overline{\zeta}+3/2-\omega_{pq}}}, \tag{55}$$

where ε is the symmetry factor (ε=1 if $p \neq q$ and ε=2 if $p=q$), $\sigma_{ref} = \sigma_{pq}\left(T_{ref}\right)$, $\overline{\zeta} = \left(\zeta_p + \zeta_q\right)/2$, $\omega_{pq} = \left(\omega_p + \omega_q\right)/2$, m_r is the reduced mass, $m_r = m_p m_q / \left(m_p + m_q\right)$, $\Gamma(j)$ is the gamma function, $\Gamma(j) = \int_0^{\infty} x^{j-1}\exp(-x)\,dx$.

f. Gas-Surface Interactions

When Δr given by equation (40) is longer than the distance to the wall, a molecule-surface collision occurs. Collision can be followed by reflection, deposition, or can cause a chemical reaction with the wall material. DSMC codes adopt two reflection models. Specular reflection model reverses molecule's incident velocity vector with respect to the outward normal to the surface, corresponding to the adiabatic condition. Diffuse reflection model replaces the molecule by the same one but with a new velocity vector generated according to the equilibrium distribution consistent with the surface temperature (Dirichlet temperature condition). New velocity vector components are given by equations (39).

Both models can be activated simultaneously to achieve a better agreement with the experimentally observed reflection mechanisms by introducing the accommodation coefficient a_c – here it is defined as a fraction of molecules reflected diffusively. The vast majority of experimental studies has shown that for real microscopically rough surfaces a_c is close to unity [123]. However, if the surface is smooth and has been outgassed through exposure to high vacuum and high temperature, or if the molecular weight ratio of the gas and the surface is small in comparison with unity, or if the translational component of molecular energy is larger than several electron volts, the diffuse assumption may no longer be valid.

Under PS-PVD conditions, surfaces are constantly exposed to vacuum and are expected to have high temperatures, light gases like H_2 and H have molar weights smaller than those of wall and substrate materials and translational energies of incident molecules may have energies exceeding several electron volts. Thus, the diffuse reflection model has to be corrected by adjusting the accommodation coefficient.

Zero accommodation coefficient results in a specular reflection of the molecules with no energy being transferred to the wall. In macroscopic terms this can be interpreted as Neumann boundary condition ($\partial T/\partial n = 0$), implying full thermal insulation with zero heat flux through the surface. Either full accommodation under conditions when the diffuse model is valid, or partial accommodation with empirically adjusted a_c represents Dirichlet boundary condition (T=*const*).

II.2.5.6. Sampling of Macroscopic Properties

DSMC operates with microscopic quantities, such as velocities of individual molecules and their internal energies. For practical purposes, these values need to be converted into macroscopic averaged quantities, like density, temperature, pressure and mass average velocity. This conversion procedure is called sampling and is executed once per each sampling time step Δt_{samp}, which is typically several hundred times larger than the collision time step. Sampling procedure calculates microscopic quantities per each collision mesh cell according to the following equations:

$$n = \frac{F_N}{V_{cell}} N = \frac{F_N}{V_{cell}} \sum_{p=1}^{N_s} N_p = \sum_{p=1}^{N_s} n_p \ , \tag{56}$$

$$\rho = \frac{F_N}{V_{cell}} \sum_{q=1}^{N} m_q N_q \ , \tag{57}$$

$$\vec{v} = \sum_{q=1}^{N} \left(m_q \vec{\vec{c}}_q \right) \Big/ \sum_{q=1}^{N} m_q \ , \tag{58}$$

$$T = \frac{1}{3Nk_B} \sum_{q=1}^{N} m_q \sum_{j=1}^{3} \left(c_{q,j} - v_j \right)^2 \ , \tag{59}$$

$$p = \rho R T \ , \tag{60}$$

where V_{cell} is the volume of a cell, N is the number of simulated molecules per cell, N_s is the number of unique species or the number of gas mixture components, n_p is the number density of species p, m_q is the mass of a specie q, q is the summation index over all species.

Microscopic treatment allows calculation of other interesting quantities such as temperature components, associated with various molecular degrees of freedom or temperatures of individual gas mixture components:

$$T_x = \frac{1}{3Nk_B} \sum_{p=1}^{N} m_p \left(c_{p,x} - v_x \right)^2 \ , \tag{61}$$

$$T_{x,p} = \frac{m_p}{3Nk_B} \sum_{q=1}^{Np} \left(c_{q,x} - v_x \right)^2 \ , \tag{62}$$

$$T_{rot} = \frac{2}{k_B} \sum_{q=1}^{N} E_{rot,q} \Big/ \sum_{q=1}^{N} \zeta_{rot,q} \ , \tag{63}$$

$$T_{vib} = \Theta_{vib} \Big/ \ln\left(1 + 1/\bar{i}\right) , \tag{64}$$

$$T_{ov} = \left(T_x + T_y + T_z + \zeta_{rot} T_{rot} + \zeta_{vib} T_{vib} \right) \Big/ \left(3 + \zeta_{rot} + \zeta_{vib} \right) , \tag{65}$$

where T_x is the translational temperature in the x direction, $T_{x,p}$ is the translational temperature of species p in the x direction, T_{rot} is the rotational temperature, i is the average vibrational level, and T_{ov} is the overall temperature.

The ideal gas equation of state (60) is generally derived for equilibrium gas, but it can be applied for non-equilibrium conditions when the temperature is calculated as a function of translational energy components. Translational temperature (59) and its components (61) are related by the following equation:

$$T = \left(T_x + T_y + T_z\right)/3 . \tag{66}$$

Translational temperature component and specie temperature components (62) are connected as follows:

$$T_x = \sum_{p=1}^{N_s} x_p T_{x,p} , \tag{67}$$

where x_p is the molar fraction of species p, $x_p = n_p/n$.

In the following sections, the translational temperature will be regarded as *temperature*.

II.3. Powder Transport and Evaporation

II.3.1. Aspects of Particle-Plasma Interaction

In the present study, we add a high pressure chamber (HPC) to improve the conventional PS-PVD process and reach APS levels of heat transfer to the powder particles. As mentioned in I.3.1.3, injection direction considerably affects the particle trajectory. Beside this, there are plenty of other factors influencing its acceleration and heating related to process' physics. Among these factors are jet instability and rarefaction effect.

Particle dispersion in the plasma flow, as shown by Williamson et al [126], is significantly affected by injection velocity distribution and turbulence, as illustrated by in Figure 45 (a). According to experimental observations, particle injection directions are uniformly distributed within a cone with axis aligned with the mean direction of the carrier gas injector. This is caused by random collisions of particles between each other and between them and the injector wall. The injection directions distribution schematic with respect to the injector axis (b) and corresponding spatial dispersion of particles passing through a plane located 10 cm from the torch exit are shown in Figure 45 ("base" and "cone angle").

Plasma velocity and temperature fluctuations in time result in non-uniform particle heating. As indicated in Figure 46, particle temperature and velocity variations due to arc fluctuations reach 600 °C and 200 m/s for alumina powders for a plasma forming gas of Ar/H_2 mixture classically used in plasma spraying and so, arc operating in restrike mode. The measurements were done at the torch axis, at 50 mm downstream from the torch exit. For zirconia particles at the same location, lower variations were observed (160 °C for a mean temperature of 2861 °C and 27 m/s for a mean velocity of 206 m/s). The period of fluctuations coincided with that of the voltage fluctuations [28]. The residence time of particles within the plasma jet varies from 0.4 ms (20-µm particles) to 1.4 ms (60-µm particles) for a nozzle with an internal diameter equal to 7 mm. With the restrike mode frequency about 18.9 kHz, each particle withstands between 10 and 14 fluctuation periods during its flight time [127].

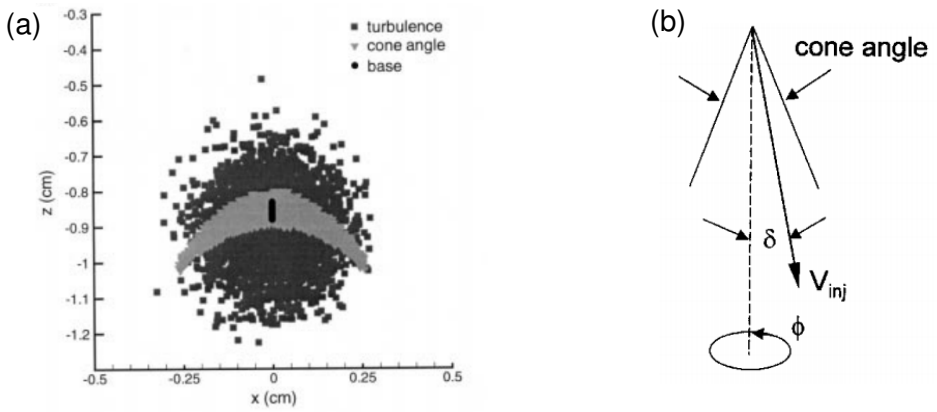

Figure 45: (a) Calculated spray patterns for particles passing through a plane 10 cm from the torch face. The effects of velocity dispersion and turbulence are considered individually; (b) Particle injection directions [126]

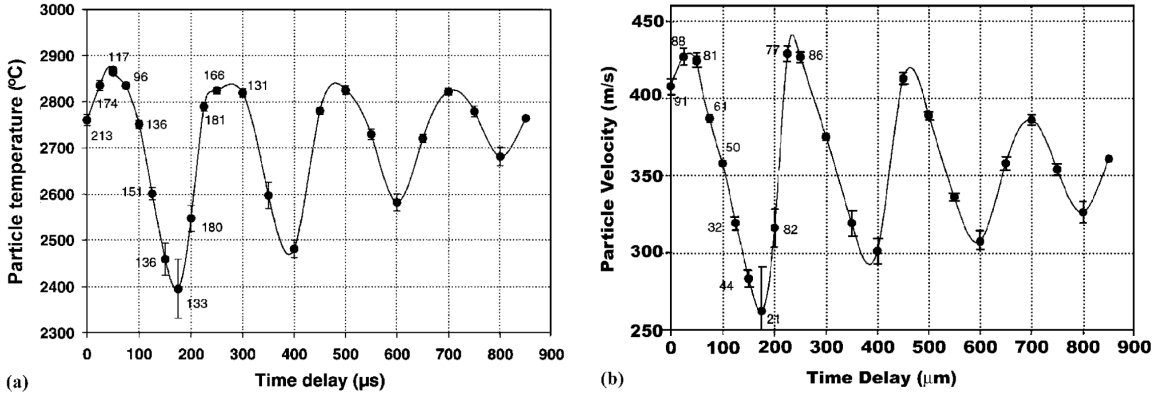

Figure 46: (a) Temperature fluctuation of alumina particles as a function of time delay. (b) Fluctuation of the average velocity of alumina particles as a function of time delay. Error bars are the 1 σ confidence interval on the mean value. Numerical data are the sample standard deviations. The measurements were done at the torch axis, at 50 mm from the torch exit [28].

Furthermore, particle heating is affected by the turbulence. Figure 33 shows the schematic of the large-scale turbulence, occurring when the hot plasma jet enters the ambient gas at rest (HPC) and mixes with it. During this mixing, entrainment of cold surrounding gas into the jet happens. Thus, particles may enter the flow within the cold gas bubbles, isolating the powder of the hot plasma [18]. In addition, particle interactions with eddies result in deviation of particles from their “undisturbed” trajectories, leading to so-called turbulent dispersion. The effect of turbulence on spray patterns is shown in Figure 45a.

Physical vapor formed during the evaporation process undergoes active turbulence-driven mixing with the plasma gas and follows the flow along with the remaining molten particles. Up to 57 % of zirconia feedstock can be transferred to vapor [11]. Powder evaporation process consumes the energy of the flow, while turbulent mixing with the surrounding gas further reduces the jet temperature. In addition, the vapor boundary layer surrounding the particles reduces the vapor diffusivity and the heat transferred to the particles. Moreover, thermodynamic and transport properties of the surrounding gas are affected by this vapor layer

and thermal boundary layer surrounding the particles [128]. At a certain point, jet temperature becomes lower than boiling temperature of the feedstock powder material triggering nucleation of the physical vapor.

For the particles traveling in the plasma flow, Knudsen number can be defined as the ratio between the molecular mean free path and the diameter of the particle. Even under atmospheric pressure, these Knudsen number values can be approaching unity due to powder melting and evaporation, leading to a decrease of grain sizes. When the grain size becomes small enough, rarefaction-related phenomena, like temperature jump (violation for Fourier's law) and velocity slip (deviation from Newton's law a viscosity) become apparent, reducing the heat flow towards the particle and decreasing the drag force acting on it [74].

Feasibility of the proposed system (PS) is dependent on numerous factors. One of them is the absence of expansion nozzle clogging. The gas flow that enters the expansion nozzle should not contain any residual powder particles. Even though in the present study, liquid droplet deposition is not considered, physical vapor formed from evaporating particles can condensate on the nozzle walls as well. Furthermore, this vapor is the source material needed for the growth of coatings in the LPC. Thus, a reliable prediction of powder particle dynamics and evaporation is needed.

II.3.2. Discrete Phase Modeling

Multiphase or discrete phase modeling (DPM) is an essential part of plasma spray simulation which has been investigated over the years [79, 129–134]. All these studies use the so-called Euler-Lagrange approach. This fact means that the gas flow is treated with a continuum/CFD approach (typically by solving RANS equations), while powder particles are modeled individually as discrete entities in a Lagrangian way within the calculated gas flow field. The dispersed phase represented by powder grains can exchange mass, momentum and energy with the plasma gas and can even be the source of vapor species.

II.3.2.1. General Description and Assumptions

The main assumptions for a typical Euler-Lagrange discrete phase model are [25]:

- Powder particles are spherical, isotropic and homogeneous;
- Particle-particle interactions are not considered. This assumption is valid for low volume fractions of the discrete phase (<10%) [82];
- Particle movement is caused by the drag force and is influenced by gas flow turbulent fluctuations that cause their dispersion. Gravity, Basset force and thermophoretic force are negligible and not taken into account [128].

Additional assumptions for gas-particle heat exchange include [25, 135, 136]:

- Heat exchange between the particles and gas occurs through convection and radiation;
- Two-way coupling between discrete and continuous phases is established – powder evaporation consumes enthalpy of the flow and is a source of the physical vapor;
- The internal temperature field of particles is uniform – radial temperature gradients and internal heat conduction are neglected; this assumption does not represent the real temperature distribution. The use of averaged, uniform temperatures leads to underestimation of heat received by particles [137];
- Plasma jet temperature and velocity fluctuations are not considered.

The validity of these assumptions for APS classical conditions was confirmed in the thesis reports of Matthias de Sousa and Pierre Fuzet [25, 26].

II.3.2.2. Particle Motion

The motion of particles is governed by Newton's second law of motion:

$$m_p \frac{d\vec{v}_p}{dt} = \overrightarrow{F_d}\,, \tag{68}$$

where m_p is the mass of powder particle p, v_p is its velocity and $\overrightarrow{F_d}$ is the drag force. As shown by Douce [128], the other forces like Basset or thermophoretic force are negligible in comparison with the drag force.

The drag force acting on the particle is described by the following expression:

$$\overrightarrow{F_d} = \frac{\pi d_p^2}{8} \rho \left|\vec{v}_p - \vec{v}\right| \left(\vec{v} - \vec{v}_p\right) C_d\,, \tag{69}$$

where C_d is the drag coefficient – an experimentally obtained dimensionless quantity, which shows the ratio between the drag force and the force produced by the dynamic pressure of the gas.

Drag coefficient is dependent on the flow regime, characterized by the dimensionless relative Reynolds number that is defined as:

$$\mathrm{Re}_p = \frac{\bar{\rho}_g d_p \left|\vec{v}_p - \vec{v}\right|}{\bar{\mu}_g}\,, \tag{70}$$

where $\bar{\rho}_g$ and $\bar{\mu}_g$ are the density and viscosity averaged over particle's boundary layer temperatures varying from particle surface temperature to the surrounding gas temperature far away from the particle surface:

$$\bar{\phi} = \frac{1}{T_{\max} - T_{\min}} \int_{T_{\min}}^{T_{\max}} \phi(T)\, dT\,, \tag{71}$$

where φ is the property to be averaged, $T_{\min}=\min\{T_p,T\}$ and $T_{\max}=\max\{T_p,T\}$, where T is the plasma gas temperature and T_p is the particle temperature. The averaging of the flow properties is needed to account for the cold vapor cloud surrounding the particle.

According to experimental findings, the dependency of the drag coefficient on the Reynolds number under APS conditions can be characterized by the functions listed in Annex A (Table 21).

Drag coefficient should also be corrected to account for the vapor cloud that forms around the particle during its evaporation:

$$C_d = \frac{C_{df}}{1 + \mathrm{B_t}}\,, \tag{72}$$

where $\mathrm{B_t}$ is the dimensionless Spalding heat transfer number, defined as:

$$\mathrm{B_t} = \int_{T_p}^{T} \frac{C_{p,vap}}{L_{lap}}\, dT = C_{p,vap}\left(T - T_p\right) \Big/ L_{vap}\,, \tag{73}$$

where $C_{p,vap}$ is heat capacity of physical vapor and L_{vap} is its latent heat of vaporization.

II.3.2.3. Gas-Particle Heat Exchange

The process of particle heating and vaporization can be divided into the following stages:

- Particle heating up to the melting temperature;
- Fusion of the particle at the melting temperature;
- Particle heating up to the boiling temperature with evaporation occurring at the same time;
- Boiling of the particle and its evaporation

a. Heating to Melting Temperature

The heat balance for a powder particle below its melting point is:

$$m_p C_p \frac{dT_p}{dt} = h\pi d_p^2 \left(T - T_p\right) - \varepsilon\sigma\pi d_p^2 T_p^4 , \tag{74}$$

where C_p is the specific heat of the particle, h is the heat transfer coefficient, T is the plasma gas temperature, ε_p is the particle emissivity, and σ is the Stefan-Boltzmann constant (σ = $5.67 \cdot 10^{-8}$ W·m^{-2}K^{-4}).

The first term on the right-hand side if the equation represents the heat gained by particle through convection and the second term shows the heat loss by thermal radiation.

The heat transfer coefficient h is calculated from the dimensionless Nusselt number:

$$h = \frac{\mathrm{Nu}\ \overline{\kappa}_g}{d_p} , \tag{75}$$

where $\overline{\kappa}_g$ is the average thermal conductivity of the gas in the boundary layer of the particle.

The Nusselt number for a powder particle can be calculated using the following relation [25]:

$$\mathrm{Nu} = \frac{\ln\left(1+\mathrm{B_t}\right)}{\mathrm{B_t}}\left(2 + \frac{\mathrm{Nu}_0 - 2}{F_t}\right), \tag{76}$$

where Nu_0 is the Nusselt number without the presence of the Stefan flow and F_t accounts for surface blowing that leads to a thickening of the thermal boundary layer around the particle. The former can be calculated using the following correlation:

$$\mathrm{Nu}_0 = 1 + \left(1 + \mathrm{Re}_p\,\mathrm{Pr}\right)^{0.33} \max\left(1, \mathrm{Re}_p^{0.077}\right), \tag{77}$$

where the Prandtl number is defined as follows:

$$\mathrm{Pr} = \overline{\mu}_g \overline{C}_p \big/ \overline{\kappa}_g . \tag{78}$$

The factor F_t is calculated as follows:

$$F_t = \left(1+\mathrm{B_t}\right)^{0.7} \frac{\ln(1+\mathrm{B_t})}{\mathrm{B_t}} . \tag{79}$$

The dimensionless Spalding heat transfer number $\mathrm{B_t}$ in equations (76) and (79) is calculated using the following expression:

$$\mathrm{B_t} = C_{p,vap}\left(T - T_p\right) \Big/ \left(L_{vap} + q_f / \dot{m}_{vap}\right), \tag{80}$$

where the second term of the denominator (the ratio of the heat flux entering into the droplet q_f and the vapor flux from the surface of the particle $\dot{m}_{vap}$) is present only after the evaporation onset.

g. Fusion

The heat balance for a powder particle at its melting temperature T_f is:

$$m_p \Delta H_f \frac{dX_p}{dt} = h\pi d_p^2 \left(T - T_p\right) - \varepsilon\sigma\pi d_p^2 T_p^4, \tag{81}$$

where X_p is the mass fraction of liquefied material in the particle, ΔH_f is the latent heat of melting, and T_p=T_f.

h. Heating to Boiling Temperature

The heat balance for a melted powder particle below its boiling point is:

$$q_f = m_p C_p \frac{dT_p}{dt} = h\pi d_p^2 \left(T - T_p\right) - \varepsilon\sigma\pi d_p^2 T_p^4 - \dot{m}_{vap} L_{vap}, \tag{82}$$

where $\dot{m}_{vap}$ is the vapor flux from the surface of the particle.

The last term on the right-hand side of the equation represents the heat loss due to particle vaporization. The vapor mass flux from the surface of a liquid particle below boiling temperature is a function of the dimensionless Sherwood number Sh, Spalding mass transfer number $\mathrm{B_m}$ and physical vapor diffusion coefficient D_{vap}(m²/s):

$$\dot{m}_{vap} = \pi d_p \bar{\rho} D_{vap} \mathrm{Sh} \ln\left(1 + \mathrm{B_m}\right), \tag{83}$$

where Sherwood number represents the ratio of the convective mass transfer to the rate of diffusive mass transport and is defined as follows:

$$\mathrm{Sh} = 2 + \frac{\mathrm{Sh_0} - 2}{F_m}, \tag{84}$$

where $\mathrm{Sh_0}$ is Sherwood number due to natural convection and F_m accounts for surface blowing that leads to a thickening of the boundary layer around the particle. $\mathrm{Sh_0}$ could be defined as:

$$\mathrm{Sh_0} = 1 + \left(1 + \mathrm{Re_p Sc}\right)^{0.33} \max\left(1, \mathrm{Re}_p^{0.077}\right), \tag{85}$$

where Sc is the Schmidt number -the ratio of kinematic viscosity and mass diffusivity:

$$\mathrm{Sc} = \frac{\bar{\mu}_g}{\bar{\rho}_g D_{vap}\left(T_{ref}\right)}. \tag{86}$$

The factor F_m is calculated as follows:

$$F_m = \left(1 + \mathrm{B_m}\right)^{0.7} \frac{\ln(1 + \mathrm{B_m})}{\mathrm{B_m}}. \tag{87}$$

Spalding mass transfer number, for $\mathrm{B_m}$<20 could be estimated using the expression:

$$\mathrm{B_m} = \frac{Y_{s,ref} - Y_\infty}{1 - Y_{s,ref}}, \tag{88}$$

where $Y_{s,ref}$ is the vapor mass fraction at the particle surface calculated at a reference temperature T_{ref}. so that

$$Y_{s,ref} = \frac{2}{3} Y_s + \frac{1}{3} Y_\infty, \tag{89}$$

where Y_∞ is the vapor mass fraction sufficiently far away from the particle surface, and $Y_{s,ref}$ is the vapor mass fraction at the particle surface expressed as a function of its molar fraction X_s:

$$Y_s = \frac{X_s M_{vap}}{X_s M_{vap} + (1 - X_s) M_{gas}}, \tag{90}$$

where M_{vap} is the molar mass of vapor and M_{gas} is the molar mass of the surrounding gas and X_s is calculated using the Clausius–Clapeyron relation:

$$X_s = \frac{p_{vap}}{p} = \exp\left[\left(\frac{M_{vap} L_{vap}}{R}\right)\left(\frac{1}{T_b} - \frac{1}{T_p}\right)\right], \tag{91}$$

where T_b is the boiling temperature of the particle,

The calculations of vapor diffusion coefficient for zirconia vapor is described in the third chapter.

i. Boiling and Evaporation

The heat balance described by equation (82) for a boiling powder particle becomes:

$$0 = h\pi d_p^2 \left(T - T_p\right) - \varepsilon\sigma\pi d_p^2 T_p^4 - \dot{m}_b L_{vap} \tag{92}$$

The entire heat transferred by the gas is used for particle vaporization. It is possible to express the vapor flux (or particle mass decrease) $\dot{m}_b$ through the surface of the boiling particle from equation (92). Dividing $\dot{m}_b$ by particle density and shifting from volume decrease to diameter decrease one can obtain the following expression:

$$\frac{d\left(d_p\right)}{dt} = 2\frac{h\left(T - T_p\right) - \varepsilon\sigma T_p^4}{\rho_p L_{vap}} \tag{93}$$

II.3.2.4. Adjustment to Rarefaction

Under APS conditions, plasma flow is a continuous medium (Kn<0.01). However, in regard to gas-particle interaction, the flow may be considered as rarefied. For gas-particle interaction, the Knudsen number can be defined as the ratio between mean free path λ and the diameter of the particle acting as the characteristic length scale:

$$\mathrm{Kn}_{dp} = \frac{\lambda}{d_p}. \tag{94}$$

For continuum flow, the mean free path can be estimated using the following expression:

$$\lambda = \frac{2\bar{\kappa}_g}{\bar{\rho}_g v_s \bar{C}_{pg}} \mathrm{Pr}_p \,, \tag{95}$$

where $\bar{\rho}_g$ and $\bar{C}_{pg}$ are the average gas density and heat capacity of the gas in the boundary layer of the particle, v_s is the kinematic viscosity of gas at the surface of the particle, and Pr_p is the dimensionless Prandtl number in the boundary layer of the particle.

As reported by Chen [74], Knudsen number values calculated through equations (94) and (95) for APS conditions can reach 0.2-1.0, which indicates the transitional regime of the flow around the particle (Kn_{dp}>0.01). Thus, rarefaction effects should be considered.

According to Chen, a good agreement with the experimental data can be reached if the drag coefficient (72) is multiplied by the following correction factor [134]:

$$f_{C_d} = \left[1 + \left(\frac{2-\alpha}{\alpha} \right) \left(\frac{\gamma}{1+\gamma} \right) \left(\frac{4}{\mathrm{Pr}_p} \right) Kn_{dp} \right]^{-0.45} \tag{96}$$

The heat flux or the heat transfer coefficient (75) should also be corrected by the following factor [74]:

$$f_h = \left[1 + \left(\frac{2-\alpha}{\alpha} \right) \left(\frac{\gamma}{1+\gamma} \right) \left(\frac{4}{\mathrm{Pr}_p} \right) Kn_{dp} \right]^{-1} \tag{97}$$

II.3.2.5. Numerical Considerations

Particle trajectories are obtained by numerical integration of the particle equation of motion (68) over a discrete set of time steps. The first integration of the equation (68) yields velocity at each point of the trajectory, while the second one returns the coordinates of the particle. At each time step, particle temperature, liquid fraction, mass and diameter are updated according to equations (74)-(93). Integration can be performed using a wide variety of numerical schemes. The choice of the integration scheme is justified by accuracy requirements, available computational resources, number of modeled particles and numerical stiffness due to high gradients in the plasma gas flow. Traditionally, trapezoidal or Runge-Kutta schemes are used for their relatively high speed and stability [82].

II.3.2.6. Initial Conditions

The numerical solution requires proper initial conditions. These include the initial temperature, velocity and size distribution of particles. Temperature is usually set equal to the ambient temperature. In the APS process, powder particles are usually injected with velocity vectors, randomly distributed around some general direction with absolute values also distributed around a certain mean value to account for particle-particle and wall-particle collisions. As shown by Williamson *et al* [126], to represent this scatter in the numerical model, velocity components $\vec{v} = \left(v_x, v_y, v_z \right)$ of each injected particle should be selected as follows:

$$v_x = v \cos(\phi) \sin(\delta) \,, \tag{98}$$

$$v_y = v \cos(\delta) \,, \tag{99}$$

$$v_z = v\sin(\phi)\sin(\delta), \tag{100}$$

where ϕ is the azimuthal angle, uniformly distributed between 0 and 360 degrees, δ is the polar angle, uniformly distributed between 0 and 10 degrees:

$$\phi = 2\pi R_f, \tag{101}$$

$$\delta = \pi R_f / 18, \tag{102}$$

where R_f is a random fraction that is uniformly distributed between 0 and 1. The corresponding schematic is shown in Figure 47.

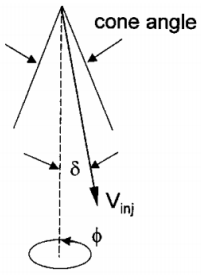

Figure 47: Schematic showing the nomenclature used to specify particle injection directions [126]

The initial particle velocity magnitude v could be taken equal to the one of the carrier gas flow inside the injector. Gas flow velocity profiles for different flow regimes are well-known and can be found elsewhere. If a flat velocity profile is set as a boundary condition at injector inlet, a sufficient length of injector pipe should be modeled to let the flow reach the fully developed stage and allow the particles adjust their velocity to the one of the flow.

The powder size distribution can be described by the Rosin-Rammler expression:

$$Y_d = e^{-(d_p/\bar{d})^n}, \tag{103}$$

where Y_d is the mass fraction of droplets of diameter greater than d, $\bar{d}$ is the size constant and n is the spread parameter. Both parameters can be deduced from powder granulometry measurements.

II.4. Nucleation and Coating Deposition

In the ideal thermal spray process, powder particles and physical vapor are deposited only on the substrate. But in reality, materials are frequently deposited on the chamber walls and other parts of the setup. When the mixture of vapor and liquid particles reaches any surface, several deposition mechanisms can be involved:

- Deposition of fully or partially liquefied powder particles with micrometric sizes;
- Deposition of nanoclusters formed via homogeneous nucleation process from physical vapor;
- Deposition via heterogeneous nucleation directly from the vapor phase.

From the perspective of deposition processes, thermal spray design and conditions should be adjusted to avoid non-substrate deposition (and possible HPC-LPC nozzle clogging) and minimize feedstock material losses. At the same time, the choice of spray parameters should facilitate the growth of coating on the substrate with the desired microstructure.

Contributions of the aforementioned mechanisms are dependent on numerous parameters, such as particle concentration, the incident angle of the vapor hitting the wall/substrate, its pressure, velocity and composition, wall/substrate material, temperature, surface roughness, etc. E.g., in APS/CPS process, coatings are mostly composed of liquid splats, formed according to the first mechanism, in EB-PVD the third mechanism dominates, and in PS-PVD all three scenarios can be observed. It was reported, that EB-PVD-like coatings obtained with PS-PVD are mostly formed by heterogeneous nucleation directly from vapor and by deposition of non-fully vaporized particles, while the contribution of homogeneous nucleation (cluster deposition) to the total coating growth can reach >10% [138]. This means that PS spraying conditions should favor the heterogeneous nucleation on the substrate and moderate homogeneous nucleation in the substrate's boundary layer [11, 139].

This section describes mechanisms of homogeneous and heterogeneous nucleation and growth of homogeneously formed nuclei and highlights main approaches to modeling of these phenomena.

II.4.1. Homogeneous Nucleation and Nuclei Growth

II.4.1.1. Mechanisms of Homogeneous Nucleation and Growth

The phase transition from vapor to liquid in the volume of vapor can be described by two processes: homogeneous nucleation and nuclei growth. Nucleation and growth processes are depicted in Figure 48. According to the classical nucleation theory (CNT), developed by Volmer and Weber [140] and then improved by Zel'dovich [141], and by other researchers. In this model, the initial ideal vapor is composed of molecules referred to as monomers. These monomers can collide and stick to each other forming embryos, composed of g monomers. Such particles are called g-mers. Cluster formation is governed by two opposing processes: monomer addition (condensation) and evaporation. If the vapor contained in the plasma gas becomes supersaturated (due to an increase of its partial pressure as a result of the change in flow conditions and/or due to powder evaporation), collisions between vapor molecules start occurring at a sufficient rate and addition reaction can start with the same rate as evaporation reaction. This results in the formation of a stable primary particle (or a stable cluster) from an embryo. Primary clusters are stable, because this state corresponds to equilibrium between liquid and vapor phase. This equilibrium is indicated by the maximum of Gibbs free energy also referred to as the energy of critical nucleus formation.

Once stable primary clusters are generated, they can start growing, forming secondary particles. Growth process occurs by addition of monomers (condensation, opposed by evaporation from cluster surface). The secondary particles are formed from the initial clusters (coagulation) by merging with other clusters creating a new shape (coalescence) or by clustering of particles retaining their shapes (agglomeration).

Under APS and/or PS-PVD conditions homogeneous nucleation and cluster growth can be illustrated by the schematic shown in Figure 49. In this process nucleation and growth are expected to occur in a cold boundary layer of a cooled substrate or a wall from zirconia vapor.

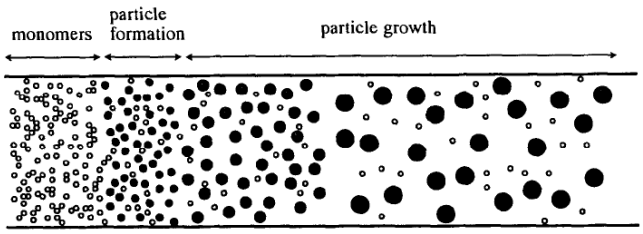

Figure 48: Schematic of homogeneous nucleation and growth process by cooling of metallic vapor. States corresponding to different vapor temperatures are depicted, the temperature decreases from left to right [142]

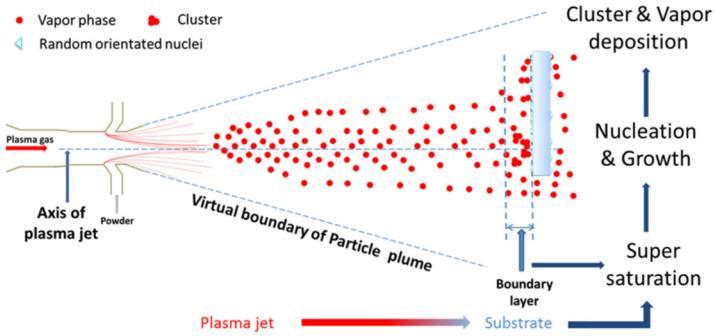

Figure 49: Schematic of cluster and vapor deposition process [11]

Upon reaching the boundary layer, depending on the substrate position and spray conditions, plasma jet temperature decreases from 4,000-6,000 K down to substrate temperature, which is usually kept at around 1,000-1,500 K. Zirconia vapor equilibrium composition evolves accordingly, as shown in Figure 50. At the temperature lower than zirconia solidification temperature (~3,000 K) zirconia vapor is mostly composed of ZrO_2 molecules. Between 3,000 K and 4,000 K noticeable amounts of atomic oxygen and zirconium monoxide are also present. Above 4,000 K vapor is mostly composed of Zr and O atoms.

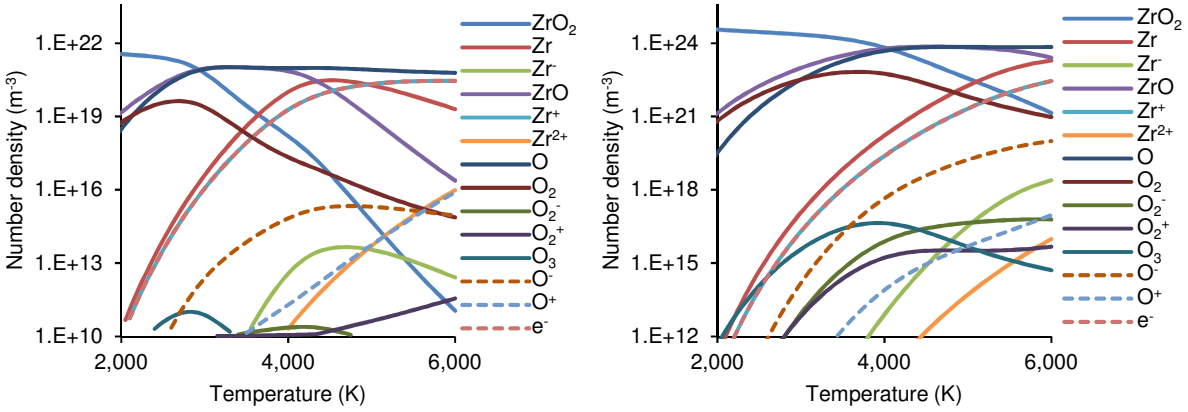

Figure 50: Equilibrium compositions ZrO_2 vapor at 100 Pa and 1 atm

II.4.1.2. Homogeneous Nucleation

Mechanisms of homogeneous nucleation were first described in studies of Volmer and Weber [140] and Zel'dovich [141], creating the foundation of classical nucleation theory. Later, CNT received "kinetic" extension by Katz and Weidersich [143]. Kinetic theory of homogeneous

nucleation (KNT) was then applied Girshick [144] to predict nucleation rates of organic and metallic vapors.

Though both CNT and KNT theories provide similar results, KNT is based on more realistic assumptions. In CNT embryo growth is driven by monomer condensation and evaporation processes. The condensation rate of ideal vapor can be deduced from gas kinetic theory, while the evaporation rate is obtained by reference to the metastable equilibrium, artificially induced by Maxwell demons – monomers lost due to condensation in CNT are assumed to be constantly replenished by artificial dissociation of embryos that grow beyond a certain size [141]. KNT is derived without resorting to Maxwell demons. The evaporation rate here is obtained with reference to the stable equilibrium of saturated vapor [144]. For this reason, KNT is often used to predict homogenous nucleation rates in plasma spraying [138, 145].

a. KNT Assumptions

KNT is based upon the following assumptions:

- The growth of embryos/nuclei to primary molecular clusters is represented by a series of two-body collisions and evaporation of monomers from embryo surface;
- Metallic vapor is the ideal gas and is considered to be in thermal equilibrium with the Maxwellian distribution of thermal velocities;
- The state of embryos can be described by macroscopic quantities (temperature, enthalpy, surface tension);
- Capillary approximation – surface energy used in KNT corresponds the one of the flat surface;
- Equilibrium cluster concentration obeys Boltzmann distribution;
- The spherical shape of nuclei is assumed;
- A steady state for nucleation rate is assumed, transient effects are ignored.

The spherical shape of nuclei can be reached, and bulk surface tension could be applied for its description only if nuclei size exceeds 10 monomers. The validity of the aforementioned assumptions depends on the specific flow conditions. Under APS conditions, when continuum approach can be applied, the flow is in LTE and nuclei sizes are fairly large, the assumptions are usually satisfied, however, under PS-PVD conditions, when rarefaction occurs and cluster size can be as low as 1-3 molecules, KNT application can become doubtful [138]. A method of confirming the last assumption is shown in the following section.

b. Homogeneous Nucleation Rate

Homogeneous nucleation rate from ideal supersaturated vapor ($m^{-3}s^{-1}$) is calculated as follows:

$$J_{\text{hom}}^{KNT} = v_1 \sqrt{\frac{2\sigma}{\pi m_1}} n_s^2 S \exp\left(\theta - \frac{4\theta^3}{27 \ln^2 S}\right), \tag{104}$$

where v_1 (m^3) the volume of a monomer, σ is the surface tension (N/m), m_1 is the mass of a monomer, n_s (m^{-3}) is the equilibrium monomer concentration for saturated vapor, S is the saturation ratio, $S = n_1 / n_S$, n_1 (m^{-3}) is the monomer concentration, θ is the dimensionless surface energy, $\theta = \sigma S_1 / (k_B T)$, S_1 (m^2) is the surface area of a single monomer. The equilibrium monomer concentration can be taken from literature.

The total free energy change (energy of critical nucleus formation) for homogeneous nucleation of an embryo containing g monomers is:

$$\frac{\Delta G_{\text{hom}}^{KNT}}{k_B T} = \theta\left(g^{2/3} - 1\right). \tag{105}$$

Equation (105) is valid even if g=1, unlike the equation for the free energy obtained within the framework of CNT:

$$\frac{\Delta G_{\text{hom}}^{CNT}}{k_B T} = \theta g^{2/3}. \tag{106}$$

Nucleation starts when S>1 and is considered to be instantaneous, critical nuclei are being generated with the rate J_{hom} and the size given by:

$$g_{\text{hom}}^{*} = \left(\frac{2\theta}{3\ln S}\right)^3, \tag{107}$$

where g_{hom}^{*} is the number of monomers in a critical nucleus.

To fulfill the steady-state assumption for the nucleation rate, the time needed to reach the steady state should be sufficiently low in comparison with the other processes (e.g. coagulation or evaporation). This time could be estimated by [138]:

$$\tau^{*} = \frac{1}{2C_{i^*}Z_{i^*}^2}, \tag{108}$$

where $Z_{i^*} = \left(\gamma/\left(2\pi k_B T\right)\right)^{0.5}$ is the Zeldovich factor with $\gamma = 8\pi S_1 \sigma/\left(9 g_{hom}^{*\,0.75}\right)$ and $C_{i^*} = 4\pi S_1 g^{*2/3} n_1 \left(k_B T/\left(2\pi m_1\right)\right)^{0.5}$ is the condensation coefficient.

II.4.1.3. Nuclei Growth

Particle growth in plasma flow is usually described using aerosol theory, which deals with particle size distribution function (PSDF). The PSDF is a function which represents the probability of particles having a volume in a small range around some specified volume. Aerosol theory can be used to predict the evolution of PSDF with time.

PSDF can be represented as a discrete distribution, like it is done in sectional [146] and nodal models [147]. The advantage of these methods is that they do not involve any *a priori* assumptions about the shape of PSDF. However, they assume the presence of a large number of particles with discrete sizes. This means that the growth process for PSDF which describes *N* size intervals involves the solution of *N* differential equations, where each equation represents the balance of particles of a certain size. This makes discrete-type methods rater complex and computer-time consuming.

An alternative approach, developed by Hulburt and Katz [148] and Friedlander [149], treats PSDF as a continuous function. The core idea of this approach is to calculate statistical variables – moments of PSDF. This method is commonly referred to as a method of moments (MOM). The advantages of MOM are the absence of *a priori* assumptions about the shape of PSDF and lower computational cost than the one of sectional models. However, MOM does not take coagulation of particles into account.

MOM was refined by Pratsinis [150]. His approach is based on an assumption of a log-normal shape of PSDF. This assumption allows one to reduce the number of equations needed for system closure, simplifying the method. Moreover, this method also accounts for the coagulation of particles alongside condensation and evaporation processes. This method was successfully used to predict particle growth in plasma spraying [151, 152].

It is possible to reduce MOM up to two simple ordinary differential equations. The method proposed by Panda and Pratsinis [142] and Nemchinsky and Shigeta [145] does not require any assumption of PSDF and allows prediction of the average size of particles without losing the prediction accuracy in comparison with MOM. Due to the use of a single particle size, this approximation is called monodisperse approximation. A model based on this approximation can be a good tool to quickly perform a qualitative analysis of the processes, occurring in the proposed system, without invoking complex and slow approaches. This approach was already applied by Mauer to study coating formation process under PS-PVD conditions by evaluating particle size and number density [138].

a. Assumption for Aerosol Growth Model

The main assumptions of monodisperse approach are:

- Aerosol, formed during the nucleation process, is composed of uniformly-sized species, PSDF is not implemented;
- The free molecular regime for aerosol particles – kinetic collision frequency functions for rarefied flow can be applied (Kn_{dg}>10);
- The gas mixture is stationary, with uniform distributions of temperature, pressure and monomer concentration and no monomer sources;
- A collision between a g-mer and a monomer leads to condensation, resulting in the increase of a number of composing monomers g by 1. A collision between two g-mers results in coagulation. Coagulates reduce the number of g-mers and are considered as permanently lost from the system.

Model built upon these assumptions cannot be deduced from kinetic equations due to the treatment of coagulation process. Such a description should be considered as qualitative, based on common sense rather than on statistical mechanics [145]. Nevertheless, model predictions proved to coincide with prediction provided by MOM. Numerous attempts were undertaken to verify MOM-based models under APS conditions. It was shown that quantitative predictions of such models are not accurate enough, however, they provide correct trends and are deemed to be a good tool for qualitative analysis [152].

b. Growth Model

Aerosol growth process according to the monodisperse approach is described by three equations [145]. The first equation, which shows the conservation of vapor and nuclei mass, is given by:

$$\frac{dn_1}{dt} = -\frac{du_g}{dt}, \tag{109}$$

where n_1 (m^{-3}) is the number density of monomers per unit volume of the medium, $u_g = n_g g$ (m^{-3}), g is the average number of monomers in a particle (g-mer). Here, during the growth process, the number of monomers contained in the volume is being reduced by the formation of g-mers.

The second equation, which shows the change of monomer number density with time, is written as:

$$\frac{dn_g}{dt} = J_{hom} - \frac{1}{2}\beta_{gg} n_g^2 , \tag{110}$$

where β_{ij} is the collision frequency function between i-mers and j-mers. In this equation, the number of g-mers increases due to the nucleation process, but if a g-mer collides with another g-mer, both are considered to be lost. The rate of homogeneous nucleation is calculated using equation (104). The collision frequency function (m^3/s) for free molecular flow (Kn_{dg}>10) is given by the following equation:

$$\beta_{ij} = \left(\frac{3}{4\pi}\right)^{\frac{1}{6}} \sqrt{\frac{6k_B T v_1}{m_1}\left(\frac{1}{v_i}+\frac{1}{v_j}\right)}\left(v_i^{\frac{1}{3}} + v_j^{\frac{1}{3}}\right)^2 , \tag{111}$$

where v_i is the volume of an i-mer.

The last equation depicts the conservation of total volume of particles and can be written as:

$$\frac{du_g}{dt} = J_{hom} g_{hom}^* + \beta_{1g}\left(n_1 - n_s\right) n_g . \tag{112}$$

The number of monomers in a critical nucleus g_{hom}^* is obtained from equation (107). In equation (112), the total volume of particles increases due to the formation of the entire volume of critical clusters and by the growth of g-mers through collisions with monomers. The decrease of the total volume is attributed to the evaporation of monomers from g-mer surface.

Together, equations (109), (110) and (112) form a set of one algebraic and two ordinary differential equations. The initial conditions for these equations are:

$$\begin{cases} n_1\left(t=0\right) = n_{1,init} \\ n_g\left(t=0\right) = 0 \\ u_g\left(l=0\right) = 0 \end{cases} , \tag{113}$$

where $n_{1,init}$ is the initial monomer number density.

Even though the secondary particles formed during the coagulation process are deleted from the system, their resulting shape could be estimated. Coalescence occurs, and spherical secondary particles are formed if the time needed to form a spherical particle during the coagulation process is sufficiently low in comparison with the average collision time. If the colliding particles are in the liquid state, coalescence time $\tau_{coal,l}$ can be estimated by [138]:

$$\tau_{coal,l} = \frac{\mu d_{p,f}}{\sigma} , \tag{114}$$

where μ is the dynamic viscosity of zirconia and $d_{p,f}$ is the final diameter of a spherical particle.

For the solid colliding particles coalescence time $\tau_{coal,s}$ is given by [138]:

$$\tau_{coal,s} = \frac{3k_B T g}{64\pi\sigma D} , \tag{115}$$

where D is the diffusion coefficient calculates using the following expression:

$$D = D_0 \exp\left(-\frac{Q}{RT}\right), \tag{116}$$

where the reference diffusivity D_0=10^{-3} m^2/s and bulk diffusion activation energy Q=314 kJ/mol.

Coalescence times should be compared to the mean g-mer collision time τ_{col} given by:

$$\tau_{coll} = \frac{2}{\beta_{gg} n_g}. \tag{117}$$

If $\tau_{coal,s} \ll \tau_{col}$, spherical secondary particles are formed.

II.4.1.4. Numerical Considerations

Characteristic times of nucleation and growth, described by the first term of the equation (112) are usually larger than the characteristic times of growth by monomer addition, described by the second term of the same equation [138, 145]. Therefore, the numerical integration of the system has to be performed by a stable numerical scheme, e.g. a numerical scheme with a variable step size. The step size can be varied depending on the estimated local error value and the error was calculated as a difference between the solution obtained with numerical schemes of different orders. The numerical scheme is briefly described in Annex B.

II.4.2. Heterogeneous Nucleation

Heterogeneous nucleation under PS-PVD conditions is the major driving mechanism of vapor deposition. Its contribution to the expansion nozzle clogging may be substantial as well. The mechanism of heterogeneous nucleation of vapor on a surface is similar to the one described in II.4.1 for homogeneous nucleation.

Like during homogeneous nucleation, stable nuclei can form on a wall only when the plasma gas near it is supersaturated with vapor. These nuclei are also characterized by the energy of formation (lower than the formation energy in homogeneous case) and critical size. Several processes shown in Figure 51 are contributing to critical nuclei formation. The initial nucleus is formed by deposition of monomers on the substrate surface; these monomers (referred to as adatoms) through surface diffusion are gathering into bigger clusters, which can continue their growth due to new monomers arriving from the surrounding surface regions by surface diffusion or from a physical vapor, following the mechanisms of homogeneous nucleation. This growth process is opposed by monomer evaporation from nucleus surface and by monomer desorption from the wall surface (indicated as a substrate in Figure 51).

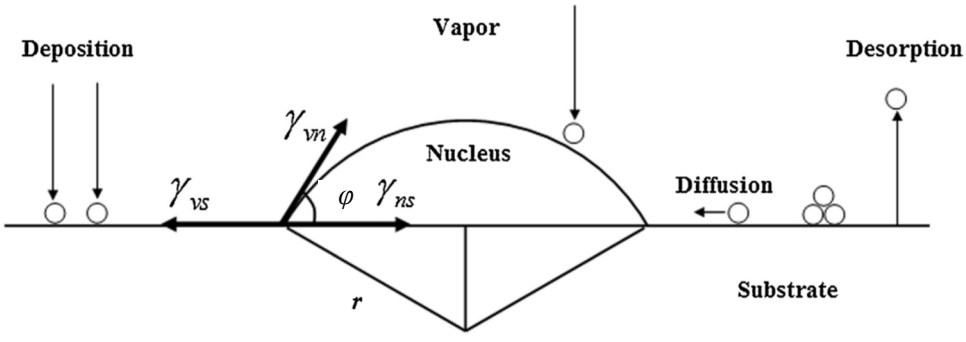

Figure 51: Heterogeneous nucleation schematic [139]

Once critical nuclei are formed, further growth is determined by surface diffusion and vapor impingement rate, as illustrated by the structure zone model, described earlier (I.3.4.2). If the coating is being formed mainly by heterogeneous nucleation and growth, surface diffusion of adatoms is significantly higher than the one of clusters, deposited when homogeneous nucleation dominates. Adsorbed atoms can cover higher distances before getting trapped at low-energy sites, which diminishes shadowing effect and enables the formation of compact columnar coatings (Zone 2 of SZM, I.3.4.2) [55].

Modeling of heterogeneous nucleation is beyond the scope of the present study; however, simulation of this process can provide a valuable insight on the mechanisms of coating formation and can be a subject of the future investigations.

II.4.3. Deposition of Vapor and Clusters

When the g-mer concentration near the wall is known, the g-mer flow rate towards its surface can be evaluated. This flow is driven by two mechanisms: Brownian diffusion and thermophoresis. The former is caused by constant collisions with plasma gas molecules, which drive particles along polygonal trajectories, which can be characterized by mean displacement or diffusion flux. The latter is caused by significant temperature gradients near cooled walls. These gradients lead to a higher gas pressure from the direction of the hotter gas. Both effects can be taken into account by the following expression:

$$J_g = n_g v_{th} - D_g \frac{\partial n_g}{\partial x}, \tag{118}$$

where J_g is the g-mer flux ($m^{-2}s^{-1}$), x is the direction towards to the surface, D (m^2/s) is the diffusion coefficient of g-mers in the surrounding gas, v_{th} (m/s) is the thermophoretic velocity [149].

Assuming equilibrium distribution of g-mer velocities and the free molecular regime ($Kn_{dp} \gg 1$), thermophoretic velocity in equation (118) can be obtained from the kinetic theory of gases as [149]:

$$v_{th} = -\frac{3\mu}{4\left(1+\pi\alpha/8\right)T\rho}\frac{\partial T}{\partial x}, \tag{119}$$

where α is the accommodation factor, α =0.8 [74, 149]. Diffusion coefficient for submicron particles in plasma flow is [149]:

$$D_g = \frac{3k_B T}{4\left(1+\pi\alpha/8\right)d_p^2\rho}\left(\frac{2m_m}{\pi k_B T}\right)^{\frac{1}{2}}, \tag{120}$$

where m_m is the molecular mass of surrounding gas molecules and ρ is the gas density.

The physical vapor that approaches the wall is also driven by diffusion forces. Monomer flux $J_{g,diff}$ towards the wall according to the Fick's law could be calculated as:

$$J_{1,diff} = -D_{vap}\frac{\partial n_1}{\partial x}, \tag{121}$$

where D_{vap} is the vapor diffusion coefficient. Calculation of D_{vap} is described in the next chapter.

II.5. Conclusion

In this chapter, an overview of modeling methods and approaches has been presented. The models presented in this chapter can be used to prove the feasibility of two-chamber PS-PVD and to estimate its possible characteristics. However, some modifications that will be presented in the next chapter are needed to fit the conditions prevailing in the process.

The discrete phase model that was previously used for alumina powder modeling [26] should be refined to work with zirconia (or any other solid material), homogeneous nucleation and growth equations need to be modified to account for the presence of temperature and pressure gradients and all of the models have to be linked (to work in succession) or coupled (to work synchronously). To ensure the quality of predictions, models should be validated or verified on the available experimental data. All these questions are addressed in the next chapter.

Chapter III. Model of the Proposed System

III.1. Introduction

This chapter contains the description of the models that were used for the design of the proposed system (PS). Because the principal assumptions and governing equations have been already described before, this chapter concerns my personal contribution to the models' development, namely:

- Modifications of the initial models for PS specific conditions, I have introduced during the study and the additional assumptions needed for these modifications;
- Validation of the models on the experimental data or their verification against numerical results obtained by other authors;
- Description of typical calculation domains, boundary conditions and meshes of the PS;
- Linking between the different models (CFD, DSMC, N&G).

Three models are presented. The first two ones are CFD-based and the last one is based on the DSMC method:

- A 3D computational fluid dynamics model of the high pressure chamber coupled with a discrete phase model of zirconia powder treatment (3D CFD + DPM) needed to evaluate the evaporation length required for the full/partial vaporization of particles of given size (injected radially) and the vapor content in the plasma flow. A 3-dimensional model was needed to capture 3D-effects, caused by radial powder injection;
- A 2D axisymmetric CFD model of the high pressure chamber (HPC) and expansion nozzle linked with kinetic nucleation and growth model (Axi-2D CFD + N&G) used to select the minimal HPC length to avoid nozzle melting and to design the nozzle by estimating its clogging rates;

and

- A 2D axisymmetric DSMC model of the low pressure chamber (LPC) linked with nucleation and growth model (Axi-2D DSMC + N&G) created to design the expansion nozzle considering nucleation and growth phenomena and rarefied gas dynamics downstream from it to obtain a jet with the biggest radius, highest physical vapor content and lowest nuclei content and size;

Axisymmetric models were used instead of 3D models due to the azimuthal uniformity of the flows inside the expansion nozzle and downstream from it. Numerical models and their extent of application are shown schematically in Figure 52.

Calculation domains, meshes and boundary conditions are described in general terms, since their dimensions and exact boundary conditions were initially unknown. The exact dimensions and boundary conditions were determined during the design process presented in the next chapter.

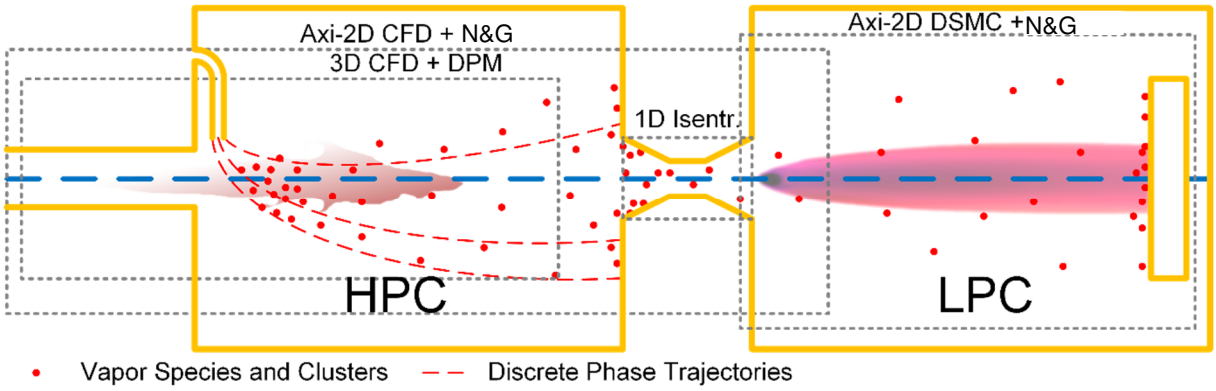

Figure 52: Schematic of PS modeling

III.2. CFD-based Models

III.2.1. General Considerations

The part of the proposed system described in the current section is highlighted in Figure 53.

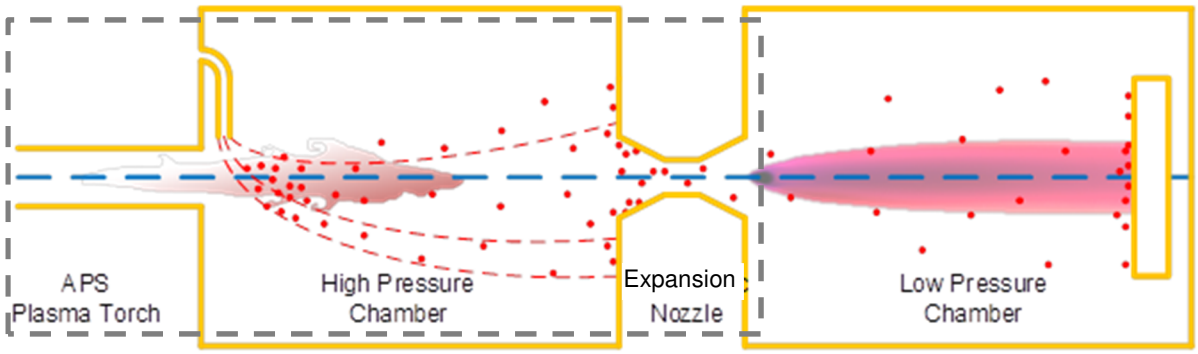

Figure 53: Proposed system schematic with highlighted CFD domains

Predictions of the time-averaged behavior of thermal plasma flow inside of the plasma torch nozzle, high pressure chamber and the expansion nozzle were made by means of the one-temperature Continuum Fluid Dynamics (CFD) approach, traditionally used to simulate plasma flows under APS conditions.

III.2.1.1. CFD Models' Objective and Dimension

Two types of models have been developed: (i) 3D model which comprised APS plasma torch nozzle and the HPC and (ii) axisymmetric 2D models that included the torch nozzle, HPC and the expansion nozzle. The first model was developed to evaluate the evaporation length required for the full/partial vaporization of particles of given size (injected radially) and physical vapor content in HPC. 3D model was needed to represent 3D effects due to radial powder injection of conventional plasma spray torches that breaks the axisymmetric nature of the steady plasma flow. The objective of the second model (2D) was to simulate the flow fields in front of and inside the expansion nozzle in order to design it avoiding nucleation-induced clogging and/or wall melting. The fluid dynamics of the second model was simplified in comparison with the first one to 2D approximation in order to reduce the computational costs of HPC modeling. Such a simplification was possible due to the absence of 3D effects in the part of the model near the expansion nozzle. The additional assumption of axial symmetry, as

shown by Fuzet and Sousa [25, 26], is valid for plasma flows under classical APS conditions at distances exceeding about 10 cm from the torch outlet.

III.2.1.2. CFD Code and Numerical Scheme

The discretized set of partial differential RANS equations was solved with Ansys Fluent 16.2 [153] CFD code using the pressure based solver (3D case without the nozzle) and the density-based solver for high-speed compressible flows (the axisymmetric 2D case with the nozzle). The choice of the code was dictated by the availability of user documentation and vast experience of the code utilization in the laboratory.

Under the conditions of the study, a considerable numerical stiffness of the equations to be solved should be anticipated. Numerical stiffness can be characterized by a ratio between the absolute values of the biggest and the smallest eigenvalues of the system of ODEs (26). If the ratio is too big, this would mean that some of the processes are happening significantly faster than others. In case of the RANS equations, these eigenvalues are proportional to the flow velocity for the continuity equation and to the speed of sound for momentum and energy conservation equations, where the pressure is present as a variable. At low Mach numbers, this difference may cause numerical instability if the time step is not small enough – large time steps will not allow the solver to resolve the fastest processes.

To tackle this issue, the so-called time-derivative preconditioning algorithm (AUSM) was used [154]. This algorithm modifies the time-derivative term in the conservation equations (25), allowing the acoustic speed to be rescaled, thus reducing the stiffness of the system to be solved. This algorithm is suitable only for pseudo-transient simulations – simulations where the goal is to achieve a steady, stationary solution.

III.2.1.3. Turbulence Model

For turbulence simulation, Shear-Stress Transport (SST) k-ω model was chosen. The choice was motivated by the ability of the model to handle compressibility effects (apparent in the expansion nozzle), high velocity gradients near walls (present in both torch and expansion nozzles) and laminar/turbulent transition of compressible flow (which happens when the flow leaves the torch nozzle and when it enters the expansion nozzle). In the thesis of de Sousa [25], it was shown that under classic APS conditions SST k-ω model gives the best predictions of plasma temperature and velocity in comparison with classical k-ε and k-ω models.

III.2.1.4. Transport and thermodynamic properties

Three gases were considered in the models. 80 mol% Ar + 20 mol% H_2 (further referred to as Ar/H_2) was acting as a plasma-forming gas, pure Ar as a carrier gas (was not included in 2D models), and ZrO_2 as a physical vapor formed during powder vaporization.

The plasma compositions of each of these gases were calculated by Pascal André [86] for pressures and temperatures varied from 1 to 2×10^5 Pa and from 150 to 30,000 K respectively using the method of minimization of Gibbs free energy. Corresponding thermodynamic and transport properties were calculated by André using the Chapman–Enskog method and took into account the dissociation, recombination, and ionization effects. Properties of the gas mixture are calculated by means of mixing laws described in the previous chapter depending on the mass or molar fraction of each mixture component.

A fast algorithm was implemented into ANSYS Fluent to facilitate the calculation of mixture properties. The main goal of the algorithm was to calculate transport and thermodynamic properties of any given mixture for any given pressure and temperature within the data range. The data were stored in a tabulated form. Calculation consisted in searching the interval in 2D (pressure-temperature) space that contained the point of interest. Then, a linear interpolation was performed between the known property values on the borders of the interval for each component of the mixture. Final mixture properties were calculated based on the mixing rules presented in the second chapter (II.2.3.6.b, p.55).

III.2.2. Coupled 3D CFD and Discrete Phase Model of HPC

The part of the proposed system represented by a 3D CFD-DPM coupled model is highlighted in Figure 52. The primary goal of this model was to determine the distance of maximal powder evaporation. The 3D formulation was required due to radial injection of powder in conventional spray torches, that was causing azimuthal non-uniformity of the flow. Note that the discrete phase model can be coupled with a 2D CFD model as well, however, in the present work, this option was not needed.

III.2.2.1. Model Assumptions

Alongside with the assumptions used by CFD (II.2.3.2, p.47) and DPM (II.3.2.1, p. 74), the present model was built upon the following additional assumptions:

- The domain and the fields inside it are specularly symmetric and can be represented by a half of the actual geometry with a symmetry boundary condition used along one of the boundaries;
- Plasma formation is not modeled and is represented by the introduction of preheated gas with radially uniform temperature through torch nozzle inlet. The use of uniform temperature profile on the torch nozzle inlet has insignificant influence over the flow profile on the torch outlet and mostly determined by the heat transfer between the flow and the nozzle cooling system.

The validity of the assumptions was explored in the reports of Fuzet and de Sousa [25, 26]. No additional assumptions to DPM were made.

III.2.2.2. DPM Model Improvements

The original discrete phase model implemented by Fuzet and de Sousa needed to be adopted to zirconia powder treatment. In particular, zirconia vapor diffusion coefficient was used for estimation of vapor mass flux from molten droplet surface in equation (82), p.77. A new approximate expression for diffusion coefficient was found in literature and introduced to the model to account for the change of powder material [155].

The diffusion coefficient of physical vapor in thermal plasma was estimated using kinetic theory to account for forces of attraction and repulsion between molecules by using Lennard-Jones potential of interaction between nonpolar, nonreacting molecules. The resulting equation had the following form [155, eq. 24-33]:

$$D_{vap} = \frac{0.001858 T_{film}^{\frac{3}{2}}}{\left(p/p_{ref}\right)\sigma_{vap-gas}^{2}\Omega_{D}}\left(\frac{1}{10M_{vap}}+\frac{1}{10M_{gas}}\right)^{\frac{1}{2}}10^{-5}, \quad (122)$$

where T_{film} is the weight-average gas temperature near particle boundary, $T_{film} = \frac{2}{3}T_p + \frac{1}{3}T$, T_p is the particle temperature, T is the surrounding gas temperature, $\sigma_{vap\text{-}gas}$ is the collision diameter (Å), $\sigma_{vap-gas} = \left(\sigma_{vap} + \sigma_{gas}\right)/2$, Ω_D is the collision integral for molecular diffusion, M_{vap} is the molar mass of zirconia. Collision diameter of zirconia vapor was estimated using the following expression:

$$\sigma_{vap} = 1.18\sqrt[3]{\frac{M_{vap}}{\rho_{ZrO_2} Na}} \times 10^{10}, \tag{123}$$

where ρ_{ZrO2} is the density of molten zirconia (see Table 23), Na is the Avogadro constant. Collision integral was approximated by the following function based on the tabulated data from Welty [155]:

$$\Omega_D = 0.9601\left(\frac{\varepsilon_{vap-gas}}{k_B T_{film}}\right)^{-0.682} + 0.5, \tag{124}$$

where $\varepsilon_{vap-gas} = \sqrt{\varepsilon_{vap}\varepsilon_{gas}}$, $\varepsilon_{vap} = 1.15T_b$, T_b is the boiling temperature of zirconia and ε_{gas} is the intermolecular potential well depth. $\sigma_{vap\text{-}gas}$ and ε_{gas} are two major parameters of the Lennard-Jones model that describes intermolecular potential by the following equation:

$$V_{inter} = 4\varepsilon_{vap-gas}\left[\left(\frac{\sigma_{vap-gas}}{r}\right)^{12} - \left(\frac{\sigma_{vap-gas}}{r}\right)^{6}\right], \tag{125}$$

where r is the distance between the centers of colliding molecules. Lennard-Jones parameters for various gases are shown in Table 22 in Annex A.

III.2.2.3. CFD-DPM Dynamic Coupling

The 3D CFD model was dynamically coupled with a discrete phase model for powder particles transport and evaporation, implemented by Matthias de Sousa [25] in Fluent code. The DPM model used the classical Euler-Lagrange approach for particle movement description and estimated particle diameter evolution according to heat balance equations (74)-(92).

Dynamic coupling between CFD and DPM models was automatically managed by ANSYS Fluent by introducing a set amount of powder particles through injector once per every 10 steps of CFD solution, updating momentum, enthalpy and ZrO_2 vapor mass fraction sources, distributed through domain along powder trajectories.

III.2.2.4. Calculation Domain and General Boundary Conditions

a. Calculation Domain

The three-dimensional domain used for steady state CFD and DPM simulations is shown in Figure 54.

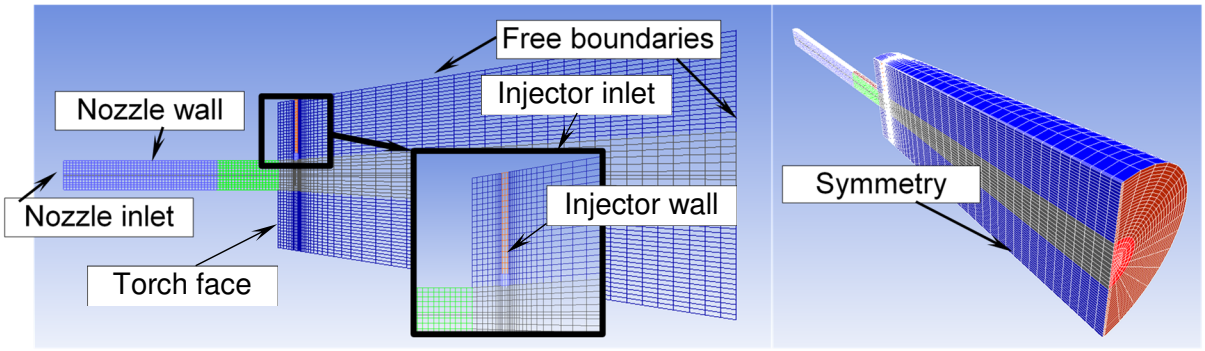

Figure 54: 3D CFD computational domain

The calculation domain consisted of three parts. The horizontal half-cylinder represented the nozzle of the plasma torch. The vertical half-cylinder (orange) represented the powder injector, and the conical frustum corresponded to free boundaries, located within HPC. The entire HPC was not included into the model, since the phenomena of interest were expected only within a small space along the torch axis. Because of the specular symmetry, the layout of the model represented a half of actual domain with a symmetry boundary condition applied along the central plane.

b. Mesh-Building Considerations

The structured computational grid consisted of ~3.5 × 10^4 hexahedral cells with sizes varying from 0.3 to 4.5 mm. The mesh was refined in the high-gradient regions (inside of the plasma gun, jet axis, walls) and in the regions with fine geometric objects (powder injector). The refinement process was performed iteratively until the solution became grid independent.

c. Boundary Conditions

General boundary conditions for simulations are presented in Table 4. Specific model dimensions and boundary conditions values vary depending on the case of interest and are listed in the corresponding sections of the next chapter.

c.i. Boundary Condition for Gas Flow

Mass Flow Inlet: The formation of a plasma jet in the torch was not modeled in this study, and a uniformly preheated gas was introduced at the inlet boundary of the domain.

The mass flow rate of plasma-forming gas ($\dot{m}$) and temperature (T) were set as mass inlet boundary conditions. The temperature T corresponded to the average temperature reached by the gas due to the ohmic heating in the plasma torch. It was derived from the average specific enthalpy ($h(T)$) of the plasma gas calculated from the following energy balance:

$$P_{elec} = V \times I = h(T) \times \dot{m}, \tag{126}$$

where V is the arc voltage and I is the arc current. The temperature of the nozzle wall was set so as to cool down the flow according to the actual torch efficiency and to get realistic radial flow profiles. The plasma gas mass flow rate was calculated based on the known volume flow rate:

$$\dot{m} = 5\rho_{st}\dot{V}/3 \cdot 10^{-5}, \tag{127}$$

where ρ_{st} is plasma gas density under standard conditions and $\dot{V}$ is volume flow rate in standard liters per minute. The resulting mass flow rate was divided by 2 to account for the specular symmetry of the model.

Walls: no-slip boundary condition was applied at the walls.

Open/free boundaries: for the open boundaries, the pressure (p) and temperature were imposed: the temperature is imposed if the flow was going inside the domain, zero flux was used if it was going outside of the domain (the same was applied for mass fractions and turbulence variables k and ω).

Turbulence boundary conditions: turbulence was described by intensity I_t and some relevant geometry dimension (hydraulic diameter D_H or length scale l or characteristic length L).

Turbulence intensity in the torch nozzle inlet was estimated according to the following empirical correlation for established pipe flows [153]:

$$I_t = 0.16\left(\mathrm{Re}_{D_H}\right)^{-1/8} = 0.16\left(\frac{\rho v_{avg} D_H}{\mu}\right)^{-1/8}, \tag{128}$$

where ρ is the plasma gas density on the inlet, μ is the dynamic viscosity and average gas velocity v_{avg} were determined iteratively. Hydraulic diameter D_H of a circular tube is equal to its internal diameter.

Turbulence length scale of plasma flow inlet was calculated based on the approximate empirical relationship:

$$l = \frac{0.07L}{C_\mu^{3/4}}, \tag{129}$$

where $L=D_H$, C_μ is an empirical constant specified in the turbulence model, $C_\mu=0.07$.

Boundary values for turbulence kinetic energy k and specific dissipation rate ω were automatically calculated by ANSYS Fluent, based on the known I_t, D_H and l according to the following relationships:

$$k = \frac{3}{2}\left(v_{avg} I_t\right)^2, \tag{130}$$

$$\omega = \frac{k^{1/2}}{C_\mu l}. \tag{131}$$

Powder carrier gas injection: Boundary conditions for carrier gas included composition, temperature, pressure and velocity. Carrier gas flow rate was set by imposing an average fixed gas velocity:

$$v_{cg} = \dot{m}_{cg} \Big/ \left(\rho_{cg} \pi R_{inj}^2\right), \tag{132}$$

where R_{inj} is the internal radius of the injector. The carrier gas mass flow rate $\dot{m}_{cg}$ was calculated using equation (127), based on a known volume flow rate.

Backflow turbulence parameters on the outlets (intensity and length scale) were based on the ones introduced by Pierre Fuzet [26]. The gas composition on the inlets was set by specifying mass fractions w_i of possible mixture components.

Table 4: General CFD boundary conditions for 3D CFD Model. n and τ correspond to normal and tangent vector components

Boundary	p	v_τ	v_n	T	w_i	k	ω
Mass inlet	calculated	$v_\tau = 0$	$v_n = v_{inlet}$ to get $\dot{m} = \rho v_n S$	$T = T_{inlet}$	$w_i = w_{inlet}$	$k = k_{inlet}$ (eq. (130))	$\omega = \omega_{inlet}$ (eq. (131))
Free boundary	$p = p_{boundary}$	$\frac{\partial v_\tau}{\partial n} = 0$	$\frac{\partial v_n}{\partial n} = 0$	$\begin{cases} \frac{\partial T}{\partial n} = 0, & \frac{\partial v_n}{\partial n} > 0 \\ T = T_{out}, & \frac{\partial v_n}{\partial n} \le 0 \end{cases}$	Same type as T	Same type as T	Same type as T
Wall	$\frac{\partial p}{\partial n} = 0$	$v_\tau = 0$	$v_n = 0$	$T = T_{wall}$ or $\frac{\partial T}{\partial n} = \Phi_{wall}$	$\frac{\partial X_i}{\partial n} = 0$	0	$\frac{\partial \omega}{\partial n} = 0$

c.ii. Boundary Conditions Used by Discrete Phase Model

Powder injection was characterized by particle mass flow rate $\dot{m}_p$, diameter d_p and initial temperature T_p. Initial velocity magnitude of powder particles v_p was set equal to the flow velocity. However, to represent the experimentally observed scatter of injection directions, random perturbation to the velocity vector was introduced according to the equations (98)-(102). Particle temperature was fixed and set to 300 K.

Table 23 with the properties used for zirconia particles and liquid zirconia droplets can be found in Annex A.

III.2.2.5. Model Validation

An attempt to validate the code under APS conditions (33 slm Ar, 11 slm H_2, torch nozzle diameter - 6 mm, 600 A, 58.3 V) with zirconia powders has been undertaken.

In order to verify the model for prediction of zirconia evaporation within the present study, an experiment was designed. The scheme of the experiment is shown in Figure 55. F4 (Oerlikon–Metco) plasma torch operating under conditions shown in Table 5, was directed towards a volume filled with water to capture the residual powder after its interaction with the plasma jet. Initial and resulting powder size distributions were obtained through laser diffraction spectroscopy.

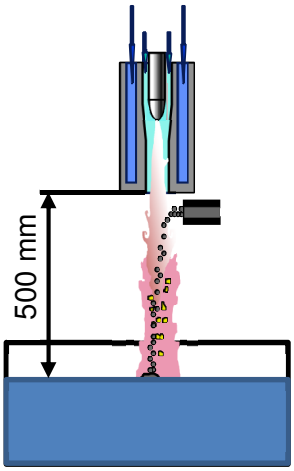

Figure 55: Schematic of the experiment to verify particle size evolution prediction. Water tank surface was equal to 0.2 × 0.3 m^2

Table 5: APS operating parameters for desecrate phase model verification

Parameter	Value
Plasma gas flow rate, slm	33 (Ar) / 11 (H_2)
Carrier gas flow rate, slm	6.5 (Ar)
Nozzle exit diameter, mm	6
Injector diameter, mm	1.4
Current (I), A	600
Arc voltage (V), V	58.3
Electric power (P_{elec}), kW	35.0
Plasma torch efficiency (η), %	53.4
Ambient pressure, Pa	101,325
Ambient temperature, K	300

The results are not presented: it appeared that the choice of experimental conditions (small nozzle diameter and quite coarse powders) was not optimal. The plasma jet velocity was too high leading to small flight time and consequently insignificant vaporization. The results were inconclusive, while the use of nozzles with a bigger diameter resulted in powder coagulation – a phenomenon that was not included into the powder model. Another attempt to validate the code will be undertaken in the future with better-adjusted parameters. Nonetheless, vaporization model is not the core of the thesis and is only needed to estimate the amount of vapor generated in HPC. It is well known that it is possible to vaporize particles even under low pressure conditions (PS-PVD) [114], and in this regards the present discrete phase model gives realistic results that correlate with experimental observations.

III.2.3. Linked 2D Axisymmetric CFD and N&G Model of HPC and Expansion Nozzle

The part of the proposed system represented by a 2D axisymmetric CFD-N&G linked model is highlighted in Figure 52. This model was created to evaluate nozzle wall temperatures and

clogging rates. Note that nucleation and growth model can be linked with a 3D CFD model and any DSMC model as well. In the present work the field of application was limited to 2D cases and linking with 3D cases was not explored.

III.2.3.1. Model Assumptions

Along with the assumptions used by CFD (II.2.3.2, p.47), kinetic nucleation theory (II.4.1.2.a, p.83) and growth equations (II.4.1.3.a, p.85, N&G), the proposed model is based on the following additional assumptions:

- The calculation domain and the fields inside it are axially symmetric. Indeed, as shown by Fuzet and Sousa [25, 26], under classical APS conditions 3D effects stop being apparent at distances exceeding 10 cm from the torch outlet;
- Powder particles are either fully evaporated or excluded from the domain before leaving the HPC, since there are engineering solutions based on particle/gas inertia difference, that allow separation of vapor and powder grains, e.g. two-torch layout, developed by Braillard et al. [156];
- The flow is compressible. A medium where nucleation and growth were taking place is assumed to be non-uniform, with significant temperature, pressure and velocity gradients;
- The resulting plasma flow is frozen and uninfluenced by nucleation and growth phenomena, particles formed by N&G do not influence the flow parameters due to their low concentration and small size;
- The nuclei formed during nucleation and growth process were assumed to follow the plasma flow due to their small size (dimensionless Stokes number was assumed to be far below unity, $\mathrm{Stk} \ll 1$), this assumption was confirmed in the study performed by Mauer [138];
- Under conditions of the study, nuclei were being formed solely from ZrO_2 atoms, the presence of ZrO, Zr and O atoms was neglected. According to the equilibrium composition of ZrO_2 vapor, calculated by prof. André shown in Figure 56, this assumption is roughly valid for temperatures lower than 4,000 K for atmospheric pressure or 3,000 K for 100 Pa;
- Nozzle clogging was assumed to be caused by diffusion-driven vapor deposition and by g-mer deposition, driven by diffusion and thermophoretic force. Any molecules or particles arriving at the surface were adsorbed with 100% probability. The maximal probability was chosen to get the conservative estimates of the clogging rate;
- The amount of vapor and g-mers consumed during the deposition process to the expansion nozzle wall was insignificant in comparison with the actual vapor and g-mer flow rate through the nozzle, thus, deposition process was not affecting nucleation and growth processes. This assumption was confirmed during the calculations presented in the next chapter.
- Energy barrier for adsorption was neglected. Desorption was considered improbable due to high desorption energy barrier. Since the exact values for these barriers were unknown, the most conservative approach for clogging rate estimation has been taken, ensuring the overestimation of clogging rate.

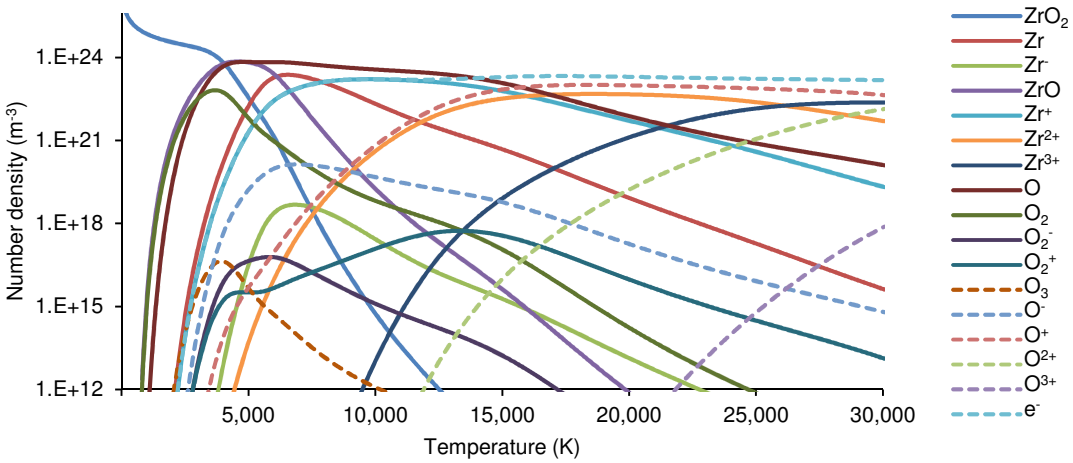

Figure 56: Equilibrium zirconia vapor composition at 1 atm

III.2.3.2. Nucleation and Growth Model Improvements

Original nucleation and growth (N&G) model introduced by Nemchinsky derived for stationary gases at constant pressure and temperature had to be modified due to high pressure and temperature variations inside the expansion nozzle. In addition, calculation of deposition rate required knowledge of g-mer field gradients, unavailable directly from the modeling results due to the use of Lagrangian specification for g-mer flow. A tool capable of transferring monomer and g-mer flows from Lagrangian to Eulerian specification was needed.

a. Modifications to Account for Flow Fields Variations

Homogeneous nucleation and nuclei growth processes were predicted for an infinitesimal volume, which travels along a plasma gas streamline. For stationary 2-dimensional flow streamlines were calculated by integration of the velocity field $\vec{v} = \left(v_x, v_y\right)$ tangent starting from some arbitrary point (x_{s0}, y_{s0}):

$$\begin{cases} \dfrac{dy_s}{dx_s} = \dfrac{v_y}{v_x} \\ y_s\left(x_{s0}\right) = y_{s0} \end{cases} \tag{133}$$

Flow parameters along each streamline were extracted from CFD simulation and were used to predict homogeneous nucleation and nuclei growth for an infinitesimal volume traveling along them.

Since the integration of equations (109)-(113) that represent conservation of species and formation and growth of g-mers was being performed along the streamlines, the transition from time derivative to position derivative along the streamline was made, assuming that the flow was stationary and the change of its parameters was related only to movement of the volume along the streamline with the velocity v_l (m/s):

$$\frac{df}{dt} = \cancel{\frac{\partial f}{\partial t}} + v_l \frac{\partial f}{\partial l}, \tag{134}$$

where f is any flow field which changes along the streamline.

Flow conditions along a streamline can vary drastically. In order to take into account compressibility effects, homogeneous nucleation and growth model by Nemchinsky and Shigeta (described in II.4.1) was modified. Modifications concerned equations (109)-(113) originally formulated for uniform medium (uniform pressure, temperature, velocity and vapor concentration). These equations were re-formulated in terms of number densities per unit mass of the medium $n' = n/\rho$, which allowed to account for infinitesimal volume compression and expansion during its travel along the streamline. This approach was first used by Kosh and Friedlander [157] and Kruis *et al* [158].

The aerosol growth process was described by three equations. The first equation, which shows the total ZrO_2 mass conservation, was given by:

$$\frac{dn_1'}{dl} = -\frac{du_g'}{dl} + \frac{dn_{1,init}'}{dl}, \tag{135}$$

where n_1' (kg^{-1}) is the number density of monomers per unit mass of the medium, $n_1' = n_1/\rho$, $u_g' = n_g' g$ (kg^{-1}), l (m) is the distance along streamline, g is the average number of monomers in a particle, $n_{1,init}'$ is the initial monomer number density, derived from 3D simulation of HPC, where ZrO_2 vapor molecules were generated by powder particle evaporation. Here, during the travel of infinitesimal unit of mass along the streamline, the number of monomers contained in this mass is being reduced by formation of g-mers (the first term on the right-hand side of the equation), but new monomers appear due to vaporization of ZrO_2 powder and by diffusion of ZrO_2 vapor from the neighboring regions (the second term on the right-hand side of the equation).

The second equation, which shows the change of g-mer number density along the streamline, was written as:

$$\frac{dn_g'}{dl} = \frac{J_{hom}^{KNT}}{\rho v_l} - \frac{1}{2}\frac{\beta_{gg}}{v_l} n_g'^2 \rho, \tag{136}$$

The last equation depicting the conservation of total volume of particles was written as:

$$\frac{du_g'}{dl} = \frac{J_{\text{hom}}^{KNT} g_{hom}^*}{\rho v_l} + \frac{\beta_{1g}}{v_l}\left(n_{1,init}' - u_g' - n_s'\right) n_g' \rho. \tag{137}$$

Tabulated data for equilibrium monomer concentrations n'_s at various temperatures were taken from literature and approximated by the following function [159]:

$$p_s = 10^{\left(13.312 - 37421.0/(T-273)\right)} \tag{138}$$

$$n_s' = p_s \Big/ k_B T \rho. \tag{139}$$

Approximation (138) allows calculating saturation pressure p_S of ZrO_2 for temperature varying from 2200 to 6000 K with relative error less than 10% (coefficient of determination R^2=0.9999).

b. Initial Conditions and Modifications to Account for Process Dynamics

Together, equations (135), (136) and (137) form a set of one algebraic and two ordinary differential equations with unknown n_1', n_g' and u_g'. The initial conditions for these equations are:

$$\begin{cases} n_1'(l=0) = n_{1,init}'(l=0) \\ n_g'(l=0) = 0 \\ u_g'(l=0) = 0 \end{cases} \quad (140)$$

Characteristic times (or distances) of growth by nucleation, described by the first term of the equation (137), were several orders of magnitude smaller than characteristic times (or distances) of growth by monomer addition, described by the second term of the same equation. This made the system of equations stiff. Therefore, numerical integration of the system was performed by the numerical scheme with a variable step size, developed on programming language Python [160]. The step size was varied depending on the estimated local error value. The error was calculated as a difference between the solution obtained with the 4th order Runge-Kutta scheme and the solution received with the 3rd order Runge-Kutta scheme. Integration scheme is described in Annex B.

The parameters used by the model are shown in Table 6.

Table 6: Parameters of homogeneous N&G model

Parameter	Value
ZrO_2 molar mass, kg/mol	0.123218
Molecular volume, m^3	1.81×10^{-29} [161]
Surface tension of ZrO_2 droplet, N/m	1.5 [162]

Conditions along the streamline can vary drastically, making possible the situation when the saturation ratio is lower than unity. Moreover, under certain conditions, coagulation and evaporation can become dominating processes, reducing g-mer concentration and size to zero. This may lead to non-physical results during the integration process. In order to avoid such situations, correction factors were introduced to equations (135)-(137):

$$\begin{cases} \dfrac{dn_1'}{dl} = -\dfrac{du_g'}{dl} + \dfrac{dn_{1,init}'}{dl} \\ \dfrac{dn_g'}{dl} = C_1(S)\dfrac{J_{\text{hom}}^{KNT}}{\rho v_l} - C_2(g)\dfrac{1}{2}\dfrac{\beta_{gg}}{v_l} n_g'^2 \rho \\ \dfrac{du_g'}{dl} = C_1(S)\dfrac{J_{\text{hom}}^{KNT} g_c^*}{\rho v_l} + C_2(g)\dfrac{\beta_{1g}}{v_l}\left(n_{1,init}' - u_g' - n_s'\right) n_g' \rho \end{cases} . \quad (141)$$

Here C_1 and C_2 are given by:

$$C_1 = \begin{cases} 1, & S > 1 \\ 0, & S \le 1 \end{cases} \quad (142)$$

and

$$C_2 = \begin{cases} 1, & g > 1 \\ 0, & g \le 1 \end{cases} . \quad (143)$$

C_1 ensures that nucleation process is stopped for saturation ratio lower than unity and C_2 stops g-mer-related processes, if g-mers cease to exist and being transformed to monomers. In

addition, on every integration step, the algorithm ensures that the integration variables are not negative or infinite.

c. Wall Clogging Rate

There are three major mechanisms, governing deposition to the expansion nozzle walls:

- Deposition of fully or partially liquefied powder particles with micrometric sizes;
- Deposition of nanoclusters formed via homogeneous nucleation process from physical vapor;
- Deposition via heterogeneous nucleation directly from the vapor phase.

Under conditions of the present study, micrometric particles were not considered, as technical solution exists to separate the vapor flux from non-fully vaporized particles due to their respective inertia [156]. Deposits were assumed to be composed of nanoclusters and adsorbed vapor molecules. The former were attracted to the wall surface by thermophoretic force and through Brownian diffusion, as shown by equation (118). The latter were approaching the walls driven solely by diffusion (equation (121)). Consequent vapor deposition followed the mechanisms described in II.4.2. In the present study, it was assumed that there's no energy barrier for adsorption. Desorption was rather improbable due to high desorption energy barrier. Thus, the deposition rate $\dot{d}$ (m/s) was estimated through the following expression:

$$\dot{d} = \dot{d}_1 + \dot{d}_g = \frac{m_1}{\rho_{coat}}\left(J_{1,diff} + gJ_g \right), \tag{144}$$

where equation (118) for g-mer flux was written in the following form:

$$J_g = \frac{3}{4\left(1+\pi\alpha/8\right)}\left[\frac{n_g'\mu}{T}\frac{\partial T}{\partial n} + \frac{2}{d_1^2 g^{2/3}}\sqrt{\frac{m_{1gas}k_B T}{2\pi}}\frac{\partial n_g'}{\partial n} \right] \tag{145}$$

Vapor diffusion coefficient in thermal plasma was estimated using the equation (122). To obtain monomer and g-mer field gradients normal to the walls required by equation (145), resulting monomer and g-mer fields calculated along the streamlines were interpolated to a regular rectangular mesh with constant axial and radial cell sizes. The nearest neighbor interpolation algorithm was used. The knowledge of nozzle walls locations in relation the mesh cells enabled estimation of normal derivatives. Such an approach could only work in the areas where the streamlines are in close proximity to the walls (e.g. inside of the nozzle). An attempt to apply the approach to the areas far from the streamlines (e.g. the face of the expansion nozzle in LPC) would lead to derivatives being equal to zero, resulting in zero deposition rates.

Following the assumption that in the expansion nozzle deposition rate $\dot{d}$ is significantly lower than g-mer and monomer flow rate through the nozzle, the influence of deposition to the nozzle wall on the solution of the system (141) was neglected. The validity of this assumption was confirmed during the calculations presented in the next chapter.

III.2.3.3. Linking of Axisymmetric 2D CFD and Nucleation and Growth Models

2D axisymmetric CFD model was "linked" to homogeneous nucleation and growth model. Linking, unlike coupling, implies one-way interaction – results produced by CFD were used by external code, written within the framework of the present study in Python 2.7 language and optimized for interaction with data produced by ANSYS Fluent and SPARTA codes. The results

produced by this code had no influence over the original flow fields (except from monomer concentration field).

III.2.3.4. Linking of 3D CFD and Axisymmetric 2D CFD Models

The 2D axisymmetric model was not coupled with the discrete phase model (DPM) since the 2D model was unable to fully capture 3D effects associated with the radial powder injection. Nonetheless, the 2D model required a way of taking vapor generation and corresponding energy loss into account.

Linking between the models was organized in the following way: (i) integration of the enthalpy source term of the energy equation (6) and species source term of the species conservation equation (9) over the 3D CFD domain by the means of ANSYS Fluent; (ii) introduction of the corresponding sources into the axisymmetric CFD model.

The preliminary study made with 3D CFD DPM model revealed that the majority of powder evaporation was confined within a small volume near the powder injector outlet. Thus, the sources were approximatively localized near the locations of the original sources, i.e. in a volume located inside the torch nozzle exit, as shown in Figure 58.

III.2.3.5. N&G Model Verification

Nucleation and growth model linked with it needed to be verified. Proper validation of the model linked with CFD model under APS conditions was impossible due to the lack of experimental data.

Homogeneous nucleation and growth model was verified within the framework of the present study on a synthetic test case used by Nemchinsky [145]. In the test case, the gas mixture was stationary with uniform distributions of temperature, pressure and monomer concentration and with no monomer sources. Under such conditions, the solution was dependent only on two parameters – dimensionless surface energy θ and initial supersaturation S_0. Two cases were considered: a case with θ=19 and S_0=200, representative of materials with high surface tension or high molecular volumes, like metallic or organic vapors, and a case with θ=8 and S_0=6 which corresponded to water [163]. The results of validation are shown in Figure 57.

The current model appeared to be in excellent agreement with the original implementation and with the results produced by the MOM. However, the model was not verified for the cases with pressure and temperature gradients, and no experimental verification was made due to the lack of experimental data.

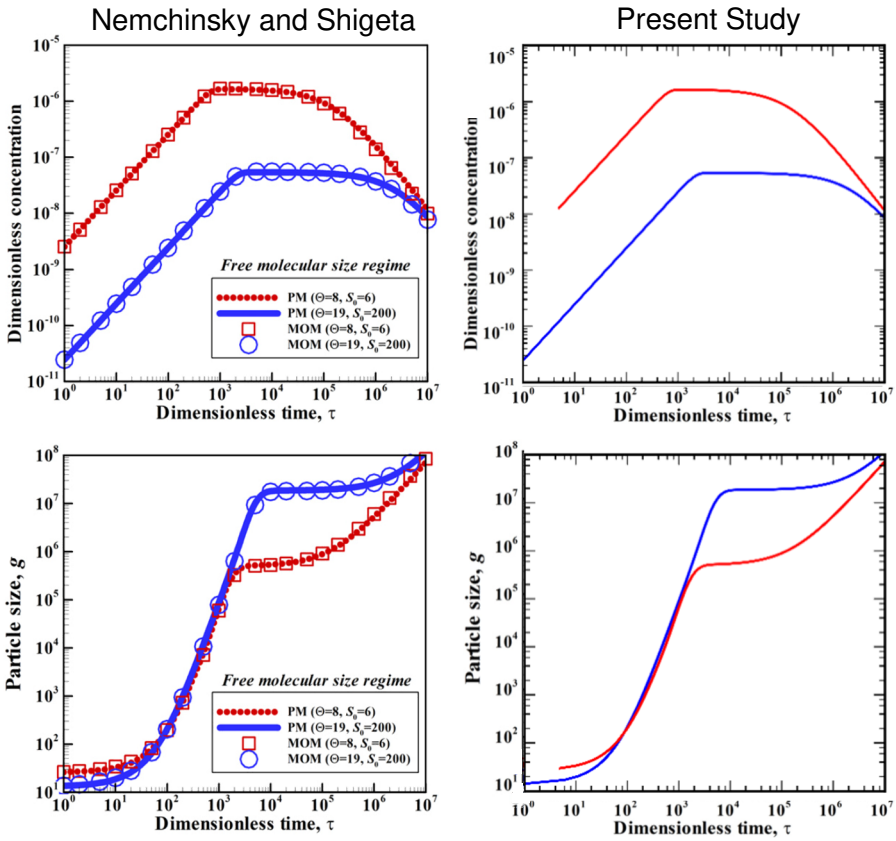

Figure 57: Model validation results. Left column: results (concentration, size) produced by the original model by Nemchinsky and Shigeta (PM) [145] in comparison with the results obtained with the method of moments (MOM) by Girshick [163]. Right column: results produced by the current implementation of the model. The red line starts at $\tau = 5$, as the initial time step is equal to 5

III.2.3.6. General 2D Calculation Domain and Boundary Conditions

a. Calculation Domain

The two-dimensional axisymmetric domain used for steady state CFD simulations of the expansion nozzle is shown in Figure 58.

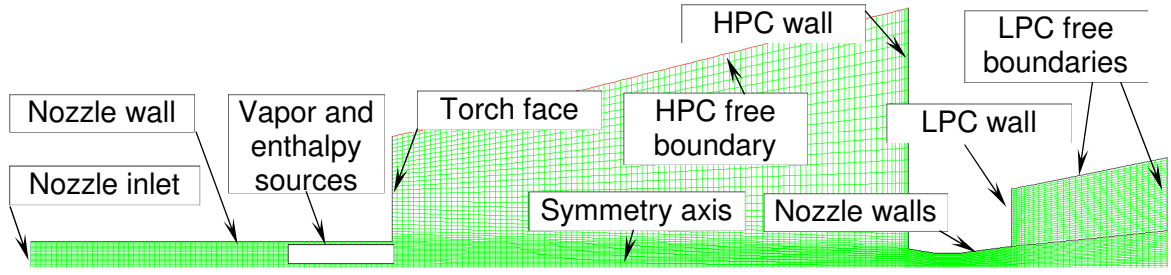

Figure 58: CFD computational domain for the nozzle. HPC – high pressure chamber, LPC – low pressure chamber

The domain consisted of four parts. The first horizontal cylinder represented the torch nozzle. The second part – a conical frustum – was the HPC with the initial length determined in the preceding 3D simulation. The HPC radius was assumed to be equal to the one of the LPC (at least 20 cm), however, the entire HPC was not included into the model in the radial direction,

since the phenomena of interest were expected only within a small space along the torch axis. The third part – a convergent-divergent nozzle was modeled as convergent frustum followed by a cylindrical throat and a divergent frustum. Throat diameter was initially estimated using isentropic approach and was later refined considering viscosity dissipation effect by means of this CFD model. The right divergent frustum corresponded to a fraction of the low pressure chamber (LPC). The rest of the LPC was not included in the model since supersonic flow formed inside the expansion nozzle had no effect over the gas flow upstream. Nevertheless, a part of the LPC was needed to correctly calculate the flow profiles (temperature, density, velocity, composition) needed as the boundary conditions for the DSMC model.

b. Mesh-Building Considerations

The structured computational grid consisted of ~10^4 quadrilateral cells with sizes ranging from 0.2 to 1.5 mm. The mesh was refined in the high-pressure regions (inside of the plasma torch nozzle) and in the high-gradient regions (inside of the expansion nozzle, walls). The refinement process was performed iteratively until the solution became grid independent.

c. Boundary Conditions and Source Terms

Boundary conditions applied to axisymmetric 2D cases were effectively identical to the ones introduced in the 3D case. The only difference was caused by the presence of the HPC wall and the expansion nozzle, which required thin wall boundary conditions. General boundary conditions used in the model are listed in Table 4.

Thin wall boundary condition was used on HPC and expansion nozzle walls to account for possible zirconia vapor or clusters deposited on them. Moreover, a layer of zirconia was assumed to be necessary to protect the expansion nozzle made of copper from melting and to slow down the clogging process by increasing maximum wall temperature. Thin wall BC requires specification of wall material (and its heat conductivity λ), wall thickness δ (or Δx) and either Dirichlet or Neumann or Cauchy boundary conditions on the side of the wall opposite to the flow, as illustrated by Figure 59. Given the aforementioned parameters, ANSYS Fluent will solve a 1D steady heat conduction equation to compute the thermal resistance of the wall [153].

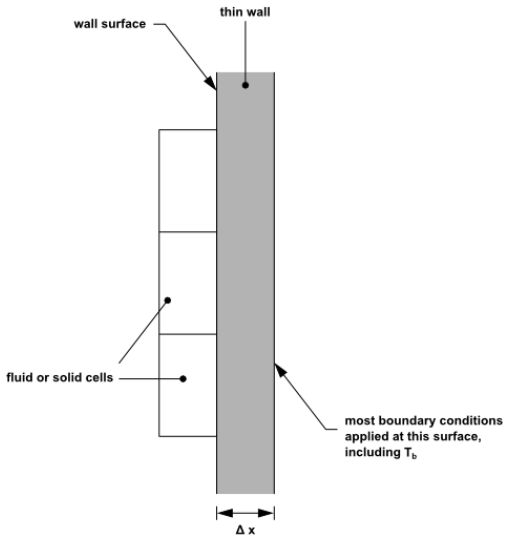

Figure 59: A Thin Wall boundary condition

As shown in Figure 58 enthalpy and zirconia species source terms, needed for linking between 3D CFD and axisymmetric CFD models, were introduced within a small cylinder near the torch nozzle outlet. Such a position was selected due to its proximity to the original sources, located near the injector outlet.

III.3. Linked DSMC and Nucleation and Growth Model of the Low Pressure Chamber

The part of the proposed system described in the current section is highlighted in Figure 52. DSMC approach linked with nucleation and growth model was used to predict the behavior of the plasma gas and physical vapor flow in the LPC. Nucleation and growth (N&G) model predictions were needed to estimate ZrO_2 distribution through different phases throughout the domain, coating growth rates on walls and possible microstructures.

Since N&G model linked with DSMC was already described in the previous section and doesn't require any additional assumptions, the following sections concern only Monte Carlo part of the low pressure chamber model as well as the way its inlet boundary conditions are linked with previous 2D-CFD calculations.

III.3.1. DSMC Code Selection

DSMC simulations were performed with the code SPARTA (11 Jul 2016 version), distributed under the terms of the GPL license [164, 165]. The choice was motivated by free and open-source nature of the code, availability of detailed documentation and tutorials, support of axisymmetric geometries, and because of the support of massively parallel calculations on CPUs and/or GPUs. Other codes, like DS2V, dsmcFOAM, SMILE and ICARUS were considered, however, they have failed to fit the selected requirements.

III.3.2. Model Assumptions

Alongside with the assumptions, typical for classical kinetic theory and DSMC-codes (II.2.5.4, p.61), additional assumptions were adopted:

- The plasma gas was considered neutral, composed only of Ar, H_2 and H molecules, and ionization reactions were not considered. Hydrogen dissociation and recombination reactions were considered. According to equilibrium compositions of argon-hydrogen plasma calculated by prof. André [86], for very low pressure conditions, this assumption is valid for temperatures lower than 7,000 K (when ionization degree is lower than 1%), however comparison with equilibrium should be taken with a grain of salt, since high degrees of disequilibrium and rarefaction are possible;
- The flow was stationary and axisymmetric;
- The collision mesh coincided with the sampling mesh. This was due to the absence of the concept of separate meshes in the code SPARTA.
- The rotational temperature in SPARTA code was calculated by averaging $T_{rot,x}$ and $T_{rot,y}$ into a single parameter T_{rot}.

III.3.3. Formulation of Boundary Conditions and Linking to CFD

The Code SPARTA uses number density n, velocity components v_x and v_y, temperature T and molar fractions of mixture components x_i as boundary conditions. For the wall boundary conditions, SPARTA uses wall temperature T and accommodation factor a_c. For more information on wall boundary conditions refer to the second chapter.

The original flow profiles on the expansion nozzle outlet were taken from the preceding 2D-CFD simulations. A Python 2.7 script was written to extract data from ANSYS Fluent solution files and automatically form an input script for SPARTA simulation. The script was extracting macroscopic gas flow parameters and transforming them into the form, acceptable for the Code SPARTA. Pressure and temperature profiles were converted to number density profiles using the ideal gas law:

$$n = {p}/{k_B T} \tag{146}$$

Though pressure-based free boundary condition can be set instead of number density and velocity, this option heavily relies on sampling and was deemed unreliable.

Mass fractions of the gas mixture components were converted to molar fractions of composing molecules using equation (22).

Generally, besides symmetry along the axis, three types of boundary conditions listed in Table 7 were used in DSMC simulations.

Table 7: General DSMC boundary conditions

Boundary	Set values
Inlets and outlets	T, n, v, x_i
Walls	T, a_c

The boundary-handling algorithms of the Code SPARTA were designed to maintain the selected average velocity by introducing new particles or letting the particles approaching the boundary escape, which resembles velocity outlet boundary conditions of CFD codes like ANSYS Fluent. One of the implications of such a way of setting the boundary conditions is the inability of the Code to automatically control the outflow velocity based on a chosen outlet pressure akin to pressure outlet boundary of CFD codes. The shortcomings of this approach became apparent during the simulations and can be seen in the next chapter.

III.3.4. Model Validation

SPARTA predictions have been validated against multiple sets of experimental data. Supersonic expansion of a pure Ar plasma jet produced by a low power plasma torch was validated based on the previous results by Selezneva [84] and by using the predictions provided by Bird's DSMC code DS2V [123]. Supersonic expansion of Ar-H_2 plasma was validated on experimental data from a real PS-PVD setup operating at a high power level, closer to the conditions of the present study. The data were provided by Dr. Mauer.

III.3.4.1. Pure Argon Low Power Plasma Jet

a. Operation Conditions and Model Assumptions

The case studied by Selezneva *et al.* concerned plasma jet used for deposition of various materials by means of Expanding Thermal Plasma (ETP) technique – a process, similar to PS-PVD or plasma spray chemical vapor deposition (PS-CVD). The simulation was done effectively under the same principal assumptions as the ones used for LPC modeling. The major difference in the assumptions was caused by the absence of diatomic gases and low

power level, which led to a total absence of flow chemistry or ionization. The parameters of the experimental setup used by Selezneva et al are listed in Table 8.

Table 8: Operating parameters of Selezneva's experimental setup

Parameter	Value
Plasma gas flow rate, slm	3 (Ar)
Nozzle exit diameter, mm	4
Net electric power input to gas, kW	5
Chamber pressure, Pa	100

b. Calculation Domain and Mesh

The two-dimensional axisymmetric computational domain used for this validation step is shown in Figure 60. The domain consisted of two cylindrical parts. The first part represented a part of the nozzle and the second part represented the deposition chamber.

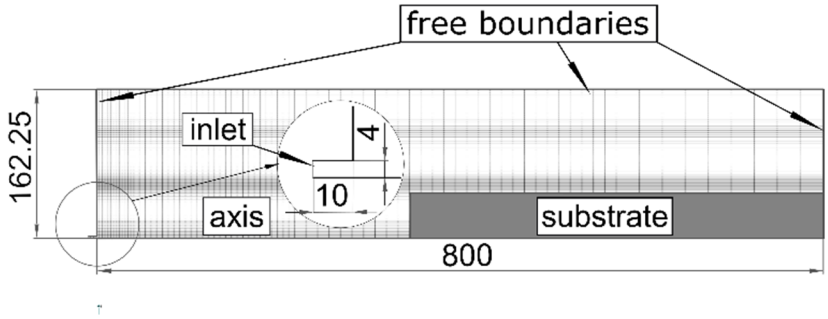

Figure 60: DSMC computational domain used for the SPARTA validation on Selezneva's data [73] (dimensions are in mm)

The sampling/collisional grid was defined so as to resemble the grid in the original research of Selezneva *et al* [84] who used DSMC code DS2V: the size of the rectangular cells varied from 3.125 to 25 mm and from 0.6 to 4.8 mm in axial and radial directions, respectively.

c. Boundary Conditions and Simulation Parameters

The boundary conditions for the simulation are listed in Table 9. At the walls, the condition of diffusive reflection was set with an accommodation factor a_c =0.25, which meant that 75% of the molecules were reflected specularly, while the rest underwent diffusive reflection, altering their velocities according to the wall temperature (300 K). This factor was iteratively adjusted during the process of simulation in the Code SPARTA to drive temperature on the torch nozzle outlet towards the experimentally measured value. The number of simulated molecules was 2.2×10^6 ($F_N = 5 \times 10^{17}$). The time step was equal to 10^{-7} s.

Table 9: DSMC boundary conditions used for validation based on Selezneva's data

Boundary	T, K	n, m^{-3}	v, m/s
Nozzle inlet	12,000	10^{23}	2,000
Free boundaries	300	2.4×10^{22}	0

Simulations considered only elastic collisions. Since pure Ar was used as plasma gas, the VHS molecular model with the parameters given in Table 24 was used except for the scattering parameter α that was set to unity.

d. Results

The temperature and velocity of the argon plasma jet were determined by Selezneva et al [84] from laser-induced fluorescence spectroscopy measurements around 811 nm on the Ar[4s] atoms. The velocity was derived from the moment balance, and temperature from the adiabatic relation between density and temperature. The errors of measurements were evaluated to be less than 10%. The variation of gas temperature and velocity along the jet axis is displayed in Figure 61.

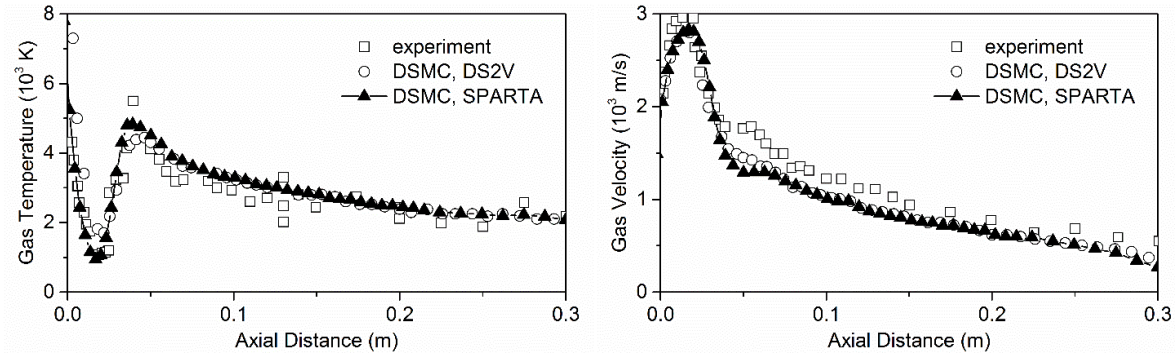

Figure 61: Variation of plasma gas temperature and gas velocity along the torch axis

The gas velocity and temperature predicted in SPARTA are in good agreement with the experimental data. However, a slight deviation from Selezneva's DSMC predictions is noticeable in the near-shock region. It can mostly be attributed to the differences in the sampling grid cell sizes, as the averaging of the flow properties over larger volumes in high gradient regions may substantially distort the result. Another possible explanation is the utilization of different collision model parameters, since their values were not mentioned in the original article [84].

III.3.4.2. Argon-Hydrogen Plasma Jet

a. Experimental Setup Parameters

Validation on Selezneva's data confirmed the right choice of DSMC parameters for pure Ar at low torch power levels. However, under the conditions of the present study, diatomic hydrogen was present in the system as well and the torch was operating at higher power levels, compounding the simulation. Moreover, a proof of the continuum breakdown was needed to justify the use of DSMC approach. A new experiment designed and conducted by He and Mauer (Institute of Energy and Climate Research IEK-1: Materials Synthesis and Processing, Julich, Germany) provided the means of DSMC validation for argon-hydrogen mixture under well-known PS-PVD conditions. The experimental setup is shown in Figure 62. Ar/H_2 plasma flow issued from the Oerlikon Metco F4-VB plasma torch, adapted to low pressure conditions was expanding into the deposition chamber pumped down to 150 Pa. For plasma characterization, an ARYELLE 200 (Laser Technik Berlin (LTB), Berlin, Germany) spectrometer was applied scanning a wavelength range of 381-786 nm. Plasma radiation was collected through a borosilicate glass window and an achromatic lens, transferred by an optical fiber to the 50 µm entrance slit and detected by a 1024x1024 charge-coupled device (CCD)

array. The system was equipped with an Echelle grating and the spectral resolution obtained is 15.9-31.8 pm. Calibration was carried out with a spectral Hg lamp [55].

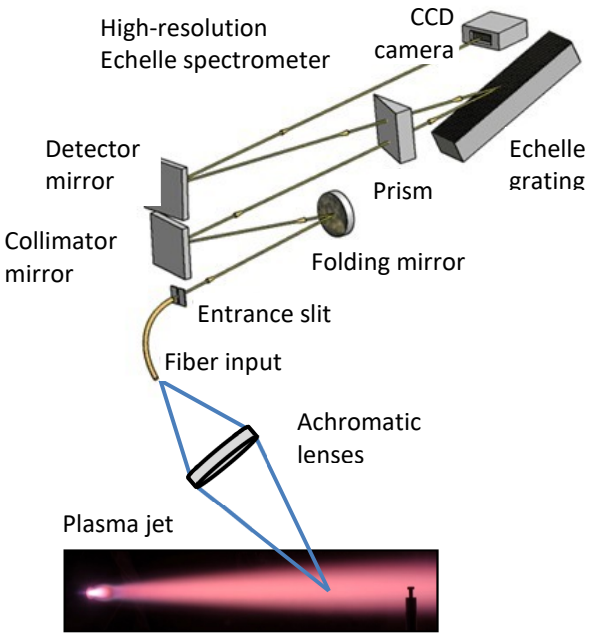

Figure 62: Experimental setup used for plasma temperature measurements

The parameters of the experimental setup adopted by He and Mauer are listed in Table 10.

Table 10: Operating parameters of the experimental setup of He and Mauer

Parameter	Value
Plasma gas flow rate, slm	50 (Ar)/12 (H_2)
Carrier gas flow rate, slm	4 (Ar)
Nozzle exit diameter, mm	11.5
Current, A	600
Arc voltage, V	74.8
Electric power, kW	44.5
Plasma torch efficiency, %	58.4
Chamber pressure, Pa	150

b. CFD Calculation

In order to calculate the boundary profiles for DSMC simulation and to compare continuum and non-continuum approaches, a CFD simulation of the experimental setup was performed. CFD layout is shown in Figure 63. Flow profiles on the torch outlet were later used to set inlet boundary condition for the DSMC simulation.

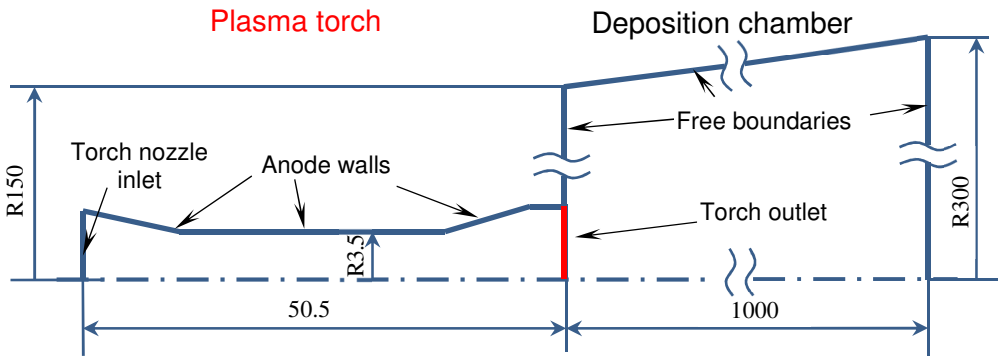

Figure 63: CFD computational domain used for the SPARTA validation on data from He and Mauer (sizes in mm)

Summarized boundary conditions for CFD calculation are listed in Table 11. The structured computational grid consisted of ~4×10^4 quadrilateral cells with sizes ranging from 0.4 to 7 mm. The mesh was refined in the high-pressure regions (inside of the plasma torch nozzle) and in the high-gradient regions (along the deposition chamber axis). The refinement process was performed iteratively until the solution became grid independent.

Table 11: Summarized CFD boundary conditions for SPARTA validation

Boundary	p -related	v_τ-related	v_n-related	T-related	I_t	L
Torch nozzle inlet	…	$v_\tau = 0$	$\dot{m} = 1.35 \times 10^{-3}$ kg/s	T=13,663 K	I_t=0.07%	D_H=0.005 m
Anode walls	$\frac{\partial p}{\partial n} = 0$	$v_\tau = 0$	$v_n = 0$	T=3,450 K	…	…
Free boundaries	p=150 Pa	$\frac{\partial v_\tau}{\partial n} = 0$	$\frac{\partial v_n}{\partial n} = 0$	T=673 K	I_t=3.0%	l=1 m

c. DSMC Simulation Domain and Mesh

The simulation was performed using the same assumptions as used for LPC simulations. The two-dimensional axisymmetric computational domain used for this validation step is shown in Figure 64. The domain was represented by a cylinder with the radius equal to 0.15 m and 1 m in length. The sampling grid composed of quadrilateral cells was chosen so as to minimize the statistical noise in the low-pressure regions. The grid was uniform and had 668 and 261 cells in the axial and radial direction, respectively, with the cell size equal to 1.5 mm × 0.575 mm, which allowed at least 20 simulated molecules per cell and led to a maximal error of about 10% for the 2σ confidence interval. In SPARTA code, the collision grid coincided with the sampling grid.

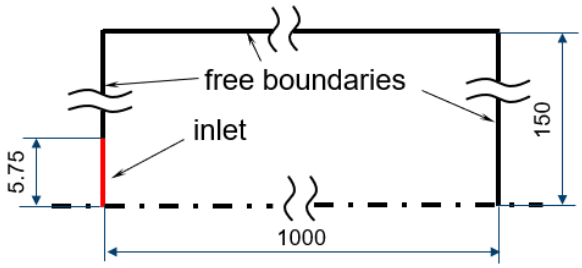

Figure 64: DSMC computational domain used for the SPARTA validation on data from He and Mauer (sizes in mm)

d. Boundary Conditions and Simulation Parameters

Flow profiles on the torch outlet (Figure 63) obtained from the preceding CFD simulation were used to set inlet boundary condition for the DSMC simulation. The time step (10^{-7} s) was chosen shorter than the average residence time of a molecule in a cell and estimated mean collision time (~ 10^{-6} s). The boundary conditions for the simulation are listed in Table 12. The number of simulated molecules was 10^7 ($F_N = 2.5 \times 10^{17}$).

Table 12: DSMC boundary conditions used for validation on He's data

Boundary	T, K	n, m^{-3}	v, m/s	x_{Ar}	x_{H2}	x_H
Nozzle outlet*	9,720	10^{23}	2,750	0.67	0.00	0.33
Free boundaries	2,000	5×10^{21}	0	0.80	0.20	0.00

*Radial profiles were set, averaged values are displayed for convenience.

e. Results

CFD and DSMC simulations have been performed to validate DSMC code SPARTA under PS-PVD conditions. The resulting temperature fields, as well as a RGB-interpreted photo of the jet, are shown in Figure 65.

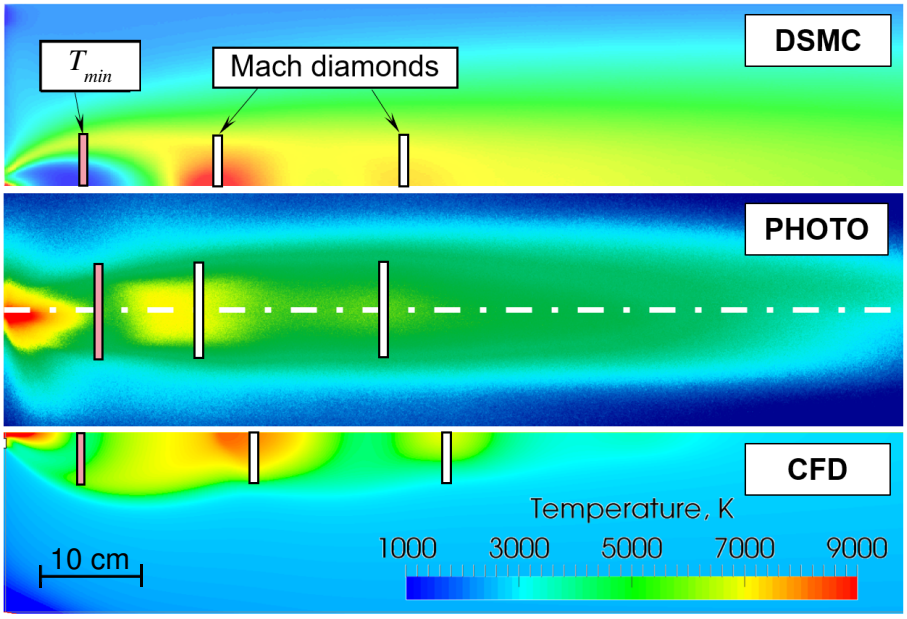

Figure 65: Comparison of temperature fields obtained with CFD and DSMC simulations. Photo: RGB color interpretation, no units

Both CFD and DSMC revealed the correct location of the first temperature minimum and the correct number of shocks (2). However, Mach diamonds were shifted downstream in comparison with the jet photograph. The greater shift was observed for CFD results.

Figure 66 contains axial distributions of various heavy species temperatures. The figure to the left shows a comparison between hydrogen temperature obtained from DSMC simulation, experimentally measured hydrogen temperature, and gas temperature retrieved from CFD simulation (due to equilibrium assumption, hydrogen temperature in CFD equals to thermodynamic temperature). About two barrel shocks are revealed by DSMC, following temperature fields are rapidly smoothened, unlike CFD predictions where nearly three barrel

shocks are visible. The smoothening of the shocks in SPARTA is caused by the presence of hydrogen in the gas mixture as it has better diffusion properties than argon due to a smaller collision cross-section. This effect can't be seen in CFD since the mixture is treated like a single species gas, so the diffusion effects are not considered. Despite the same initial temperatures, CFD temperature rapidly decreases, substantially deviating from the experimental values. DSMC results are in a close proximity with the experimental data.

The figure to the right shows the temperature of various species composing the gas, obtained with DSMC. Thermal disequilibrium prevails in the first shock and then disappears rapidly.

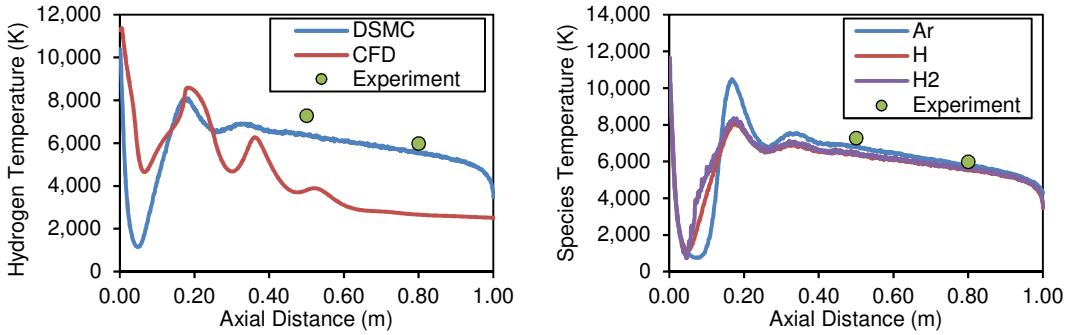

Figure 66: Hydrogen temperatures (left) and species temperatures (right) along the torch axis starting from the torch outlet

To illustrate the degree of rarefaction that happens in the flow along the torch axis, gradient-length local (GLL) Knudsen number field was calculated according to the following formula [166, 167]:

$$\mathrm{Kn} = \max\left(\mathrm{Kn}_{\rho}, \mathrm{Kn}_{T}, \mathrm{Kn}_{v}\right), \tag{147}$$

where for ρ is the gas density, T is the gas temperature and v is the flow velocity, and Kn for any field φ was calculated using the following expression:

$$\mathrm{Kn}_{\phi} = \frac{\lambda}{\phi}\left|\nabla\phi\right|, \tag{148}$$

where λ is the mean free path of the gas mixture, that can be calculated as follows [123]:

$$\lambda = \sum_{p=1}^{s}\frac{n_p}{n}\left[\sum_{q=1}^{g}\left\{\pi\left(d_{ref}\right)_{pq}^{2} n_q \left(\frac{\left(T_{ref}\right)_{pq}}{T}\right)^{\omega_{pq}-1/2}\left(1+\frac{m_p}{m_q}\right)^{1/2}\right\}\right]^{-1}, \tag{149}$$

where n_p, n_q are the number densities of the species p and q, respectively, and g is the total number of gases in the mixture. The values of d_{ref} and ω_{pq} for pure Ar, H_2 and H are given in Table 24 in Annex A. The values of d_{ref} and ω_{pq} for gas mixtures ($p \neq q$) were calculated by averaging the parameters of pure gases.

According to literature, continuum breakdown was expected to occur when Kn value exceeded 0.05 [73, 84, 167]. Indeed, according to the results shown in Figure 67, this value is exceeded in the first shock due to the rapid gas expansion. Thus, the substantial difference in temperature field predictions between CFD and DSMC can be attributed to the CFD treatment of the non-equilibrium regions behind the shocks where, as a result of rarefaction, deviations from both thermodynamic and chemical equilibrium occur.

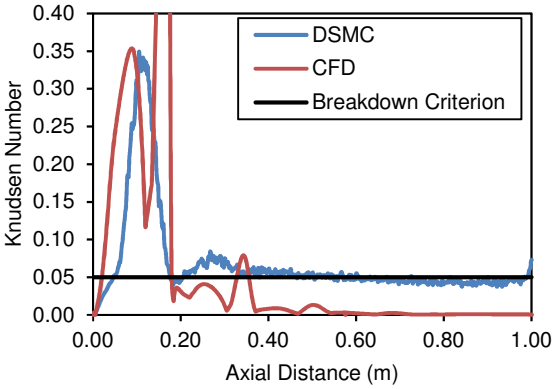

Figure 67: Knudsen number along the torch axis starting from the torch outlet

Radial temperature distributions at 500 and 800 mm from the torch outlet are shown in Figure 68. Despite the large difference between the DSMC and experimental results in the shockwave region, the fields like pressure, density or velocity are comparable downstream. DSMC predicts downstream temperature rather well, unlike CFD that under-predicts it.

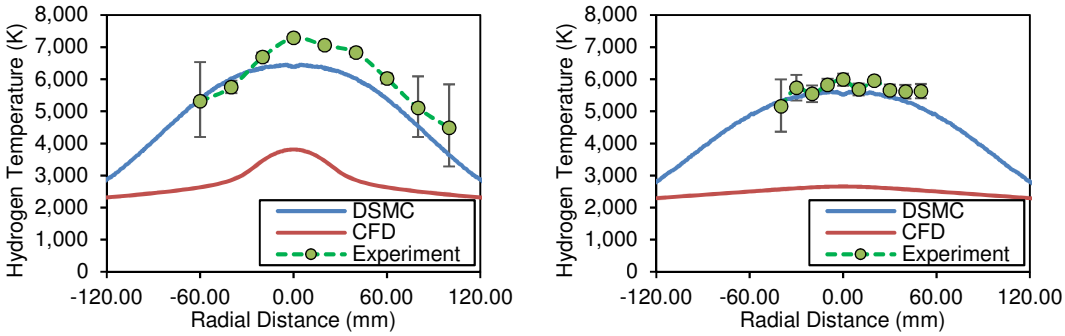

Figure 68: Comparison of temperatures in the radial direction at 500 mm (left) and 800 mm (right) from the torch outlet

Thus, DSMC code SPARTA was validated on the experimental data under PS-PVD conditions, showing good agreement with the experimental results downstream from the shockwave region. It was also shown that the use of CFD under PS-PVD conditions could lead to substantial temperature prediction errors and gradient-length local Knudsen number could be used to detect the continuum breakdown.

More in-depth exploration of continuum breakdown mechanics under PS-PVD conditions could be found in the article, published within the framework of the present study [73].

III.3.5. Zirconia Vapor Consideration and Linking to Nucleation and Growth Model

Nucleation and Growth model requires the knowledge of zirconia vapor mass fractions along flow streamlines. As shown in Figure 56, the composition of zirconia vapor drastically varies with temperature. The proper simulation of such vapor requires the information about chemical reaction rates of all the vapor components as well as their VHS/VSS parameters needed by DSMC collision models. These data can only be measured experimentally and are absent in the literature. Thus, to predict zirconia vapor transport, additional assumptions were adopted:

- Zirconia vapor was fully dissociated and consisted of neutral monoatomic oxygen and zirconium atoms. This assumption, according to equilibrium vapor composition calculated by André, is valid for the temperature range from 4,400 K to 5,000 K (Figure

69). Under the conditions of the study, due to the low overall thermal efficiency of the process, lower temperatures and thus higher fractions of ZrO_2 were anticipated, however, ZrO_2 molecules and recombination reactions were not modeled due to a lack of experimental data (reaction rates and ZrO_2 VSS parameters);

- Nucleation and growth processes were assumed to happen from a gas composed solely from ZrO_2 molecules. The concentration of ZrO_2 molecules was derived from concentrations of Zr and O;
- Reactions between plasma gas and physical vapor were neglected which was possible due to the low content of the latter.

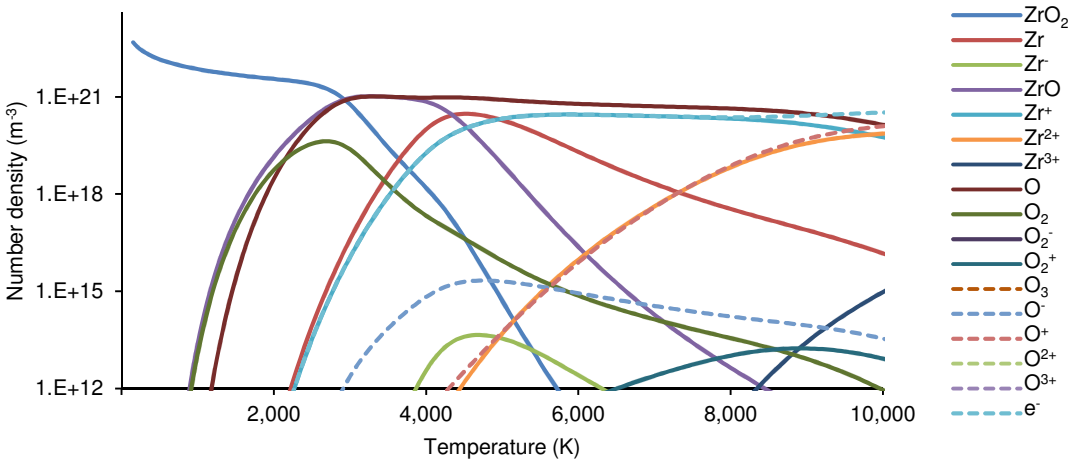

Figure 69: Equilibrium zirconia vapor composition at 100 Pa

III.3.6. General Simulation Domain and Simulation Parameters

III.3.6.1. Simulation Domain

The 2D axisymmetric domain for DSMC simulation is shown in Figure 70. To reduce the computational cost and restrict the calculation to the low-pressure region, the domain did not include the expansion nozzle and LPC walls and was represented by a cylinder, with a surface serving as a free boundary. The gas inlet of the domain coincided with the expansion nozzle outlet of axisymmetric 2D CFD models.

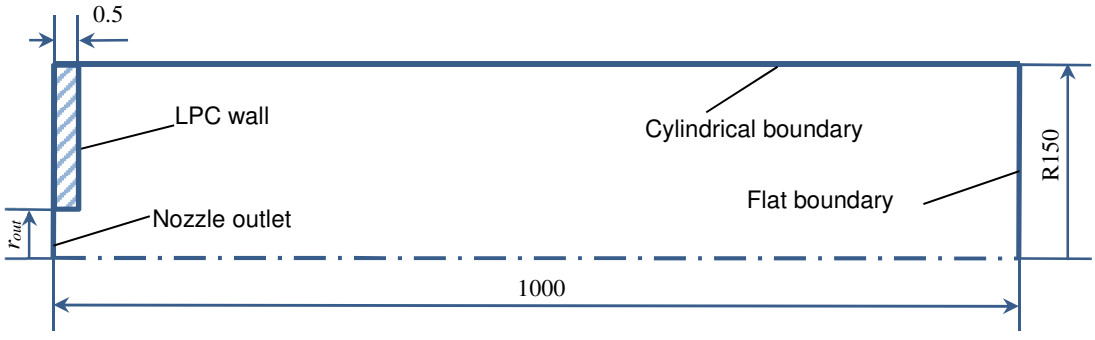

Figure 70: DSMC computational domain

III.3.6.2. Simulation Parameters

The boundary conditions for the DSMC simulations (temperatures, mean velocities, and molecular number densities) were derived from preceding 2D axisymmetric CFD simulation. The number of simulated molecules was held around 10^7 ($F_N = 2.5 \times 10^{17}$).

In the present study both elastic and inelastic collisions, which may occur in a reacting flow, were considered. The flow was composed of Ar, H_2, H, Zr and O atoms. Hydrogen and ZrO_2 molecules entering the domain through the nozzle were considered as fully dissociated. The VSS parameters of the atoms (used by equations (49) and (50)) are listed in Table 24, Table 25 shows the parameters used for flow chemistry simulation (needed for equation (55)), and Table 26 (Annex A) — the additional molecular parameters required for simulation. VSS collision model parameters and chemical constants used for the simulations are described in Annex A.

III.3.6.3. Mesh Generation

The sampling grid composed of quadrilateral cells was chosen so as to minimize the statistical noise in the low-pressure regions. The grid was uniform and had 667 and 265 cells in the axial and radial direction, respectively, with the cell size equal to 1.5 mm × 0.5 mm, which allowed at least 20 simulated molecules per cell and led to a maximal error of about 10% for the 2σ confidence interval. In SPARTA code, the collision grid coincided with the sampling grid. The time step (10^{-7} s) was chosen shorter than the average residence time of a molecule in a cell and estimated mean collision time (~ 10^{-6} s).

III.4. Conclusion

To prove the proposed system feasibility, commonly used approaches based on continuum fluid dynamics, kinetic theory and theory of homogeneous nucleation have been adopted. The models have been adapted to the process-specific conditions.

The updates I made within the framework of the study, concerned mainly the discrete phase model (vapor diffusion coefficient), and the model of nucleation and growth (taking pressure, temperature and gas velocity gradients into account) and their one-way (Flow → N&G) linking. These models have been verified or validated based on the available data. Linking of the models was performed by means of the interpreted high-level programming language Python 2.7.

The system was split into three distinct domains (torch nozzle + HPC, torch nozzle + HPC + expansion nozzle, LPC) created to check certain aspects of its feasibility. The design of the proposed system with the help of the models presented in this chapter can be done in the following succession:

1. Selection of spraying operating conditions favoring particles evaporation (low velocity, high thermal conductivity and enthalpy of the plasma jet);
2. Estimation of initial HPC length by using 3D CFD including particle modeling (DPM) to estimate the distance needed to reach the maximal evaporation degree of powder of given size and with the selected spraying conditions;
3. Estimation of expansion nozzle throat diameter based on the desired pressure in the LPC using 1D isentropic approximation;

4. Adjustment of HPC length by ensuring that the expansion nozzle temperature and HPC wall temperature are below the melting point using 2D CFD model. Refinement of the nozzle throat diameter by taking viscous forces, ignored in the initial 1D isentropic estimation into account. Adjustment of expansion nozzle length and divergence angle as well as its cooling regime to avoid wall melting and minimize clogging using 2D CFD linked with nucleation and growth model;
5. Modeling of LPC flow behavior and cluster formation by means of DSMC linked with nucleation and growth model. Optimization of nozzle geometry by iterating its divergence angle in order to obtain a jet with the biggest radius to ensure radial uniformity of the coating. Estimation of possible substrate locations that favor EB-PVD-like coating formation.

The aforementioned algorithm is capable of providing rough estimates of powder dynamics, vapor generation rates, vapor condensation rates, cluster content, and zirconia deposition rates. Possible calculation errors appearing in some parameters, such as vapor and cluster deposition rate or vapor content in the low pressure chamber, are basically dependent of the errors accumulated in the preceding CFD, DPM and N&G simulations. However, these errors can be minimized by further developing the models.

CFD can be enhanced by taking thermal radiation emitted by plasma gas into account. DPM can be updated to account for temperature gradients inside the powder particles and by considering possible collisions between them which can result in coagulation. All these enhancements, however, need to be validated by well-designed experiments.

Additionally, nucleation and growth model can be expanded to take particle size distribution functions and possible coagulation into account. Some of the errors can be caused by linking algorithms, and by the fact that the models are not fully coupled. Two-way coupling between CFD, N&G and DSMC can partially resolve this issue.

Nevertheless, there will always be a certain amount of errors, due to ever-present simulation errors, uncertainties in material properties and the general complexity of multiphysics systems. Better designed experiments for validation and verification of the models under the process-specific conditions as well as the experiments designed to obtain better model parameters (like reaction rates for DSMC chemistry) will increase the predictive qualities or, at least, provide a good estimation of prediction errors.

Chapter IV. System Design

IV.1. Introduction

This chapter is devoted to the use of the models and algorithms presented in the previous chapter to prove the feasibility of the hybrid CPS-PS-PVD system, referred to as the proposed system (PS), and to design it. This is done by (i) choosing preferable operating parameters of the plasma torch and determining the initial dimensions of the system using simplified models, (ii) refining nozzle's shape using more precise models, and (iii) performing nozzle shape optimization and exploring the influence of pressure on spray conditions (composition, temperature, jet sizes, etc.) in the low pressure deposition chamber.

The initial operating parameters of the torch were chosen (IV.2) according to the data presented in the literature review (I.3.6, I.4) to favor powder evaporation.

The initial dimensions (IV.3) of the system included the high pressure chamber (HPC) length and the expansion nozzle throat radius. The HPC length was estimated using 3D CFD model coupled with a discrete phase model for zirconia powder injection by tracking the distance needed to reach maximal evaporation degree of various powders. A simple isentropic approach was used for estimating the expansion nozzle throat radius.

The refinement of the initial dimensions (IV.4) was done with the help axisymmetric 2D CFD model by confirming that nozzle walls (which were not included into the 3D CFD model) do not melt considering torch's proximity and through adjusting the expansion nozzle throat radius to account for viscous stresses ignored during isentropic estimation.

The expansion nozzle that separates the high pressure chamber (HPC) and the low pressure chamber (LPC) is the "bottleneck" of the system – it can melt due to heating by the hot plasma jet, so it needs to be cooled properly. However, an excessive heat flux dissipated by the nozzle wall could result in physical vapor supersaturation and zirconia nuclei formation inside of the nozzle, leading to its clogging. Moreover, the geometry of the divergent part of the nozzle could have a noticeable impact on the gas flow expansion and cooling, ultimately affecting the clogging rates in that area. Thus, the system's feasibility was determined by confirming that the flow conditions inside the nozzle do not lead to excessive clogging rates by using nucleation and growth model linked with 2D CFD model.

The nozzle design optimization (IV.5) was done by analyzing its wall temperatures, flow cluster content (density and size) and zirconia deposition rates to the wall for various nozzle geometries by using the axisymmetric 2D CFD model linked with nucleation and growth model. Additional design optimizations were made by exploring the influence of various divergence angles on the LPC jet parameters using 2D DSMC model linked with nucleation and growth model. The criteria for quality coating formation were the jet diameter (since higher diameter leads to a more uniform coating), jet composition (high content of vapor and nanoclusters is preferable to low content of vapor and high content of microscopic clusters) and jet temperature (that should be high enough to minimize nucleation rates and favor high adatom mobility on the substrate surface).

The optimal divergence angle that favors quality coatings production was selected for two pressures maintained in LPC – 100 and 1,000 Pa. The former pressure is the one that is usually used in the PS-PVD process and the latter represents the level consistent with ATEX EU directive on equipment that involves work with explosive atmospheres [168].

The schematic of the proposed system is shown in Figure 71.

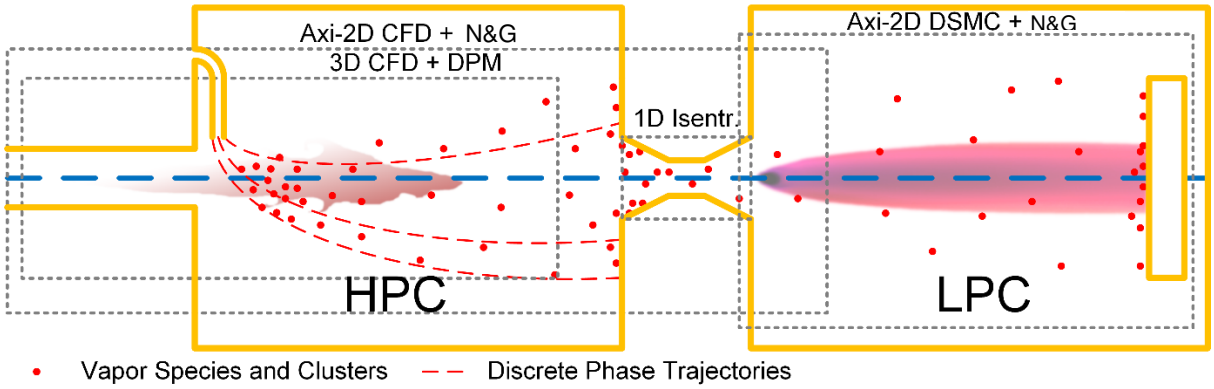

Figure 71: Schematic of PS modeling

To summarize, the design and optimization process followed the algorithm, shown in Figure 72. Rectangles represent calculations or value reassignment, rhombi – conditional operations.

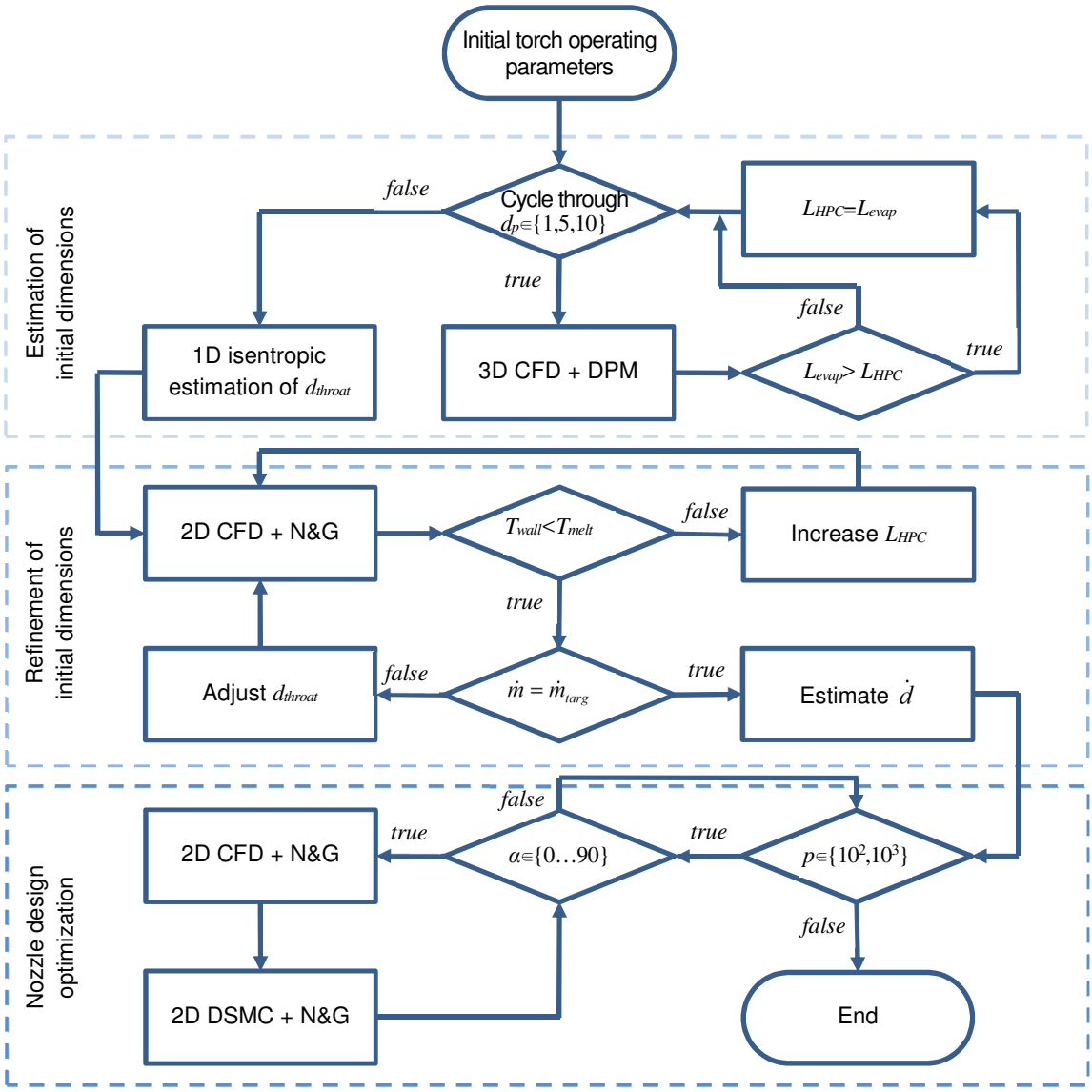

Figure 72: Flowchart of calculation activities

Following the flowchart, at first, initial operating parameters of the torch were selected (among other things, including the plasma forming gas and carrier gas mas flow rates $\dot{m}_{pg}$ and $\dot{m}_{cg}$, and the powder feed rate, together forming the target mass flow rate $\dot{m}_{targ}$). The initial high pressure chamber length L_{HPC} was thus determined as a distance needed to get a maximal degree of powder vaporization L_{evap} reached with various powders (with grain diameters d_p equal to 1, 5 or 10 µm). On the flowchart, a set of considered diameters is shown in curly brackets (d_p={1,5,10}) within the conditional operator. This represents a cycle through diameters, signifying that for each diameter from the set (if any chosen diameter lies within the set, it is a Boolean *true*) the operations that followed the "*true*" path were executed. When 3D CFD calculations were performed for each diameter from the set, following the Boolean *false* path, flow parameters at the downstream boundary of the 3D domain were used to approximately estimate the diameter of the expansion nozzle throat d_{throat} by an isentropic approach.

Next, L_{HPC} and d_{throat} were refined in a series of 2D CFD calculations. If the maximal nozzle wall temperature T_{wall} was higher than its melting temperature T_{melt}, L_{HPC} was being increased. If the mass flow rate through the expansion nozzle $\dot{m}$ was too different from the target mass flow rate $\dot{m}_{targ}$, comprising plasma gas, carrier gas and vapor flow rates, throat diameter was being adjusted as well. Nozzle clogging rate $\dot{d}$ was then calculated to ensure process' feasibility for acceptable periods of time.

After L_{HPC} and d_{throat} were refined, a series of linked 2D CFD, 2D DSMC and N&G calculations were performed to analyze the impact of the expansion nozzle divergence angle α (that was varied between 0° and 90°) and LPC pressure p (100 or 1,000 Pa) on the nozzle clogging rates and LPC flow parameters.

The set of resulting data was analyzed, recommendations for the design of the divergent part were given and the conclusion on the system's feasibility was made.

IV.2. Determination of Torch Operating Parameters

As it was mentioned in the first chapter, the PS-PVD process makes deposition of EB-PVD-like coating possible with higher deposition rates and for lower prices, but still requires powerful torches, helium as a plasma forming gas and extra fine powders to operate. To address these limitations, a new system is proposed, combining elements of APS and PS-PVD. The aim was to increase the amount of heat received by a powder particle by the following means:

- Introduction of a controlled atmosphere chamber with near-atmospheric pressure between the torch nozzle and the deposition chamber to increase the amount of heat transferred from plasma gas to powder particles in comparison with classical PS-PVD;
- The use of APS/CAPS torch with a nozzle diameter, larger in comparison with PS-PVD torch nozzles – higher diameter was expected to lead to a lower flow velocity and turbulent mixing, resulting in higher residence times of powder particles inside the jet core;
- Selection of argon/hydrogen mixture as a plasma-forming gas to provide specific enthalpy and heat conductivity sufficient for zirconia melting and evaporation, and avoiding the use of expensive helium.

Thus, spray parameters shown in Table 13, inspired by the conditions introduced in the work by Pierre Fuzet [26] and based on the conditions achievable in APS (Table 1, p.39), were

adopted. The major difference in comparison with the classical APS was the user of the torch with increased nozzle diameter – instead of typical 6 or 8 mm, a 10 mm nozzle was used.

Table 13: Torch operating parameters

Parameter	Value
Plasma gas flow rate, slm	40 (Ar)/10 (H_2)
Carrier gas flow rate, slm	4 (Ar)
Nozzle exit diameter, mm	10
Injector diameter, mm	1.4
Current (I), A	600
Arc voltage (V), V	63.5
Electric power (P_{elec}), kW	38.1
Plasma torch efficiency (η), %	45.9
Chamber pressure, Pa	10^5
Powder feed rate, g/min	5
Powder diameter (d_p), µm	1, 5 or 10

Three powders distinguished by the grain size were selected. As described in I.3.4.1 (p.32) typical agglomerated PS-PVD powders are composed of particles less than 25 µm in diameter. When these powder are exposed to heat, they decay into grains around 1 micron in diameter. Therefore, such size was selected to represent powders typically used in PS-PVD. Two additional diameters (5 and 10 µm) were used to demonstrate the possibility of system application to coarser and thus cheaper APS powders.

Powder feed rate was set to 5 g/min. This value was chosen to resemble feed rates, commonly set in PS-PVD (1-20 g/min, I.3.5, p.39). The selected value was chosen closer to the lower boundary of the typical interval to produce reasonable vapor content inside the expansion nozzle to delay its clogging.

IV.3. Estimation of Initial Dimensions

IV.3.1. Initial HPC Length

The initial high pressure chamber length was determined based on the distance powder should travel inside the jet to reach maximum evaporation. The dimensions applied to 3D CFD model coupled with the discrete phase model are shown in Figure 73 (proportions are not respected). The detailed description of the model is given in III.2.2 (p.94).

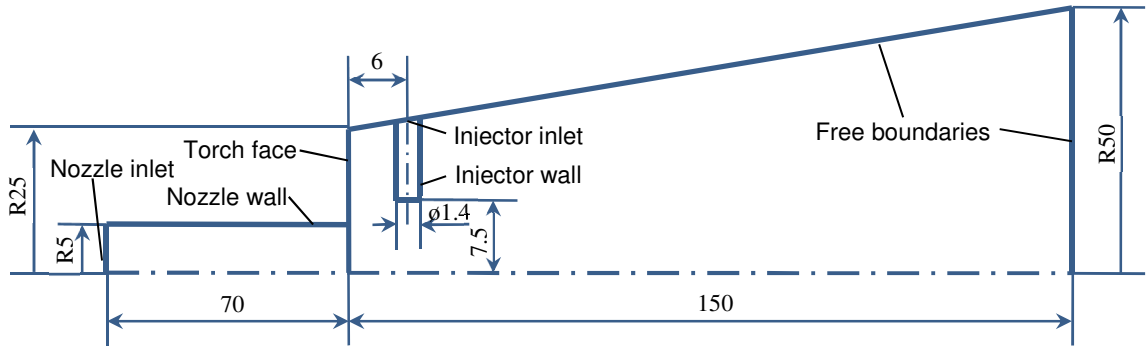

Figure 73: Dimensions of 3D CFD model of the high pressure chamber (in mm)

Based on the torch operating parameters (Table 13), boundary conditions were calculated according to the guidelines, presented in III.2.2.4 (p.96). The resulting boundary conditions are shown in Table 14. Three gases were considered during the calculation: Ar/H_2 mixture as a plasma forming gas, Ar as a carrier gas, and ZrO_2 vapor produced by powder evaporation. Carrier gas velocity was adjusted to maximize the amount of 10 µm particles entering the jet core. The same adjustments were not performed for 1 µm and 5 µm powders since their low inertia required higher carrier gas flow rates which were reducing the resulting jet temperature.

Table 14: CFD boundary conditions for 3D CFD Model

Boundary	p -related	v_τ-related	v_n-related	T-related	w_i-related	I_t	L
Torch nozzle inlet	calculated	$v_\tau = 0$	$\dot{m}_{pg} = 5.4 \times 10^{-4}$ kg/s	T=13,820 K	$w_{Ar/H2}$=1.0	I_t=3.2%	D_H=0.01 m
Injector inlet	calculated	$v_\tau = 0$	v_n =21.65 m/s	T=300 K	w_{Ar}=1.0	I_t=3.0%	D_H=0.0014 m
Free boundaries	p=101,325 Pa	$\frac{\partial v_\tau}{\partial n} = 0$	$\frac{\partial v_n}{\partial n} = 0$	T=400 K	$w_{Ar/H2}$=1.0	I_t=3.0%	l=0.15 m
Torch nozzle wall	$\frac{\partial p}{\partial n} = 0$	$v_\tau = 0$	$v_n = 0$	T=5,500 K	$\frac{\partial w_i}{\partial n} = 0$	…	…
Injector wall and torch face	$\frac{\partial p}{\partial n} = 0$	$v_\tau = 0$	$v_n = 0$	$\frac{\partial T}{\partial n} = 0$	$\frac{\partial w_i}{\partial n} = 0$	…	…

The solution was calculated until the residuals (of density, energy, species and turbulence variables) have reached values lower than 10^{-3}. Enthalpy, momentum and vapor sources due to zirconia powder evaporation were updated once per every 10 flow iterations. The resulting particle trajectories that show particle diameter evolution are shown in Figure 74. Variation of particle diameters along particle trajectories is shown in Figure 75. For easier interpretation of the results, the turbulent dispersion for visualization shown in Figure 75 was disabled. The resulting evaporation degrees of zirconia powder, as well as the distances from the torch nozzle outlet along the torch axis that were required to reach these degrees of evaporation, are shown in Table 15. The table contains values averaged over a large number of particles, so that the error of the result would be lower than 10% for the 2σ confidence interval.

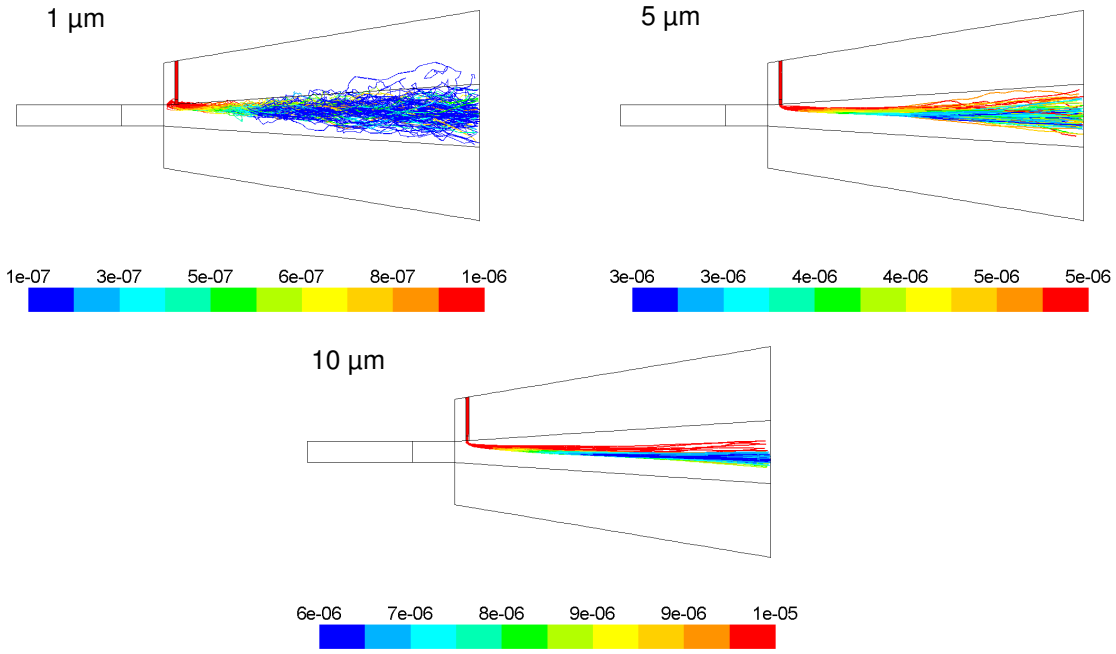

Figure 74: Particle trajectories for various powder injections. Color represents particle diameter (m). Higher dispersion is observed for finer powders

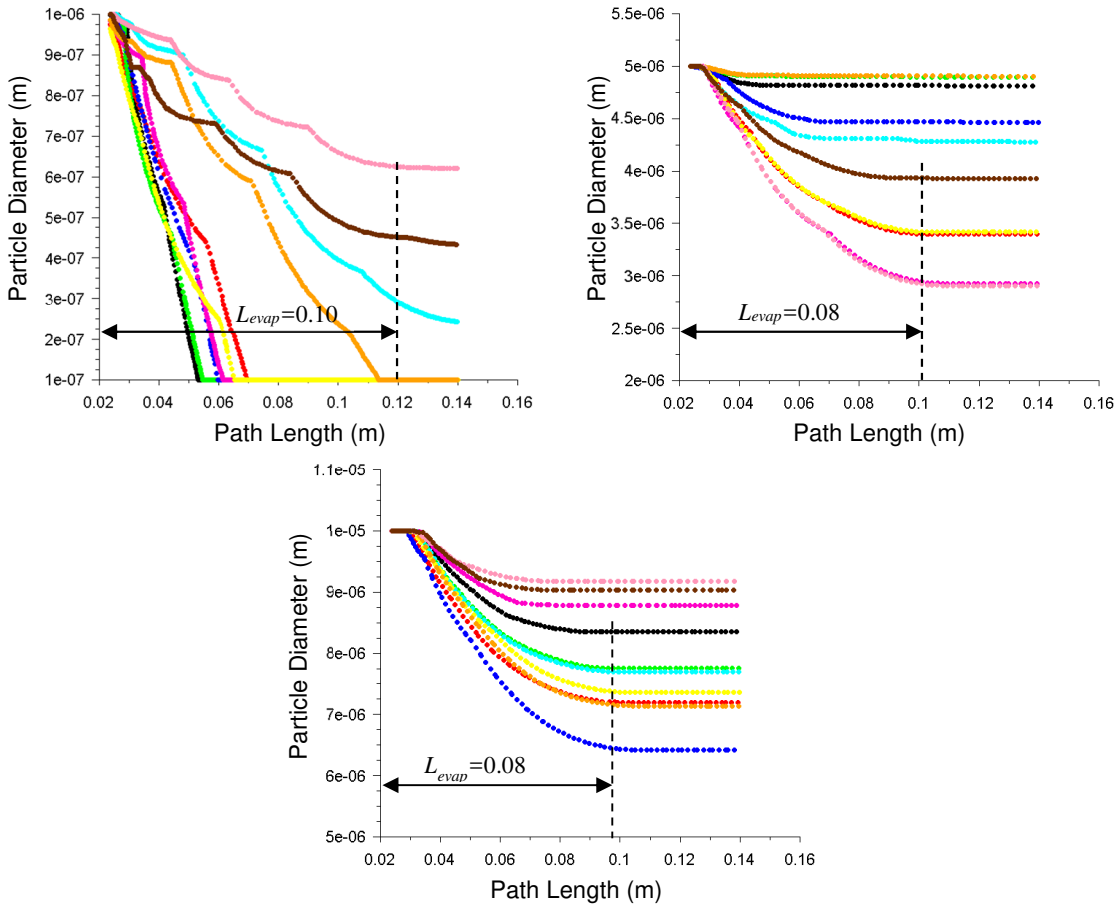

Figure 75: Evolution of particle diameters along particle trajectories. 10 particles are injected. The plots start at 0.02 m – a location that approximately corresponds to the location of injector outlet. Turbulent dispersion is disabled

Table 15: Evaporation degrees and evaporation distances of various powders

Powder diameter d_p, µm	1	5	10
Evaporation degree, wt%	72.1	66.0	60.8
Evaporation distance L_{evap}, cm	10.3	8.3	7.9

The performed simulations revealed that finer powders are capable of reaching higher evaporation degrees, however, complete evaporation was not reached due to significant Knudsen effect (described in II.2.2, p.45 and in II.3.2.4, p.78), that lowered the heat flux from plasma jet to powder particles. Another reason for the incomplete evaporation was turbulent dispersion that was driving micrometric particles away from the jet and deflection effect apparent for fine particles with low inertia. The turbulent dispersion was also responsible for driving powder particles back towards the jet, which is noticeable in Figure 74. Because of that, evaporation of fine powder particles continued up to 10 cm from the torch outlet or up to 12 cm along their path length as can be seen in Figure 75. Particle trajectories for coarser powders were less affected by turbulent dispersion, which led to smaller evaporation distances. Thus, since the system was designed to be capable of treating powders of various sizes, a conservative choice was made, and the initial length of the high pressure chamber was set to be 10 cm.

IV.3.2. Cross Section of the Expansion Nozzle Throat

The further work was based on a 3D CFD case with the injection of 10 µm powder, since the use of coarse powders was one of the possible advantages of the system and thus was prioritized over the use of more fine ones. In addition, the other powders were not considered due to a small difference in the resulting amount of vapor they generate. The nozzle diameter choice was made so that the mass flow rate through the expansion nozzle was equal to the mass flow rates of plasma gas, carrier gas and physical vapor to maintain 1 atmosphere in the high pressure chamber without significant involvement of gas pumps.

To estimate the diameter of the expansion nozzle throat, the isentropic approach presented in II.2.4.3 (p.58) has been utilized. Equation (31) for the throat diameter required the knowledge of gas pressure, temperature (or density) and adiabatic ratio upstream from the nozzle and gas flow rate through it. The temperature was considered to be as high as 4,000 K. This value was calculated by averaging temperatures from a circular region in 3D CFD domain located at L_{evap}=10 cm from the torch outlet. This region is indicated in Figure 76.

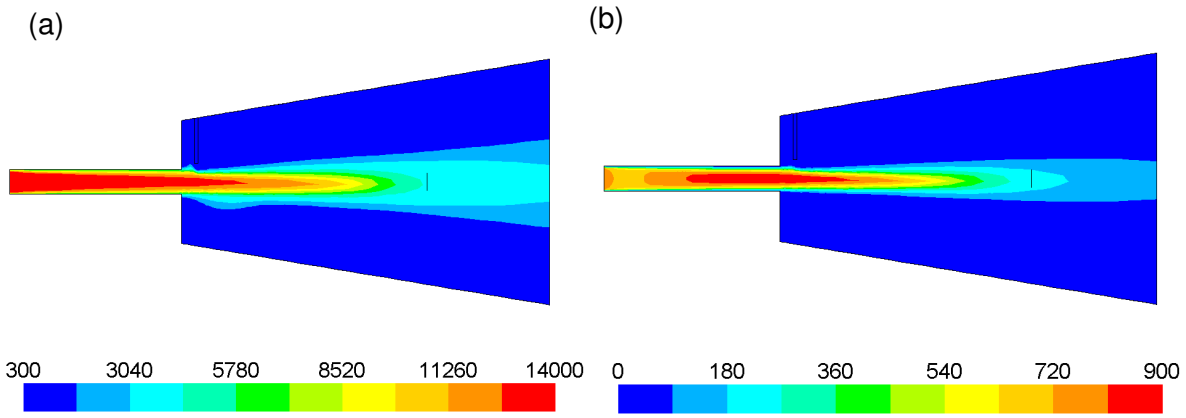

Figure 76: (a) Temperature (K) and (b) velocity (m/s) fields in HPC predicted by 3D CFD model

The target mass flow rate $\dot{m}_{targ}$ was estimated by taking plasma gas (50 slm or 1.08 g/s) and carrier gas (4 slm or 0.11 g/s) flow rates, and physical vapor flow (0.608*5 g/min or 0.10 g/s) into account and was equal to 1.29 g/s. Due to the high mass fraction of the plasma gas, the adiabatic ratio of Ar/H_2 at 4,000 K and 1 atm (γ=1.17) was used. The resulting expansion nozzle throat diameter d_{throat} was estimated to be 5.2 mm (r_{throat}=2.6).

IV.3.3. Nozzle Dimensions

The main parameter of the expansion nozzle is its critical cross section (or, its radius). The other important dimensions that are shown in Figure 77 include nozzle length L_{nozz} (including the lengths of convergent part L_{conv}, cylindrical part L_{cyl} and the divergent part L_{div}), and angles of its converging and diverging parts α_{conv} and α_{div}.

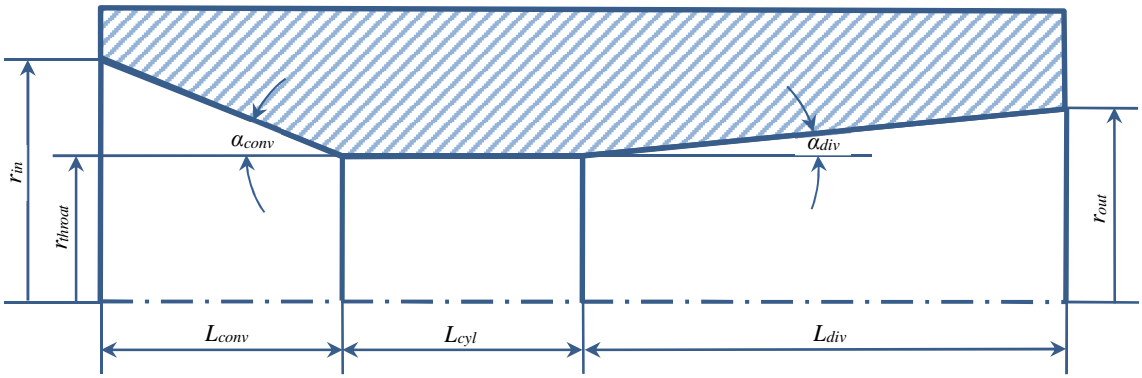

Figure 77: Expansion nozzle dimensions

The nozzle wall is exposed to gases with high temperatures. Thus, it should be cooled by using cooling channels with water or any other appropriate coolant. However, cooling reduces jet temperature and facilitates nucleation and growth favoring nozzle clogging. Because of that, nozzle length has to be minimal, while its temperature should be maximal. On the other hand, the minimal length is limited to 20 mm by cooling system's machining limitations: each cooling channel should be at least 3 mm in width and positioned at least 3 mm far from the neighboring cooling channels/walls. Thus, a nozzle with 3 cooling channels should be about 21 mm long. Therefore, the minimal possible nozzle length was fixed at 20 mm.

The choice of convergence angle and length of the convergent part is not critical to the system's feasibility. The only limitation is caused by the possible separation of the gas boundary layer and appearance of the recirculation zone in the cylindrical region due to gas inertia. Hence, a small convergence angle was selected by setting the nozzle inlet radius r_{in} to 3.5 mm and convergent part length L_{conv} to 5 mm (α_{conv} = 10°).

The throat is the critical segment the expansion nozzle. Clogging of the throat can result in the system's dysfunction. Thus, the remaining fraction of the nozzle length was distributed between the cylindrical part and the divergent part with the priority given to the latter to reduce the length of the former, providing more control over flow expansion and reducing the possibility of the throat clogging (L_{cyl}=5 mm versus L_{div}=10 mm).

The importance of non-zero divergence angle was highlighted in I.3.4.5 (p.38) – the use of a torch with the divergent extension has led to progressive expansion and wider jet with more uniform velocity profiles. However, in the original research by Sun et al [61] the methods of selecting this angle were not mentioned. In addition, method of characteristics commonly used for the design of divergent nozzles was not applicable to the nozzle under consideration due

to its limited length. Thus, the initial value for the divergence angle was arbitrary set through the nozzle outlet radius r_{out} put equal to 4 mm (corresponding to α_{div} = 8°).

The initial dimensions of the expansion nozzle are summarized in Table 16.

Table 16: Summary of initial dimensions of the expansion nozzle (dimensions are in mm)

Dimension	Convergent part	Cylindrical part	Divergent part
Length, mm	5.0	5.0	10.0
Maximal radius, mm	3.5	2.6	4.0
Angle, deg	10.2	0.0	8.0

IV.4. Nozzle Design Refinement

Once the initial diameter of nozzle throat and the length of the high pressure chamber were established, an axisymmetric 2D CFD model was used to refine the initial length of the high pressure chamber and the throat cross section of the expansion nozzle. Refinement of HPC length was needed to prevent or confirm the absence of HPC and nozzle walls melting, while the throat cross section needed to be adjusted to account for viscous stresses, which were not considered in the initial 1D isentropic estimation. Subsequently, when the refinement process was complete, a confirmation that physical vapor and nuclei formed in the nozzle are not causing its clogging has been made.

IV.4.1. HPC Length Refinement

Expansion nozzle walls, as well as the adjacent high pressure chamber wall, are constantly exposed to high-temperature plasma jet. Preceding 3D CFD calculation revealed that average jet temperature at 10 cm after the torch outlet is about 4,000 K. However, typical materials used in spay equipment shown in I.3.1 (p.22) have significantly lower melting points. Chambers are usually made of stainless steel with T_{melt}~1,673 K and plasma torches that have to withstand higher temperatures are usually made of copper, which has a relatively low melting point (T_{melt}=1,358 K) but high thermal conductivity (387.6 W/m/K), and tungsten due to its high melting point (T_{melt}=3,695 K). A similar approach was used to select material for the expansion nozzle. Copper was chosen as a primary material for the nozzle, with thick 200 µm zirconia coating applied to its walls to serve as a thermal barrier. Zirconia (T_{melt}=2,953 K) was chosen due to the ability to produce such coating on site. The feasibility of the system was dependent on zirconia layer melting.

The dimensions applied to the axisymmetric 2D CFD model are shown in Figure 78 (proportions are not respected). The detailed description of the model is given in III.2.3 (p.99).

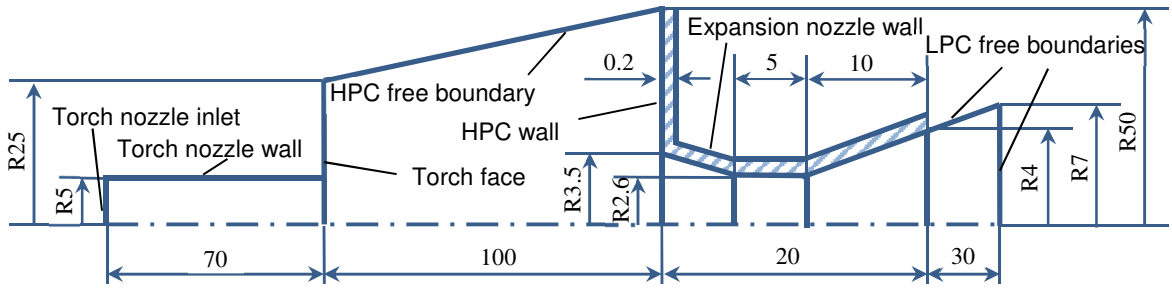

Figure 78: Dimensions of 2D CFD model of the high pressure chamber and expansion nozzle coated with zirconia layer (in mm). 45 degrees hatch pattern is applied to the coating

Boundary conditions based on the torch operating parameters (Table 13) were mostly inherited from the preceding 3D CFD calculation. However, due to the change of plasma gun nozzle representation from 3D to 2D form, some of the boundary conditions (like torch nozzle wall temperature and inlet mass flow rate) needed to be reevaluated according to the guidelines, presented in III.2.2.4 (p.96). Thin wall boundary condition was imposed on HPC and expansion nozzle walls to account for the presence of δ=200 µm of zirconia coating. Wall temperatures were set as copper melting temperature minus 100 degrees to ensure that copper will not melt. The same boundary condition was applied to the HPC wall, assuming that the wall region included into the simulation domain was still made of copper, even if it won't be the case for the experimental device. The resulting boundary conditions are shown in Table 17.

Table 17: CFD boundary conditions for 2D CFD Model

Boundary	p -related	v_τ-related	v_n-related	T-related	w_i-related	I_t	L
Torch nozzle inlet	-	$v_\tau = 0$	$\dot{m} = 1.08 \times 10^{-3}$ kg/s	T=13,820 K	$w_{Ar/H2}$=1.0	I_t=3.2%	D_H=0.01 m
HPC free boundary	p=101,325 Pa	$\frac{\partial v_\tau}{\partial n} = 0$	$\frac{\partial v_n}{\partial n} = 0$	T=400 K	$w_{Ar/H2}$=1.0	I_t=3.0%	l=0.01 m
Torch nozzle wall	$\frac{\partial p}{\partial n} = 0$	$v_\tau = 0$	$v_n = 0$	T=4,100 K	$\frac{\partial w_i}{\partial n} = 0$	-	-
HPC and expansion nozzle walls	$\frac{\partial p}{\partial n} = 0$	$v_\tau = 0$	$v_n = 0$	thin wall T=1,258 K δ=0.2 mm λ=2 W/m/K	$\frac{\partial w_i}{\partial n} = 0$	-	-
LPC free boundaries	p=100 Pa	$\frac{\partial v_\tau}{\partial n} = 0$	$\frac{\partial v_n}{\partial n} = 0$	T=300 K	$w_{Ar/H2}$=1.0	I_t=3.0%	l=0.008 m

In order to account for zirconia vapor generation, following the guidelines presented in III.2.3.4 (p.105) species and enthalpy sources were introduced to the dedicated region – a cylinder occupying the last 20 mm of the torch nozzle (Figure 58, p.106). Corresponding volumetric sources were 30.9 kg/m^3/s and -1.46×10^8 W/m^3 respectively were obtained by integrating the volumetric sources produced in the preceding 3D CFD calculations. The distributions of original species and enthalpy sources used to calculate integral sources for the 2D model are shown in Figure 79. The solution was being performed until the residuals have reached values lower than 10^{-3}. The resulting variations of coating temperatures along their exterior surfaces are shown in Figure 80.

The highest temperature (2,887 K) was reached in a small region around the nozzle inlet, which was lower than zirconia melting temperature T_{melt}=2,953 K. The absence of phase transitions at such a high temperature was ensured by using yttria-stabilized zirconia. Therefore, no additional refinements of the high pressure chamber length were needed and the final length was set to L_{HPC} = 10 cm. However, in the future refinements, it is advised to slightly increase this size to account for plasma jet temperature oscillations caused by arc voltage fluctuations and turbulence (described in I.3.1.2, p.24 and II.2.3.1, p.46) and to add a safety margin.

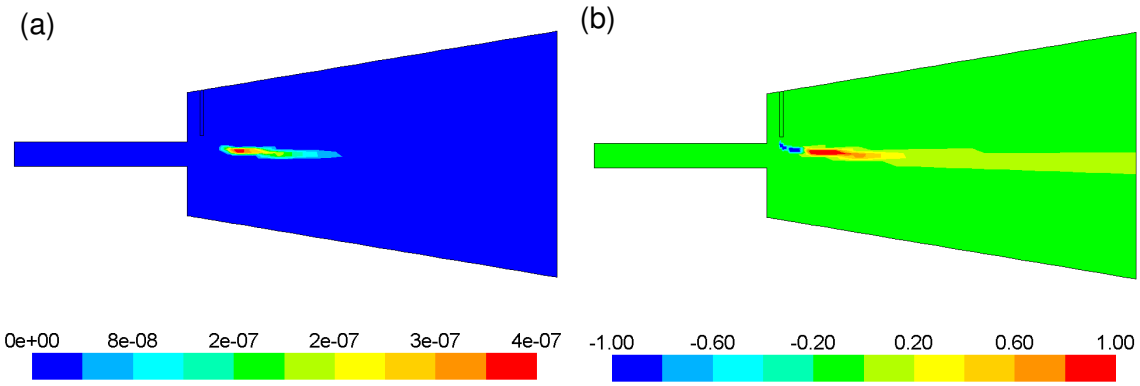

Figure 79: (a) Species source (kg/s) and (b) enthalpy source (W) fields, obtained from 3D CFD calculation. Negative enthalpy source signifies the region where heat transfers from plasma to particles, positive enthalpy – heat transfer in the reverse direction, since particle temperature exceeds the one of the plasma jet

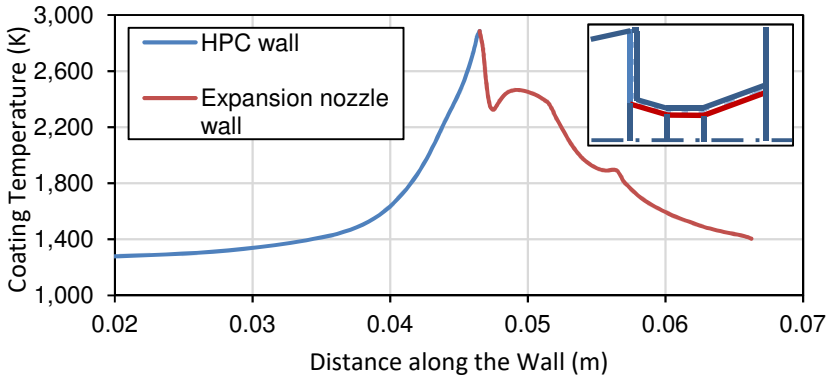

Figure 80: Maximal temperature of zirconia coating along the walls of HPC and expansion nozzle, obtained from 2D CFD calculation

IV.4.2. Expansion Nozzle Throat Cross Section Refinement

The initial 2D CFD calculation with the parameters listed in the previous section has shown that the calculated mass flow rate through the expansion nozzle $\dot{m}$ =1.00 × 10^{-3} kg/s was expectedly lower than the flow rate formed by plasma gas mixed with carrier gas and physical vapor $\dot{m}_{tot}$ =1.29 × 10^{-3} kg/s. Nozzle diameter was increased from 5.2 to 5.4 to raise the mass flow rate through it. An additional 2D CFD simulation confirmed the increase of the flow rate to 1.26 × 10^{-3} kg/s which was close enough to the target level considering the accuracy of nozzle manufacturing. Because the nozzle inlet and outlet radii were fixed, the change of the throat diameter led to a small decrease of convergence and divergence angles (their values became 9.1° and 7.4° accordingly).

Pressure field inside of the expansion nozzle is shown in Figure 81. High radial uniformity of pressure profiles indicates the absence of the boundary layer separation confirming the adequacy of convergent angle selection. The rectilinearity of the streamlines inside of the expansion nozzle shown in Figure 82 confirms the absence of recirculation.

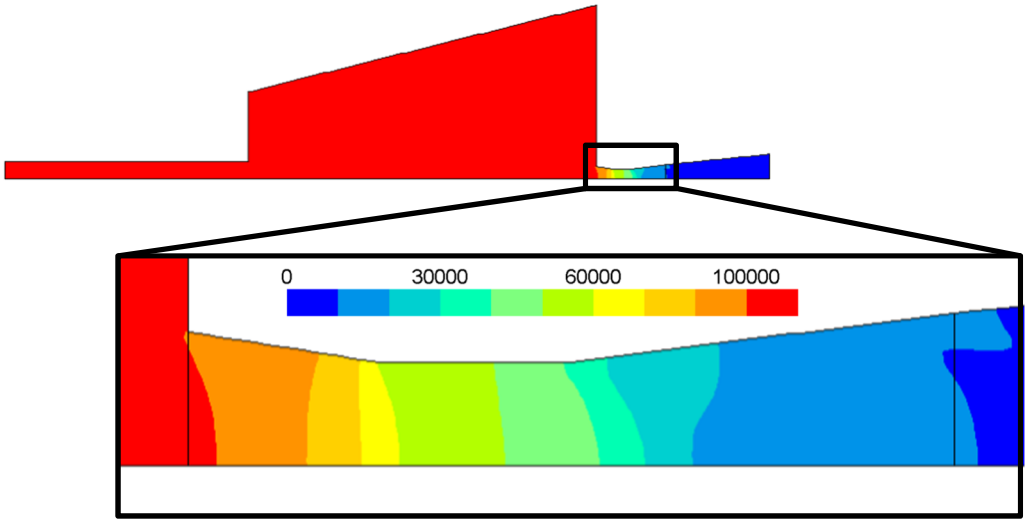

Figure 81: Contours of pressure (Pa) inside of the expansion nozzle predicted by 2D CFD model

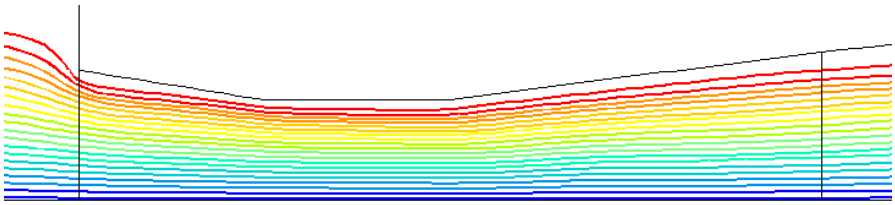

Figure 82: Streamlines inside off the expansion nozzle

IV.4.3. Nozzle Clogging Rate

This section describes a calculation made with nucleation and growth model. This calculation was needed to confirm that the nozzle was not susceptible to clogging at rates that may compromise the entire system. This section also sets an example the future calculations presented in the following sections would follow.

Ideally, expansion nozzle maintenance should be synchronized with plasma torch maintenance, that usually happens approximately once per 40-60 hours of operation under nominal parameters listed in Table 13. In the case when clogging is inevitable, reduction of throat cross section area due to an increase of zirconia layer thickness δ could significantly affect plasma-nozzle heat exchange and mass flow rate through the nozzle. This can result in wall melting and pollution of vapor with liquid zirconia droplets and changes in supersonic jet characteristics that could reduce consistency and reproducibility of zirconia coatings. In the present work, this effect was not studied and the threshold value for maximal acceptable cross section reduction was chosen based on its characteristic size. Thus, the maximal clogging rate was introduced as the ratio, between the characteristic scale (1 mm), which is rather large but still representative, and the desired operation time (40 hours) and was equal to 7 nm/s or about 1.5×10^{-10} kg/s per cylindric segment surface.

20 streamlines were calculated starting from torch nozzle outlet. Simulation of nucleation and growth was performed along the streamlines shown in Figure 82. The validity of the assumptions adopted by the model was confirmed by estimating characteristic times of the modeled processes (II.4.1, p.81). The average time needed to reach the steady state (1.3×10^{-7} s) was lower than the average integration step (5×10^{-7} s) indicating that during the integration process steady-state nucleation assumption was mostly fulfilled. However, there

were some steps when it was possibly violated. Compared with other characteristic flow times including the minimal time needed for the flow to pass through a mesh cell (1.3×10^{-7} s) and the average simulation time inside the nozzle (~10^{-5} s) steady-state assumption was considered mostly fulfilled. The spherical shape of secondary particles formed during the cluster coalescence was confirmed by comparing coagulation time (~10^{-12} s) with g-mer collision time (~10^{-5} s) during every step of integration. A significant difference between these times indicated that the secondary particles had enough time to obtain a spherical shape between their collisions. This also meant that coalescence was a negligible process with characteristic times comparable to characteristic flow time inside the nozzle.

The initial and resulting physical vapor (monomer) number densities shown in Figure 83 indicate that nucleation and growth processes do not influence vapor content in the nozzle significantly. A small decrease of vapor content is noticeable only in a small near-wall region (<0.5 mm) of cylindrical and divergent parts. Nuclei (g-mer) concentration and g-mer size fields inside the expansion nozzle shown in Figure 84 also confirm that intense nucleation and growth happen mostly in near-wall regions. The plasma gas mixed with physical vapor enters the nozzle and undergoes an intense cooling caused by flow expansion and heat exchange with cold walls that leads to supersaturation approximatively in the middle of the cylindrical part of the nozzle where nucleation and growth begin. Nucleation and growth processes continue up to the nozzle outlet and even beyond it, consuming vapor. In near-wall region regions, where nucleation and growth are prominent, the vapor is converted to nuclei approximately 100 monomers in size (or 4.6 times the size of a zirconia molecule). When the flow reaches the nozzle outlet 25% of the total zirconia vapor mass is converted to nuclei, composed in an average of 35 zirconia molecules (3.3 times the size of a zirconia molecule)

The resulting clogging rates including the contributions of vapor (1-mers) and nuclei (g-mers) are shown in Figure 85. The negative monomer or g-mer fluxes signify the direction towards the nozzle axis. No deposition occurs in the convergent part. Vapor is driven towards the axis by diffusion forces, since vapor number density decreases in the direction normal to the wall, while g-mers are simply not present in this part. In the middle of the cylindrical part nucleation consumes vapor and diffusion starts driving monomers towards the wall. Recently formed nuclei having maximal concentration near the wall undergo diffusion towards the axis. The thermophoretic force that acts in the opposite direction is negligible. Thus, nozzle clogging is caused solely by monomer adsorption. A small positive g-mer deposition rate peak observed in the divergent part can be attributed to numerical noise caused by the chosen interpolation technique. In total, upon reaching the outlet about 0.275% of zirconia mass was lost to deposition on nozzle walls.

The resulting clogging rates exceeded the critical threshold value by the factor of 9. This means that instead of 40 hours of work, nozzle maintenance should be performed every 4.5 hours. Note that this value is a conservative estimate since in the selected approach every vapor molecule that approaches the wall is adsorbed, which may not be the case in the actual system. Moreover, clogging rate calculation does not account for the “history” of the flow – the solution of nucleation and growth equations is considered frozen and the reduction of vapor content due to adsorption that happens upstream in the nozzle does not reduce the vapor content downstream. Thus, downstream clogging rates, especially in the divergent part, are heavily overestimated and 4.5 hours seems to be a good value that confirms process’ feasibility during prolonged operation periods. A small positive peak in the divergent part of the nozzle is a numerical error caused by the chosen interpolation technique (see III.2.3.2.c, p.104).

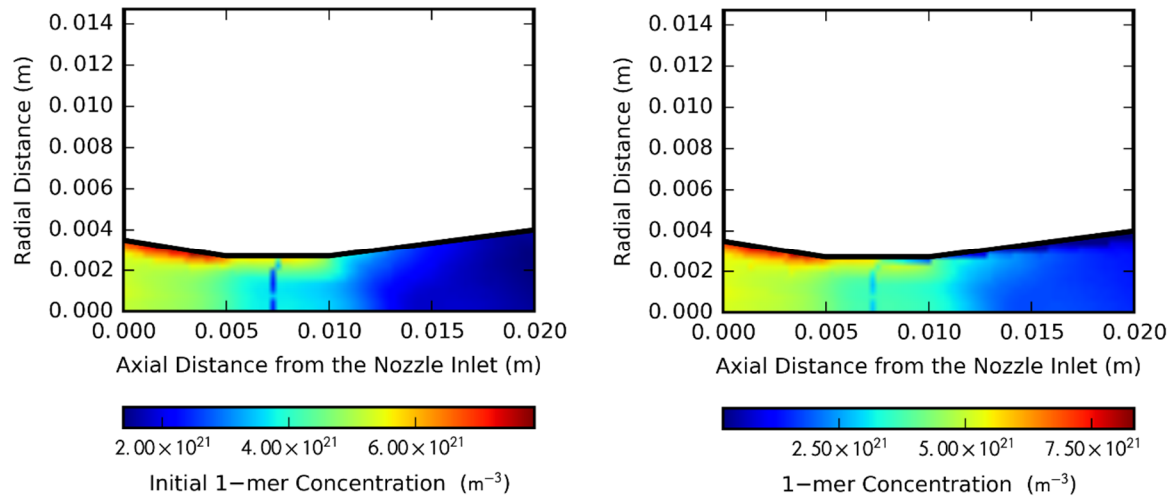

Figure 83: Physical vapor species (monomer) concentrations inside of the expansion with (right) and without (left) considering nucleation and growth processes

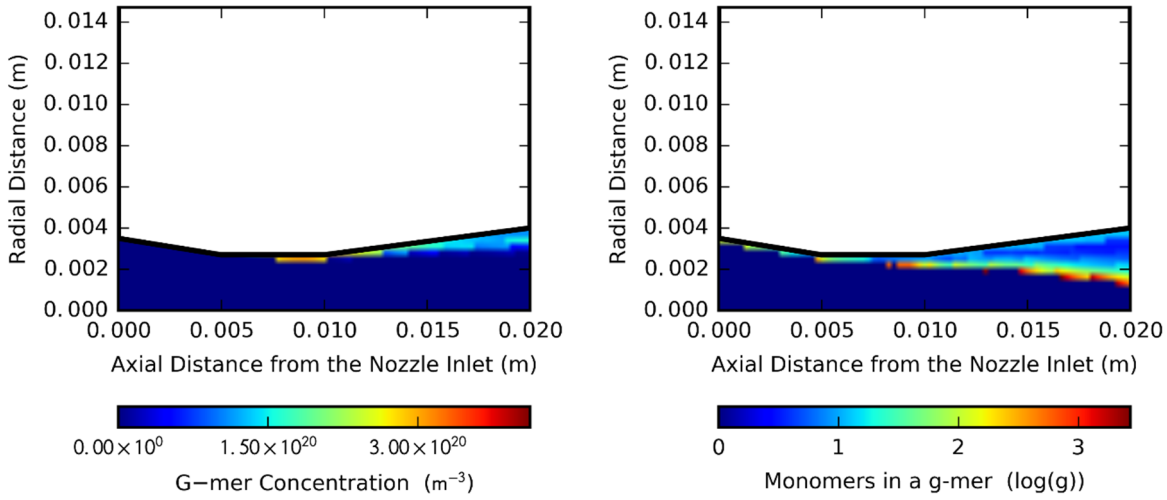

Figure 84: G-mer concentration and size inside of the expansion nozzle

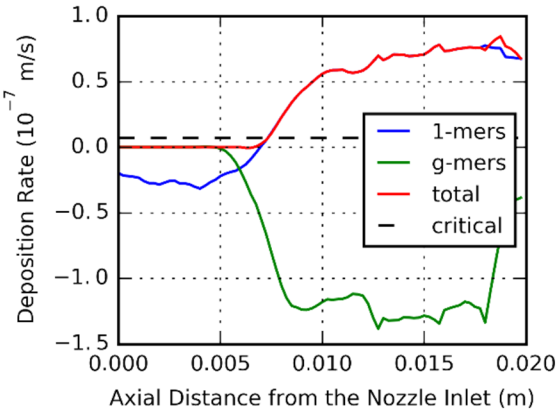

Figure 85: Expansion nozzle clogging rates

As a result, the calculations performed in the present section show that 10 cm length of the high pressure chamber is sufficient to avoid the melting of the expansion nozzle, convergence angle is not too steep and does not cause separation of the boundary layer. Nozzle diameter was refined to account for viscous forces. The refined dimensions of the expansion nozzle are highlighted in Table 18.

Table 18: Summary of refined dimensions of the expansion nozzle

Dimension	Convergent part	Cylindrical part	Divergent part
Length, mm	5.0	5.0	10.0
Maximal radius, mm	3.5	**2.7**	4.0
Angle, deg	**9.1**	0.0	**7.4**

IV.5. Nozzle Design Optimization

In this section we will try answering three questions:

- Is it possible to reduce nozzle clogging in the divergent region by variation of its divergence angle?
- How does the variation of the divergence angle and pressure in the low pressure chamber influence jet parameters?
- What is the optimal divergence angle for each fixed pressure?

With a set of linked 2D-CFD, DSMC and nucleation and growth models, a number of calculations were performed for various parameters listed in Table 19. Divergence angles were varied from 0° to 90° with a step ~30° by changing the maximum radius and length of the divergent part of the nozzle but preserving its length at 10 mm if possible. The angles beyond 36° were considered at the expanse of the total length. More angles were considered in the 0°-36° segment, since more accurate trends in this region were desired for better design justification. Cases beyond 36° were studied to get a better understanding of supersonic jet physics.

Two pressures were explored. 100 Pa was chosen since it represented a typically used pressure in PS-PVD processes. 1,000 Pa was selected since that was the minimal pressure achievable with pumps that comply with ATEX EU directive on equipment that involves work with explosive atmospheres, like SOGEVAC SV630 BF produced by Leybold GmbH, Germany. Pumping speed characteristics of SV630 BF are shown in Figure 86. The pump has a so-called gas ballast feature that prevents condensation inside the pump. However, the use of this feature restricts minimal achievable pressure to 100 Pa and pumping speed to 100 m^3/h or 0.36 g/s (if gas temperature is 300 K). For the chosen plasma torch parameters, the mass flow rate through the expansion nozzle is too high (1.29 g/s), thus reaching 100 Pa is impossible. Nevertheless, with SV630 BF it is possible to maintain higher pressures. The desirable pumping speed could be reached under 1,000 Pa.

2D CFD simulations were performed for various nozzle geometries. For each nozzle geometry, nucleation and growth and deposition processes were analyzed following the example described in the previous section. Following to the guidelines for DSMC simulations presented in III.3.3 (p.108), the results of 2D CFD simulation on the outlet from the expansion nozzle were used to impose boundary profiles on the low pressure chamber inlets for DSMC

simulations. The profiles are listed in Annex C. CFD solution was assumed to be accurate up to the nozzle exit, based on the verification results presented in the previous chapter (III.3.4.2 p.111). The assumption was later confirmed by analyzing the resulting Kn number distributions. Presence of nuclei on DSMC inlets was neglected and corresponding mass of vapor molecules was introduced instead based on the results from the previous section which showed that 75% of zirconia stays in the vapor phase and cluster size is close to the size of a single molecule.

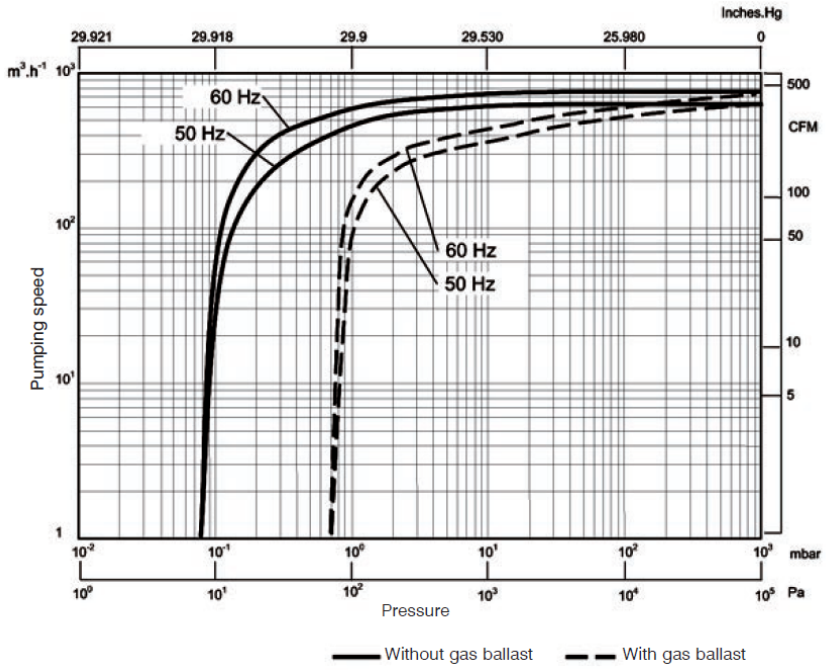

Figure 86: Pumping speed characteristics of SOGEVAC SV630 BF [169]

Table 19: List of the varied parameters of the expansion nozzle and low pressure chamber

Case ID	HPC pressure $p_{LPC,}$, Pa	Divergence angle α_{div}, deg	Outlet radius r_{out}, mm	Divergent part length L_{div}, mm
N00L	100	0.0	2.7	10.0
N07L	100	7.4	4.0	10.0
N16L	100	15.6	5.5	10.0
N36L	100	36.1	10.0	10.0
N68L	100	67.9	15.0	5.0
N90L	100	90.0	2.7	0.0
N00H	1,000	0.0	2.7	10.0
N07H	1,000	7.4	4.0	10.0
N16H	1,000	15.6	5.5	10.0
N36H	1,000	36.1	10.0	10.0
N68H	1,000	67.9	15.0	5.0
N90H	1,000	90.0	2.7	0.0

IV.5.1. Study of Nozzle Clogging Rate Dependency on Divergence Angle

The flow leaving the nozzle was supersonic and under-expanded for all 12 cases. Because of that, pressure set in HPC had no influence over the flow conditions inside the nozzle. Thus, instead of 12 cases, only first six were considered. Figure 87 contains nuclei number density fields inside the expansion nozzle for various divergence angles.

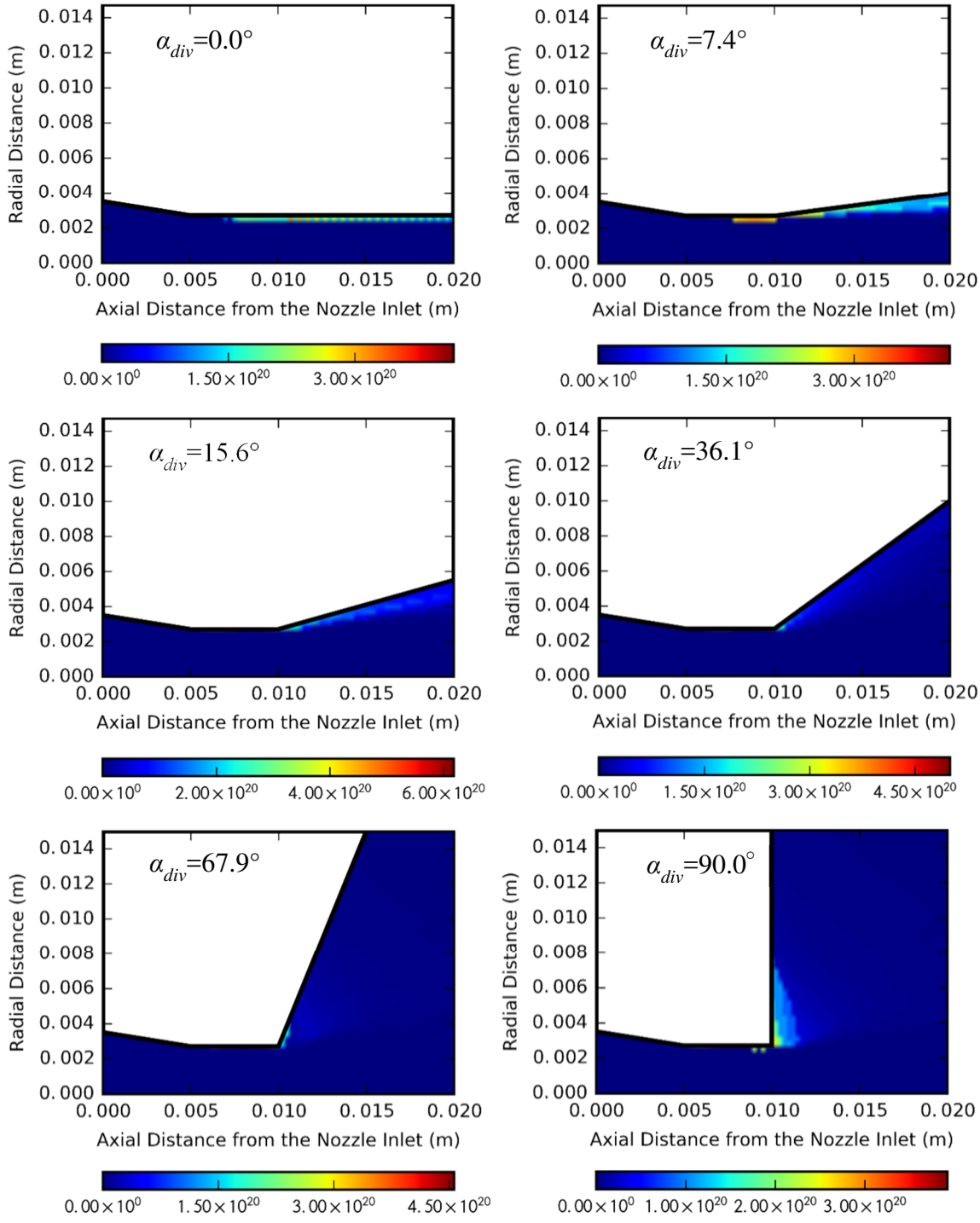

Figure 87: G-mer concentration inside of the expansion nozzle

As was observed in the preceding section, nuclei formation and growth happen exclusively in the wall vicinity, where the temperature is the lowest and supersaturation is the highest. Even though a faster temperature decrease associated with α_{div} increase leads to higher

supersaturations, it also reduces the equilibrium monomer concentration for saturated vapor, which has a strong influence over the nucleation rate (see eq. (104)). An increase of α_{div} leads to a reduction of nucleation and growth rates resulting in a lower nuclei content and size on the nozzle outlet. Figure 88 contains nuclei size fields expressed in the number of composing zirconia molecules inside the expansion nozzle for various divergence angles.

Note, that even though Figure 88 indicates the presence of bigger nuclei in regions closer to the axis in the proximity of outlets, their concentration is negligible. Clogging rates for different nozzle geometries are shown in Figure 89.

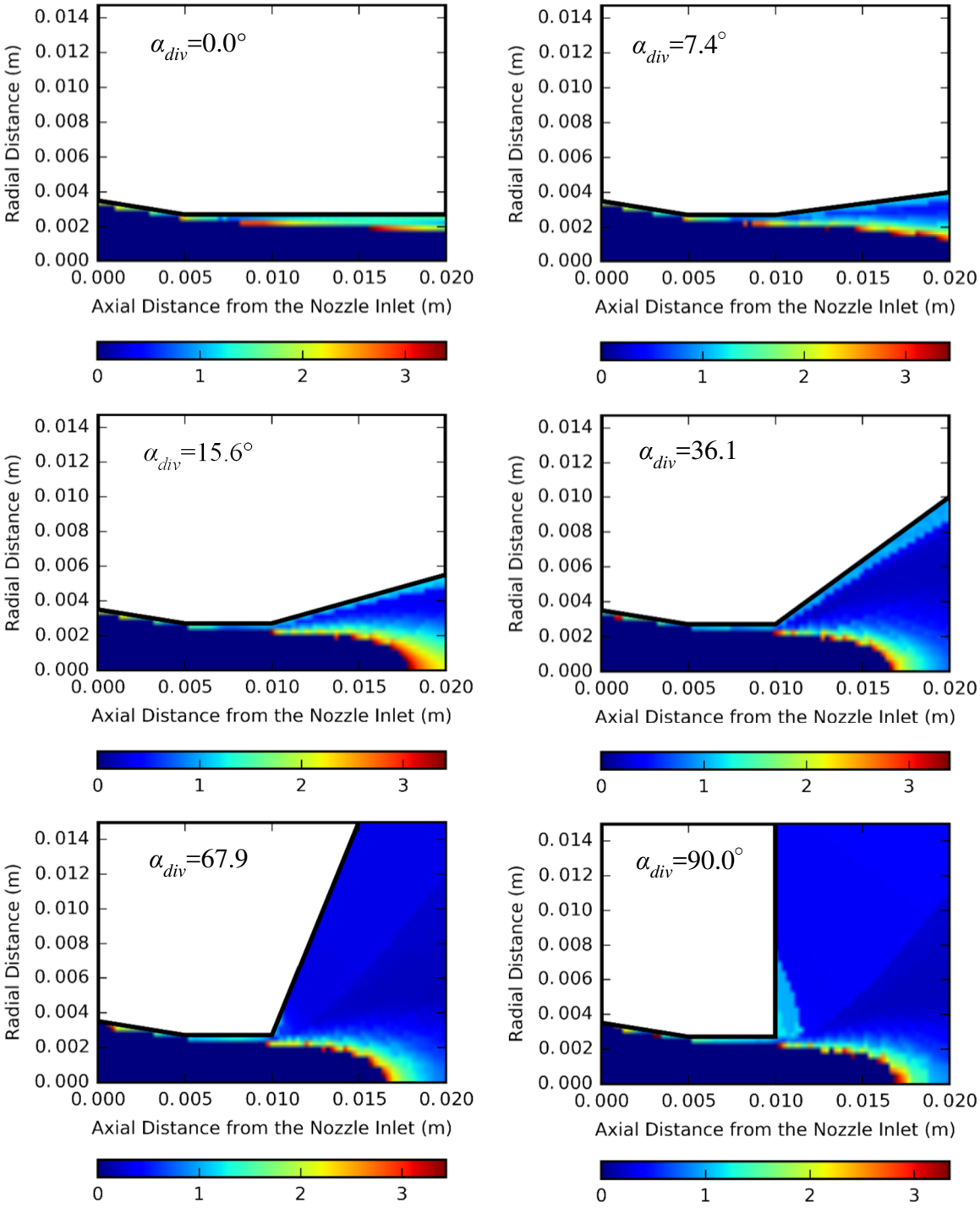

Figure 88: Logarithm of number of monomers in a g-mer

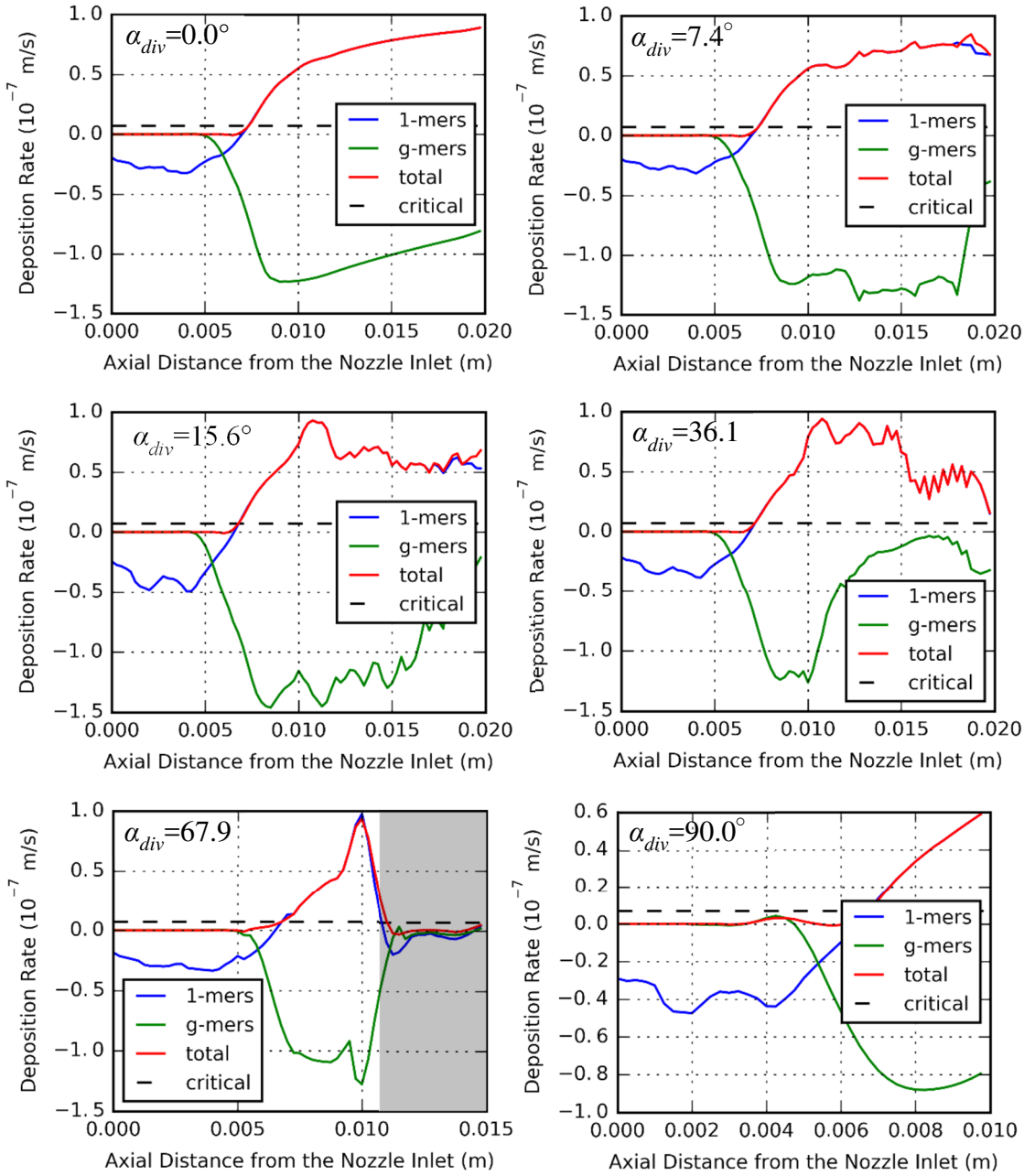

Figure 89: Nozzle clogging rates. Gray region indicates the low accuracy of the results

Larger divergence angle reduces monomer and g-mer number density in the divergent part, contributing to the reduction of clogging rates as well. The minimal clogging rate is observed for α_{div}=67.9°, however, this result is doubtful due to high errors caused by the chosen interpolation technique (see III.2.3.2.c, p.104). The shortcomings of this technique start being apparent at α_{div}=36.1° manifesting themselves in numerical noise. Thus, among 2 cm long nozzles (α_{div}=0.0°…36.1°), the ones with greater divergence angle exhibit lower clogging rates.

Another effect caused by divergence angle α_{div} increase is the decrease of g-mer flux from the wall surface. Gradual flow cooling and expansion create conditions that favor nucleation and growth in the areas located closer to the nozzle axis, as can be seen in Figure 88. This reduces nuclei concentration gradients causing the reduction of g-mer diffusion flux in the direction from the wall towards the nozzle axis. For α_{div} equal 15.6° and 36.1° g-mer flux approaches zero,

suggesting that for longer nozzles (> 2 cm) g-mers attracted by thermophoretic and diffusion forces could start contributing to nozzle clogging.

Figure 90-Figure 93 summarize the averaged results of the study discussed above. Figure 90 shows clogging rates averaged along cylindrical and divergent segments of the nozzle wall and divided by the critical clogging rate value. An increase of divergence angle slightly influences gas expansion in the cylindrical part of the nozzle ultimately increasing its clogging rates and decreases clogging rate of divergent parts.

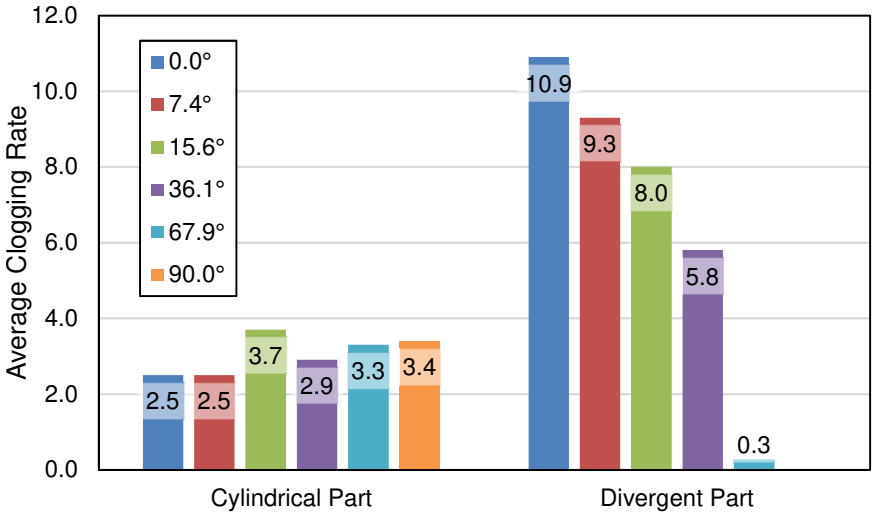

Figure 90: Average dimensionless clogging rates of nozzle walls

Figure 91 shows the average nucleus volume in the flow that leaves the nozzle. Nucleus volume is expressed in a number of composing monomers and nucleus size is its radius divided by the radius of a single zirconia molecule. Maximal cluster sizes are observed for straight nozzles, indicating that expansion caused by divergence angle increase favors evaporation of already formed g-mers.

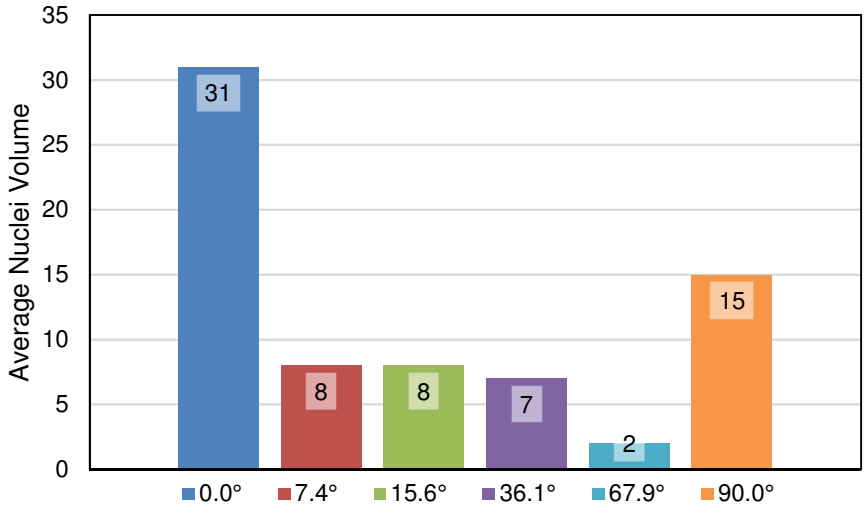

Figure 91: Average nuclei volume on the nozzle outlet expressed in a number of monomers per nucleus

Figure 92 shows how much zirconia have stayed in the vapor phase and was not converted to nuclei. These values were calculated as a ratio between monomer fluxes through the nozzle outlet and inlet. As shown above, an increase of α_{div} slows nucleation process down resulting

in higher vapor content in the jet issued from the nozzle. Together Figure 91 and Figure 92 show that g-mer content in the jet issued from the nozzle into the low pressure chamber is significantly lower than monomer content and resulting clusters are composed of the small amount of monomers and are likely to be evaporated under rarefied conditions of the LPC. Thus, in the following DSMC simulations cluster presence was not considered.

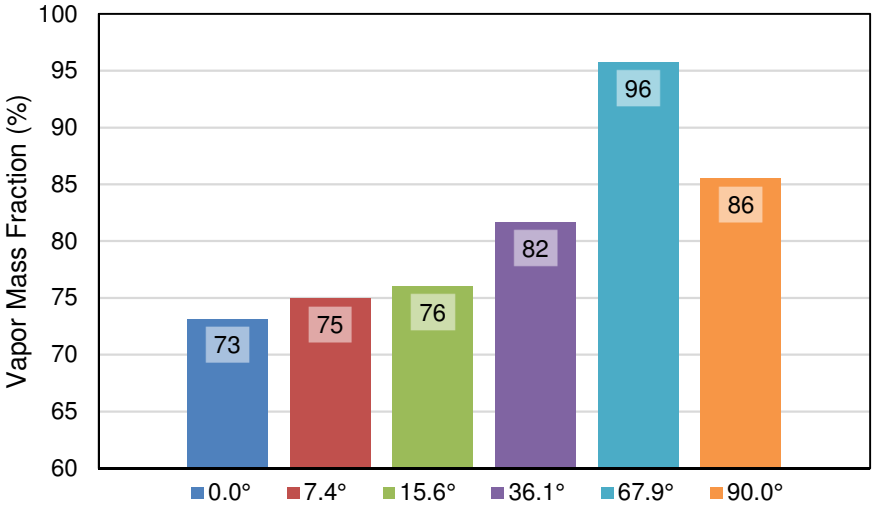

Figure 92: Fraction of zirconia mass that stayed in vapor phase upon reaching the nozzle outlet

Figure 93 shows the mass fraction of zirconia lost through vapor deposition to the nozzle walls. These values were calculated as a ratio between the integral deposition rate (in kg/s) and monomer mass flow rate through the nozzle inlet. This fraction generally increases due to the increase of the wall area of the divergent part and higher supersaturation due to lower near-wall temperatures. Thus, a nozzle with α_{div}=36.1° adsorbs the maximal amount of vapor, however, the magnitude of this loss is negligible in comparison with vapor flow rate through the nozzle. Vapor loss in the nozzle with α_{div}=67.9° is significantly underestimated due to underestimation of the corresponding clogging rate caused by significant underestimation of near-wall gradients triggered by re-interpolation errors (see III.2.3.2.c, p.104).

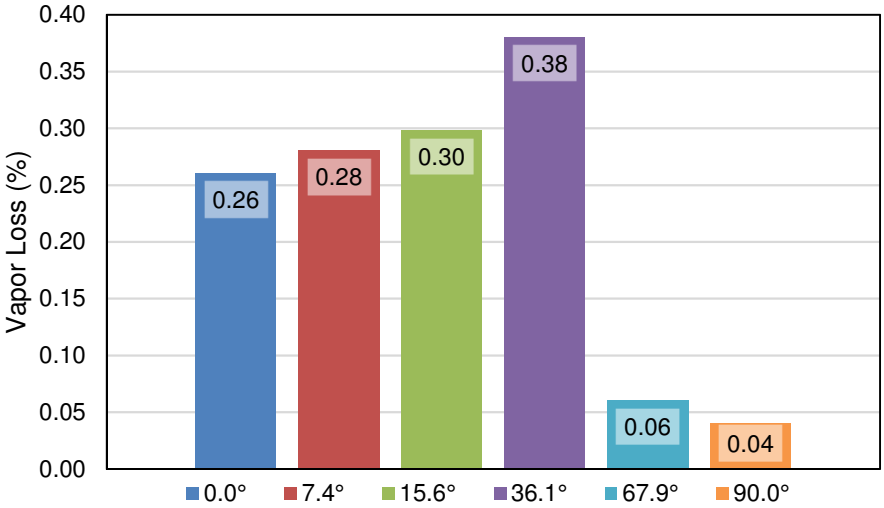

Figure 93: Fraction of zirconia mass that got adsorbed by the nozzle walls

The results presented in this section suggest that it is indeed possible to reduce clogging rates in the divergent part of the nozzle by increasing its divergence angle. Selecting a larger angle

like α_{div}=36.1° results in lower clogging rates. In addition, this leads to higher vapor concentration and smaller nuclei size on the nozzle outlet which is preferential for EB-PVD-like columnar coatings formation in the low pressure chamber. However, vapor content and monomer size and quantity may change before zirconia reaches the substrate – depending on the jet parameters dictated by chamber pressure and expansion nozzle shape, preliminary nucleation and growth may happen in the low pressure chamber upstream from the assumed substrate position. Even though there is no direct evidence that spray composition in terms of vapor to cluster content can influence the resulting coating microstructure, it can contribute to the understanding of deposition mechanisms and can be useful for deposition rate estimation.

IV.5.2. Study of Jet Structure Dependency on Divergence Angle

IV.5.2.1. Example Case Study

In order to present supersonic jet characteristics typical for the low pressure chamber, a default case N07L that corresponds to the initial nozzle (α_{div}=7.4°, r_{out}=4 mm, p_{LPC}=100 Pa) geometry described in IV.3.3 was studied.

The length of the simulated fraction of the low pressure chamber was selected to be 1 m, based on the structure spatial distribution model (I.3.4.3, p.35), since under classical PS-PVD conditions EB-PVD-like microstructures were observed at 1 m distance. Due to a lower jet temperate and thus higher supersaturation ratio in comparison with classical PS-PVD conditions, the formation of such microstructures was expected to start earlier in the jet regions closer to the expansion nozzle outlet (LPC inlet). Domain radius was set to 0.15 m due to the fact that typically observed PS-PVD jets (I.3.4.1, p.32 and I.3.4.4, p.36) do not exceed this size. The same dimensions were applied to all consequent simulations.

The dimensions used in the axisymmetric 2D DSMC model are shown in Figure 94 (proportions are not respected). The detailed description of the model is given in III.3.6 (p.117). The wall of the low pressure chamber was slightly extruded downstream to avoid possible artifacts caused by the generation of molecule velocity vectors in the tangential direction.

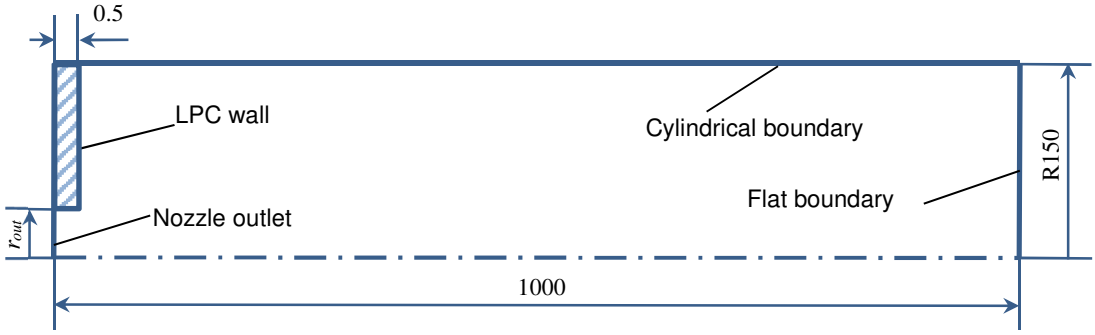

Figure 94: Dimensions of 2D DSMC model of the low pressure chamber (in mm)

Boundary conditions on the LPC inlet which corresponded to the expansion nozzle outlet were based on the results of preceding 2D CFD simulation and were calculated using the automated procedure, described in III.3.3 (p.108). Number density profile was derived from pressure and temperature profiles using ideal gas law, molar fractions of species were estimated using equilibrium compositions provided by P. André. The resulting boundary conditions are shown in Table 20. The resulting boundary profiles can be found in Annex C.

Table 20: DSMC boundary conditions for case N07L

Boundary	T, K	n, m^{-3}	v_x, m/s	v_y, m/s	x_{Ar}	x_{H2}	x_H	x_{Zr}	x_O	α
Nozzle outlet*	2,877	2.69×10^{22}	1,993	115	0.73	0.115	0.14	0.005	0.01	…
LPC wall	1,258	…	0.0	0.0	…	…	…	…	…	0.25
Cylindrical boundary	673	1.08×10^{22}	0.0	0.0	0.80	0.20	0.00	0.00	0.00	…
Flat boundary	673	1.08×10^{22}	0.0	0.0	0.80	0.20	0.00	0.00	0.00	…

*Radial profiles were set, averaged values are displayed for convenience.

Simulation results are shown in Figure 95. The resulting supersonic under-expanded flow contains several (~ 4) normal shock waves (Mach disks) with temperature varying from 300 to 4,000 K. Downstream fields are affected by setting zero velocity boundary condition that led to significant temperature increase near it. The jet core temperature decreases slowly and throughout the domain stays within 2,100 – 2,800 K interval. Pressure fluctuations that follow the initial expansion gradually reduce their amplitude from 30 – 300 Pa to 100 – 130 Pa. The selected boundary condition on the downstream flat boundary led to an increase of pressure in a small near-boundary area up to 300 Pa. Jet radius defined as the radius of supersonic region stays around 4 cm throughout the domain. In the jet core, gas velocity is maintained around 2,000 m/s and Mach number exceeds the sonic barrier throughout the entire length of the domain. As can be seen on the last figure, zirconia mass fraction deduced from the known zirconium and oxygen fractions stays in the range between 1 to 4% in the jet core and is negligible outside of it. Heavy zirconium molecules don't scatter far from the jet core preserving their initial trajectories along the jet axis. Lighter oxygen diffuses further to the jet fringe, however, the 1:2 ratio between zirconium and oxygen molecules is mostly preserved inside the jet, ensuring the possibility of stoichiometric zirconium dioxide formation. The ratio is shown in Figure 96. The stoichiometric "green" region roughly coincides with the supersonic region of the jet.

The resulting Knudsen number field shown in Figure 97 indicates continuum breakdown observed in the jet during its initial expansion and on the fringes of the jet due to high flow gradients in these areas (orange and red regions with $\mathrm{Kn}>0.05$). This confirms the necessity of DSMC utilization under the chosen conditions. Some statistical noise is visible in the figure at the periphery of the jet.

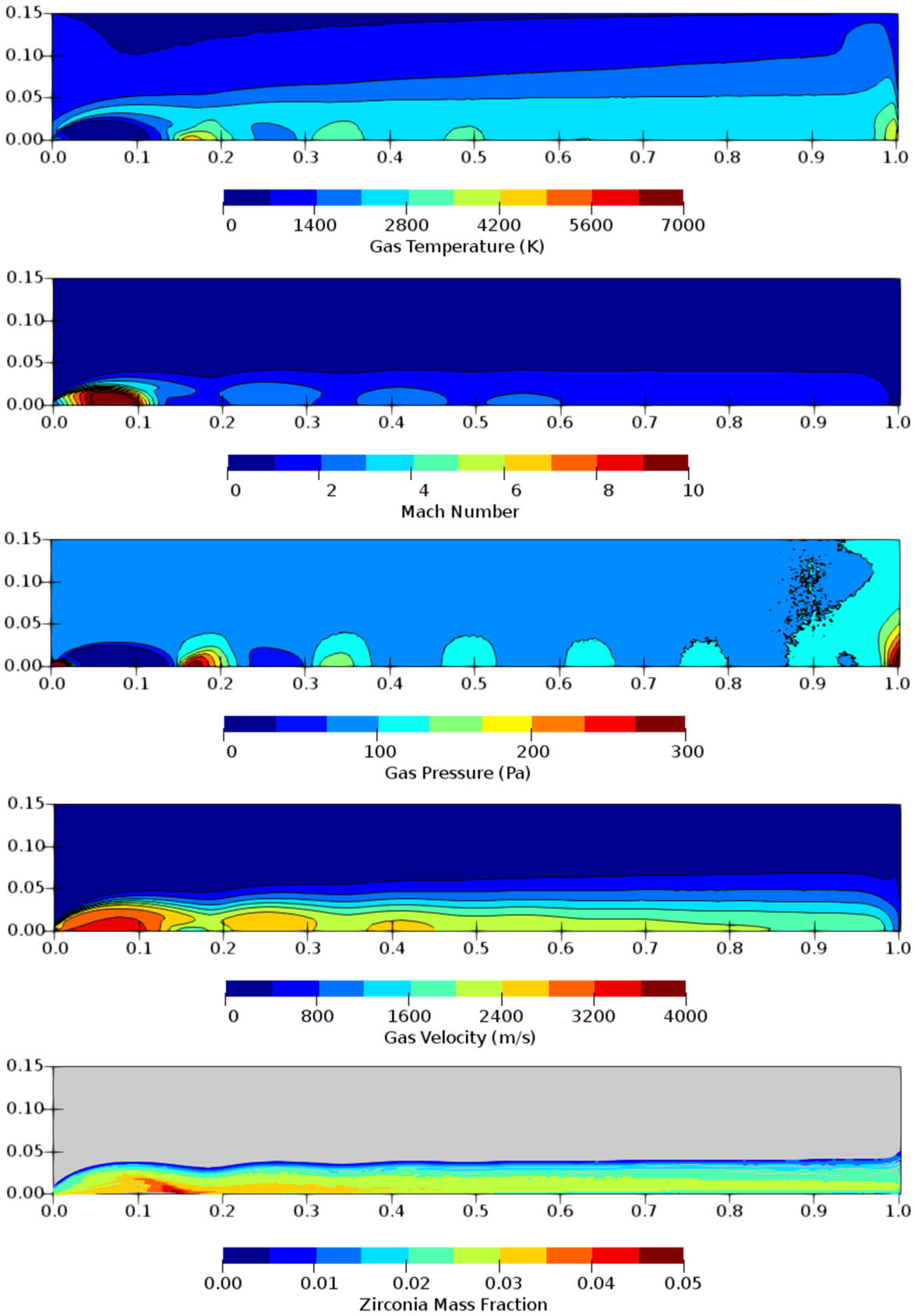

Figure 95: Results of 2D DSMC simulation for case N07L (α_{div}=7.4°, p_{LPC}=100 Pa)

Further calculations were performed by applying the nucleation and growth model along three streamlines emitted from the nozzle outlet/chamber inlet. The streamlines can be seen in Figure 98. The “blue” or “0” streamline was emitted along the axis, the “red”/“2” one – along the jet fringe, and the “green”/“1” – from the point located in the middle between the fringe and the axis.

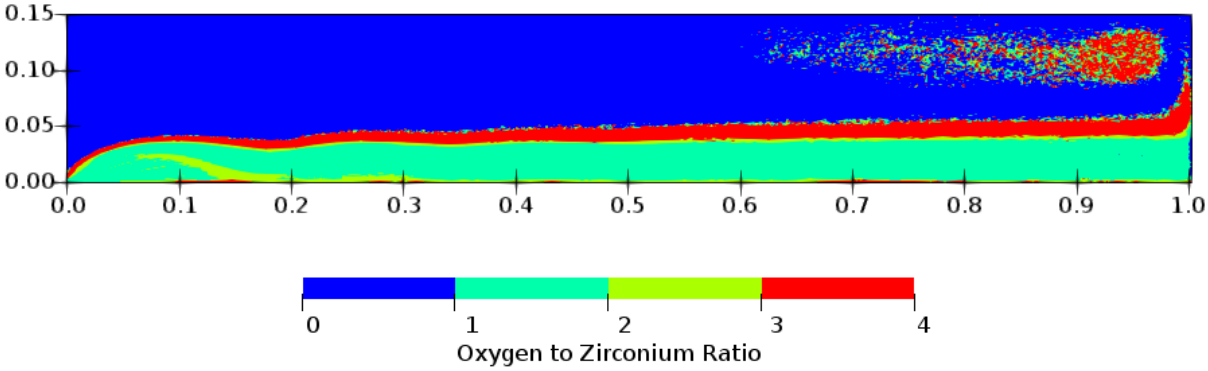

Figure 96: Oxygen to zirconium number density ratio in case N07L (α_{div}=7.4°, p_{LPC}=100 Pa)

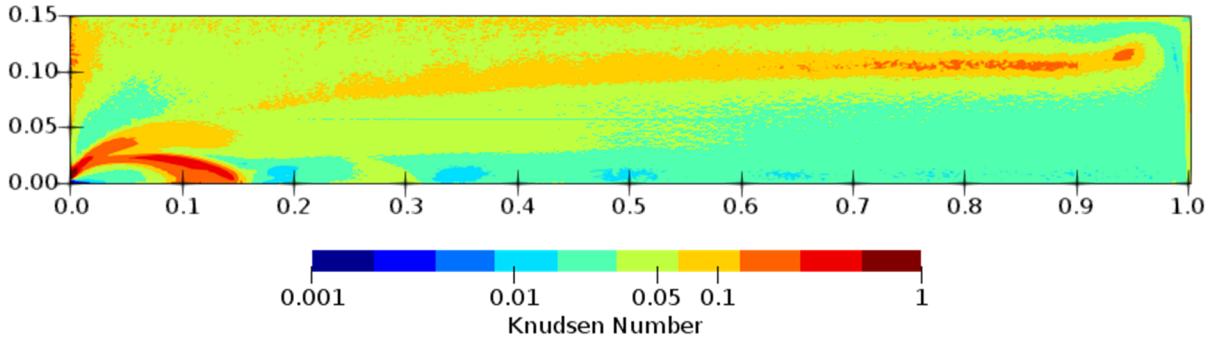

Figure 97: Knudsen number field in case N07L (α_{div}=7.4°, p_{LPC}=100 Pa)

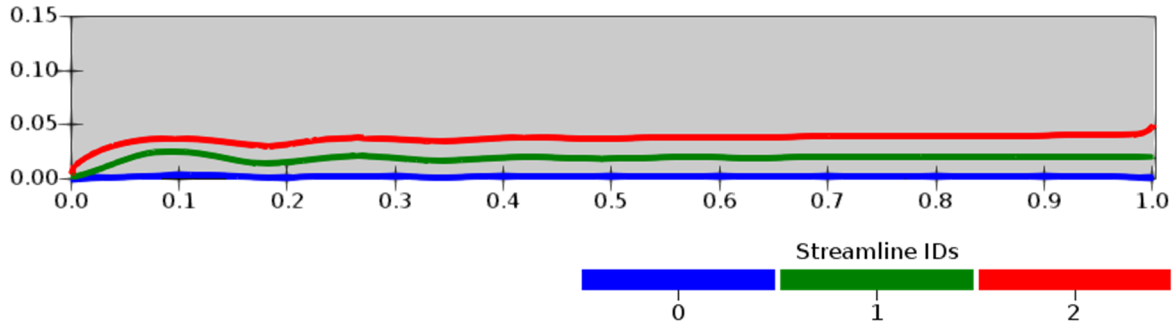

Figure 98: Streamlines used for nucleation and growth analyses in case N07L (α_{div}=7.4°, p_{LPC}=100 Pa)

Low temperatures and high supersaturations that are shown in Figure 99 create conditions preferable for nucleation (low temperature and high supersaturation ratio greater than unity). Along with the initial monomer concentration the curves indicate a high radial uniformity of conditions between “0” and “1” streamlines.

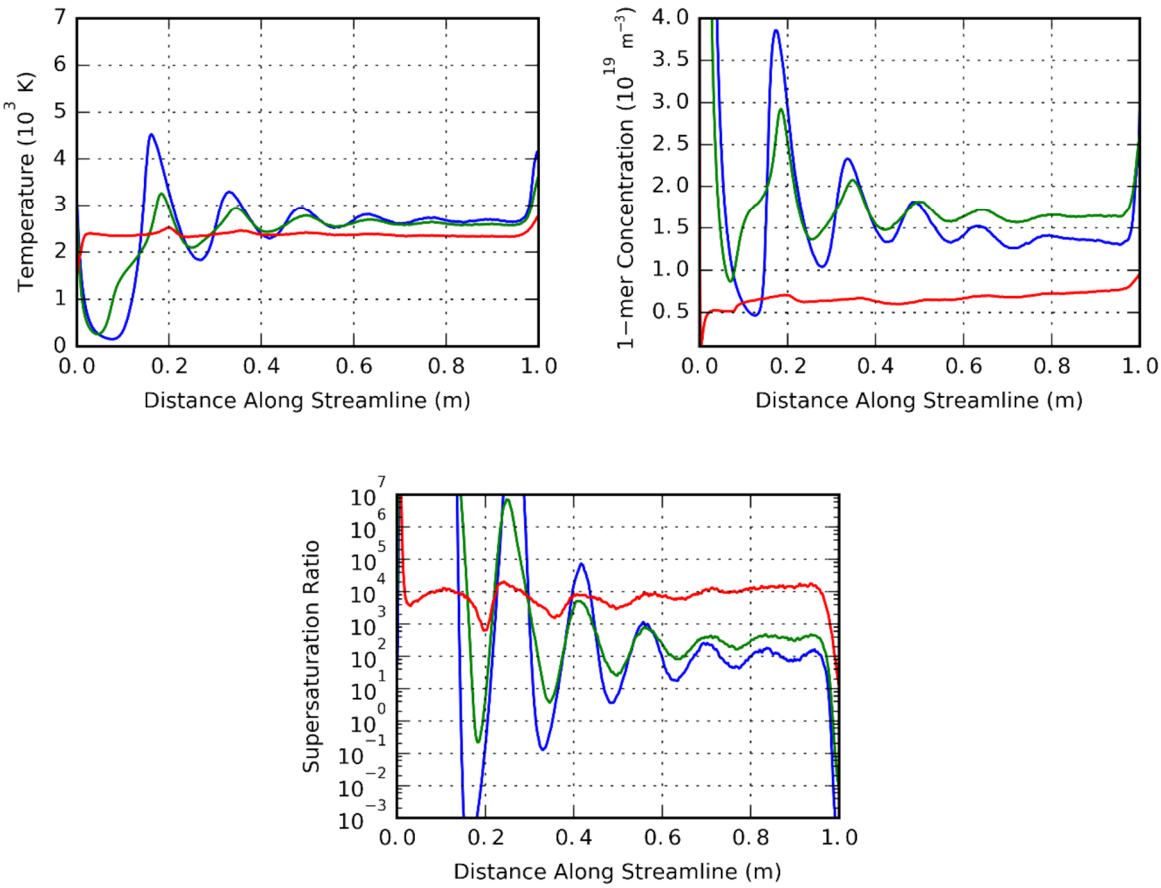

Figure 99: Temperatures, initial physical vapor number densities and supersaturation ratios along streamlines in case N07L (α_{div}=7.4°, p_{LPC}=100 Pa)

The results of nucleation and growth predictions along the streamlines are shown in Figure 100. Due to the rarefaction effects, the majority of the model assumptions (e.g. continuum, Maxwellian and Boltzmann equilibria assumptions) becomes invalid. Thus, these results should be treated with a grain of salt in the regions where this rarefaction occurs. The area where predictions can be invalid coincides with the continuum breakdown region discussed above and for the selected streamlines could be interpreted as the first 30 cm along them.

Initial expansion through the nozzle is accompanied by cooling and leads to high degrees of supersaturation, however, as indicated above, further expansion into the low pressure chamber results in a substantial rarefaction, and no nucleation or growth occurs due to a low collision frequency at the first stages. This effect can be noticed in the nucleation rate distribution along the initial regions of the streamlines – nucleation rates along the first 10 cm of “blue” and “green” streamlines are negligible. Due to the processes described in II.2.5.1 (p.59), the first Mach diamond located at 18 cm from the nozzle outlet is being formed by the compression fan. Temperature increase inside of the shock further delays the nucleation process.

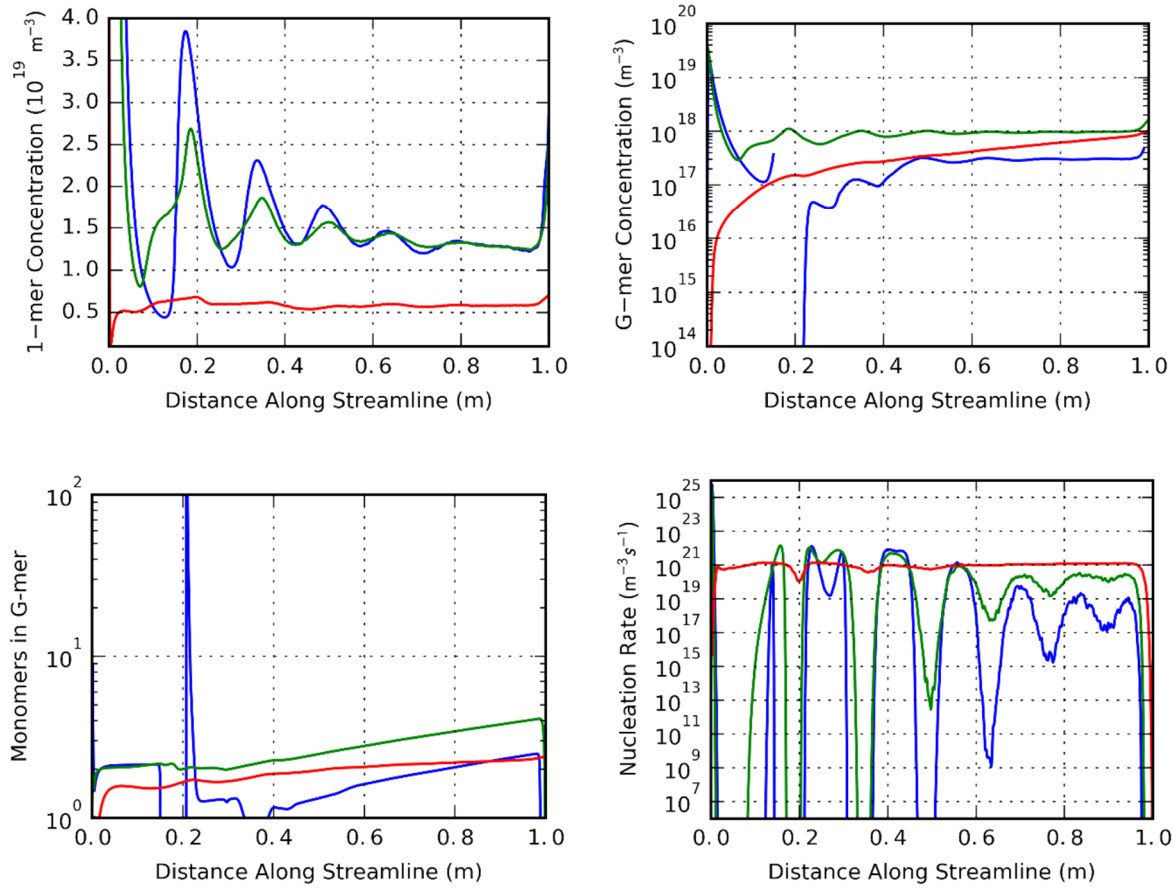

Figure 100: Resulting physical vapor concentrations, g-mer concentrations, g-mer sizes and supersaturation ratios along streamlines in case N07L (α_{div}=7.4°, p_{LPC}=100 Pa)

A peak in g-mer size observed at 20 cm from the inlet is caused by compression and monomer-g-mer collision frequency increase. This result could be neglected since the abrupt growth is followed by equivalently fast evaporation triggered by the subsequent expansion, resulting in the reestablishment of the pre-growth state. Discontinuity of g-mer concentration can be observed in the same region, indicating the violation continuum assumption used by nucleation and growth model. Thus, the results might not reflect the actual processes happening in this part of the jet.

Nucleation process downstream from the first shock (>20 cm from the inlet) is governed by temperature variations. The flow is characterized by alternating compression and expansion regions (and corresponding temperature peaks and minima). This time rarefaction effects are not prominent due to a lower amplitude of pressure variation. Accompanied by temperature decrease, each expansion leads to a noticeable increase of supersaturation ratio and nucleation rates. Similarly, each compression and temperature increase suppresses nucleation process. However, despite significant fluctuations, both supersaturation ratio and nucleation rate preserve relatively high values throughout the rest of the streamline leading to slow but steady nucleation and growth processes.

Nucleation and growth processes on the jet fringe flow slightly differently in comparison with regions closer to the axis. Due to higher supersaturations and less apparent shocks cluster formation and growth happen in a gradual, uniform manner. However, due to a low vapor

content resulting g-mer concentration and size do not differ drastically from the values reached in the jet core.

Nevertheless, the resulting zirconia flow is effectively indistinguishable from pure physical vapor – the maximal size of g-mers upon reaching the end of simulation domain does not exceed 3 monomers and g-mer concentration is 5-10 times lower than the one of monomers. Introduction of a cold substrate could facilitate nucleation and growth processes in its cold boundary layer leading to a significant reduction of vapor content.

So far, there are no studies that reveal a correlation between the cluster size and content and the resulting coating microstructure, however, it may be assumed that clusters due to a low surface mobility are likely to become centers of heterogeneous nucleation and coating growth, which is beneficial for the initial stages of coating formation.

In order to evaluate potential microstructures attainable in the present process, the structure zone model (SZM) discussed in I.3.4.2 (p.35) could be applied. Considering that physical vapor and nanocluster mix travel predominately along the streamlines, confined within an area 5 cm in radius, it is possible the estimate the impingement rate of zirconia molecules to a plate with the same radius. With the initial vapor mass flux ~10^{-4} kg/s the maximum impingement rate could reach 0.1 mol/s/m^2. With such a high value, the resulting microstructure according to SZM is determined by the surface mobility of the adatoms. Low temperatures of the jet (<4,000 K after 20 cm from the nozzle outlet) reduce the restrictions on the substrate positioning, allowing to place it at almost any point of the deposition chamber while maintaining any selected temperature. This allows the control over adatom surface mobility and over the resulting microstructure, which can be varied from feather-like columnar for low substrate surface temperatures (<0.65T_{melt}) to compact columnar at higher substrate surface temperatures.

IV.5.2.2. Low Pressure Cases

In order to study the influence of the expansion nozzle design on the jet parameters, the approach demonstrated in the previous section was applied for the cases N00L – N90L described in Table 19. Simulation results are summarized in figures Figure 101 - Figure 104. The observations made for the case N07L in the previous section are valid for the remaining cases as well. Thus, the present section we will focus only on the general trends.

The increase of α_{div} leads to the increase of jet core temperature downstream from the shocks with a maximum at α_{div} =67.9°. Higher jet core temperature leads to lower radial uniformity of the temperature field. The jets obtained with α_{div} =36.1° and α_{div} =67.9° have the biggest radii. The latter, however, is slightly less uniform radially in terms of temperature and more uniform in terms of physical vapor content due to high initial radial velocity components of the jet.

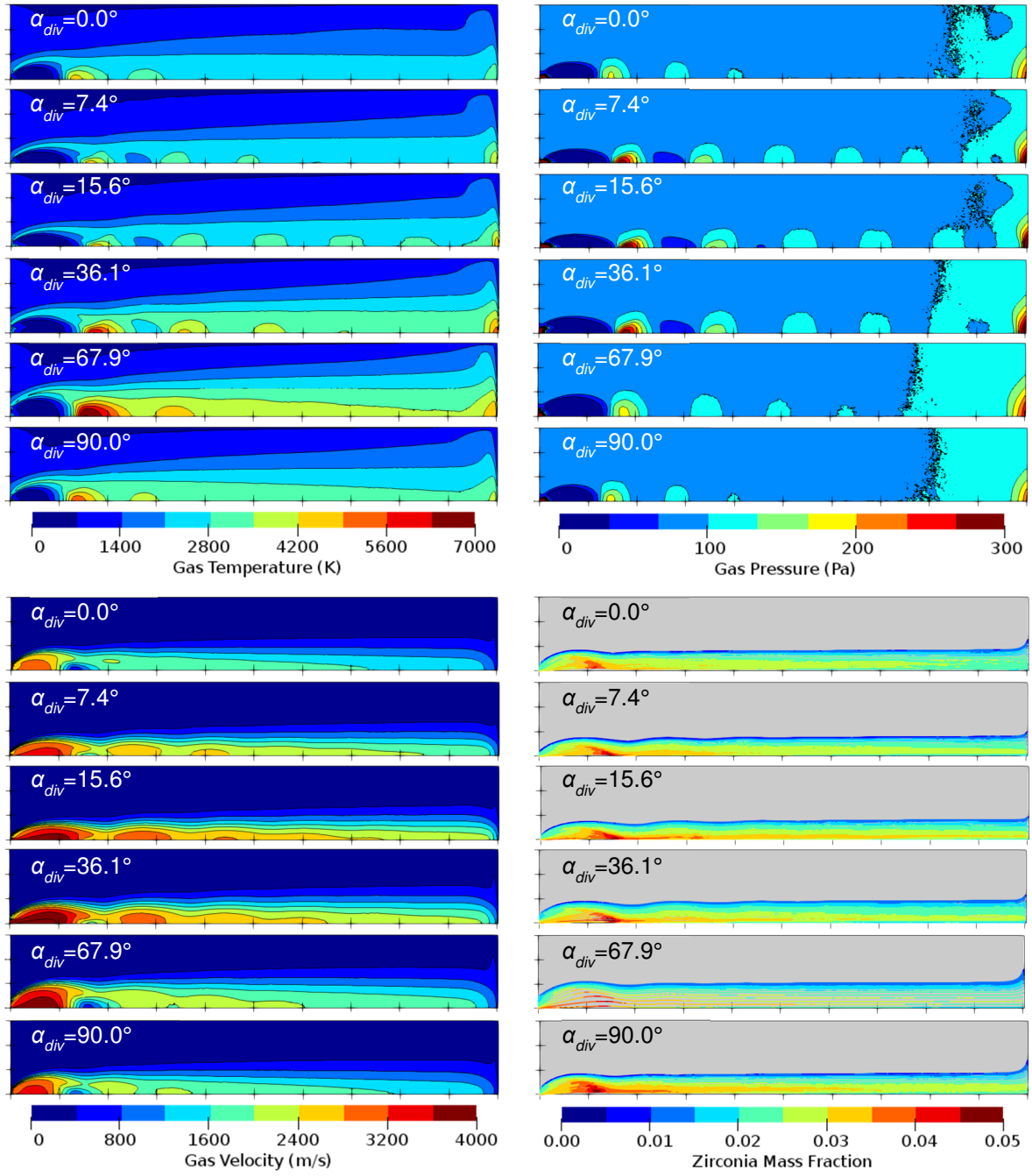

Figure 101: Results of 2D DSMC simulations for p_{LPC}=100 Pa cases

The case N90L with 90° divergence angle appeared to be qualitatively similar to the case with zero divergence angle. Indeed, since the shape of the jet is mostly determined by the shape of the nozzle and straight nozzles with α_{div} =0.0° and α_{div} =90.0° differ only in length, the resulting jets differ only in maximal temperature due to higher heat loss in the longer (α_{div} =0.0°) nozzle. The fields in the case N68L with α_{div} =67.9° also resemble the ones typical for α_{div} =90.0° case due to the flow separation that happens in the divergent part of the nozzle.

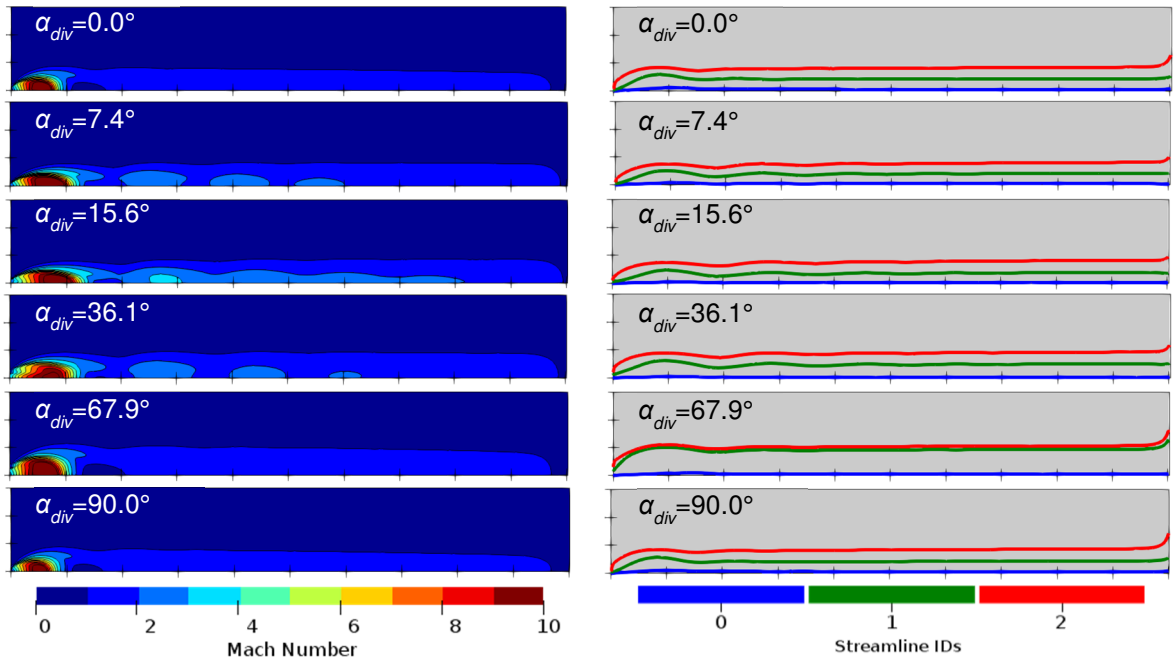

Figure 102: Resulting Mach number fields and streamlines for nucleation and growth predictions for p_{LPC}=100 Pa cases

Figure 102 shows the streamlines used for nucleation and growth predictions. Temperatures along corresponding streamlines, as well as the initial monomer concentrations and resulting supersaturation ratios are shown in Figure 103. The results of nucleation and growth modeling including the resulting monomer and g-mer concentrations and g-mer sizes are shown in Figure 104. In cases with high divergence angles (α_{div} =36.1° and α_{div} =67.9°), where the vapor is spread over a bigger volume and jet core temperatures are the highest, supersaturation ratios in the jet core barely exceed unity, making nucleation process impossible. In contrast, the other cases favor nucleation process, however, the resulting g-mer content is still significantly lower than the one of physical vapor, and g-mer size never exceeds 4 monomers (except from the case with α_{div} =90.0° where intense growth occurs, however the concentration of g-mer stays negligible).

Combining the results produced in the present section with the ones obtained in 2D CFD + N&G simulations, the case N36L with the divergence angle equal to 36.1° seems to be the most favorable among the considered cases, since it favors minimal nozzle clogging rates while contributing to the formation of radially uniform coatings. The case N68L with α_{div} =67.9° seems to be promising as well, but the accuracy of the predictions provided by nucleation and growth model does not allow to make a definitive conclusion. The further studies to optimize the process should be focused on a narrower set of divergence angles around 36°.

The preferable substrate position in PS-PVD is usually limited by the jet temperature. However, in the proposed system, due to the additional heat losses through the nozzle walls (~10% of the initial electric power), the substrate could be placed closer to the nozzle outlet. The only consideration that should be taken into account – the proximity of the barrel shocks since their position can oscillate due to arc voltage fluctuations inside of the plasma torch, resulting in temporal non-uniformity of jet parameters in the substrate boundary layer. For the preferable case N36L, the location where the barrel shocks weaken is at about 60 cm from the nozzle outlet.

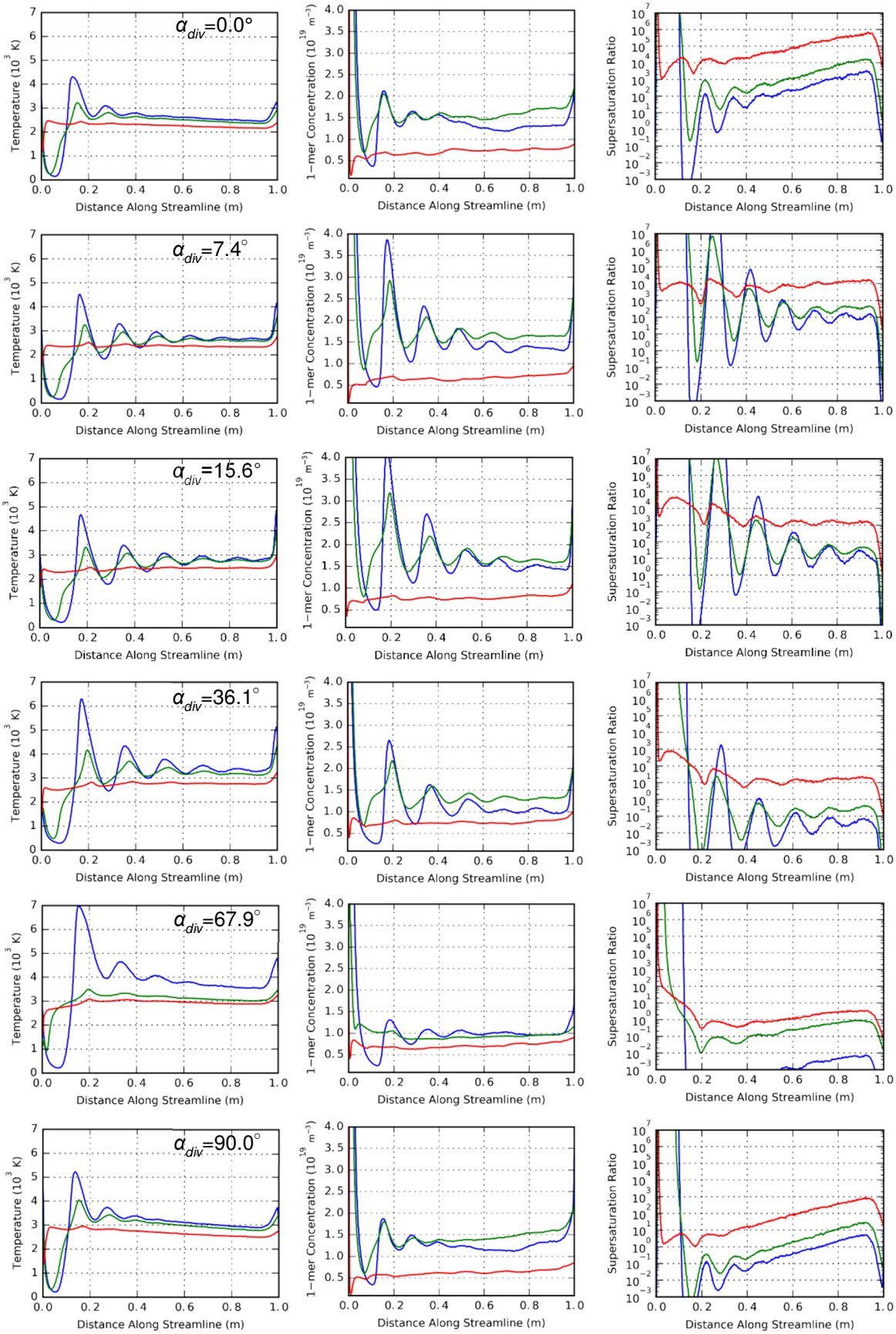

Figure 103: Temperatures, initial physical vapor number densities and supersaturation ratios along streamlines (p_{LPC}=100 Pa)

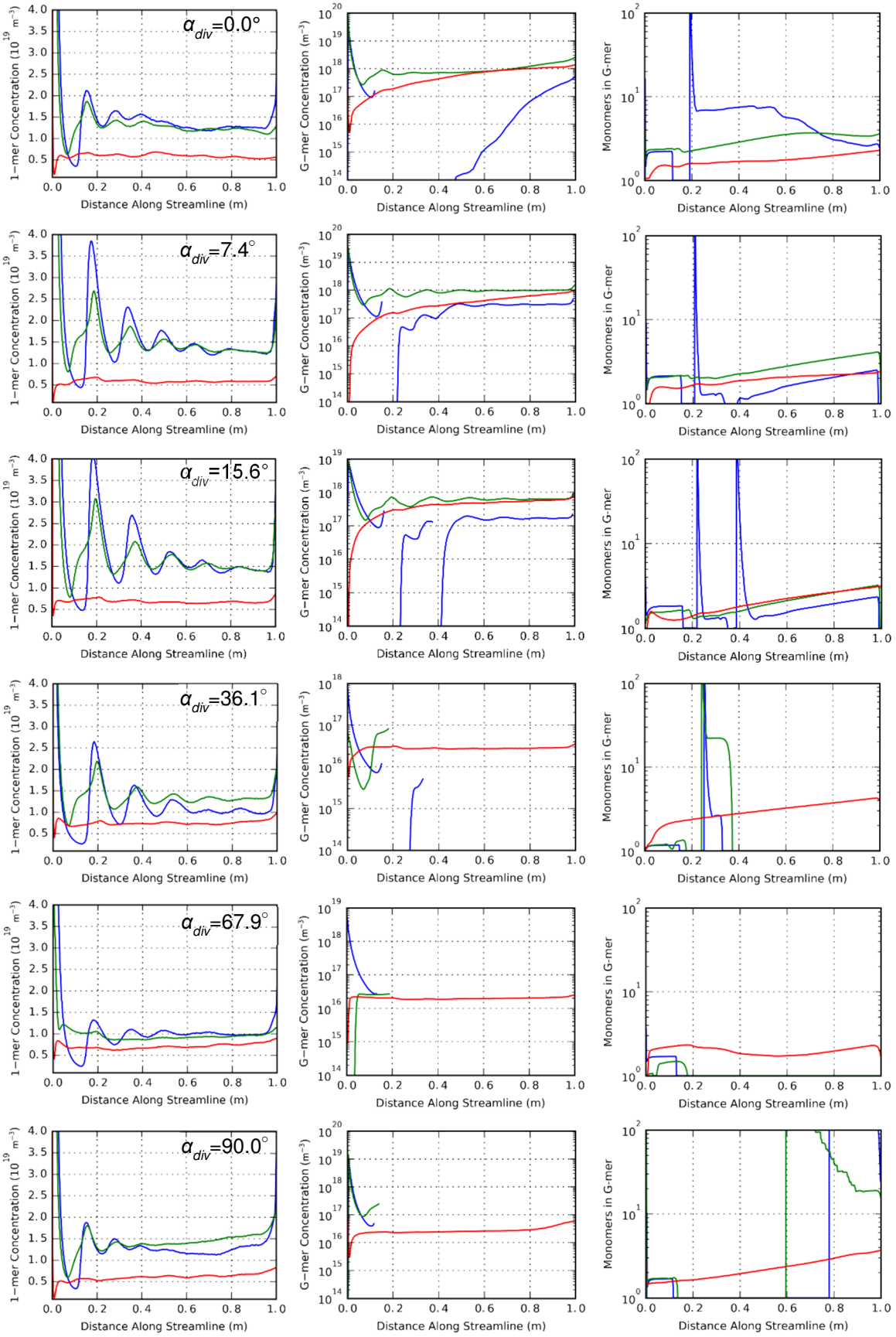

Figure 104: Resulting physical vapor concentrations, g-mer concentrations and g-mer sizes along streamlines for p_{LPC}=100 Pa cases

IV.5.2.3. High Pressure Cases

In order to comply with the restrictions made on the vacuum pump, a set of cases with p_{LPC}=1,000 Pa was considered. The study was conducted using DSMC approach. As shown in Figure 105, a continuum breakdown region (Kn>0.05) is present, making the predictions of CFD approach doubtful. However, since the region is confined within a small area near the nozzle outlet, the error brought by the breakdown might be negligible.

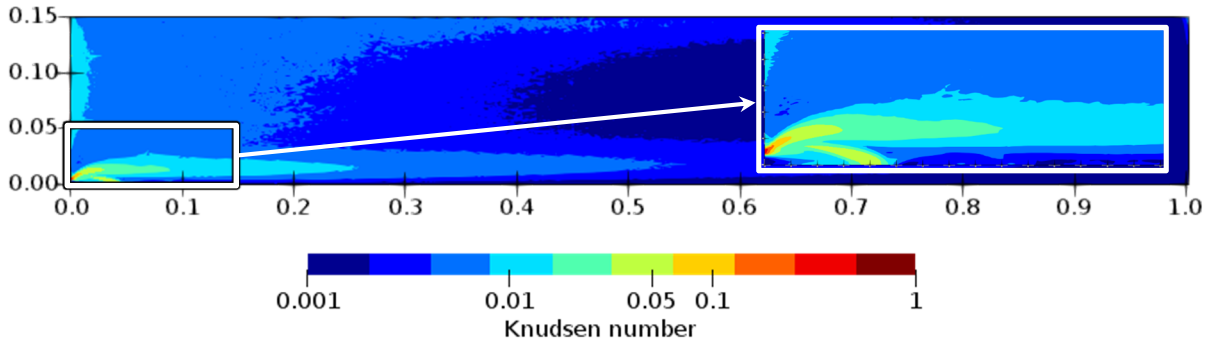

Figure 105: Knudsen number field in case N07H (α_{div}=7.4°, p_{LPC}=1,000 Pa)

The results are shown in figures Figure 106 - Figure 109. The majority of observations concerning the jet shape for the cases N00L-N90L are still valid for the cases N00H-N90H. The major difference from the preceding cases is the scale of the jet which became 4 times smaller. The jet radius decreased from 4 cm at 100 Pa to approximately 1 cm at 1,000 Pa. The same happened with the positions of normal shocks – the first Mach disk moved from 12 cm from the nozzle outlet to approximately 4 cm from the nozzle outlet. Such behavior was confirmed empirically in the study of C.H. Lewis [170] who showed that the distance to the first normal shock is proportional to $\sqrt{p_{out}/p_{LPC}}$, where p_{out} is the pressure on the nozzle outlet. According to this empirical relation tenfold increase of the chamber pressure should result in roughly 3.2 times decrease of the distance to the shock.

As a result, the same conclusions regarding the preferential divergence angle at 100 Pa could be applied at 1,000 Pa as well. The divergence angle α_{div} =36.1° seems to be the best among the considered angles in terms of the jet width. For the preferable case N36H, the preferable substrate location where the barrel shocks weaken is about 20 cm from the nozzle outlet.

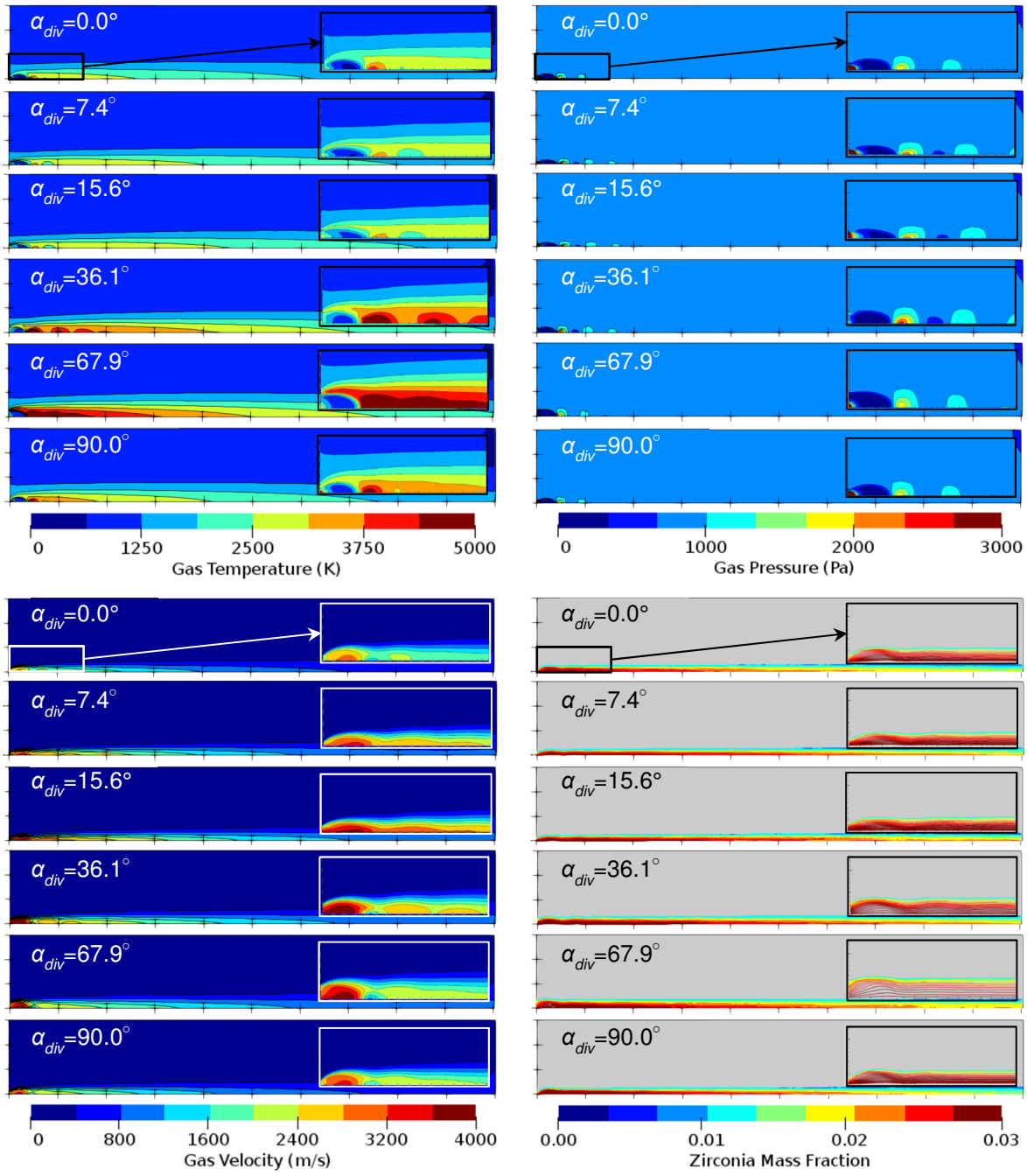

Figure 106: Results of 2D DSMC simulations for p_{LPC}=1,000 Pa cases

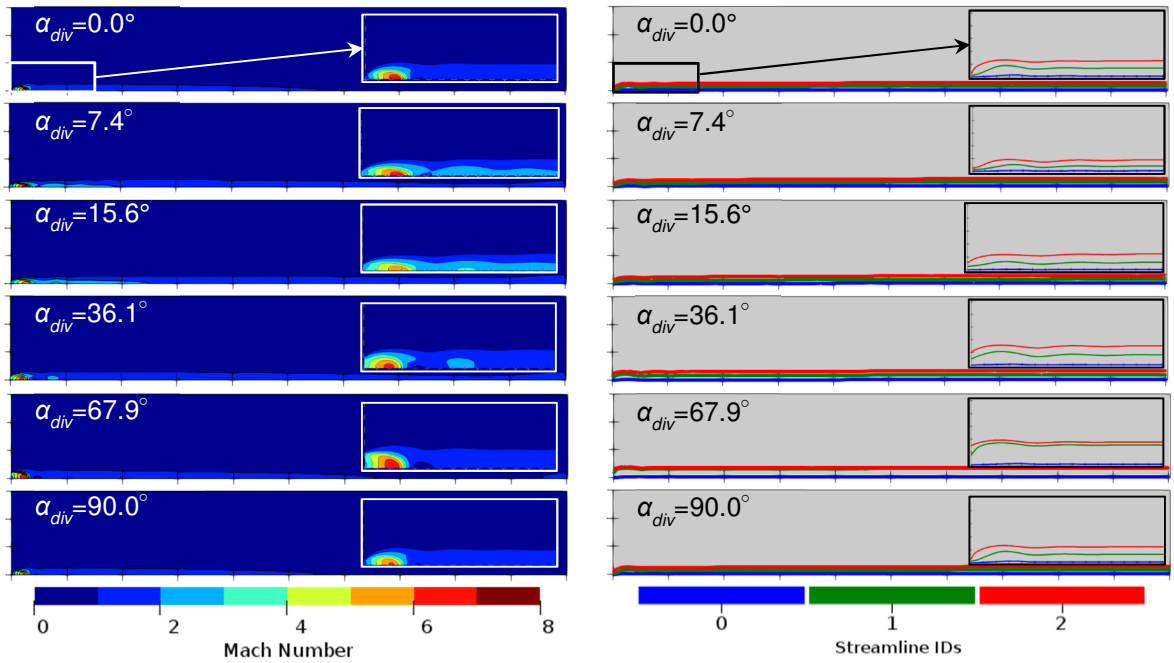

Figure 107: Resulting Mach number fields and streamlines for nucleation and growth predictions for p_{LPC}=1,000 Pa cases

Figure 107 shows the streamlines used for nucleation and growth predictions. Temperatures along corresponding streamlines, as well as the initial monomer concentrations and resulting supersaturation ratios are shown in Figure 108. The results of nucleation and growth modeling including the resulting monomer and g-mer concentrations and g-mer sizes are shown in Figure 109.

Unlike 100 Pa cases, due to lower temperatures more intense nucleation and growth are observed. In the majority of cases, the entire volume of physical vapor converts to clusters upon reaching 60 cm from the nozzle outlet. In cases with high divergence angles (α_{div} =36.1° and α_{div} =67.9°), where the vapor is spread over a bigger volume and jet core temperatures are the highest, the physical vapor is present in the jet up to 80 cm from the nozzle outlet. The resulting clusters contain at least 10 monomers.

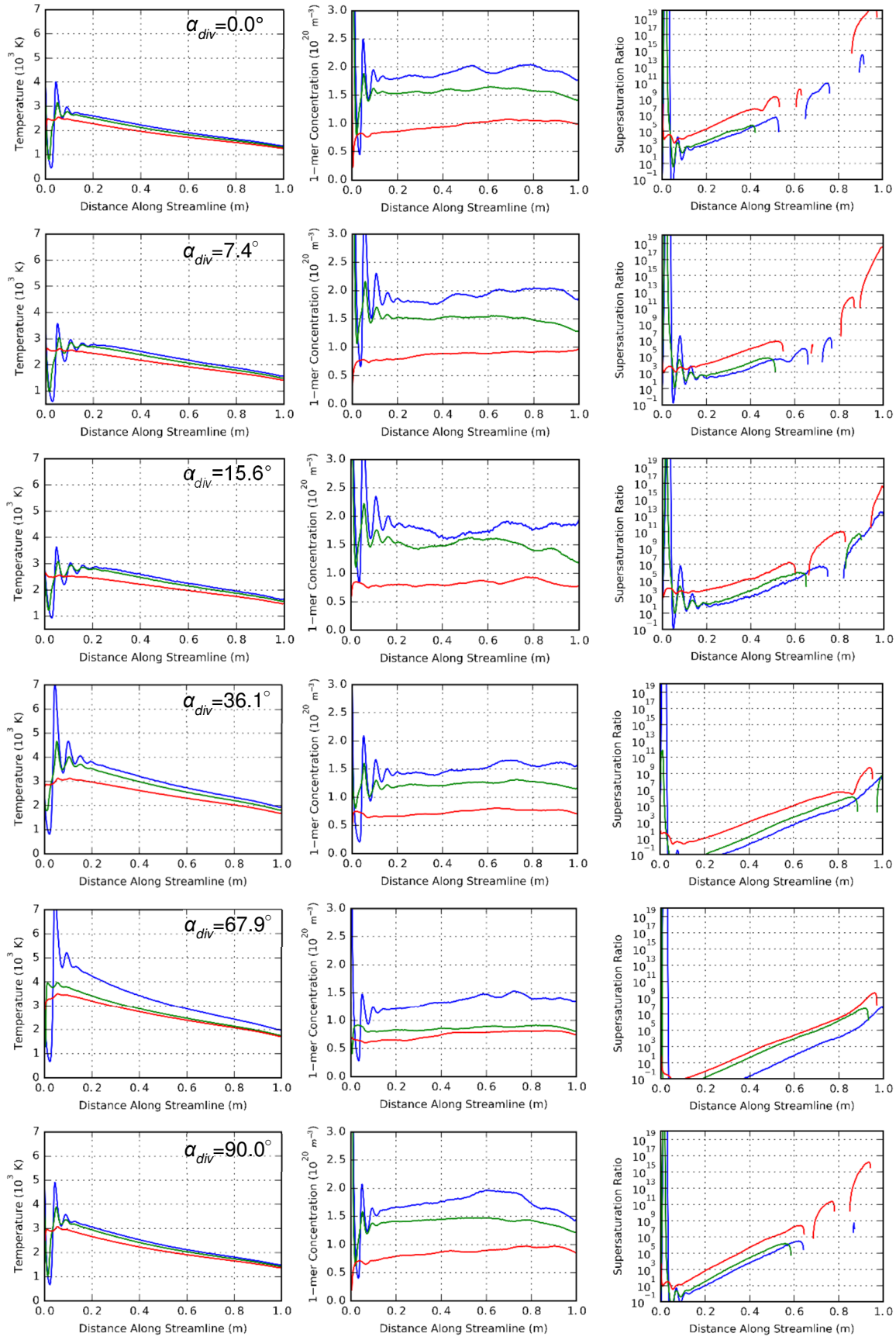

Figure 108: Temperatures, initial physical vapor number densities and supersaturation ratios along streamlines (p_{LPC}=1,000 Pa)

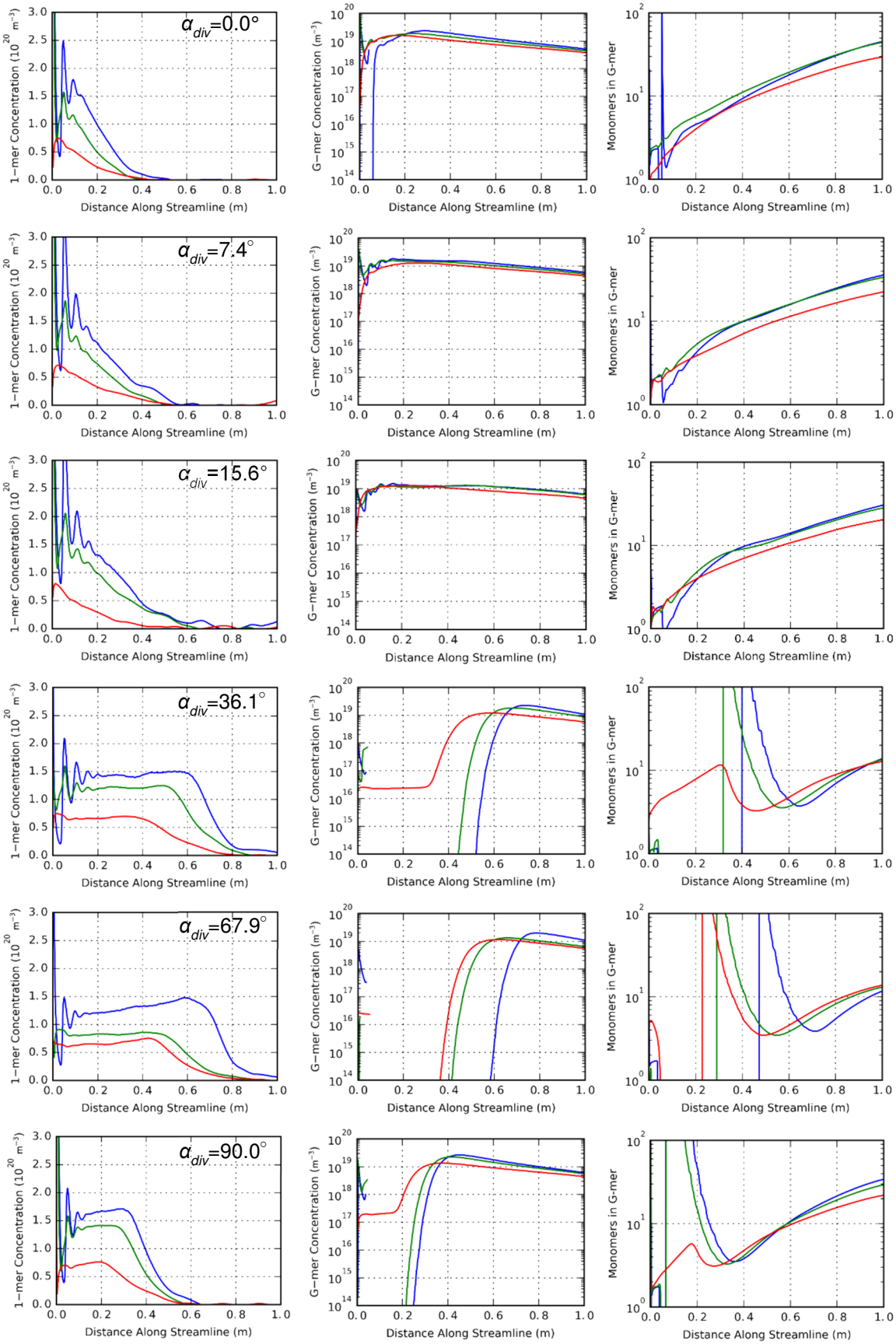

Figure 109: Resulting physical vapor concentrations, g-mer concentrations and g-mer sizes along streamlines for p_{LPC}=1,000 Pa cases

IV.6. Conclusion

In this chapter, an attempt has been made to design and optimize the hybrid CAPS-PS-PVD process. Plasma torch parameters have been chosen to favor vapor formation, high pressure chamber length was selected to maximize vapor content and avoid nozzle wall melting. And, finally, nozzle geometry was interactively adjusted to minimize clogging and produce a wide and uniform supersonic jet at various pressures maintained in the low pressure chamber.

The high pressure chamber length was estimated to be 10 cm. The resulting nozzle dimensions are shown in Figure 110. It was revealed that for both 100 Pa and 1,000 Pa the same nozzle with α_{div} =36.1° produces the jet with optimal parameters. This angle was deemed optimal, due to (i) gradual decrease of clogging rates of the divergent part associated with the divergence angle increase and (ii) because of the maximal jet radius that insured more structurally uniform coatings. It was revealed the first effect was caused by the diminished vapor concentration gradients that resulted in a smaller vapor flux towards the wall. The maximum of the jet radius appeared due to supersonic flow separation at higher divergence angles that was making the flow narrow and effectively indistinguishable from the low divergence angle cases.

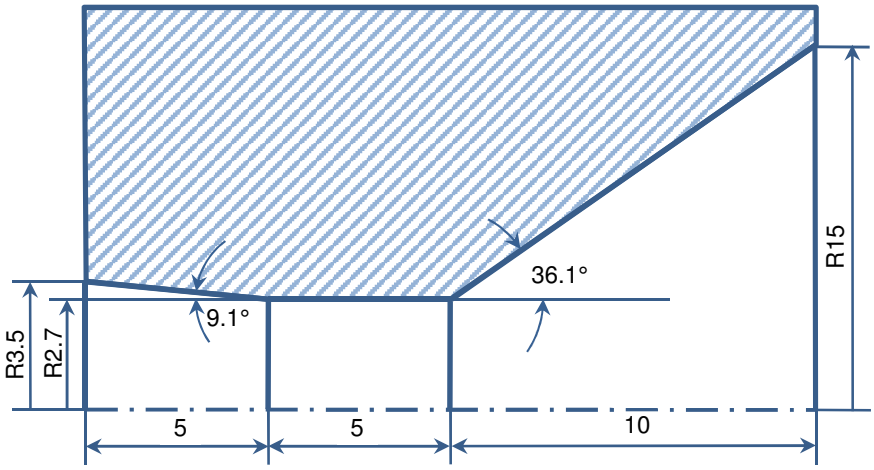

Figure 110: Refined expansion nozzle dimensions (in mm)

The system with the selected parameter was proven to be feasible with some restrictions on the duration of the expansion nozzle operation time due to possible clogging in the cylindrical and divergent parts.

The minimal distance to the substrate from the nozzle outlet has been estimated based in the barrel shock locations. For 100 Pa this distance is about 60 cm, and for 1,000 Pa case, it is about 20 cm.

Numerical investigations performed within this chapter provide a background for further, more detailed numerical and experimental studies. In the future, after the improvements to the models proposed in the conclusion to the previous chapter are implemented, the study should continue to further refine the nozzle geometry. Since a limited number of cases with significant differences in divergence angle have been studied, there still room for improvements. A number of calculations with a smaller angular step should be made around α_{div} =36.1° to further optimize the geometry.

Nozzle for 1,000 Pa could be designed using the method of characteristics to reach the optimally expanded jet. Unfortunately, the same cannot be done for p_{LPC}=100 Pa, where the jet is always under-expanded.

The models of nucleation and growth and coating deposition applied in this chapter for estimation of nozzle clogging rates could be applied to estimate deposition rates to the substrates placed in the low pressure chamber.

General Conclusion and Perspectives

In the present thesis, a new two-step plasma spray – physical vapor deposition process was designed by means of numerical modeling. Unlike classical PS-PVD, where both the powder vaporization and coating process take place at a low pressure, the new proposed system was composed of two chambers separated by an expansion nozzle:

- The first, high pressure chamber (10^5 Pa) was introduced to facilitate powder evaporation;
- The second, low pressure chamber (100 – 1,000 Pa) has been designed for microstructured coatings deposition by condensation from the vapor phase.

High pressure increased powder residence time inside the jet and improved plasma-particle heat exchange, allowing the use of conventional low-power APS plasma torches (~40kW) and coarser powders (10 µm) in comparison with the ones currently used in PS-PVD (~150 kW, 1 µm). However, various complications presented themselves: the expansion nozzle separating the high and low pressure chambers was susceptible to erosion and clogging. The research tried to answer the two following questions:

- Is the proposed system feasible, considering the aforementioned problems of clogging and erosion?
- What is the optimal shape of the expansion nozzle?

To answer these questions a number of physical theories were applied, including classical fluid dynamics, Newtonian mechanics, kinetic theory for gases and kinetic theory of homogeneous nucleation. Each part of the process (high pressure chamber, expansion nozzle, low pressure chamber) required specific treatment. Thus, the conclusions are grouped according to these domains.

1. High Pressure Chamber

1.1. Model

A computational fluid dynamics (CFD) model of the gas flow coupled with a discrete phase model of zirconia powder processing was used to estimate the length of the high pressure chamber by tracking the maximal distance required for the evaporation of zirconia powder of realistic size and for appropriate spraying conditions. The model was refined to account for the presence of multiple gases and specifically zirconia vapor in the flow and was adjusted to accurately represent zirconia powder injection, dynamics and evaporation. A structured hexahedral (3D) mesh with flow-aligned cells was created to represent a part of the high pressure chamber (HPC).

1.2. Physics and Engineering

The investigation of the powder evaporation process in the HPC with the help of the 3D version of the CFD-DPM model revealed that despite an increase of the vapor content with a decrease of powder particle size, the resulting evaporation degree of zirconia does not grow significantly. For different powders with the initial particle size varying from 10 µm to 1 µm evaporation degree changed only from 60 wt% to 70 wt%, respectively. This effect was caused by an increased effect of rarefaction that significantly reduced the heat flux to particles despite the atmospheric pressure held in HPC.

Through the use of 3D CFD-DPM, it was shown that 10 cm is sufficient to attain maximal evaporation of any zirconium powder with particle diameter varying from 1 to 10 µm.

1.3. Outlook

The CFD-model could be enhanced by taking the plasma gas radiation into account. The discrete phase model can be adjusted to account for the temperature gradients inside the powder particles, their coagulation and plasma gas radiation towards the particles. Furthermore, a number of the well-designed experiments should be performed to validate the discrete phase model.

A 3D CFD model should be refined to test a two-torch layout that provides inertia-based filtering of the vapor flow from the solid particles, as shown in Figure 111.

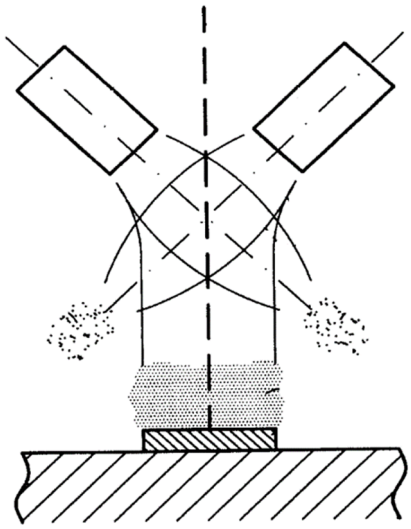

Figure 111: A view showing plasma jets crossing, together with the resulting plasma and filtered solid particles [156]

2. Expansion Nozzle

2.1. Model

The isentropic approach was used to estimate the initial expansion nozzle throat diameter that corresponded to the known gas mass flow rate. A 2D axisymmetric version of the computational fluid dynamics model was linked with the model of vapor nucleation and growth (N&G) processes in order to refine the initial sizes of the high pressure chamber and expansion nozzle by taking the nozzle wall temperatures (to avoid erosion/melting), clogging rates (vapor condensation, cluster deposition) and viscous forces into account. The nucleation and growth model based on the kinetic nucleation theory for incompressible flows was expanded to compressible ones. The model was verified for the incompressible case by comparison with reference simulations.

A number of scripts have been written in the interpreted high-level programming language Python 2.7 to perform and/or assist calculations. Nucleation and growth equations were solved with variable step-size 3rd order Runge-Kutta-based integrator. To analyze and visualize the results, a powerful post-processing tool was created. Another script has been written to manage the one-way linking between CFD and N&G models. The nearest-neighbor

interpolation algorithm was implemented to calculate the vapor and cluster fluxes towards the walls.

A structured quadrilateral (2D) mesh was created to represent a part of the HPC, the expansion nozzle and a part of the low pressure chamber (LPC).

A 20 mm long convergent-divergent nozzle geometry was proposed. Axisymmetric CFD-N&G model was then used to refine the initial nozzle diameter estimated using the isentropic approach and to perform the expansion nozzle optimization. The nozzle's divergence angle was varied from 0 to 90 degrees to determine the optimal shape that favors lower clogging rates.

2.2. Physics and Engineering

Nucleation and growth modeling inside the expansion nozzle revealed that deposits are formed mostly from the vapor phase which is attracted to the nozzle wall by the high concentration gradients, caused by the initial vapor concentration non-uniformity. The clusters formed inside the nozzle were mostly driven away from the wall due to the intense diffusion flux towards the axis, where cluster concentration was low due to higher temperatures and thus lower supersaturation.

An increase of the nozzle divergence angle led to lower clogging rates in the corresponding part due to a decrease in the concentration gradients caused by the gradual nozzle cross-section increase. However, this also resulted in a faster temperature decrease and growth of cluster concentration in regions closer to the nozzle axis. This effect for nozzles longer than 20 mm can result in a change of cluster flux direction to the one towards the wall.

Regardless of the divergence angle, the majority of zirconia remained in the vapor phase upon leaving the expansion nozzle (>73 wt%) and vapor loss due to deposition was negligible (<0.4 wt%).

The isentropic calculation followed by axisymmetric CFD simulations have shown that a zirconia-coated (coating thickness equal to 200 µm) convergent-divergent nozzle placed at 10 cm distance from the torch outlet should have a 5.4-mm in diameter throat. A nozzle with this position and dimensions will not undergo melting and erosion. The maximal wall temperature ~2,900 K was reached in a small initial region of the convergent part.

The application of the nucleation and growth model revealed that clogging does not happen in the convergent part due to substantially high gas temperatures, however, the process starts in the subsequent cylindrical part. The estimated clogging rate (~0.1 µm/s) is low enough to allow system operation for several hours. Considering that the estimation was conservative and each vapor molecule colliding with the wall was assumed to be adsorbed, the real clogging rate should be lower, allowing system operation during periods comparable with the period of cathode life time (~40 hours).

Thus, I have shown the absence of nozzle erosion and demonstrated that the clogging rate lies within an acceptable range, proving that the two-chamber PS-PVD system with the expansion nozzle between the chambers is feasible. However, the validity of this result could be questioned due to a high amount of assumptions and simplifications adopted in the present work, especially for the larger divergence angles (>36.1°) when numerical artifacts caused by the interpolation technique become apparent. Thus, the results obtained with the nucleation and growth model should be treated as qualitative ones.

2.3. Outlook

The nucleation and growth model could be updated in a variety of ways, e.g. by introducing the particle size distribution functions and by taking the coagulation process into account. A new Monte Carlo-based algorithm, capable of reliable predictions under rarefied conditions could be implemented. A more detailed vapor adsorption and cluster deposition model that accounts for heterogeneous nucleation and the subsequent growth could provide further insights into the clogging and coating formation processes.

The nucleation and growth model can provide better predictions of clogging and deposition rates if it is coupled with the CFD and DSMC models. A dynamic CFD-DSMC coupling could make it possible to study the non-stationary effects in the proposed system, e.g. the effect of arc voltage fluctuations on the temperature fluctuations in the low pressure chamber.

Experiments should be designed to validate the nucleation and growth model. Furthermore, a set of experiments is needed to obtain better model parameters (like zirconia vapor properties for N&G).

The use of a tungsten nozzle with the higher melting point than a zirconia-coated copper one could allow higher jet temperatures, drastically minimizing the clogging rate.

3. Low Pressure Chamber

3.1. Model

A direct simulation Monte Carlo (DSMC) code was linked with the N&G model to further refine the expansion nozzle shape by analyzing the jet parameters (temperatures, velocities, radii, vapor and cluster content, and cluster size) in the low pressure chamber depending on the nozzle divergence angle. The DSMC model was first validated for a low electric power input (5 kW) with pure argon as a plasma-forming gas and high electric power input (26 kW) with a mixture of argon and hydrogen as plasma-forming gas.

A Python script has been written to manage the one-way CFD-DSMC and DSMC-N&G linking. A structured quadrilateral (2D) mesh was generated to represent a part of the LPC.

DSMC-N&G model was applied to further optimize the nozzle by analyzing the radius of the resulting jet in the LPC. Two LPC pressures were considered: 100 Pa – a typical pressure for PS-PVD processes, and 1,000 Pa – a pressure, compliant with ATEX regulations.

3.2. Physics and Engineering

During the verification of the DSMC model, it was confirmed that a continuum assumption-based computational fluid dynamics model is incapable of predicting the rarefied gas behavior and the breakdown criterion Kn=0.05 was proposed. If gradient-based Knudsen number exceeds 0.05, the CFD predictions could be rather doubtful.

With the help of the DSMC model linked with the N&G model, zirconia processing inside the supersonic jet was studied. It was revealed that if the pressure in the LPC is kept around 100 Pa, the rarefaction (Kn>0.05 at multiple broad areas) prevents the plasma jet from cooling (temperature stays at ~ 3,000 K) and flow conditions do not favor nucleation and growth regardless of the nozzle geometry. Even if clusters are formed, their size does not exceed 3 monomers. If the pressure in the LPC is kept around 1,000 Pa, rarefaction stops being apparent (Kn<0.05 throughout the major part of the domain), the flow rapidly cools to ~2,000 K resulting in intense nucleation and growth. This leads to a complete transformation of vapor

into clusters at the distance around ~0.5 m from the nozzle outlet. The cluster size in this case reaches up to 100 monomers per g-mer (or 10 nm in diameter).

An increase in the expansion nozzle divergence angle results in a gradual increase of the jet radius and uniformity up to α_{div} =36.1°, followed by a slow decrease of these parameters to the values close to the initial ones. This happens due to the separation of the gas boundary layer, making the resulting flow indistinguishable from the case when the flow leaves the cylindrical nozzle (α_{div}=0.0°).

Since an increase in the nozzle divergence angle led to a decrease of the clogging rates of the divergent part and indicated the presence of the jet diameter maximum, **the optimal divergence angle among the considered angles was determined to be about 36° for both considered low pressure chamber pressures.**

By analyzing the shock locations, the minimal distance for the substrate location has been determined. This distance was calculated to be 60 cm and 20 cm for the 100 Pa and 1,000 Pa cases, respectively. The gas temperature at these locations did not exceed 4,000 K allowing an efficient substrate cooling and thus a high degree of control of the coating microstructure. Thus, different coating microstructures can be obtained by changing the LPC pressure and/or the spray distance, allowing other applications besides TBC deposition.

3.3. Outlook

The DSMC model can be enhanced by improving the flow chemistry and making it possible to introduce substrates with realistic boundary conditions into the domain. This could be achieved by coupling of DSMC with a thermodynamics model. Introduction of a substrate could help estimate the possible deposition rates and coating microstructures. However, a set of experiments is needed to obtain better reaction rates for DSMC chemistry.

The DSMC model could also be coupled with Monte Carlo-based models of nucleation and cluster growth, and coating formation and growth.

For the 1,000 Pa deposition chamber, the expansion nozzle could be designed using the method of characteristics to ensure the optimal expansion. This can reduce or terminate the shockwave region, reducing the minimal deposition distance and thus the size of the low pressure chamber.

References

[1] I. E. Agency, *World Energy Outlook 2017*. 2017.

[2] “Forecast International: Forecast International Predicts a World Market for 5,480 Industrial Power Generating Gas Turbine Engines Worth $105 Billion over the Next 10 Years.” [Online]. Available: https://www.forecastinternational.com/press/release.cfm?article=13562. [Accessed: 26-Oct-2018].

[3] D. R. Clarke, M. Oechsner, and N. P. Padture, “Thermal-barrier coatings for more efficient gas-turbine engines,” *MRS Bulletin*, vol. 37, no. 10, pp. 891–898, Oct. 2012.

[4] K. Ratkovská, J. Čerňan, M. Cúttová, and K. Semrád, “The Analyses for the Casing Improvements of the MPM-20 Engine,” in *Volume 8: Microturbines, Turbochargers and Small Turbomachines; Steam Turbines*, Montreal, Quebec, Canada, 2015, p. V008T23A002.

[5] “Sumy Electron Optics.” [Online]. Available: http://seo.sumy.ua/EN/Sputtering/Sputtering.html. [Accessed: 03-Nov-2018].

[6] “Coatings for high temperature applications::TBC materials.” [Online]. Available: https://thomas-sourmail.net/coatings/tbc_materials.html. [Accessed: 03-Nov-2018].

[7] A. Feuerstein, J. Knapp, T. Taylor, A. Ashary, A. Bolcavage, and N. Hitchman, “Technical and Economical Aspects of Current Thermal Barrier Coating Systems for Gas Turbine Engines by Thermal Spray and EBPVD: A Review,” *Journal of Thermal Spray Technology*, vol. 17, no. 2, pp. 199–213, Feb. 2008.

[8] K. von Niessen and M. Gindrat, “Plasma Spray-PVD: A New Thermal Spray Process to Deposit Out of the Vapor Phase,” *Journal of Thermal Spray Technology*, vol. 20, no. 4, pp. 736–743, Apr. 2011.

[9] A. Vardelle *et al.*, “The 2016 Thermal Spray Roadmap,” *Journal of Thermal Spray Technology*, vol. 25, no. 8, pp. 1376–1440, Dec. 2016.

[10] B. J. Harder, D. Zhu, M. P. Schmitt, and D. E. Wolfe, “Microstructural Effects and Properties of Non-line-of-Sight Coating Processing via Plasma Spray-Physical Vapor Deposition,” *Journal of Thermal Spray Technology*, vol. 26, no. 6, pp. 1052–1061, May 2017.

[11] W. He, G. Mauer, M. Gindrat, R. Wäger, and R. Vaßen, “Investigations on the Nature of Ceramic Deposits in Plasma Spray–Physical Vapor Deposition,” *Journal of Thermal Spray Technology*, vol. 26, no. 1–2, pp. 83–92, Dec. 2016.

[12] E. Bakan and R. Vaßen, “Ceramic Top Coats of Plasma-Sprayed Thermal Barrier Coatings: Materials, Processes, and Properties,” *Journal of Thermal Spray Technology*, vol. 26, no. 6, pp. 992–1010, Jul. 2017.

[13] S. Stecura, “Two-layer thermal barrier coating for high temperature components,” *American Ceramic Society Bulletin*, vol. 56, no. 12, Dec. 1977.

[14] L. L. Hong and M. V. Swain, “Thermal Diffusivity and Conductivity of Dense Polycrystalline ZrO2 Ceramics: A Survey,” *Am. Ceram. Soc. Bull.*, vol. 66, pp. 799–806, 1987.

[15] L. Pawlowski, D. Lombard, and P. Fauchais, “Structure-Thermal Properties-Relationship in Plasma Sprayed Zirconia Coatings,” *J. Vac. Sci. Technol. A*, vol. 3, no. 6, pp. 2494–2500, 1985.

[16] X. Q. Cao, R. Vaßen, and D. Stoever, “Ceramic Materials for Thermal Barrier Coatings,” *J. Eur. Ceram. Soc.*, vol. 24, no. 1, pp. 1–10, 2004.

[17] ASM International, *ASM Handbook: Surface Engineering (Vol 5)*. 1999.

[18] P. L. Fauchais, J. V. R. Heberlein, and M. I. Boulos, *Thermal Spray Fundamentals*. Springer US, 2014.

[19] S. Kuroda and T. W. Clyne, “The quenching stress in thermally sprayed coatings,” *Thin Solid Films*, vol. 200, no. 1, pp. 49–66, May 1991.

[20] M. Gell, L. Xie, X. Ma, E. H. Jordan, and N. P. Padture, “Highly durable thermal barrier coatings made by the solution precursor plasma spray process,” *Surface and Coatings Technology*, vol. 177–178, pp. 97–102, Jan. 2004.

[21] N. Tassini, K. Lambrinou, I. Mircea, M. Bartsch, S. Patsias, and O. V. der Biest, “Study of the amplitude-dependent mechanical behaviour of yttria-stabilised zirconia thermal barrier coatings,” *Journal of the European Ceramic Society*, vol. 27, no. 2–3, pp. 1487–1491, Jan. 2007.

[22] A. G. Evans, D. R. Mumm, J. W. Hutchinson, G. H. Meier, and F. S. Pettit, “Mechanisms controlling the durability of thermal barrier coatings,” *Progress in Materials Science*, vol. 46, no. 5, pp. 505–553, Jan. 2001.

[23] N. P. Padture, “Thermal Barrier Coatings for Gas-Turbine Engine Applications,” *Science*, vol. 296, no. 5566, pp. 280–284, Apr. 2002.

[24] N. P. Padture, “Degradation of Thermal Barrier Coatings from Deposits and Its Mitigation,” The Ohio State University, Dec. 2012.

[25] M. De Sousa, “Contribution à la purification de déchets de silicium solaire oxydé à l’aide d’un procédé assisté par plasma thermique,” PhD thesis, Université de Limoges, 2014.

[26] P. Fuzet, “Etude expérimentale de l’ablation de matériaux thermo-ablatifs sous impacts d’alumine liquide, modélisation et développement d’un moyen d’essai,” PhD thesis, Université de Limoges, 2014.

[27] V. Rat and J. F. Coudert, “Improvement of Plasma Spray Torch Stability by Controlling Pressure and Voltage Dynamic Coupling,” *Journal of Thermal Spray Technology*, vol. 20, no. 1–2, pp. 28–38, Oct. 2010.

[28] J. F. Bisson, B. Gauthier, and C. Moreau, “Effect of Plasma Fluctuations on In-Flight Particle Parameters,” *Journal of Thermal Spray Technology*, vol. 12, no. 1, pp. 38–43, Mar. 2003.

[29] E. Pfender, J. Fincke, and R. Spores, “Entrainment of cold gas into thermal plasma jets,” *Plasma Chemistry and Plasma Processing*, vol. 11, no. 4, pp. 529–543, Dec. 1991.

[30] G. Mauer and R. Vaßen, “Plasma Spray-PVD: Plasma Characteristics and Impact on Coating Properties,” *Journal of Physics: Conference Series*, vol. 406, p. 012005, Dec. 2012.

[31] C. Chazelas, J. P. Trelles, I. Choquet, and A. Vardelle, “Main Issues for a Fully Predictive Plasma Spray Torch Model and Numerical Considerations,” *Plasma Chemistry and Plasma Processing*, vol. 37, no. 3, pp. 627–651, Mar. 2017.

[32] I. Choquet, “Gas tungsten arc models including the physics of the cathode layer: remaining issues,” *Welding in the World*, vol. 62, no. 1, pp. 177–196, Sep. 2017.

[33] G. Mauer, M. O. Jarligo, S. Rezanka, A. Hospach, and R. Vaßen, “Novel opportunities for thermal spray by PS-PVD,” *Surface and Coatings Technology*, vol. 268, pp. 52–57, Apr. 2015.

[34] S. E. Selezneva, “Modeling of Supersonic Plasma Flows,” PhD thesis, Université de Sherbrooke, Sherbrooke, Quebec, Canada, 2002.

[35] J. F. Bisson, C. Moreau, M. Dorfman, C. Dambra, and J. Mallon, “Influence of Hydrogen on the Microstructure of Plasma-Sprayed Yttria-Stabilized Zirconia Coatings,” *Journal of Thermal Spray Technology*, vol. 14, no. 1, pp. 85–90, Mar. 2005.

[36] M. Vardelle, A. Vardelle, P. Fanchais, and I. Saray, “Comparison of Classical and Axial Injection Torches for Spraying Alumina Coatings,” *Materials and Manufacturing Processes*, vol. 9, no. 4, pp. 735–755, Jul. 1994.

[37] P. Mohanty, J. Stanisic, J. Stanisic, A. George, and Y. Wang, “A Study on Arc Instability Phenomena of an Axial Injection Cathode Plasma Torch,” *Journal of Thermal Spray Technology*, vol. 19, no. 1–2, pp. 465–475, Jan. 2010.

[38] A. Joulia *et al.*, “Comparing the deposition mechanisms in suspension plasma spray (SPS) and solution precursor plasma spray (SPPS) deposition of yttria-stabilised zirconia (YSZ),” *Journal of the European Ceramic Society*, vol. 34, no. 15, pp. 3925–3940, Dec. 2014.

[39] C. Zhang *et al.*, “Study on gas permeation behaviour through atmospheric plasma-sprayed yttria stabilized zirconia coating,” *Surface and Coatings Technology*, vol. 202, no. 20, pp. 5055–5061, Jul. 2008.

[40] “Oxide Ceramic Powder Materials for Thermal Spray - Oerlikon Metco.” [Online]. Available: https://www.oerlikon.com/metco/en/products-services/coating-materials/coating-materials-thermal-spray/oxide-ceramics/. [Accessed: 27-Oct-2018].

[41] G. Balmigere, E. Meillot, S. Vincent, and J.-P. Caltagirone, “Unsteady 3D Large Eddy Simulation of an Ar-H2 Plasma Jet: Analysis of Initial Results,” in *Thermal Spray 2007: Global Coating Solutions*, Beijing, China, 2007.

[42] M. Gupta, N. Markocsan, R. Rocchio-Heller, J. Liu, X.-H. Li, and L. Östergren, “Failure Analysis of Multilayered Suspension Plasma-Sprayed Thermal Barrier Coatings for Gas Turbine Applications,” *Journal of Thermal Spray Technology*, vol. 27, no. 3, pp. 402–411, Feb. 2018.

[43] A. Ganvir, N. Curry, N. Markocsan, P. Nylén, and F.-L. Toma, “Comparative study of suspension plasma sprayed and suspension high velocity oxy-fuel sprayed YSZ thermal barrier coatings,” *Surface and Coatings Technology*, vol. 268, pp. 70–76, Apr. 2015.

[44] X. Ma and P. Ruggiero, “Practical Aspects of Suspension Plasma Spray for Thermal Barrier Coatings on Potential Gas Turbine Components,” *Journal of Thermal Spray Technology*, vol. 27, no. 4, pp. 591–602, Apr. 2018.

[45] D. Chen, E. H. Jordan, and M. Gell, “Effect of solution concentration on splat formation and coating microstructure using the solution precursor plasma spray process,” *Surface and Coatings Technology*, vol. 202, no. 10, pp. 2132–2138, Feb. 2008.

[46] X. Ma, F. Wu, J. Roth, M. Gell, and E. H. Jordan, “Low thermal conductivity thermal barrier coating deposited by the solution plasma spray process,” *Surface and Coatings Technology*, vol. 201, no. 7, pp. 4447–4452, Dec. 2006.

[47] D. Zhang, “Thermal barrier coatings prepared by electron beam physical vapor deposition (EB–PVD),” in *Thermal Barrier Coatings*, Elsevier, 2011, pp. 3–24.

[48] A. Hospach, G. Mauer, R. Vaßen, and D. Stöver, “Columnar-Structured Thermal Barrier Coatings (TBCs) by Thin Film Low-Pressure Plasma Spraying (LPPS-TF),” *Journal of Thermal Spray Technology*, vol. 20, no. 1–2, pp. 116–120, Sep. 2010.

[49] M. Peters, K. Fritscher, G. Staniek, W. A. Kaysser, and U. Schulz, “Design and Properties of Thermal Barrier Coatings for advanced turbine engines,” *Materialwissenschaft und Werkstofftechnik*, vol. 28, no. 8, pp. 357–362, Aug. 1997.

[50] B. A. Movchan and K. Y. Yakovchuk, “High-Temperature Protective Coatings Produced by EB-PVD,” *Journal of Coating Science and Technology*, vol. 1, pp. 96–110, Oct. 2014.

[51] T. R. Kakuda, A. M. Limarga, T. D. Bennett, and D. R. Clarke, “Evolution of thermal properties of EB-PVD 7YSZ thermal barrier coatings with thermal cycling,” *Acta Materialia*, vol. 57, no. 8, pp. 2583–2591, May 2009.

[52] U. Schulz, B. Saruhan, K. Fritscher, and C. Leyens, “Review on Advanced EB-PVD Ceramic Topcoats for TBC Applications,” *International Journal of Applied Ceramic Technology*, vol. 1, no. 4, pp. 302–315, Jan. 2005.

[53] J. A. Thornton, “Influence of apparatus geometry and deposition conditions on the structure and topography of thick sputtered coatings,” *Journal of Vacuum Science and Technology*, vol. 11, no. 4, pp. 666–670, Jul. 1974.

[54] M. Gindrat, A. Refke, and R. Schmid, “Process Characterization of LPPS Thin Film Processes with Optical Diagnostics,” in *Thermal Spray 2007: Global Coating Solutions*, Beijing, China, 2007.

[55] G. Mauer, A. Hospach, N. Zotov, and R. Vaßen, “Process Conditions and Microstructures of Ceramic Coatings by Gas Phase Deposition Based on Plasma Spraying,” *Journal of Thermal Spray Technology*, vol. 22, no. 2–3, pp. 83–89, Nov. 2012.

[56] C. Li, H. Guo, L. Gao, L. Wei, S. Gong, and H. Xu, “Microstructures of Yttria-Stabilized Zirconia Coatings by Plasma Spray-Physical Vapor Deposition,” *Journal of Thermal Spray Technology*, vol. 24, no. 3, pp. 534–541, Dec. 2014.

[57] G. Mauer, “Plasma Characteristics and Plasma-Feedstock Interaction Under PS-PVD Process Conditions,” *Plasma Chemistry and Plasma Processing*, vol. 34, no. 5, pp. 1171–1186, Jun. 2014.

[58] G. Mauer, A. Hospach, and R. Vaßen, “Process Development and Coating Characteristics of Plasma Spray-PVD,” *Surface and Coatings Technology*, vol. 220, pp. 219–224, Apr. 2013.

[59] Y. Gao, D. Yang, C. Sun, and Z. Chen, “Deposition of YSZ Coatings in a Chamber at Pressures below 100 Pa Using Low-Power Plasma Spraying with an Internal Injection Powder Feeding,” *Journal of Thermal Spray Technology*, vol. 22, no. 7, pp. 1253–1258, Aug. 2013.

[60] R. Bolot, D. Sokolov, D. Klein, and C. Coddet, “Nozzle Developments for Thermal Spray at Very Low Pressure,” *Journal of Thermal Spray Technology*, vol. 15, no. 4, pp. 827–833, Dec. 2006.

[61] C. Sun, Y. Gao, D. Yang, and Y. Fu, “Effects of the nozzle design on the properties of plasma jet and formation of YSZ coatings under low pressure conditions,” *Chinese Journal of Mechanical Engineering*, vol. 29, no. 5, pp. 954–961, Jun. 2016.

[62] M.-J. Liu, M. Zhang, Q. Zhang, G.-J. Yang, C.-X. Li, and C.-J. Li, “Evaporation of Droplets in Plasma Spray–Physical Vapor Deposition Based on Energy Compensation Between Self-Cooling and Plasma Heat Transfer,” *Journal of Thermal Spray Technology*, vol. 26, no. 7, pp. 1641–1650, Aug. 2017.

[63] B. Vautherin, “Elaboration par projection plasma réactive sous très basse pression de dépôts de matériaux dans le système Aluminium-Titane-Azote,” PhD thesis, Belfort-Montbéliard, 2014.

[64] K. von Niessen, M. Gindrat, and A. Refke, “Vapor Phase Deposition Using Plasma Spray-PVD™,” *Journal of Thermal Spray Technology*, vol. 19, no. 1–2, pp. 502–509, Nov. 2009.

[65] N. M. Yanar, M. Helminiak, G. H. Meier, and F. S. Pettit, “Comparison of the Failures during Cyclic Oxidation of Yttria-Stabilized (7 to 8 Weight Percent) Zirconia Thermal Barrier Coatings Fabricated via Electron Beam Physical Vapor Deposition and Air Plasma Spray,” *Metallurgical and Materials Transactions A*, vol. 42, no. 4, pp. 905–921, Nov. 2010.

[66] S. Rezanka, D. E. Mack, G. Mauer, D. Sebold, O. Guillon, and R. Vaßen, “Investigation of the resistance of open-column-structured PS-PVD TBCs to erosive and high-temperature corrosive attack,” *Surface and Coatings Technology*, vol. 324, pp. 222–235, Sep. 2017.

[67] V. Teixeira, M. Andritschky, H. Gruhn, W. Malléner, H. P. Buchkremer, and D. Stöver, “Failure of Physical Vapor Deposition/Plasma-Sprayed Thermal Barrier Coatings during Thermal Cycling,” *Journal of Thermal Spray Technology*, vol. 9, no. 2, pp. 191–197, Jun. 2000.

[68] K. S. Fancey and A. Matthews, “Ionization assisted physical vapor deposition of zirconia thermal barrier coatings,” *Journal of Vacuum Science & Technology A: Vacuum, Surfaces, and Films*, vol. 4, no. 6, pp. 2656–2660, Nov. 1986.

[69] A. Shinozawa, K. Eguchi, M. Kambara, and T. Yoshida, “Feather-like Structured YSZ Coatings at Fast Rates by Plasma Spray Physical Vapor Deposition,” *Journal of Thermal Spray Technology*, vol. 19, no. 1–2, pp. 190–197, Oct. 2009.

[70] X. F. Zhang *et al.*, “Mechanisms governing the thermal shock and tensile fracture of PS-PVD 7YSZ TBC,” *Ceramics International*, vol. 44, no. 4, pp. 3973–3980, Mar. 2018.

[71] J. A. M. van der Mullen, “Excitation equilibria in plasmas: a classification,” *Physics Reports*, vol. 191, no. 2–3, pp. 109–220, Jul. 1990.

[72] Khan and K. Mohammad, *Fluid mechanics and machinery*. Oxford University Press, 2015.

[73] D. Ivchenko, T. Zhang, G. Mariaux, A. Vardelle, S. Goutier, and T. E. Itina, “On the Validity of Continuum Computational Fluid Dynamics Approach Under Very Low-Pressure Plasma Spray Conditions,” *Journal of Thermal Spray Technology*, vol. 27, no. 1–2, pp. 3–13, Nov. 2017.

[74] X. Chen and E. Pfender, “Effect of the Knudsen number on heat transfer to a particle immersed into a thermal plasma,” *Plasma Chemistry and Plasma Processing*, vol. 3, no. 1, pp. 97–113, Mar. 1983.

[75] K. Ramachandran, “Numerical modelling of plasma spray process,” *Journal of Physics: Conference Series*, vol. 208, p. 012052, Feb. 2010.

[76] N. El-Kaddah, J. McKelliget, and J. Szekely, “Heat transfer and fluid flow in plasma spraying,” *Metallurgical Transactions B*, vol. 15, no. 1, pp. 59–70, Jan. 1984.

[77] H.-P. Li and X. Chen, “Three-dimensional simulation of a plasma jet with transverse particle and carrier gas injection,” *Thin Solid Films*, vol. 390, no. 1–2, pp. 175–180, Jun. 2001.

[78] P. C. Huang, J. Hebeylein, and E. Pfender, “A two-fluid model of turbulence for a thermal plasma jet,” *Plasma Chemistry and Plasma Processing*, vol. 15, no. 1, pp. 25–46, Mar. 1995.

[79] K. Bobzin *et al.*, “Simulation of the Particle Melting Degree in Air Plasma Spraying,” *Journal of Physics: Conference Series*, vol. 825, p. 012002, Apr. 2017.

[80] G. Mariaux, “Modélisation des écoulements instationnaires et génie des procédés, Habilitation à Diriger des Recherches,” Université de Limoges, juin 2012.

[81] M. Shigeta, “Turbulence modelling of thermal plasma flows,” *Journal of Physics D: Applied Physics*, vol. 49, no. 49, p. 493001, Nov. 2016.

[82] ANSYS, Inc., *ANSYS Fluent Theory Guide*. 2016.

[83] F. R. Menter, “Two-equation eddy-viscosity turbulence models for engineering applications,” *AIAA Journal*, vol. 32, no. 8, pp. 1598–1605, Aug. 1994.

[84] S. E. Selezneva, M. I. Boulos, M. C. M. van de Sanden, R. Engeln, and D. C. Schram, “Stationary supersonic plasma expansion: continuum fluid mechanics versus direct simulation Monte Carlo method,” *Journal of Physics D: Applied Physics*, vol. 35, no. 12, pp. 1362–1372, Jun. 2002.

[85] A. B. Murphy, “Transport Coefficients of Hydrogen and Argon–Hydrogen Plasmas,” *Plasma Chemistry and Plasma Processing*, vol. 20, no. 3, pp. 279–297, 2000.

[86] P. André *et al.*, “Transport coefficients in thermal plasma. Applications to Mars and Titan atmospheres,” *The European Physical Journal D*, vol. 57, no. 2, pp. 227–234, Feb. 2010.

[87] A. B. Murphy, “Thermal plasmas in gas mixtures,” *Journal of Physics D: Applied Physics*, vol. 34, no. 20, pp. R151–R173, Oct. 2001.

[88] R. Johnson, Ed., *Handbook of Fluid Dynamics, Second Edition*. CRC Press, 2016.

[89] A. Gleizes, Y. Cressault, and P. Teulet, “Mixing rules for thermal plasma properties in mixtures of argon, air and metallic vapours,” *Plasma Sources Science and Technology*, vol. 19, no. 5, p. 055013, Sep. 2010.

[90] S. Chapman, T. G. Cowling, and D. Burnett, *The Mathematical Theory of Non-uniform Gases: An Account of the Kinetic Theory of Viscosity, Thermal Conduction and Diffusion in Gases*. Cambridge University Press, 1990.

[91] A. J. Chorin, “Numerical Solution of the Navier-Stokes Equations,” *Mathematics of Computation*, vol. 22, no. 104, p. 745, Oct. 1968.

[92] “Code_Saturne.” [Online]. Available: https://www.code-saturne.org/cms/. [Accessed: 15-Jul-2018].

[93] OpenCFD, “OpenFOAM® - Official home of The Open Source Computational Fluid Dynamics (CFD) Toolbox.” [Online]. Available: http://www.openfoam.com. [Accessed: 15-Jul-2018].

[94] “OpenFVM project.” [Online]. Available: http://openfvm.sourceforge.net/. [Accessed: 15-Jul-2018].

[95] “Engineering Simulation & 3D Design Software | ANSYS.” [Online]. Available: //www.ansys.com/. [Accessed: 15-Jul-2018].

[96] “COMSOL Multiphysics® Modeling Software.” [Online]. Available: https://www.comsol.com/. [Accessed: 15-Jul-2018].

[97] “CHAM | Your Gateway to CFD Success.” [Online]. Available: http://www.cham.co.uk/. [Accessed: 15-Jul-2018].

[98] J. D. Anderson, *Modern Compressible Flow: With Historical Perspective*, 3rd ed. McGraw-Hill, 2003.

[99] Y. Gao, D. M. Yang, and J. Gao, “Characteristics of a Plasma Torch Designed for Very Low Pressure Plasma Spraying,” *Journal of Thermal Spray Technology*, vol. 21, no. 3–4, pp. 740–744, Jan. 2012.

[100] K. Naveen Kumar, M. Gopalsamy, D. Antony, R. Krishnaraj, and C. B. V. Viswanadh, “Design and Optimization of Aerospike nozzle using CFD,” *IOP Conference Series: Materials Science and Engineering*, vol. 247, p. 012008, Oct. 2017.

[101] Z. Fuszko and R. Olšiak, “Design and CFD analysis of an axisymmetric supersonic plug nozzle for an air-air ejector,” 2016, p. 020033.

[102] K. O. Mon and C. Lee, “Optimal design of supersonic nozzle contour for altitude test facility,” *Journal of Mechanical Science and Technology*, vol. 26, no. 8, pp. 2589–2594, Aug. 2012.

[103] S. Yin, X. Suo, H. Liao, Z. Guo, and X. Wang, “Significant influence of carrier gas temperature during the cold spray process,” *Surface Engineering*, vol. 30, no. 6, pp. 443–450, Jun. 2014.

[104] T. Schmidt, F. Gaertner, and H. Kreye, “New Developments in Cold Spray Based on Higher Gas and Particle Temperatures,” *Journal of Thermal Spray Technology*, vol. 15, no. 4, pp. 488–494, Dec. 2006.

[105] G. A. Lukyanov, *Supersonic Plasma Jets*. Leningrad: Mashinostroenie, 1985.

[106] “Aerospaceweb.org | Ask Us - Shock Diamonds and Mach Disks.” [Online]. Available: http://www.aerospaceweb.org/question/propulsion/q0224.shtml. [Accessed: 15-Jul-2018].

[107] “Centered Expansion Fan.” [Online]. Available: https://www.grc.nasa.gov/www/k-12/airplane/expans.html. [Accessed: 15-Jul-2018].

[108] Y. Chou and L. Talbot, “Source-flow expansion of a partially ionized gas into a vacuum,” in *5th Aerospace Sciences Meeting*, 1967.

[109] R. C. Jenkins, “Electron-ion recombination in a sonic orifice flow,” *AIAA Journal*, vol. 9, no. 7, pp. 1383–1389, Jul. 1971.

[110] M. Usami and K. Teshima, “Molecular Simulation of Rarefied Supersonic Free Jets by DSMC Method.,” *JSME International Journal Series B*, vol. 42, no. 3, pp. 369–376, 1999.

[111] P. Wang, W. He, G. Mauer, R. Mücke, and R. Vaßen, “Computational Fluid Dynamic Analysis of Plasma Spray Physical Vapor Deposition,” presented at the ICHMT International Symposium on Advances in Computational Heat Transfer, 2017, pp. 1833–1836.

[112] B. Vautherin, M.-P. Planche, R. Bolot, A. Quet, L. Bianchi, and G. Montavon, “Vapors and Droplets Mixture Deposition of Metallic Coatings by Very Low Pressure Plasma Spraying,” *Journal of Thermal Spray Technology*, vol. 23, no. 4, pp. 596–608, Feb. 2014.

[113] N. Zhang *et al.*, “In-flight particle characterization and coating formation under low pressure plasma spray condition,” *Journal of Iron and Steel Research, International*, vol. 24, no. 3, pp. 306–312, Mar. 2017.

[114] A. Anwaar, L. Wei, H. Guo, and B. Zhang, “Plasma–Powder Feedstock Interaction During Plasma Spray–Physical Vapor Deposition,” *Journal of Thermal Spray Technology*, vol. 26, no. 3, pp. 292–301, Jan. 2017.

[115] B. Jodoin, M. Gindrat, J. L. Dorier, C. Hollenstein, M. Loch, and G. Barbezat, “Modelling and Diagnostics of a Supersonic DC Plasma Jet Expanding at Low Pressure,” Ecole Polytechnique Federale de Lausanne, LRP--713/01, 2001.

[116] N. Yu, R. Jourdain, M. Gourma, and P. Shore, “Analysis of De-Laval nozzle designs employed for plasma figuring of surfaces,” *The International Journal of Advanced Manufacturing Technology*, vol. 87, no. 1–4, pp. 735–745, Oct. 2016.

[117] K. Sinha, K. Mahesh, and G. V. Candler, “Modeling shock unsteadiness in shock/turbulence interaction,” *Physics of Fluids*, vol. 15, no. 8, pp. 2290–2297, Aug. 2003.

[118] S. E. Selezneva, M. Rajabian, D. Gravelle, and M. I. Boulos, “Study of the structure and deviation from equilibrium in direct current supersonic plasma jets,” *Journal of Physics D: Applied Physics*, vol. 34, no. 18, pp. 2862–2874, Sep. 2001.

[119] D. Burnett, “The Distribution of Molecular Velocities and the Mean Motion in a Non-Uniform Gas,” *Proceedings of the London Mathematical Society*, vol. s2-40, no. 1, pp. 382–435, 1936.

[120] X. Zhong, “On Numerical Solutions of Burnett Equations for Hypersonic Flow Past 2-D Circular Blunt Leading Edges in Continuum Transition Regime,” presented at the AIAA 24th Fluid Dynamics Conference, Orlando, FL, 1993, p. 3092.

[121] H. Zhang, S. Hu, G. Wang, and J. Zhu, “Modeling and simulation of plasma jet by lattice Boltzmann method,” *Applied Mathematical Modelling*, vol. 31, no. 6, pp. 1124–1132, Jun. 2007.

[122] T. M. Rodgers, H. Zhao, and H. N. G. Wadley, “Vapor deposition on doublet airfoil substrates: Coating thickness control,” *Journal of Vacuum Science & Technology A: Vacuum, Surfaces, and Films*, vol. 33, no. 6, p. 061509, Nov. 2015.

[123] G. A. Bird, *Molecular Gas Dynamics and The Direct Simulation of Gas Flow*. Oxford: Clarendon press, 2003.

[124] G. A. Bird, *The DSMC Method*. North Charleston: CreateSpace, 2013.

[125] C. Borgnakke and P. S. Larsen, “Statistical collision model for Monte Carlo simulation of polyatomic gas mixture,” *Journal of Computational Physics*, vol. 18, no. 4, pp. 405–420, Aug. 1975.

[126] R. L. Williamson, J. R. Fincke, and C. H. Chang, “A Computational Examination of the Sources of Statistical Variance in Particle Parameters During Thermal Plasma Spraying,” *Plasma Chemistry and Plasma Processing*, vol. 20, no. 3, pp. 299–324, 2000.

[127] P. Fauchais, M. Vardelle, A. Vardelle, L. Bianchi, and A. C. Léger, “Parameters controlling the generation and properties of plasma sprayed zirconia coatings,” *Plasma Chemistry and Plasma Processing*, vol. 16, no. S1, pp. S99–S125, Mar. 1995.

[128] A. Douce, “Etude numérique du comportement de particules métalliques injectées dans un plasma d’arc électrique,” EDF, Electricité de France, Rapport de DEA, 1995.

[129] D. Khelfi, A. A. El-Hadj, and N. Aït-Messaoudène, “Modeling of a 3D plasma thermal spraying and the effect of the particle injection angle,” p. 12.

[130] B. M. Cetegen and S. Basu, “Review of Modeling of Liquid Precursor Droplets and Particles Injected into Plasmas and High-Velocity Oxy-Fuel (HVOF) Flame Jets for Thermal Spray Deposition Applications,” *Journal of Thermal Spray Technology*, vol. 18, no. 5–6, pp. 769–793, Dec. 2009.

[131] D. Y. C. Wei, B. Farouk, and D. Apelian, “Melting Powder Particles in a Low-Pressure Plasma Jet,” *Journal of Heat Transfer*, vol. 109, no. 4, p. 971, 1987.

[132] Y. P. Wan, V. Prasad, G.-X. Wang, S. Sampath, and J. R. Fincke, “Model and Powder Particle Heating, Melting, Resolidification, and Evaporation in Plasma Spraying Processes,” *Journal of Heat Transfer*, vol. 121, no. 3, p. 691, 1999.

[133] M. Vardelle, A. Vardelle, P. Fauchais, and M. I. Boulos, “Plasma—particle momentum and heat transfer: Modelling and measurements,” *AIChE Journal*, vol. 29, no. 2, pp. 236–243, Mar. 1983.

[134] X. Chen and E. Pfender, “Behavior of small particles in a thermal plasma flow,” *Plasma Chemistry and Plasma Processing*, vol. 3, no. 3, pp. 351–366, Sep. 1983.

[135] B. Abramzon and W. A. Sirignano, “Droplet vaporization model for spray combustion calculations,” *International Journal of Heat and Mass Transfer*, vol. 32, no. 9, pp. 1605–1618, Sep. 1989.

[136] W. A. Sirignano, *Fluid Dynamics and Transport of Droplets and Sprays*. Cambridge University Press.

[137] S. Cartel, “Procédé de dépôt physique en phase vapeur assisté par plasma thermique: Modélisation fine du chauffage, de la fusion et de l’évaporation de particules céramiques injectées dans un écoulement plasma.,” Université de Limoges, Contrat Ademe/CNRS n° 0574C0112, 2006.

[138] G. Mauer and R. Vaßen, “Conditions for nucleation and growth in the substrate boundary layer at plasma spray-physical vapor deposition (PS-PVD),” *Surface and Coatings Technology*, Jun. 2018, https://doi.org/10.1016/j.surfcoat.2018.06.086.

[139] X. F. Zhang *et al.*, “Gas-deposition mechanisms of 7YSZ coating based on plasma spray-physical vapor deposition,” *Journal of the European Ceramic Society*, vol. 36, no. 3, pp. 697–703, Feb. 2016.

[140] M. Volmer and A. Weber, “Keimbildung in übersättigten Gebilden,” *Zeitschrift für Physikalische Chemie*, vol. 119U, no. 1, Jan. 1926.

[141] “On the Theory of New Phase Formation. Cavitation,” in *Selected Works of Yakov Borisovich Zeldovich, Volume I*, Princeton University Press.

[142] S. Panda and S. E. Pratsinis, “Modeling the synthesis of aluminum particles by evaporation-condensation in an aerosol flow reactor,” *Nanostructured Materials*, vol. 5, no. 7–8, pp. 755–767, Sep. 1995.

[143] J. L. Katz and H. Wiedersich, “Nucleation theory without Maxwell Demons,” *Journal of Colloid and Interface Science*, vol. 61, no. 2, pp. 351–355, Sep. 1977.

[144] S. L. Girshick and C.-P. Chiu, “Kinetic nucleation theory: A new expression for the rate of homogeneous nucleation from an ideal supersaturated vapor,” *The Journal of Chemical Physics*, vol. 93, no. 2, pp. 1273–1277, Jul. 1990.

[145] V. A. Nemchinsky and M. Shigeta, “Simple equations to describe aerosol growth,” *Modelling and Simulation in Materials Science and Engineering*, vol. 20, no. 4, p. 045017, May 2012.

[146] N. Rao *et al.*, “Nanoparticle formation using a plasma expansion process,” *Plasma Chemistry and Plasma Processing*, vol. 15, no. 4, pp. 581–606, Dec. 1995.

[147] M. Shigeta and T. Watanabe, “Growth mechanism of silicon-based functional nanoparticles fabricated by inductively coupled thermal plasmas,” *Journal of Physics D: Applied Physics*, vol. 40, no. 8, pp. 2407–2419, Apr. 2007.

[148] H. M. Hulburt and S. Katz, “Some problems in particle technology,” *Chemical Engineering Science*, vol. 19, no. 8, pp. 555–574, Aug. 1964.

[149] S. K. Friedlander, *Smoke, Dust, and Haze: Fundamentals of Aerosol Dynamics*, 2nd ed. Oxford University Press, 2000.

[150] S. E. Pratsinis, “Simultaneous nucleation, condensation, and coagulation in aerosol reactors,” *Journal of Colloid and Interface Science*, vol. 124, no. 2, pp. 416–427, Aug. 1988.

[151] P. Proulx and J.-F. Bilodeau, “A model for ultrafine powder production in a plasma reactor,” *Plasma Chemistry and Plasma Processing*, vol. 11, no. 3, pp. 371–386, Sep. 1991.

[152] M. Shigeta and T. Watanabe, “Numerical investigation of cooling effect on platinum nanoparticle formation in inductively coupled thermal plasmas,” *Journal of Applied Physics*, vol. 103, no. 7, p. 074903, Apr. 2008.

[153] ANSYS, Inc., *ANSYS Fluent User’s Guide*. 2016.

[154] J. M. Weiss and W. A. Smith, “Preconditioning applied to variable and constant density flows,” *AIAA Journal*, vol. 33, no. 11, pp. 2050–2057, Nov. 1995.

[155] J. Welty, C. E. Wicks, G. L. Rorrer, and R. E. Wilson, *Fundamentals of Momentum, Heat and Mass Transfer*, 5th ed. Wiley, 2007.

[156] F. Braillard, J. Menuey, E. Nogues, A. Tricoire, and M. Vardelle, “Method of depositing a thermal barrier by plasma torch,” US8449677B2, 28-May-2013.

[157] W. Koch and S. K. Friedlander, “Particle Growth by Coalescence and Agglomeration,” *Particle & Particle Systems Characterization*, vol. 8, no. 1–4, pp. 86–89, 1991.

[158] F. E. Kruis, K. A. Kusters, S. E. Pratsinis, and B. Scarlett, “A Simple Model for the Evolution of the Characteristics of Aggregate Particles Undergoing Coagulation and Sintering,” *Aerosol Science and Technology*, vol. 19, no. 4, pp. 514–526, Jan. 1993.

[159] G. V. Samsonov (auth.) and G. V. Samsonov (eds.), *The Oxide Handbook*, 1st ed. Springer US, 1973.

[160] “Welcome to Python.org,” *Python.org*. [Online]. Available: https://www.python.org/. [Accessed: 05-Aug-2018].

[161] A. Stoklosa, “Molar Volume, Ionic Radii in Stoichiometric and Nonstoichiometric Metal Oxides,” in *Stoichiometry and Materials Science - When Numbers Matter*, A. Innocenti, Ed. InTech, 2012.

[162] M. Rösner-Kuhn, W. H. Hofmeister, G. Kuppermann, R. J. Bayuzick, and M. G. Frohberg, “Investigations of the influence of oxygen on the surface tension of zirconium by the oscillating drop technique,” *Surface Science*, vol. 443, no. 3, pp. 159–164, Dec. 1999.

[163] S. L. Girshick, C.-P. Chiu, and P. H. McMurry, “Time-Dependent Aerosol Models and Homogeneous Nucleation Rates,” *Aerosol Science and Technology*, vol. 13, no. 4, pp. 465–477, Jan. 1990.

[164] M. A. Gallis, J. R. Torczynski, S. J. Plimpton, D. J. Rader, and T. Koehler, “Direct simulation Monte Carlo: The quest for speed,” 2014.

[165] “SPARTA Direct Simulation Monte Carlo Simulator.” [Online]. Available: https://sparta.sandia.gov/. [Accessed: 07-Aug-2018].

[166] I. D. Boyd, “Predicting Breakdown of the Continuum Equations Under Rarefied Flow Conditions,” in *AIP Conference Proceedings*, 2003.

[167] W.-L. Wang and I. D. Boyd, “Predicting continuum breakdown in hypersonic viscous flows,” *Physics of Fluids*, vol. 15, no. 1, pp. 91–100, Jan. 2003.

[168] *Directive 2014/34/EU of the European Parliament and of the Council of 26 February 2014 on the harmonisation of the laws of the Member States relating to equipment and protective systems intended for use in potentially explosive atmospheres (recast) Text with EEA relevance*, vol. OJ L. 2014.

[169] Leybold GmbH, “SOGEVAC SV 630 BF | Leybold,” *Leybold Online Shop*. [Online]. Available: https://www.leyboldproducts.com/products/oil-sealed-vacuum-pumps/sogevac/sogevac-b/pumps/610/sogevac-sv-630-bf. [Accessed: 04-Nov-2018].

[170] D. J. Carlson and C. H. Lewis, “Normal shock location in underexpanded gas and gas-particle jets,” *AIAA Journal*, vol. 2, no. 4, pp. 776–777, Apr. 1964.

[171] R. C. Reid, J. M. Prausnitz, and B. E. Poling, *The properties of gases and liquids*, 4th ed. McGraw-Hill, 1987.

[172] M. Y. Plotnikov and E. V. Shkarupa, “Heterogeneous activation of rarefied hydrogen in thin tubes,” *Vacuum*, vol. 129, pp. 31–37, Jul. 2016.

[173] J. Fan, I. D. Boyd, and C. Shelton, “Monte Carlo modeling of YBCO vapor deposition,” *AIP Conference Proceedings*, vol. 585, no. 1, pp. 214–221, Aug. 2001.

[174] J. H. Park, E. Pfender, and C. H. Chang, “Reduction of Chemical Reactions in Nitrogen and Nitrogen-Hydrogen Plasma Jets Flowing into Atmospheric Air,” *Plasma Chemistry and Plasma Processing*, vol. 20, no. 2, pp. 165–181, 2000.

[175] R. J. Gallagher and J. B. Fenn, “Rotational relaxation of molecular hydrogen,” *The Journal of Chemical Physics*, vol. 60, no. 9, pp. 3492–3499, May 1974.

[176] Leif Rune Hellevik, *Numerical Methods for Engineers*. Trondheim, Norway: NTNU, 2018.

Annexes

Annex A. Reference Data 178
Annex B. Variable Step Numerical Scheme 180
Annex C. Boundary Profiles on the Expansion Nozzle Outlet 181

Annex A. Reference Data

Table 21: Drag coefficients at different flow regimes [18]

Flow regime	Drag coefficient	
$Re_p \leq 0.2$	$C_{df} = \frac{24}{\mathrm{Re}_p}$	(150)
$0.2 < Re_p \leq 2$	$C_{df} = \frac{24}{\mathrm{Re}_p}\left(1 + 3\mathrm{Re}_p/16\right)$	(151)
$2 < Re_p \leq 20$	$C_{df} = \frac{24}{\mathrm{Re}_p}\left(1 + 0.110\mathrm{Re}_p^{0.810}\right)$	(152)
$20 < Re_p \leq 200$	$C_{df} = \frac{24}{\mathrm{Re}_p}\left(1 + 0.189\mathrm{Re}_p^{0.632}\right)$	(153)
$Re_p > 200$	$C_{df} = \frac{24}{\mathrm{Re}_p} + \frac{6}{1+\sqrt{\mathrm{Re}_p}} + 0.4$	(154)

Table 22: Lennard-Jones model parameters [155, 171]

Gas specie	σ_{gas}, Å	ε_{gas}/k_B, K
Air	3.711	78.6
Ar	3.542	93.3
H_2	2.827	59.7

Table 23: Properties of solid and liquid ZrO_2 [137]

Property	Value
Density, kg/m^3	5,680
Specific heat, J/kg/K	750
Melting temperature, K	2,953
Boiling temperature, K	4,548
Particle emissivity	0.8
Molar mass, kg/mol	0.123
Melting enthalpy, J/kg	706,050
Evaporation enthalpy, J/kg	5,066,550

Table 24: VSS collision model parameters under standard conditions (p_{ref}=101,325 Pa, T_{ref}=273.15 K) except Zr (T_{ref}=2,000 K) [123, 172, 173]

Species	d_{ref}, × 10^{-10} m	m, × 10^{-27} kg	ω	α
Ar	4.11	66.40	0.81	1.40
H_2	2.88	3.34	0.67	1.35
H	2.30	1.67	0.66	1.26
Zr	5.941	151.48	0.853	1.00
O	3.96	53.12	0.77	1.40

Table 25: Chemical reactions in Ar-H_2 plasma [174]

Reaction	Λ, × 10^{-14} m^3/s	η	E_a , × 10^{-19} J
$H_2 + Ar \rightarrow 2H + Ar$	8.449	-0.362	7.190
$H_2 + H \rightarrow 3H$	9,762.000	-0.362	7.190
$2H_2 \rightarrow 2H + H_2$	21.120	-0.362	7.190
$H + H \rightarrow H_2$	16.260	-0.600	0.000

Table 26: Parameters of Ar and H_2 species used in DSMC calculations [123, 175]

Species	M, g/mol	ζ_{rot}	Z_{rot}	ζ_{vib}	Z_{vib}	Θ_{vib}, K
Ar	39.948	0	-	0	-	-
H_2	2.016	2	300	2	30,000	6,159
H	1.008	0	-	0	-	-
Zr	91.224	0	-	0	-	-
O	32.000	0	-	0	-	-

Annex B. Variable Step Numerical Scheme

The solution of nucleation and growth equations (141), p.102 was performed using 3rd order Runge-Kutta (RK3) numerical scheme with step size control. Integration step size h_{n+1} was determined based on the value of local truncation error. On each integration step, local truncation error (LTE) was determined as relative difference between RK3 solution and a higher accuracy 4th order RK4 solution according to the following formula:

$$LTE = \left| \frac{y_{n+1}^{RK3} - y_{n+1}^{RK4}}{y_{n+1}^{RK4}} \right|, \tag{155}$$

where 3rd order solution y_{n+1}^{RK3} on $n+1$ step was given by:

$$\begin{aligned} k_1 &= f\left(x_n, y_n\right) \\ k_2 &= f\left(x_n + \frac{h_n}{2}, y_n + \frac{h_n}{2} k_1\right) \\ k_3 &= f\left(x_n + h_n, y_n - h_n k_1 + 2h_n k_2\right) \\ y_{n+1}^{RK3} &= y_n^{RK4} + \frac{h_n}{6}\left(k_1 + 4k_2 + k_3\right) \end{aligned}, \tag{156}$$

and 4th order solution y_{n+1}^{RK4} on $n+1$ step was given by:

$$\begin{aligned} k_1 &= f\left(x_n, y_n\right) \\ k_2 &= f\left(x_n + \frac{h_n}{2}, y_n + \frac{h_n}{2} k_1\right) \\ k_3 &= f\left(x_n + \frac{h_n}{2}, y_n + \frac{h_n}{2} k_2\right) \\ k_4 &= f\left(x_n + h_n, y_n + h_n k_3\right) \\ y_{n+1}^{RK4} &= y_n^{RK4} + \frac{h_n}{6}\left(k_1 + 2k_2 + 2k_3 + k_4\right) \end{aligned}, \tag{157}$$

where f is the right side of the system (141).

The new integration step h_{n+1} was calculated using the following expression:

$$h_{n+1} = \begin{cases} \max\left(\max\left(0.8h_n \left(\frac{LTE_{\max}}{LTE} \right)^{0.5}, \frac{h_n}{5} \right), h_{\min} \right), & LTE > LTE_{\max} \\ \min\left(\min\left(0.8h_n \left(\frac{LTE_{\max}}{LTE} \right)^{0.5}, 5h_n \right), h_{\max} \right), & LTE < LTE_{\min} \end{cases}, \tag{158}$$

where $LTE_{\min}$ and $LTE_{\max}$ are the initially specified threshold values for minimal and maximal local truncation errors, respectively, and $h_{\min}$ and $h_{\max}$ are the initially specified minimal and maximal step size values. The maximal amount of step size refinements was limited to prevent infinite loops, caused by possible solution discontinuities [176].

Annex C. Boundary Profiles on the Expansion Nozzle Outlet

Table 27: Boundary profiles on N00L expansion nozzle outlet derived from 2D CFD calculation

r, mm	T, K	n,×10^{23} m^{-3}	v_x, m/s	v_y, m/s	x_{H2}	x_H	x_{Zr}	x_O
0.000	5,481	5.031	2,168	0	0.000	0.328	0.007	0.014
0.575	5,031	5.476	2,072	-7	0.001	0.327	0.007	0.013
1.150	4,164	6.600	1,901	-10	0.009	0.315	0.006	0.012
1.725	3,587	7.596	1,701	-1	0.046	0.254	0.006	0.011
2.300	3,033	8.696	1,237	21	0.133	0.108	0.005	0.011
2.700	2,288	11.390	505	10	0.194	0.007	0.005	0.010

Table 28: Boundary profiles on N07L expansion nozzle outlet derived from 2D CFD calculation

r, mm	T, K	n,×10^{23} m^{-3}	v_x, m/s	v_y, m/s	x_{H2}	x_H	x_{Zr}	x_O
0.000	3,851	2.084	2,962	7	0.007	0.316	0.008	0.015
0.575	3,766	2.125	2,916	34	0.010	0.312	0.007	0.015
1.150	3,531	2.243	2,765	78	0.023	0.291	0.007	0.013
1.725	3,300	2.347	2,576	118	0.048	0.249	0.006	0.012
2.300	3,091	2.422	2,390	149	0.084	0.189	0.006	0.012
2.875	2,871	2.534	2,183	170	0.127	0.118	0.006	0.011
3.450	2,601	2.916	1,652	125	0.168	0.050	0.005	0.010
4.000	1,897	4.153	416	34	0.197	0.001	0.005	0.009

Table 29: Boundary profiles on N16L expansion nozzle outlet derived from 2D CFD calculation

r, mm	T, K	n,×10^{23} m^{-3}	v_x, m/s	v_y, m/s	x_{H2}	x_H	x_{Zr}	x_O
0.000	3,287	0.768	3,542	8	0.023	0.289	0.008	0.016
0.575	3,272	0.788	3,509	29	0.025	0.286	0.008	0.016
1.150	3,215	0.840	3,407	73	0.032	0.275	0.008	0.016
1.725	3,130	0.896	3,258	137	0.045	0.253	0.007	0.015
2.300	3,032	0.954	3,083	212	0.063	0.223	0.007	0.014
2.875	2,869	1.048	2,808	322	0.099	0.164	0.006	0.013
3.450	2,745	1.114	2,624	387	0.126	0.119	0.006	0.012
4.025	2,600	1.183	2,416	437	0.153	0.075	0.006	0.012
4.600	2,424	1.272	2,039	431	0.175	0.037	0.006	0.011
5.175	2,027	1.586	963	217	0.195	0.004	0.005	0.010
5.500	1,944	1.800	500	100	0.195	0.004	0.005	0.010

Table 30: Boundary profiles on N36L expansion nozzle outlet derived from 2D CFD calculation

r, mm	T, K	n,×10^{22} m^{-3}	v_x, m/s	v_y, m/s	x_{H2}	x_H	x_{Zr}	x_O
0.000	2,960	4.790	3,694	83	0.055	0.236	0.008	0.017
0.575	2,930	4.546	3,707	85	0.059	0.229	0.008	0.017
1.150	2,890	4.452	3,609	401	0.066	0.218	0.008	0.016
1.725	2,835	4.199	3,532	556	0.075	0.203	0.008	0.016
2.300	2,776	3.945	3,440	704	0.086	0.185	0.008	0.015
2.875	2,718	3.689	3,339	847	0.097	0.167	0.007	0.015
3.450	2,646	3.275	3,246	985	0.110	0.145	0.007	0.014
4.025	2,594	3.076	3,139	1,101	0.121	0.127	0.007	0.014
4.600	2,506	2.996	2,921	1,258	0.140	0.096	0.007	0.013
5.175	2,455	3.011	2,825	1,296	0.150	0.079	0.007	0.013
5.750	2,399	3.075	2,732	1,313	0.160	0.063	0.006	0.013
6.325	2,336	3.179	2,636	1,324	0.169	0.048	0.006	0.013
6.900	2,254	3.167	2,546	1,328	0.178	0.033	0.006	0.012
7.475	2,183	3.278	2,431	1,321	0.184	0.022	0.006	0.012
8.050	2,112	3.992	2,040	1,128	0.189	0.014	0.006	0.011
8.625	2,142	5.126	1,537	739	0.189	0.015	0.005	0.010
9.200	2,076	6.329	673	260	0.193	0.009	0.005	0.010
10.000	1,744	7.977	-15	7	0.198	0.001	0.005	0.010

Table 31: Boundary profiles on N68L expansion nozzle outlet derived from 2D CFD calculation

r, mm	T, K	n,×10^{22} m^{-3}	v_x, m/s	v_y, m/s	x_{H2}	x_H	x_{Zr}	x_O
0.000	3,726	11.18	3,431	20	0.006	0.317	0.008	0.016
0.575	3,649	11.61	3,369	188	0.009	0.314	0.008	0.016
1.150	3,556	11.91	3,300	290	0.012	0.308	0.008	0.015
1.725	3,202	11.50	3,014	643	0.042	0.259	0.007	0.014
2.300	3,148	10.51	3,036	670	0.047	0.250	0.007	0.014
2.875	2,968	9.887	2,800	916	0.077	0.201	0.006	0.013
3.450	2,718	7.452	2,548	1,241	0.121	0.128	0.006	0.012
4.025	2,695	6.843	2,575	1,262	0.123	0.125	0.006	0.013
4.600	2,436	4.902	2,248	1,592	0.161	0.061	0.006	0.012
5.175	2,426	4.589	2,280	1,603	0.161	0.061	0.006	0.012
5.750	2,122	2.849	1,919	1,913	0.187	0.018	0.006	0.012
6.325	2,128	2.731	1,959	1,916	0.186	0.019	0.006	0.012
6.900	1,683	1.833	1,600	2,136	0.197	0.001	0.006	0.011
8.050	1,483	1.301	1,389	2,119	0.198	0.000	0.006	0.011
9.200	1,501	1.260	1,431	2,137	0.198	0.000	0.006	0.011
9.775	1,387	1.183	1,219	1,962	0.198	0.000	0.005	0.011
10.350	1,383	1.134	1,267	2,012	0.198	0.000	0.005	0.011
10.925	1,507	1.012	964	1,646	0.198	0.000	0.005	0.010
11.500	1,497	0.989	1,043	1,736	0.198	0.000	0.005	0.011
12.075	1,745	0.964	651	1,120	0.197	0.002	0.005	0.010
12.650	1,840	1.238	328	460	0.196	0.004	0.005	0.010
13.800	1,806	1.585	81	83	0.196	0.003	0.005	0.010
14.375	1,755	1.775	0	0	0.197	0.002	0.005	0.010
15.000	1,728	1.934	0	0	0.197	0.001	0.005	0.010

Table 32: Boundary profiles on N90L expansion nozzle outlet derived from 2D CFD calculation

r, mm	T, K	n,×10^{23} m^{-3}	v_x, m/s	v_y, m/s	x_{H2}	x_H	x_{Zr}	x_O
0.000	7,657	3.938	2,330	2	0.000	0.327	0.008	0.016
0.575	7,122	4.191	2,252	13	0.000	0.328	0.008	0.015
1.150	5,920	4.889	2,085	28	0.000	0.329	0.007	0.013
1.725	4,188	6.426	1,863	58	0.008	0.317	0.006	0.011
2.300	3,242	6.479	1,675	235	0.091	0.178	0.005	0.011
2.700	2,080	2.207	1,232	1,121	0.195	0.005	0.005	0.010

List of Illustrations

Figure 1: Electricity demand by selected region [1].....17

Figure 2: Cutaway view of Engine Alliance GP7200 aircraft engine, photograph of a turbine blade (~10 cm long) with thermal-barrier coating (TBC) from the high-pressure hot section of the engine, and a scanning electron microscope (SEM) image of a cross-section of an electron beam physical vapor deposited 7 wt% yttria-stabilized zirconia TBC [3].....18

Figure 3: (a) TBC coating deposition on a turbine blade by APS, (b) Physical vapor jet generated during EB-PVD [4, 5] 18

Figure 4: (a) APS and (b) EB-PVD thermal barrier coatings and their schematic microstructures [6, 7].....19

Figure 5: PS-PVD process schematic [11].....19

Figure 6: Proposed process schematic.....20

Figure 7: A standard TBCs [12] 21

Figure 8: APS process schematic. Courtesy of Praxair Surface Technologies, Inc.....23

Figure 9: TBC deposited by APS [7].....23

Figure 10: Schematic CAD drawing of F4 plasma gun interior [18].....25

Figure 11: Schematic drawing of a typical plasma spray gun [18].....25

Figure 12: Arc voltage evolution (F4 plasma gun, Ar-H_2 (45-10 slm), 500 A) [27] 26

Figure 13: Schematic representation of trajectories of particles with different masses. The heavy particles cross the plasma jet, while the light particles do not enter the plasma jet core. The size distribution of the particles results in a particle flux distribution indicated in the inset figure [18] 28

Figure 14: Size distributions of commercially available YSZ powders of size ranges [39].....28

Figure 15: Scanning electron microscope (SEM) photomicrographs of typical Oerlikon-Metco agglomerated and sintered yttria-stabilized zirconium oxide materials (left - Metco 204D, right: Metco 231A) [40] 29

Figure 16: Columnar microstructures of 8YSZ-TBCs applied by SPS process. (a) Dense columnar microstructure obtained at an electric power of 40 kW; (b) dense and porosity-laminated columnar microstructure; and (c) porous columnar microstructure at an electric power of 37 kW and/or a spray distance of 85 mm [44] 30

Figure 17: SEM micrograph of a polished cross-section view of an SPPS TBC [20].....30

Figure 18: (a) EB–PVD equipment schematic [47], (b) EB–PVD ingot [50].....31

Figure 19: TBC deposited by EB–PVD process [7].....31

Figure 20: Schematic of condensate structure depending on substrate temperature T_s/T_m (T_m is the melting temperature) [50].....32

Figure 21: Images of the plasma jet expanding at different pressures (a) 95 kPa (950 mbar/APS), (b) 5 kPa (50 mbar/VPS/ LPPS), and (c) 0.1 kPa (1 mbar/PS-PVD) [8].....33

Figure 22: SEM photomicrograph of Metco 6700 spray-dried powder with d_{50}=10 µm [40]...34

Figure 23: (a) Dense TBC multilayer system consecutively build-up with PS-PVD technology [54], and (b) TBC multilayer with a columnar structured EB-PVD-like coating on top of the dense ceramic interlayer and metallic bond coat as deposited subsequently with PS-PVD technology [54] 34

Figure 24: Factors influencing the coating properties in plasma spray process [18] 34

Figure 25: PS-PVD structure zone model [55] 35

Figure 26: Structure spatial distribution model (SSDM) of PS-PVD YSZ coatings [56] 36

Figure 27: Photographs of PS-PVD plasma jets using different gas compositions; on the left without any powder, on the right with YSZ powder injection. Chamber pressure and net power input were kept constant at 200 Pa and 60 kW, respectively, in all cases; the numbers denote the argon, helium and hydrogen flows (slpm) as well as the arc currents (A) [58] 37

Figure 28: Calculated enthalpy transferred to spherical particles for three investigated plasma parameters as a function of the particle diameter; the horizontal lines indicate the mass-specific enthalpies which are required to melt and evaporate the particles, respectively [57] 37

Figure 29: Schematic CAD design of two nozzles (left – short anode nozzle, right – long anode nozzle) [61] 38

Figure 30: Schematic of the proposed system 41

Figure 31: Physical phenomena associated with the proposed system 43

Figure 32: Different stages of departure from thermodynamic equilibrium in thermal plasmas [30] 45

Figure 33: Schematic of the large-scale turbulence and cold gas entrainment in a plasma jet issuing into a cold gas environment [18] 47

Figure 34: Hundred consecutive measurements of the peak temperature [18] 47

Figure 35: Equilibrium compositions of Ar/H_2 mixture (left) and ZrO_2 vapor (right) at 1 atm [86] 53

Figure 36: Specific heat and viscosity of 80 vol%Ar/20 vol%H_2 gas mixture at 100 Pa and 10^5 Pa [86] 54

Figure 37: Supersonic nozzle [98] 57

Figure 38: (a) - Supersonic under-expanded plasma jet structure: I – initial zone, II – transitional zone, III – main zone, 1 – free expansion region, 2 – jet boundary layer, 3 – plane where pressure inside of the jet equalizes with chamber pressure, 4 – jet boundary, 5 – radial profiles of velocity [105]; (b) - Wave structures in the initial region of the underexpanded flow [106] 59

Figure 39: Photograph of PS-PVD plasma jets emitted from 03CP plasma torch. Chamber pressure and net power input were kept constant at 200 Pa and 60 kW [58] 60

Figure 40: The flowchart for the DS2V program [124] 63

Figure 41: Maxwellian distribution functions for the molecular velocity and for a molecular velocity component 65

Figure 42: Collision scheme of two hard sphere molecules 67

Figure 43: Intermolecular force field 67

Figure 44: Degrees of freedom of a diatomic molecule 69

Figure 45: (a) Calculated spray patterns for particles passing through a plane 10 cm from the torch face. The effects of velocity dispersion and turbulence are considered individually; (b) Particle injection directions [126] 73

Figure 46: (a) Temperature fluctuation of alumina particles as a function of time delay. (b) Fluctuation of the average velocity of alumina particles as a function of time delay. Error bars are the 1 σ confidence interval on the mean value. Numerical data are the sample standard deviations. The measurements were done at the torch axis, at 50 mm from the torch exit [28]. 73

Figure 47: Schematic showing the nomenclature used to specify particle injection directions [126] 80

Figure 48: Schematic of homogeneous nucleation and growth process by cooling of metallic vapor. States corresponding to different vapor temperatures are depicted, the temperature decreases from left to right [142] 82

Figure 49: Schematic of cluster and vapor deposition process [11] 82

Figure 50: Equilibrium compositions ZrO_2 vapor at 100 Pa and 1 atm 82

Figure 51: Heterogeneous nucleation schematic [139] 87

Figure 52: Schematic of PS modeling 92

Figure 53: Proposed system schematic with highlighted CFD domains 92

Figure 54: 3D CFD computational domain 96

Figure 55: Schematic of the experiment to verify particle size evolution prediction. Water tank surface was equal to 0.2 × 0.3 m^2 99

Figure 56: Equilibrium zirconia vapor composition at 1 atm 101

Figure 57: Model validation results. Left column: results (concentration, size) produced by the original model by Nemchinsky and Shigeta (PM) [145] in comparison with the results obtained with the method of moments (MOM) by Girshick [163]. Right column: results produced by the current implementation of the model. The red line starts at $\tau = 5$, as the initial time step is equal to 5 106

Figure 58: CFD computational domain for the nozzle. HPC – high pressure chamber, LPC – low pressure chamber 106

Figure 59: A Thin Wall boundary condition 107

Figure 60: DSMC computational domain used for the SPARTA validation on Selezneva's data [73] (dimensions are in mm) 110

Figure 61: Variation of plasma gas temperature and gas velocity along the torch axis 111

Figure 62: Experimental setup used for plasma temperature measurements 112

Figure 63: CFD computational domain used for the SPARTA validation on data from He and Mauer (sizes in mm) 113

Figure 64: DSMC computational domain used for the SPARTA validation on data from He and Mauer (sizes in mm) 113

Figure 65: Comparison of temperature fields obtained with CFD and DSMC simulations. Photo: RGB color interpretation, no units....114

Figure 66: Hydrogen temperatures (left) and species temperatures (right) along the torch axis starting from the torch outlet....115

Figure 67: Knudsen number along the torch axis starting from the torch outlet....116

Figure 68: Comparison of temperatures in the radial direction at 500 mm (left) and 800 mm (right) from the torch outlet....116

Figure 69: Equilibrium zirconia vapor composition at 100 Pa....117

Figure 70: DSMC computational domain....117

Figure 71: Schematic of PS modeling....122

Figure 72: Flowchart of calculation activities....122

Figure 73: Dimensions of 3D CFD model of the high pressure chamber (in mm)....125

Figure 74: Particle trajectories for various powder injections. Color represents particle diameter (m). Higher dispersion is observed for finer powders....126

Figure 75: Evolution of particle diameters along particle trajectories. 10 particles are injected. The plots start at 0.02 m – a location that approximately corresponds to the location of injector outlet. Turbulent dispersion is disabled....126

Figure 76: (a) Temperature (K) and (b) velocity (m/s) fields in HPC predicted by 3D CFD model....127

Figure 77: Expansion nozzle dimensions....128

Figure 78: Dimensions of 2D CFD model of the high pressure chamber and expansion nozzle coated with zirconia layer (in mm). 45 degrees hatch pattern is applied to the coating....129

Figure 79: (a) Species source (kg/s) and (b) enthalpy source (W) fields, obtained from 3D CFD calculation. Negative enthalpy source signifies the region where heat transfers from plasma to particles, positive enthalpy – heat transfer in the reverse direction, since particle temperature exceeds the one of the plasma jet....131

Figure 80: Maximal temperature of zirconia coating along the walls of HPC and expansion nozzle, obtained from 2D CFD calculation....131

Figure 81: Contours of pressure (Pa) inside of the expansion nozzle predicted by 2D CFD model....132

Figure 82: Streamlines inside off the expansion nozzle....132

Figure 83: Physical vapor species (monomer) concentrations inside of the expansion with (right) and without (left) considering nucleation and growth processes....134

Figure 84: G-mer concentration and size inside of the expansion nozzle....134

Figure 85: Expansion nozzle clogging rates....134

Figure 86: Pumping speed characteristics of SOGEVAC SV630 BF [169]....136

Figure 87: G-mer concentration inside of the expansion nozzle....137

Figure 88: Logarithm of number of monomers in a g-mer 138
Figure 89: Nozzle clogging rates. Gray region indicates the low accuracy of the results.....139
Figure 90: Average dimensionless clogging rates of nozzle walls.....140
Figure 91: Average nuclei volume on the nozzle outlet expressed in a number of monomers per nucleus.....140
Figure 92: Fraction of zirconia mass that stayed in vapor phase upon reaching the nozzle outlet 141
Figure 93: Fraction of zirconia mass that got adsorbed by the nozzle walls.....141
Figure 94: Dimensions of 2D DSMC model of the low pressure chamber (in mm).....142
Figure 95: Results of 2D DSMC simulation for case N07L (α_{div}=7.4°, p_{LPC}=100 Pa) 144
Figure 96: Oxygen to zirconium number density ratio in case N07L (α_{div}=7.4°, p_{LPC}=100 Pa) 145
Figure 97: Knudsen number field in case N07L (α_{div}=7.4°, p_{LPC}=100 Pa).....145
Figure 98: Streamlines used for nucleation and growth analyses in case N07L (α_{div}=7.4°, p_{LPC}=100 Pa).....145
Figure 99: Temperatures, initial physical vapor number densities and supersaturation ratios along streamlines in case N07L (α_{div}=7.4°, p_{LPC}=100 Pa) 146
Figure 100: Resulting physical vapor concentrations, g-mer concentrations, g-mer sizes and supersaturation ratios along streamlines in case N07L (α_{div}=7.4°, p_{LPC}=100 Pa) 147
Figure 101: Results of 2D DSMC simulations for p_{LPC}=100 Pa cases 149
Figure 102: Resulting Mach number fields and streamlines for nucleation and growth predictions for p_{LPC}=100 Pa cases 150
Figure 103: Temperatures, initial physical vapor number densities and supersaturation ratios along streamlines (p_{LPC}=100 Pa).....151
Figure 104: Resulting physical vapor concentrations, g-mer concentrations and g-mer sizes along streamlines for p_{LPC}=100 Pa cases.....152
Figure 105: Knudsen number field in case N07H (α_{div}=7.4°, p_{LPC}=1,000 Pa) 153
Figure 106: Results of 2D DSMC simulations for p_{LPC}=1,000 Pa cases.....154
Figure 107: Resulting Mach number fields and streamlines for nucleation and growth predictions for p_{LPC}=1,000 Pa cases 155
Figure 108: Temperatures, initial physical vapor number densities and supersaturation ratios along streamlines (p_{LPC}=1,000 Pa).....156
Figure 109: Resulting physical vapor concentrations, g-mer concentrations and g-mer sizes along streamlines for p_{LPC}=1,000 Pa cases.....157
Figure 110: Refined expansion nozzle dimensions (in mm).....158
Figure 111: A view showing plasma jets crossing, together with the resulting plasma and filtered solid particles [156].....162

List of Tables

Table 1: Operating parameters of APS, EB-PVD and PS-PVD processes [12, 17, 47, 63] ...39

Table 2: Deposition characteristics of APS, EB-PVD and PS-PVD processes [8, 12, 17, 47, 49, 63–70] ...40

Table 3: Qualitative comparison of the flow conditions in the different parts of the proposed system with reference to the standard conditions (low temperature, high pressure, zero gradients, very small mean free path, local thermal equilibrium, no turbulence) ...44

Table 4: General CFD boundary conditions for 3D CFD Model. n and τ correspond to normal and tangent vector components ...98

Table 5: APS operating parameters for desecrate phase model verification ...99

Table 6: Parameters of homogeneous N&G model ...103

Table 7: General DSMC boundary conditions...109

Table 8: Operating parameters of Selezneva's experimental setup ...110

Table 9: DSMC boundary conditions used for validation based on Selezneva's data ...110

Table 10: Operating parameters of the experimental setup of He and Mauer ...112

Table 11: Summarized CFD boundary conditions for SPARTA validation...113

Table 12: DSMC boundary conditions used for validation on He's data...114

Table 13: Torch operating parameters...124

Table 14: CFD boundary conditions for 3D CFD Model ...125

Table 15: Evaporation degrees and evaporation distances of various powders ...127

Table 16: Summary of initial dimensions of the expansion nozzle (dimensions are in mm).129

Table 17: CFD boundary conditions for 2D CFD Model ...130

Table 18: Summary of refined dimensions of the expansion nozzle...135

Table 19: List of the varied parameters of the expansion nozzle and low pressure chamber ...136

Table 20: DSMC boundary conditions for case N07L ...143

Table 21: Drag coefficients at different flow regimes [18]...178

Table 22: Lennard-Jones model parameters [155, 171]...178

Table 23: Properties of solid and liquid ZrO_2 [137] ...178

Table 24: VSS collision model parameters under standard conditions (p_{ref}=101,325 Pa, T_{ref}=273.15 K) except Zr (T_{ref}=2,000 K) [123, 172, 173]...179

Table 25: Chemical reactions in Ar-H_2 plasma [174]...179

Table 26: Parameters of Ar and H_2 species used in DSMC calculations [123, 175] ...179

Table 27: Boundary profiles on N00L expansion nozzle outlet derived from 2D CFD calculation ...181

Table 28: Boundary profiles on N07L expansion nozzle outlet derived from 2D CFD calculation 181
Table 29: Boundary profiles on N16L expansion nozzle outlet derived from 2D CFD calculation 181
Table 30: Boundary profiles on N36L expansion nozzle outlet derived from 2D CFD calculation 182
Table 31: Boundary profiles on N68L expansion nozzle outlet derived from 2D CFD calculation 183
Table 32: Boundary profiles on N90L expansion nozzle outlet derived from 2D CFD calculation 183

Modélisation et dimensionnement d'un procédé de dépôt physique en phase vapeur assisté par plasma thermique

Le procédé de dépôt physique en phase vapeur assisté par plasma thermique (PS-PVD) consiste à évaporer le matériau sous forme de poudre à l'aide d'un jet de plasma d'arc soufflé pour produire des dépôts de structures variées obtenus par condensation de la vapeur et/ou dépôt des nano-agrégats. Dans le procédé de PS-PVD classique, l'intégralité du traitement du matériau est réalisée dans une enceinte sous faible pression, ce qui limite les phénomènes d'évaporation ou nécessite d'utiliser des torches de puissance importante. Dans ce travail, une extension du procédé de PS-PVD conventionnel à un procédé à deux enceintes est proposée puis explorée par voie de modélisation et de simulation numérique : la poudre est évaporée dans une enceinte haute pression (10^5 Pa) reliée par une tuyère de détente à une enceinte de dépôt basse pression (100 ou 1 000 Pa), permettant une évaporation énergétiquement plus efficace de poudre de Zircone Yttriée de granulométrie élevée, tout en utilisant des torches de puissance raisonnable. L'érosion et le colmatage de la tuyère de détente peuvent limiter la faisabilité d'un tel système. Aussi, par la mise en œuvre de modèles numériques de mécanique des fluides et basé sur la théorie cinétique de la nucléation et de la croissance d'agrégats, on montre que, par l'ajustement des dimensions du système et des paramètres opératoires ces deux problèmes peuvent être contournés ou minimisés. En particulier, l'angle de divergence de la tuyère de détente est optimisé pour diminuer le risque de colmatage et obtenir le jet et le dépôt les plus uniformes possibles à l'aide des modèles susmentionnés, associés à un modèle DSMC (Monte-Carlo) du flux de gaz plasmagène raréfié. Pour une pression de 100 Pa, les résultats montrent que la barrière thermique serait formée par condensation de vapeur alors que pour 1 000 Pa, elle serait majoritairement formée par dépôt de nano-agrégats.

Mots-clés : PS-PVD, plasma, nucléation-croissance, modélisation-simulation numérique, dépôt, barrières thermique

Modeling and design of a physical vapor deposition process assisted by thermal plasma (PS-PVD)

Plasma Spray Physical Vapor Deposition (PS-PVD) aims to substantially evaporate material in powder form by means of a DC plasma jet to produce coatings with various microstructures built by vapor condensation and/or by deposition of nanoclusters. In the conventional PS-PVD process, all the material treatment takes place in a medium vacuum atmosphere, limiting the evaporation process or requiring very high-power torches. In the present work, an extension of conventional PS-PVD process as a two-chamber process is proposed and investigated by means of numerical modeling: the powder is vaporized in a high pressure chamber (10^5 Pa) connected to the low pressure (100 or 1,000 Pa) deposition chamber by an expansion nozzle, allowing more energetically efficient evaporation of coarse YSZ powders using relatively low power plasma torches. Expansion nozzle erosion and clogging can obstruct the feasibility of such a system. In the present work, through the use of computational fluid dynamics, kinetic nucleation theory and cluster growth equations it is shown through careful adjustment of system dimensions and operating parameters both problems can be avoided or minimized. Divergence angle of the expansion nozzle is optimized to decrease the clogging risk and to reach the most uniform coating and spray characteristics using the aforementioned approaches linked with a DSMC model of the rarefied plasma gas flow. Results show that for 100 Pa, the thermal barrier coating would be mainly built from vapor deposition unlike 1,000 Pa for which it is mainly built by cluster deposition.

Keywords: PS-PVD, modeling, numerical simulation, continuum breakdown, nucleation and growth, CFD, DSMC, coating, thermal barrier coatings (TBC)